



Universitat Autònoma de Barcelona

**ADVERTIMENT.** L'accés als continguts d'aquesta tesi queda condicionat a l'acceptació de les condicions d'ús establertes per la següent llicència Creative Commons:  [http://cat.creativecommons.org/?page\\_id=184](http://cat.creativecommons.org/?page_id=184)

**ADVERTENCIA.** El acceso a los contenidos de esta tesis queda condicionado a la aceptación de las condiciones de uso establecidas por la siguiente licencia Creative Commons:  <http://es.creativecommons.org/blog/licencias/>

**WARNING.** The access to the contents of this doctoral thesis it is limited to the acceptance of the use conditions set by the following Creative Commons license:  <https://creativecommons.org/licenses/?lang=en>



# **Plasmon-enhanced catalytic reactions for renewable fuels**

**Viktoria Golovanova**

**Tesi doctoral**

Programa de doctorat en Ciència de Materials

**Directors:** Prof. Joan Ramón Morante, Dra. Teresa Andreu

**Tutor:** Prof. Jordi Arbiol

Departament de Física

Facultat de Ciències

2022





Memòria presentada per aspirar al Grau de Doctor per

**Viktoria Golovanova**

Vist i plau

Prof. Joan Ramón Morante  
(Director)

Dra. Teresa Andreu  
(Directora)

Prof. Jordi Arbiol  
(Tutor)

Barcelona, 23 de maig de 2022



El **Dr. Joan Ramón Morante Leonart**, director del Institut de Recerca en Energia de Catalunya i Catedràtic d'Universitat del Departament d'Enginyeria Electrònica i Biomèdica de la Universitat de Barcelona

la **Dra. Teresa Andreu Arbella**, Professora Lectora del Departament de Ciència de Materials i Química Física de la Universitat de Barcelona,

i el **Dr. Jordi Arbiol Cobos**, Professor ICREA de Institut Català de Nanociència i Nanotecnologia,

**CERTIFIQUEN:**

Que Viktoria Golovanova ha realitzat sota la seva direcció el treball d'investigació que s'exposa a la memòria titulada "Plasmon-enhanced catalytic reactions for renewable fuels" per optar al grau de Doctor per la Universitat Autònoma de Barcelona.

Que el disseny dels experiments, síntesi de mostres, llur caracterització, l'anàlisi dels resultats, la redacció dels articles i d'aquesta memòria són fruit del treball d'investigació realitzat per Viktoria Golovanova.

I perquè així consti, signen el present certificat,

Prof. Joan Ramón Morante

Dra. Teresa Andreu

Prof. Jordi Arbiol

Barcelona, 23 de maig de 2022



---

*“In my life I have found two things of priceless worth - learning and loving. Nothing else - not fame, not power, not achievement for its own sake - can possibly have the same lasting value. For when your life is over, if you can say 'I have learned' and 'I have loved,' you will also be able to say 'I have been happy.’”*

— Arthur C. Clarke, Rama II

---

*“Science is no more than an investigation of a miracle we can never explain, and art is an interpretation of that miracle.”*

— Ray Bradbury, The Martian Chronicles

---

- Ross: *I’m Doctor Ross Geller.*
- Rachel: *Ross, please. This is a hospital, okay? This actually means something here.*

— Friends, S10E13

---





## Acknowledgments

I am truly thankful to so many people that made my PhD possible, despite hard times and moments of doubt. As a theoretical physicist, it was a challenge for me to enter an unknown field of experimental chemistry, but the experience and knowledge I gained during this path is priceless. I feel that I have learnt much more than a new field, and have become a stronger person thanks to everyone along the way.

First of all, I would like to thank my directors, Prof. Joan Ramón Morante and Dra. Teresa Andreu for this great opportunity to perform a work in a new challenging topic and the trust that you put in me. Joan Ramón, your deep knowledge and bold ideas are always inspiring, and I hope to use the experience I gained from you further on. Teresa, you are a true example of a perfect combination of a sharp scientist and a kind sensitive person. I am very lucky to have worked with you and I hope that our way will intersect many times in the future as well. I also want to say thank you to Prof. Jordi Arbiol, who was the tutor of my thesis, for his valuable advices and fruitful collaboration.

I am very thankful to IREC and especially the ESEH group. You are indeed the best people to spend working hours, discuss interesting subjects, share coffee and lunches. Thank you, all the current and ex-members of this group that I had the pleasure to work with: Nina, Sebastián, Elias, Marisa, Antonio, Jordi J., Jordi G., Elena, Paolo, Lorenzo, Hemesh, Kuba, José Miguel, Martí, Carles, Monalisa, Tandava, Marcelo, Andreina.

I want to thank the DOC-FAM team, every 21 of you. Sohini and Fabiã, thank you for being amazing friends and reaching out for me always even when I am lazy to do so. And of course to Monalisa and Tandava, who have shared so many good moments with me inside and outside the lab. Tandava, I am waiting for your wedding to visit India!

I am also grateful to my dear friends from other groups in IREC, especially Solar and NI groups for best parties and volleyball games. Angélica, you are the most socially active and the most cheerful scientist I know, thank you for your positive vibes. Maxim, thank you for your sincere support and understanding, which helped me to go through difficult times, огромное спасибо. Alex, thanks for sharing amazing food and lots of fun moments.

Quiero decir muchas gracias a Kele por ayudarme con mis primeros pasos en el doctorado, y ser mi grande motivación para aprender castellano. Gràcies a Carles por creer en mi y también organizar las mejores calçotadas en Catalunya. A Martí

## Acknowledgements

---

por ser el ángel de la guarda de nuestro lab y a Dioudlé y Albert por ser los ángeles de la guarda de todo el IREC. Gracias a Francisco por ser un loco adicto al trabajo y compartir los fines de semana trabajando conmigo, y a Diogo por alimentarme cuando yo estaba perdida en trabajo.

Muchas gracias a Santi por su invaluable apoyo. No tengo palabras para describir lo importante que ha sido tu aporte, especialmente durante los últimos pasos. Marce, eres el menos latino que puedas imaginar, pero el mejor amigo. Andres, eres única, y no hay mucho más que añadir. Estoy infinitamente agradecida por su sincera amistad y espero que sepan lo importantes que son para mí.

Huge shoutout to my friends from Ukraine, especially the D&D&X3 group. Витя, Кирилл, Леся, Женя, Костя, Даша, а также Ксюша, Митя, Богдан, Андрей и Леша: огромное спасибо за вашу поддержку и дружбу на протяжении стольких лет. Ребята, мир обязательно наступит! И тогда мы снова встретимся с вами в любой точке земного шара, чтобы обсуждать странные темы и играть в настолки.

And lastly, I want to express my gratitude to my family, for constant support, life and scientific advices and the chance to live a life full of joy and opportunities. To my mom, who is the most frank person on the entire planet and my brilliant dad, who became the reason I chose this scientific path. Many thanks to my sister and her family for being such a joyful part of my life. And separate thank you to my grandmother, for her deep understanding and kind heart.

I gratefully acknowledge the European Union's Horizon 2020 research and innovation programme under the Marie Skłodowska-Curie grant agreement No. 754397 (DOC-FAM) for financial support of this thesis. This work was partially supported by the projects CCU+OX (PID2019-108136RB-C33) and CERES (PID2020-116093RB-C42) funded by MCIN/AEI/10.13039/501100011033/, MINECO projects WINCOST (ENE2016-80788-C5-5-R) and RESOL (ENE2017-85087-C3). The experimental work was mostly performed at IREC who acknowledges Generalitat de Catalunya for financial support through the CERCA Programme, M2E (2017 SGR 1246).

I would also like to express my gratitude to several research groups and their leaders that have given me the opportunity to perform a substantial part of my experiments, learn new techniques and become a part of their teams. I sincerely thank Prof. Jordi Martorell and Organic Nanostructured Photovoltaics group at ICFO, Prof. Nikolai Tkachenko and Chemistry and Advanced Materials (CAM) group of Tampere University, and Prof. Jordi Ignés-Mullol and SOC&SAM group of University of Barcelona for this amazing working experience and productive collaboration.

I also wish to thank Prof. Sara Bals and EMAT research group of University of Antwerp and Prof. Jordi Arbiol and Advanced Electron Nanoscopy group of ICN2 for the in-situ microscopy measurements and data analysis.

Lastly, I would like to acknowledge the Autonomous University of Barcelona for the academic support and tutoring in the framework of the doctorate programme in Materials Science.



# Index

<b>Preface</b> .....	i
Abstract.....	ii
Resumen .....	iv
Resum .....	vi
List of abbreviations.....	viii
<b>Chapter 1. Introduction</b> .....	1
1.1. General introduction.....	2
1.2. Light in catalysis.....	7
1.2.1. Catalysis overview.....	7
1.2.2. Catalytic approaches.....	8
1.2.3. Application of solar light in catalytic reactions.....	9
1.3. Plasmons.....	13
1.3.1. Bulk plasmons and plasmonic materials.....	13
1.3.2. Surface plasmon polariton.....	16
1.3.3. Localized surface plasmons.....	18
1.3.4. Mechanisms of plasmon decay.....	20
1.4. Catalytic reactions for renewable fuels.....	23
1.4.1. CO <sub>2</sub> methanation.....	23
1.4.2. Hydrogen evolution reaction (HER) .....	26
1.5. Plasmon-enhanced catalysis.....	29
1.5.1. Plasmon-enhanced CO <sub>2</sub> methanation.....	29
1.5.2. Plasmon-enhanced electrochemical reactions.....	31
1.5.3. Disentangling photothermal and charge-induced catalytic enhancements .....	32
1.6. Objectives of the thesis .....	33
1.7. References.....	35

---

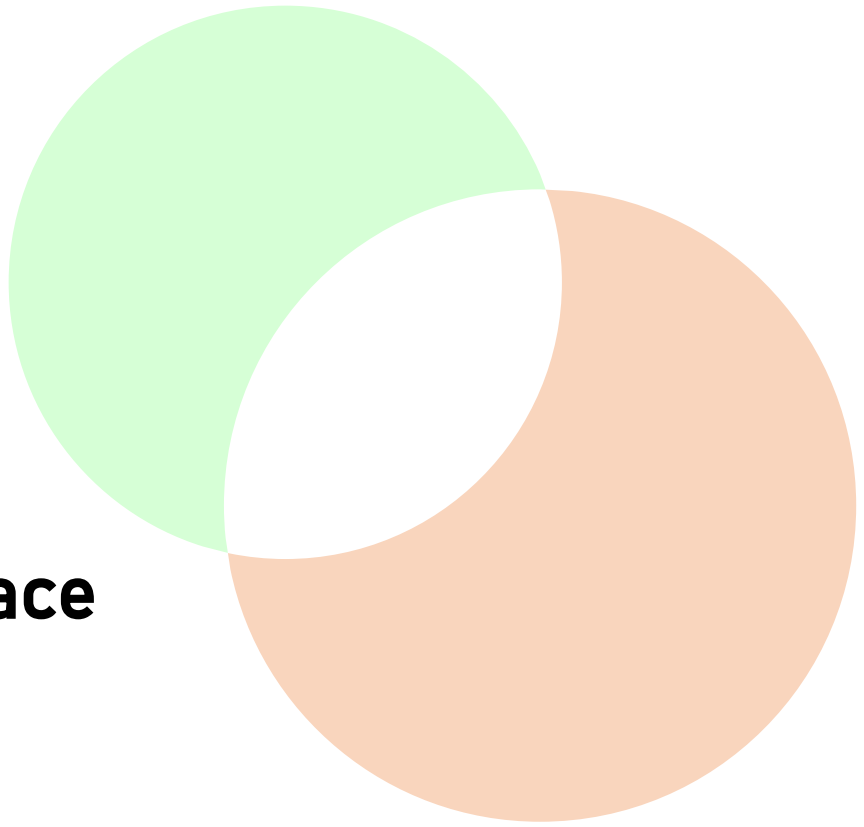
<b>Chapter 2. Plasmonic Ni/CeO<sub>2</sub>-based catalyst for light-assisted thermal methanation of CO<sub>2</sub></b> .....	48
2.1. Introduction .....	49
2.2. Experimental methodology .....	51
2.2.1. Catalyst preparation .....	51
2.2.2. Reactor setup .....	52
2.2.3. Evaluation of catalytic properties .....	54
2.2.4. Characterization techniques .....	55
2.3. Ni/CeO <sub>2</sub> hybrid catalyst characterization .....	58
2.3.1. Physical characterization of the catalyst.....	58
2.3.2. Ni/CeO <sub>2</sub> catalytic performance in the CO <sub>2</sub> methanation reaction .....	64
2.3.3. Photothermal effects .....	64
2.3.4. DRIFTS characterization .....	67
2.3.5. In-situ HRTEM/EELS study.....	69
2.4. Mechanism of photothermal CO <sub>2</sub> methanation.....	73
2.5. Energy consumption evaluation .....	80
2.6. Conclusions .....	82
2.7. References .....	83
<b>Chapter 3. Photothermal approach to enhance hydrogen production via water splitting</b> .....	86
3.1. Introduction.....	87
3.2. Experimental methods.....	89
3.2.1. Synthesis of the Ni/SBA-15 nanoparticles .....	89
3.2.2. Electrode preparation .....	89
3.2.2. Photoelectrochemical characterization setup.....	90
3.3. Characterization of the plasmonic Ni/SBA-15 nanoparticles .....	91
3.3.1. Physicochemical characterization.....	91
3.3.2. Photothermal characterization of the Ni nanoparticles .....	92

3.4. Photothermal effects on HER.....	94
3.5. Mechanism of photothermal HER enhancement .....	97
3.5.1. Pulsed illumination.....	97
3.5.2. Mechanism.....	99
3.6. Evaluation of the HER enhancement .....	101
3.7. Conclusions.....	103
3.8. References .....	104
<b>Chapter 4. Nanostructured plasmonic nickel films for electrochemical applications.....</b>	<b>106</b>
4.1. Introduction.....	107
4.2. Experimental methods.....	109
4.2.1. Synthesis of metallic NHAs.....	109
4.2.2. Photoelectrochemical and optical characterization setup .....	111
4.2.3. Theoretical calculations .....	112
4.3. Langmuir PS films.....	115
4.4. Morphology of metallic NHAs.....	117
4.5. Optical properties of metallic nanohole arrays.....	119
4.5.1. General characterization.....	119
4.5.2. Effect of geometric parameters on the NHA optical properties.....	123
4.6. Electrochemical measurements .....	126
4.7. Mechanism of the reaction enhancement.....	130
4.8. Conclusions.....	132
4.9. References .....	133
<b>Chapter 5. Conclusions and outlook .....</b>	<b>136</b>
5.1. Conclusions.....	137
5.2. Outlook and future work .....	140



---

<b>Appendix A</b> .....	142
Appendix A.1. Supplementary catalyst characterization .....	143
Appendix A.2. Transmission spectra of the optical long-pass filters .....	146
Appendix A.3. Supplementary in-situ HRTEM/EELS characterization .....	148
<b>Appendix B</b> .....	150
Appendix B.1. Supplement catalyst characterization .....	151
<b>Appendix C</b> .....	154
Appendix C.1. Theoretical calculations of the plasmon resonance wavelength angular dependence in the hexagonal metallic NHA. ....	155
Appendix C.2. Supplementary characterization results .....	157
Appendix C.3. Numerical modeling of metallic NHA optical properties.	160
<b>Curriculum vitae</b> .....	164



# **Preface**

## Abstract

Depletion of fossil fuels and global warming caused by excessive carbon emissions has led to urgent transition to renewable energy sources (RES). However, out of all the existing RES only solar energy is able to meet the steadily growing world energy demands. The unpredictable behavior of RES requires high-capacity and long-term energy storage technologies, one of the solutions to which is the “power-to-gas” technology, which uses green electricity to generate hydrogen and convert CO<sub>2</sub> to methane.

In this context, utilization of solar light as an additional green energy source in catalytic reactions for renewable fuels production is a challenging task, which requires new approaches to catalyst and reactor design. Plasmon-assisted catalysis, being a hot emerging field due to facile tunability of plasmonic catalyst’s optical properties, usually requires expensive noble metals to ensure large plasmon lifetimes for electron-induced effects. Given the scarcity of noble metals, there appeared a need in the search for alternative plasmonic materials, which would simultaneously satisfy requirements for optical and catalytic applications. Up to now, few works have emphasized the importance of plasmon heating as the main consequence of the excited plasmon in catalytic materials, although the interest to photothermal catalysis is constantly growing. Due to the above reasoning, nickel (Ni) is an excellent candidate for plasmon-enhanced catalytic applications, being an abundant transition metal with a beneficial combination of outstanding catalytic and photothermal properties.

The main objectives of this work are i) the design of Ni-based plasmonic catalysts for renewable fuels reactions (CO<sub>2</sub> methanation and hydrogen evolution reaction -HER-), ii) their structural, optical and functional study in order to identify optimal reaction conditions and quantify the light-assisted reaction gain, and iii) defining the mechanisms of the reaction enhancement. According to the stated objectives, the performed work is divided in 4 chapters. In the first chapter of the thesis, a general overview of the problem and fundamental concepts are presented. This chapter includes the description of the main light-assisted catalytic approaches, background of plasmon theory in metals and provides a state of the art in plasmon-enhanced CO<sub>2</sub> methanation and HER. The second chapter is devoted to developing of Ni/CeO<sub>2</sub> catalyst for light-assisted CO<sub>2</sub> methanation and investigation of plasmon-induced mechanism of reaction enhancement. The synthesis procedure ensured high surface area of the catalyst, which resulted in high CO<sub>2</sub> conversion (80%) and selectivity to methane (95%). Light-assisted methanation demonstrated a 2.4-fold increase in the reaction rate, leading to a decrease in power consumption by 20%.

In-situ characterization techniques revealed a dual effect of solar irradiation on the hybrid Ni/CeO<sub>2</sub> catalyst, confirming the presence of both photothermal and electronic effects due to complementary light interaction of both components of the catalyst.

The third chapter presents a study on plasmonic Ni nanoparticles with enhanced absorption in the visible light range and their application as a photocathode for HER. Strong photothermal effect of the synthesized nanoparticles on the reaction rate allowed to increase the hydrogen production by 27% after encountering optimal conditions. Similarly, the reaction overpotential was decreased by 185 mV without any significant overall heating of the cell. Dark and illuminated measurements have shown a clear difference between the conventional heating and photothermal effect on the HER enhancement. Periodic pulsed illumination was employed to identify the mechanism of light-induced drop of the overpotential, which was divided into two main processes: i) enhanced electron transfer due to strong plasmonic heating and ii) thermal energy dissipation from the electrode to the electrolyte.

The fourth chapter is devoted to optical study of Ni nanohole arrays (NHA) and utilization of their surface plasmon in iodate reduction reaction. Tunable hollow-mask lithography method used in NHAs fabrication implied precise tuning of their geometrical parameters and, therefore, optimization of their optical properties. Dependence of the extraordinary transmission (EOT) peaks on the incident angle and hole diameter allowed to identify surface and localized plasmon modes. Wavelength-dependent photocurrent study under pulsed laser irradiation of flat and structured photocathodes with respect to its optical spectra proved the photothermal plasmonic nature of the reaction enhancement.

## Resumen

El agotamiento de los combustibles fósiles y el calentamiento global causado por las emisiones excesivas de carbono ha llevado hacia una transición urgente hacia las fuentes de energía renovables (FER). Sin embargo, de todas las FER existentes, solo la energía solar es capaz de satisfacer la creciente demanda mundial de energía. El comportamiento impredecible de las FER requiere tecnologías de almacenamiento de energía a largo plazo y de alta capacidad, siendo la tecnología “power-to-gas” una de las soluciones, que utiliza electricidad verde para generar hidrógeno y convertir el CO<sub>2</sub> en metano.

En este contexto, la utilización de la luz solar como fuente de energía verde adicional en reacciones catalíticas para la producción de combustibles renovables es una tarea desafiante que requiere de nuevos enfoques para el diseño de catalizadores y reactores. La catálisis asistida por plasmones, al ser un campo emergente candente debido a la facilidad de ajuste de las propiedades ópticas del catalizador plasmónico, generalmente requiere metales nobles costosos para garantizar una vida prolongada de los plasmones para los efectos inducidos por electrones. Dada la escasez de metales nobles, surgió la necesidad de buscar materiales plasmónicos alternativos, que satisficieran simultáneamente los requisitos para aplicaciones ópticas y catalíticas. Hasta el momento, pocos trabajos han destacado la importancia del calentamiento de plasmones como principal consecuencia del plasmón excitado en materiales catalíticos, aunque el interés por la catálisis fototérmica es cada vez mayor. Debido al razonamiento anterior, el níquel (Ni) es un excelente candidato para aplicaciones catalíticas mejoradas con plasmones, ya que es un metal de transición abundante con una combinación beneficiosa de excelentes propiedades catalíticas y fototérmicas.

Los objetivos principales de este trabajo son i) el diseño de catalizadores plasmónicos basados en Ni para reacciones de combustibles renovables (metanación de CO<sub>2</sub> y reacción de evolución de hidrógeno -HER-), ii) su estudio estructural, óptico y funcional para identificar las condiciones óptimas de reacción y cuantificar las mejoras de la reacción asistida por luz, y iii) definir los mecanismos de mejora de la reacción. De acuerdo con los objetivos planteados, el trabajo realizado se divide en 4 capítulos. En el primer capítulo de la tesis se presenta un panorama general del problema y conceptos fundamentales. Este capítulo incluye la descripción de los principales enfoques catalíticos asistidos por luz, los antecedentes de la teoría de plasmones en metales y proporciona un estado del arte en metanación de CO<sub>2</sub> mejorada con plasmones y HER. El segundo capítulo está dedicado al desarrollo del catalizador de Ni/CeO<sub>2</sub> para la metanación de CO<sub>2</sub> asistida

por luz y la investigación del mecanismo de mejora de la reacción inducido por plasmones. El procedimiento de síntesis aseguró una alta área superficial del catalizador, lo que resultó en una alta conversión de  $\text{CO}_2$  (80 %) y selectividad al metano (95 %). La metanación asistida por luz demostró un aumento de 2,4 veces en la velocidad de reacción, lo que llevó a una disminución del consumo de energía en un 20 %. Las técnicas de caracterización in situ revelaron un efecto dual de la radiación solar sobre el catalizador híbrido Ni/CeO<sub>2</sub>, lo que confirma la presencia de efectos fototérmicos y electrónicos debido a la interacción de luz complementaria de ambos componentes del catalizador.

El tercer capítulo presenta un estudio sobre nanopartículas plasmónicas de Ni con absorción mejorada en el rango de luz visible y su aplicación como fotocátodo para HER. El fuerte efecto fototérmico de las nanopartículas sintetizadas sobre la velocidad de reacción permitió aumentar la producción de hidrógeno en un 27 % después de encontrar las condiciones óptimas. De manera similar, el sobrepotencial de reacción se redujo en 185 mV sin ningún calentamiento general significativo de la celda. Las mediciones con luz y oscuridad han mostrado una clara diferencia entre el calentamiento convencional y el efecto fototérmico en la mejora de HER. Se empleó iluminación pulsada periódica para identificar el mecanismo de caída del sobrepotencial inducida por la luz, que se dividió en dos procesos principales: i) transferencia de electrones mejorada debido al fuerte calentamiento plasmónico y ii) disipación de energía térmica del electrodo al electrolito.

El cuarto capítulo está dedicado al estudio óptico de matrices de nanoagujeros de Ni (NHA) y la utilización de su plasmón superficial en la reacción de reducción de yodato. El método de litografía de máscara hueca sintonizable utilizado en la fabricación de NHA implicó un ajuste preciso de sus parámetros geométricos y, por lo tanto, la optimización de sus propiedades ópticas. La dependencia de los picos de extraordinaria transmitancia (EOT) en el ángulo de incidencia y el diámetro del agujero permitió identificar los modos de plasmón superficial y localizado. El estudio de fotocorriente dependiente de la longitud de onda bajo irradiación láser pulsada de fotocátodos planos y estructurados con respecto a su espectro óptico demostró la naturaleza plasmónica fototérmica de la mejora de la reacción.

## Resum

L'esgotament dels combustibles fòssils i l'escalfament global causat per les emissions excessives de carboni ha portat cap a una transició urgent cap a les fonts d'energia renovables (FER). No obstant això, de totes les FER existents, només l'energia solar és capaç de satisfer la creixent demanda mundial d'energia. El comportament impredecible de les FER requereix tecnologies d'emmagatzematge d'energia a llarg termini i d'alta capacitat, essent la tecnologia "power-to-gas" una de les solucions, que utilitza electricitat verda per a generar hidrogen i convertir el CO<sub>2</sub> en metà.

En aquest context, la utilització de la llum solar com a font d'energia verda addicional en reaccions catalítiques per a la producció de combustibles renovables és un gran repte que requereix nous enfocaments per al disseny de catalitzadors i reactors. La catàlisi assistida per plasmons, sent un camp emergent candent a causa de la facilitat d'ajust de les propietats òptiques del catalitzador plasmònic, generalment requereix metalls nobles costosos per a garantir una vida prolongada dels plasmons per als efectes induïts per electrons. Donada l'escassetat de metalls nobles, va sorgir la necessitat de buscar materials plasmònics alternatius, que satisfacin simultàniament els requisits per a aplicacions òptiques i catalítiques. Fins al moment, pocs treballs han destacat la importància de l'escalfament de plasmons com a principal conseqüència del plasmó excitat en materials catalítics, encara que l'interès per la catàlisi fototèrmica és cada vegada major. A causa del raonament anterior, el níquel (Ni) és un excel·lent candidat per a aplicacions catalítiques millorades amb plasmons, ja que és un metall de transició abundant amb una combinació beneficiosa d'excel·lents propietats catalítiques i fototèrmiques.

Els objectius principals d'aquest treball són i) el disseny de catalitzadors plasmònics basats en Ni per a reaccions de combustibles renovables (metanació de CO<sub>2</sub> i reacció d'evolució d'hidrogen -HER-), ii) el seu estudi estructural, òptic i funcional per a identificar les condicions òptimes de reacció i quantificar el guany en la reacció assistida per llum, i iii) definir els mecanismes de millora de la reacció. D'acord amb els objectius plantejats, el treball realitzat es divideix en 4 capítols. En el primer capítol de la tesi es presenta un panorama general del problema i conceptes fonamentals. Aquest capítol inclou la descripció dels principals enfocaments catalítics assistits per llum, els antecedents de la teoria de plasmons en metalls i proporciona un estat de l'art en metanació de CO<sub>2</sub> millorada amb plasmons i HER. El segon capítol està dedicat al desenvolupament del catalitzador de Ni/CeO<sub>2</sub> per a la metanació de CO<sub>2</sub> assistida per llum i la recerca del mecanisme de millora de la reacció induït per plasmons. El procediment de síntesi va assegurar una alta àrea

superficial del catalitzador, la qual cosa va resultar en una alta conversió de CO<sub>2</sub> (80%) i selectivitat al metà (95%). La metanació assistida per llum va demostrar un augment de 2,4 vegades en la velocitat de reacció, la qual cosa va portar a una disminució del consum d'energia en un 20%. Les tècniques de caracterització in situ van revelar un efecte dual de la radiació solar sobre el catalitzador híbrid Ni/CeO<sub>2</sub>, la qual cosa confirma la presència d'efectes fototèrmics i electrònics a causa de la interacció de llum complementària de tots dos components del catalitzador.

El tercer capítol presenta un estudi sobre nanopartícules plasmòniques de Ni amb absorció millorada en el rang de llum visible i la seva aplicació com fotocàtode per a HER. El fort efecte fototèrmic de les nanopartícules sintetitzades sobre la velocitat de reacció va permetre augmentar la producció d'hidrogen en un 27% després de trobar les condicions òptimes. De manera similar, el sobrepotencial de reacció es va reduir en 185 mV sense cap escalfament general significatiu de la cel·la. Els mesuraments amb llum i fosc han mostrat una clara diferència entre l'escalfament convencional i l'efecte fototèrmic en la millora de HER. Es va emprar il·luminació polsada periòdica per a identificar el mecanisme de caiguda del sobrepotencial induïda per la llum, que es va dividir en dos processos principals: i) transferència d'electrons millorada a causa del fort escalfament plasmònic i ii) dissipació d'energia tèrmica de l'elèctrode a l'electròlit.

El quart capítol està dedicat a l'estudi òptic de matrius de nanoforats de Ni (NHA) i la utilització del seu plasmó superficial en la reacció de reducció del iodat. El mètode de litografia de màscara buida sintonitzable utilitzat en la fabricació de NHA va implicar un ajust precís dels seus paràmetres geomètrics i, per tant, l'optimització de les seves propietats òptiques. La dependència dels pics d'extraordinària transmitància (EOT) en l'angle d'incidència i el diàmetre del forat va permetre identificar els models dels plasmons superficials i localitzats. L'estudi de fotocorrent dependent de la longitud d'ona sota irradiació làser polsant de fotocàtodes plans i estructurats respecte al seu espectre òptic va demostrar la naturalesa plasmònica fototèrmica de la millora de la reacció.

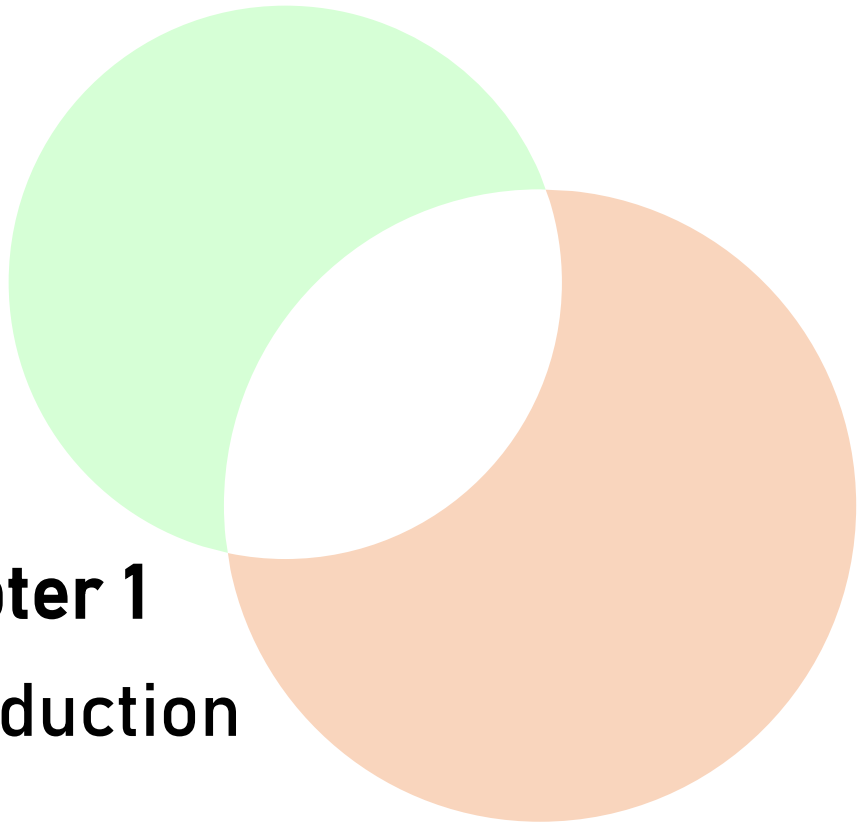


**List of abbreviations**

BET	Brunauer-Emmett-Teller
BJH	Barrett-Joyner-Halenda
CBM	Conduction band minimum
CID	Chemical interface damping
DOS	Density of states
DRIFTS	Diffuse reflectance infrared Fourier transform spectroscopy
EC	Electrochemistry (electrochemical)
ECSA	Electrochemically active surface area
EDX	Energy-dispersive X-ray spectroscopy
EELS	Electron energy loss spectroscopy
EIS	Electrochemical impedance spectroscopy
EM	Electromagnetic
EOT	Extraordinary transmission
EtOH	Ethanol
FTO	Fluorine-doped tin oxide
FWHM	Full width at half maximum
H <sub>2</sub> -TPR	Hydrogen temperature programmed reduction
HAADF	High-angle annular dark-field imaging
HCP	Hexagonal closed pack
HDI	Human development index
HER	Hydrogen evolution reaction
HOMO	Highest occupied molecular orbital
HRTEM	High-resolution transmission electron microscopy
IR	Infrared

LB	Langmuir-Blodgett
LNG	Liquefied natural gas
LSPR	Localized surface plasmon resonance
LSV	Linear sweep voltammetry
LUMO	Lowest unoccupied molecular orbital
NHA	Nanohole array
NP	Nanoparticle
NSL	Nanosphere lithography
OER	Oxygen evolution reaction
P2G	Power to gas
PEC	Photoelectrochemistry (photoelectrochemical)
PIRET	Plasmon-induced resonance energy transfer
PS	Polystyrene
PV	Photovoltaic
PVEC	Photovoltaic-electrochemical
RARs	Reasonably assured recoverable reserves
RDS	Rate-determining step
RES	Renewable energy sources
RLD	Rate-limiting step
RWGS	Reverse water gas shift reaction
SEM	Scanning electron microscopy
SERS	Surface-enhanced Raman spectroscopy
SPP	Surface plasmon polariton
SPR	Surface plasmon resonance
STEM	Scanning transmission electron microscopy
TEM	Transmission electron microscopy

TEOS	Tetraethyl orthosilicate
TM	Transverse magnetic
UV	Ultraviolet
VBM	Valence band maximum
XRD	X-ray diffraction spectroscopy



**Chapter 1**  
**Introduction**

## 1.1. General introduction

Over the past 150 years, the scientific progress of mankind has undergone almost exponential development. The human development index (HDI) has almost doubled, and continues to grow rapidly [1]. As a result of a tight correlation between HDI and energy consumption [2], the humanity has faced two of the most global anthropogenic challenges: significant depletion of fossil fuels and global warming caused by excessive carbon emissions. Both problems described above have led to the urgent need for transition to renewable sources of energy (RES), capable of meeting the current energy demands and carbon neutrality.

In 2021, 80% of total energy consumption came from fossil fuels [3], being the main source of CO<sub>2</sub> emissions, whose concentration in the atmosphere has grown from 280 to 417 ppm during the Industrial Age [4]. High CO<sub>2</sub> emission rates have caused a strong greenhouse effect and led to a world temperature increment of +1.19°C relative to 1880-1920 and a severe climate change. This rises a need to capture and recycle excess carbon dioxide in the atmosphere and direct the current economy vector towards a closed carbon-neutral cycle, favoring that the amount of carbon footprint in the environment approaches net zero. The CO<sub>2</sub> conversion into renewable fuels is especially challenging, considering that free Gibbs energy of the linear CO<sub>2</sub> molecule is quite high (4.1 eV) [5], which makes its dissociation a very energy-consuming process. Despite the essential progress in CO<sub>2</sub> reduction processes during the last decade, industrial-level CO<sub>2</sub> utilization is still a non-profitable technique from the economical point of view. In this context, an important factor is not only the CO<sub>2</sub> utilization, but also its conversion to value-added products.

Total final energy consumption has increased from 8.06 TWy to 19.24 TWy in the last 50 years [6]. However, fossil fuels are a finite energy source, and despite the discoveries of new reserves in the 2009-2018 years' span, their consumption rate is continuously growing. Figure 1.1 represents reasonably assured recoverable reserves (RARs), which shows the amount of energy that can be extracted both from finite and renewable energy sources at current given technical and economic conditions for the next 30 years [7]. Assuming the current consumption rates [3,8], the remaining reserves of oil will last for 56 years, natural gas for 49 years and coal for 202 years.

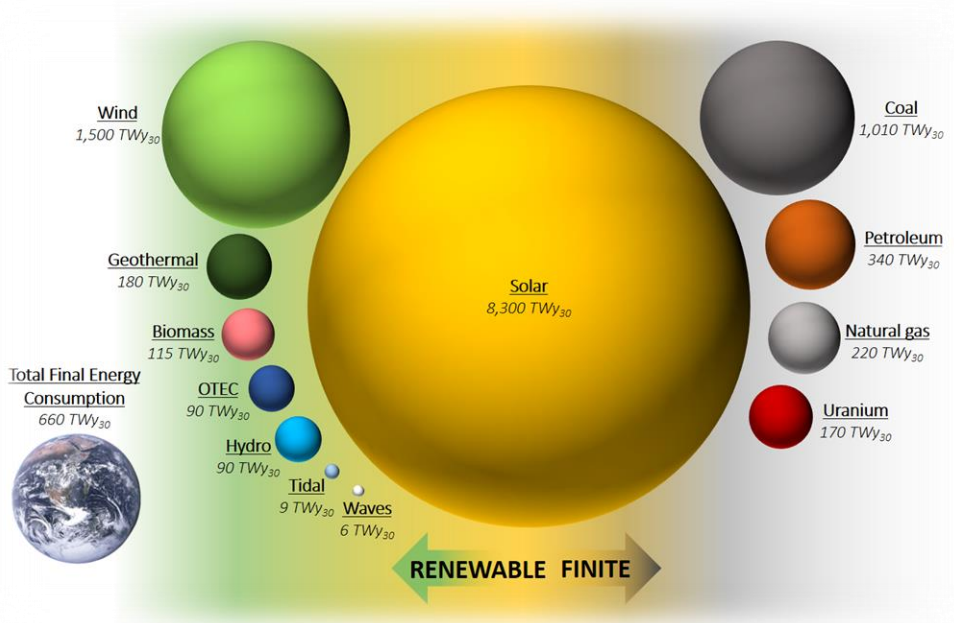


**Figure 1.1.** Reasonably Assured Recoverable Reserves (RARs) over the next 30 years updated to year 2022. The size of each sphere is proportional to the corresponding reserve. Adapted from [7].

Latest evaluations have shown that despite moderate current solar technology efficiencies and essential deployment restrictions, the solar energy source (together with wind) is the only RES able to meet the steadily growing world energy demands [7]. Although at the moment the construction of solar and wind power plants requires significant financial investment, in the long run electricity generated from alternative energy sources is much cheaper than electricity of combustible origin: as of 2020 average price of energy extracted from fuel was 77 € per MWh [9], while solar energy was equal to 48 € per MWh [9,10]. And while the price of fuel on average continues to rise due to the limitations and complexity of mining, solar energy becomes cheaper due to the establishment of processes for the solar cell production and finding and optimizing new photoactive materials. Moreover, solely solar-to-electricity efficiency is taken into account in these studies. Utilization of direct or indirect heating, i.e. photothermal impact of solar energy source, will only improve its evaluated potential in the energy supply.

The existing power grid is designed mostly for the energy supplied by the fossil fuels combustion, which is a relatively flexible technology with no weather or time dependencies. Unlike fossil fuels, RES cannot provide a stable non-variable energy supply due to the unpredictable behavior of solar, wind and other renewable

sources and, therefore, cannot be directly integrated into the current power grid. This leads to the need of long-term storage of the generated energy, which can be stored during the RES peak production and used when its efficiency is low. The renewable energy storage is also important from the point of view of energy transportation.

Out of known large-capacity energy storage technologies (flywheels, batteries, compressed air storage, pumped hydro storage and gas chemical storage) the chemical energy storage strategy, such as hydrogen and methane gas storage is the most important option for long-time and high-capacity storage (Figure 1.2(a)). Moreover, hydrogen and methane fuels possess the highest energy density among all the existing fuels, being superior to natural resources, and thus having large perspectives in the efficient fossil fuel replacement (Figure 1.2(b)).

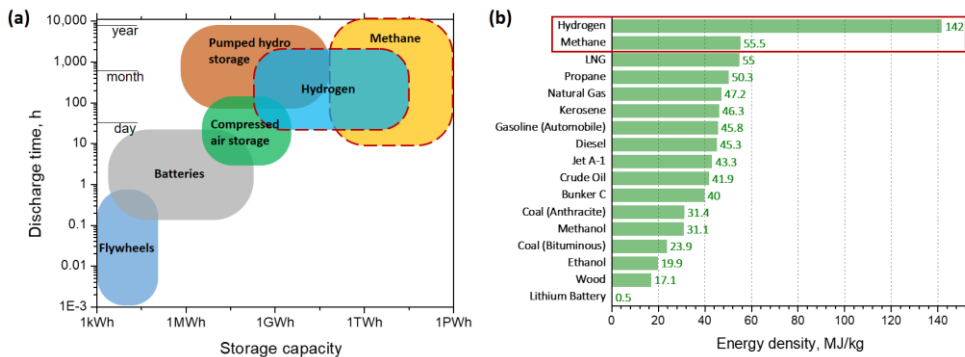


**Figure 1.2.** (a) Storage capacity of different energy storage strategies. Adapted from [11,12]; (b) Energy density values of fuels and batteries that can be released through combustion. LNG = liquefied natural gas. Adapted from [13].

It should be noted that there are three main hydrogen categories, which depend on the production strategies used: gray, blue and green. Gray and blue hydrogen both come from steam reforming of natural gas. However, during blue hydrogen generation the CO<sub>2</sub> emissions (10 kg per 1 kg of generated hydrogen) are captured and stored, unlike the gray H<sub>2</sub> technology, where the CO<sub>2</sub> is allowed to escape to the atmosphere and contribute to the greenhouse effect. In its turn, green hydrogen is produced from water electrolysis with the use of renewable electricity, thus being the cleanest and most sustainable hydrogen fuel category.

Due to the above reasoning, and also the fact that electricity transmission grids have much less capacity compared to gas transmission and storage, the power-to-gas (P2G) technology is a common route for transformation of the surplus renewable electricity to gas chemical fuels. This strategy is focused on the green hydrogen

production through water electrolysis, which can be either used as a fuel, or further into transformed methane.

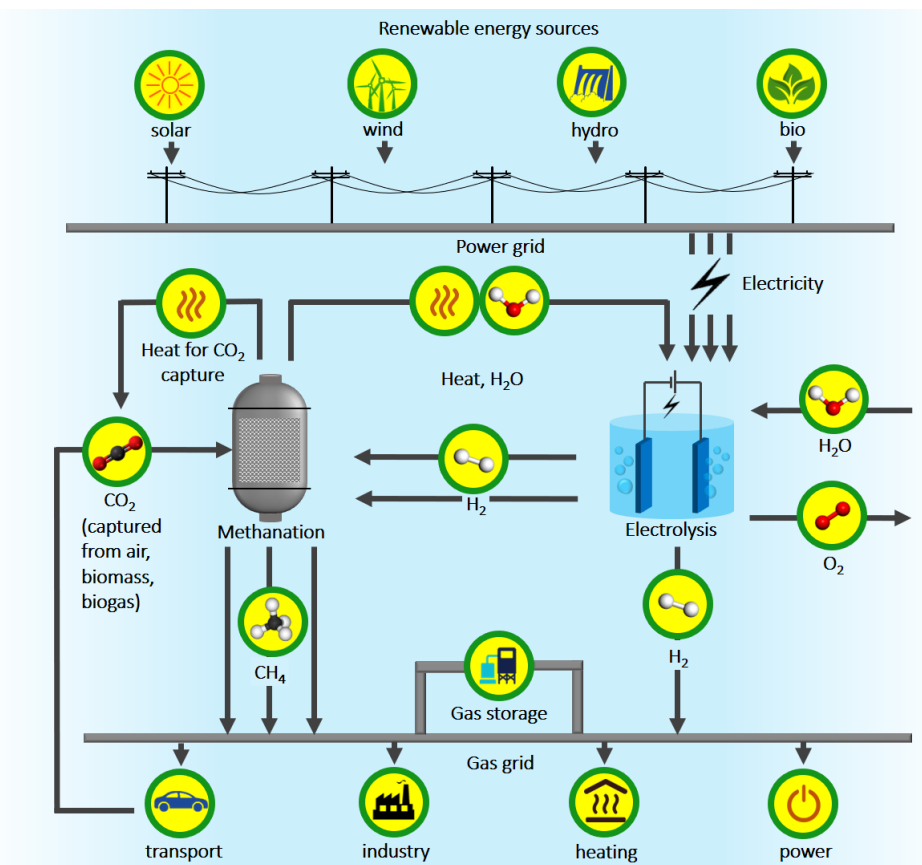


**Figure 1.3.** Scheme of the power-to-gas concept.

Full power-to-gas technology is schematically depicted in the Figure 1.3 and can be described as follows. “Green” electricity, obtained from renewable energy sources is transmitted through the power grid and used in water electrolysis for hydrogen production. Carbon dioxide, released as a result of industrial technologies, is captured from air, or collected from biogenic sources, and combined with green hydrogen to produce methane, which is also called synthetic natural gas (SNG). Water as a side product of CO<sub>2</sub> methanation is utilized as the inlet for water electrolysis, and the excess heat can be used to enhance electrolysis and CO<sub>2</sub> capture. Purified methane (> 95%) and a small amount of hydrogen (< 5-10%) can be directly injected into the natural gas grid without the need to change the current infrastructure. On the other hand, gases can also be stored or used for transportation and power production. Finally, the CO<sub>2</sub> emissions, released from the



usage of the synthetic natural gas in industrial applications, is captured for further conversion, ensuring fully closed carbon-neutral cycle.

The P2G concept allows to solve the problem of hydrogen production and consumption imbalance, obtained during water electrolysis. Complementary to creating expensive and complicated systems for hydrogen fuel storage, it can be used in synthesis of synthetic natural gas, which already has a developed infrastructure and can be easily stored.

In this context, the P2G generation of H<sub>2</sub> and CH<sub>4</sub> synthetic fuels using solar light as a green renewable energy source and CO<sub>2</sub> emissions as a carbon source for carbon-neutral industrial use is an important challenge, which requires efficient catalysts and reactor designs. The two main chemical reactions, required for the P2G technology, are hydrogen evolution reaction (HER) and CO<sub>2</sub> methanation, also known as Sabatier reaction. The latter is also a key reaction for the growth of space station techniques, which are exposed to excess H<sub>2</sub> due to water electrolysis and the urgent need to recycle exhaled CO<sub>2</sub>.

## 1.2. Light in catalysis

### 1.2.1. Catalysis overview

The goal of catalysis is to reduce the overall energy needed for the desired chemical reaction, either by reducing the energy barrier of current pathway or by changing the reaction pathway to the more energy favorable one. If the reaction requires formation of intermediate products and consists of several steps, the reaction rate is determined by highest energy barrier needed to overcome along the route and is called rate-limiting step (RLS) or rate-determining step (RDS) of the reaction.

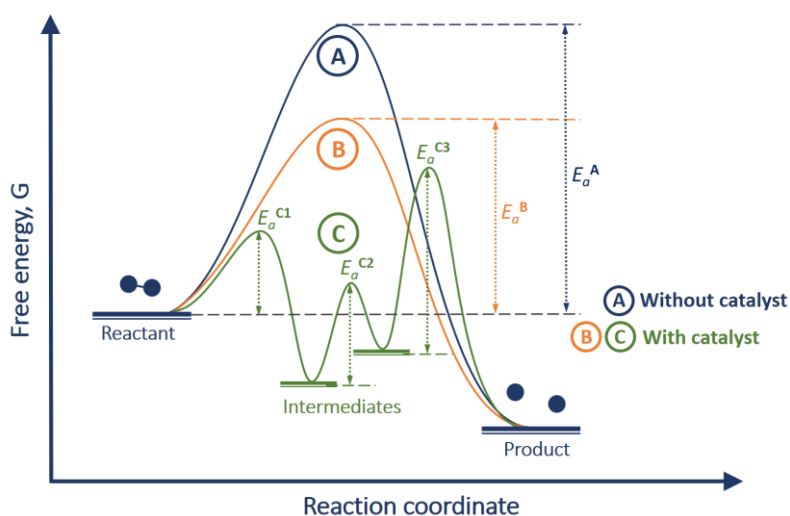


**Figure 1.4.** Free energy of a chemical reaction along the reaction coordinate with and without a catalyst.

The activation energy of the reaction is defined as the minimal additional Gibbs free energy required for the reaction to happen. As seen in Figure 1.4, the reactant has to overcome a barrier  $E_a^A$  in order to be transformed into the product. In the presence of the catalyst (B), the reaction barrier is lower ( $E_a^B < E_a^A$ ) and, therefore, the reaction rate is higher according to the Arrhenius equation:

$$k = Ae^{-\frac{E_a}{k_B T}} \quad (1.1)$$

Where  $k$  is the reaction rate,  $T$  – temperature,  $k_B$  – Boltzmann constant and  $A$  is a pre-exponential factor.

However, the catalyst (B) does not change the reaction pathway, affecting only the value of the activation energy. The reaction drastically changes when the catalyst (C) is introduced in the system: while the final product is the same as in the cases (A) and (B), the pathway is completely different, taking the reaction through additional steps with corresponding intermediate states. Here, the activation energy of the reaction (rate-determining step) is defined by the highest energy barrier over the path (C):  $E_a = E_a^{C3} > E_a^{C2} > E_a^{C1}$ .

### 1.2.2. Catalytic approaches

A chemical reaction, even if thermodynamically spontaneous, requires an energy supply to overcome the kinetic barrier. Three main approaches to catalytic processes lie in using heat, electrical power and light as the energy sources. Often these techniques are combined, as shown on the diagram in Figure 1.5. Over the recent years, various combinations of photo-, electro-, and thermal catalytic approaches have attracted an uprising interest and are a hot topic in the field of catalysis [14–16]. Mainly, this is due to the similar efficiencies one can achieve by performing the reaction at more favorable conditions, e.g. at lower temperature in case of photo-thermal approach or at lower working potential in case of thermo-electrocatalysis. It can be beneficial if the catalyst stability and lifetime requires special conditions, or to decrease the cost of the technology used by assisting the reaction with a cheaper or more abundant energy source. In this context, as was discussed in section 1.1, the use of solar renewable resource is the most reasonable economic direction, and its use as a primary energy supply for catalytic reactions or as an auxiliary source for combined approach is an essential step towards the full or partial replacement of the non-renewable energy sources with green RES.

There also exist other fundamentally different approaches to catalytic conversion of CO<sub>2</sub>, such as bio-catalysis [17], based on use of the living micro-organisms, and plasma catalysis [18], which is an emerging field of research with excellent perspectives. Combination of these techniques with the existing developed technologies opens a wide range of possibilities for achieving high conversion and selectivity values under optimal reaction conditions.

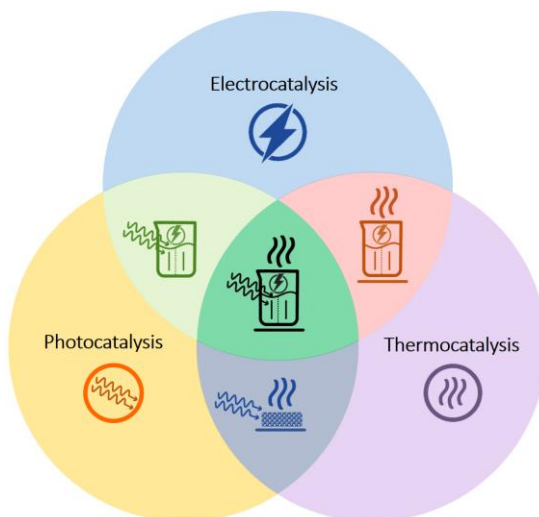


**Figure 1.5.** A diagram showing various approaches to catalysis and their corresponding combinations.

### 1.2.3. Application of solar light in catalytic reactions

In light-assisted catalysis, one of the biggest challenges is to design a photoactive catalyst which efficiently absorbs solar illumination and possesses desired catalytic properties, being chemically and thermally stable at the same time. Choice of the proper material, as well as working conditions and reactor type, depends on the way of photons utilization in catalytic reactions. The key approaches are depicted in Figure 1.6.

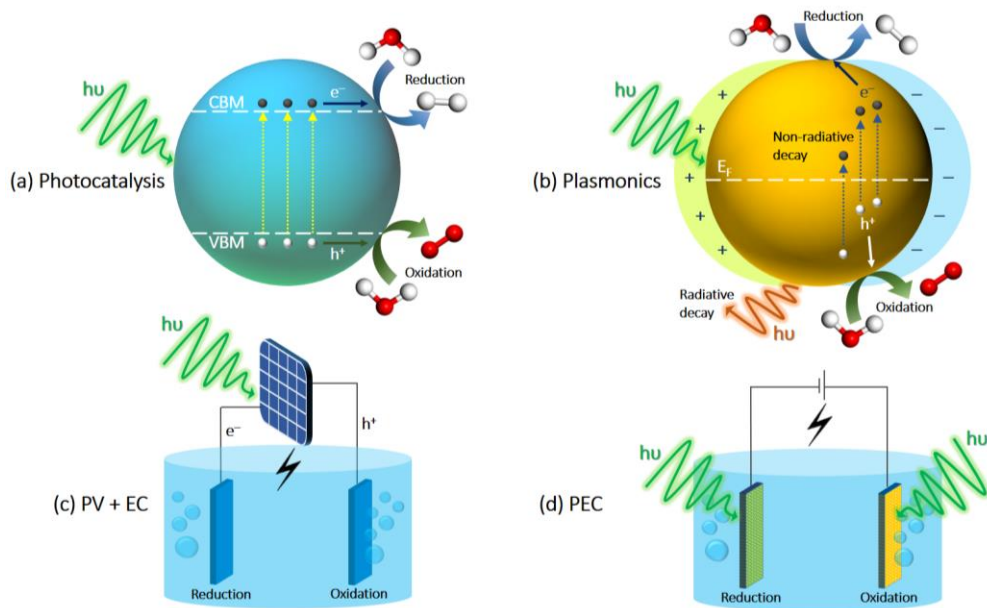


**Figure 1.6.** Different application of light in catalytic reactions.

Photocatalytic reactions are based on the use of the semiconductor material with a reasonable band gap ( $E_g$ ) for efficient visible light absorption and reasonable position of the conduction band minimum (CBM) relative to the LUMO of the reactant (Figure 1.6(a)) [19]. When the semiconductor absorbs a photon, the electrons are excited from the valence band to the conduction band of the material, leaving a hole behind. Then, if the relative position of the energy levels is favorable, the electron is transferred to the LUMO of the absorbate and participates in the reduction reaction, while the hole is transferred to HOMO of another species and oxidizes it, thus preserving the neutrality of the system. Photocatalytic materials are often decorated with metallic nanoparticles, and while the semiconductor supports are used as the main photoabsorber, the metallic nanoparticles act only as active catalytic sites [20,21]. In this case, the photoexcited electrons are first transferred to the metallic nanoparticles and then mediate the reduction reaction.

However, metallic nanoparticles can act as photoactive materials themselves if they possess plasmonic properties with the resonance lying in the range of the solar irradiation spectrum (Figure 1.6(b)). Plasmonic catalysts can efficiently absorb or scatter photons, leading to excitation of high energy carriers through plasmon decay, and their subsequent use in the chemical reactions. The theory behind plasmon resonances is described in section 1.4, and the mechanisms of plasmon-enhanced catalytic reactions are discussed in section 1.5.

Another way of harvesting solar energy for catalytic applications lies in coupling of a PV element with an electrochemical (EC) cell (Figure 1.6(c)). The solar cell generates electric power, used for an electrochemical reaction. Coupling of the PV element directly with the electrolyzer solves the problem of solar power instability, converting the light directly into the chemical fuels without the need to store electricity [22]. This configuration also makes the PVEC an autonomous device, which does not require a permanent connection to the electrical grid.

Finally, the photoelectrochemical (PEC) setup is an approach where one or both of the electrodes are photo-active (Figure 1.6(d)). The photoelectrodes can be made of classical semiconductor materials [15,23], plasmonic nanoparticles [24] or a combination of both [25–28]. It should be noted that as the photoelectrodes are usually used in aggressive media with ultra-low or ultra-high pH, they need to be chemically stable and corrosion-resistant, which significantly narrows the range of photo-active materials suitable for PEC application.

One should bear in mind that all of the described techniques can be combined with each other in order to achieve optimal reaction conditions, catalytic output and energy consumption.

Despite the fact that the main driving force in the light-assisted catalytic techniques are intended to be high-energy charge carriers, which are either directly used in the chemical reactions, or stored to produce electricity, all of the processes listed above suffer from spontaneous recombination of photo-excited electron-hole pairs, or decay of the surface plasmon in case of the metallic nanoparticles, both resulting in heating. While some light-controlled techniques require constant temperature conditions and, therefore, have the need to avoid the losses leading to increase in the temperature, the catalytic reactions usually benefit from the additional heating due to increase in the energy of the molecules. In this case, the photothermal consequence is not detrimental, but can be used as a side-effect to enhance the reaction rate, or even as a main driving force, replacing conventional heaters with renewable solar energy source.

The photo-active phase in all of the cases, although being completely different materials, should possess one common feature: exhibit strong absorption in the frequency range of interest. In other words, to effectively use the sunlight, the absorption spectrum of the catalyst should ideally match the solar radiation spectrum, or at least absorb a big portion of it. However, to perform a photocatalytic or photoelectrocatalytic redox reaction, the energy of the excited charge carriers has to be equal or higher than the corresponding redox potentials. Most of the suitable wide-gap semiconductor photocatalytic materials, such as  $\text{TiO}_2$  ( $E_g = 3.2$  eV), absorb only UV light, which corresponds only to 5% of the whole

radiation energy flux. To enhance the efficiency, a two-step photoexcitation system (so-called Z-scheme) is often applied, by analogy with photosynthesis in green plants [29]. It lies in a combined system of two semiconductor materials, each one of which is responsible for a half-reaction of the overall full redox reaction, and the electron-hole exchange between the two materials occurs through electron mediator.

The photovoltaic devices, used in PVEC setups, usually also have a narrow absorption band. One of the approaches to solve this problem, is to collect most of the solar spectrum by creating a multi-junction solar cell device where each layer would absorb a part of the frequencies and be transparent to all of the rest [30]. Up to the moment, these devices are costly and difficult to make.

However, plasmonic photocatalysts exhibit high spectral tunability, as their absorption spectra is easily modified by tuning their size and shape. Moreover, plasmonic metals are less subject to degradation than many semiconductor materials used for photocatalysis and PEC. Finally, highly efficient plasmonic heating can be used as a driving force in catalytic reactions, as opposed to semiconductor materials, which despite high losses and fast charge carrier recombination do not demonstrate photothermal properties.

## 1.3. Plasmons

### 1.3.1. Bulk plasmons and plasmonic materials

One of the approaches to describe the optical properties of a metal is to assume that its unbound electrons behave like as a free gas of non-interacting particles, existing in a field of the ion cores. This approach was proposed by Drude [31] and can describe most of the optical phenomena in metals and semiconductors.

The dielectric permittivity of a material defines its polarizability in an external electric field. Generally, it is a complex function of frequency:

$$\varepsilon(\omega) = \varepsilon'(\omega) + i\varepsilon''(\omega), \quad (1.2)$$

Where  $\varepsilon'(\omega)$  is a real part of the permittivity, which is related to the displacement currents in the material and is responsible for its polarization, while  $\varepsilon''(\omega)$  is the imaginary part, related to the conduction currents in the material and is responsible for losses in the material due to collisions of the electrons with the crystal lattice.

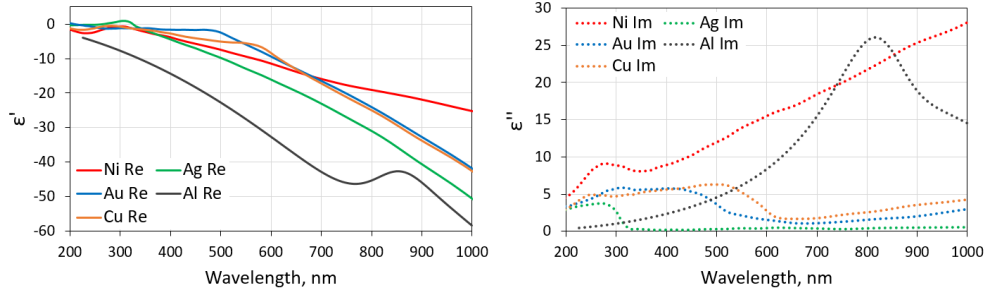


**Figure 1.7.** Real and imaginary parts of the complex dielectric permittivity of Ni, Au, Ag, Cu and Al [32].

According to the Drude-Lorentz model, which accounts also for the interband transition in metals, the dielectric permittivity of real metals depends on the frequency in the following manner:

$$\varepsilon(\omega) = \varepsilon_{\infty} - \frac{\Omega_p^2}{\omega(\omega + i\gamma)} - A \frac{\Omega_1^2}{(\omega^2 - \Omega_1^2) + i\gamma_1\omega}, \quad (1.3)$$

Where  $\varepsilon_{\infty}$  is the contribution of the bound electrons to the dielectric function,  $\gamma = \frac{1}{\tau}$  – is the inverse momentum relaxation time, or damping rate, and  $\Omega_1$  is the resonant frequency of the interband transition. The frequency  $\Omega_p$  is an eigenfrequency of the free electron gas in the metal and is defined as bulk plasmon frequency, which satisfies the following expression:



$$\Omega_p^2 = \frac{|e|^2 n}{\varepsilon_0 m_e} \quad (1.4)$$

$e$  being the electron charge,  $m_e$  – effective electron mass,  $\varepsilon_0$  – vacuum permittivity, and  $n$  – free electron density in the metal. Bulk plasmon is a longitudinal wave, representing charge density oscillations in the metal bulk.

The damping rate in the Drude-Lorentz model can be rewritten in the following manner:

$$\gamma = 2\varepsilon''(\omega) \left[ \frac{\partial \varepsilon'(\omega)}{\partial \omega} \right]^{-1} \quad (1.5)$$

As it can be seen from Equation 1.5, the damping rate is proportional to the imaginary component of the dielectric permittivity. Real and imaginary parts of the experimentally measured dielectric permittivity function for Au, Ag and Ni are shown in Figure 1.7. The main optical parameters (plasma frequency, damping rate, relative losses and energy cutoff of the interband transitions) of Au, Ag, Cu, Ni and Al are collected in Table 1.1.

**Table 1.1.** Optical parameters of some metals.  $\hbar\Omega_p$  – plasma frequency value,  $\gamma$  – damping rate,  $\varepsilon''$  – value of the imaginary component of dielectric permittivity at wavelength  $\lambda = 520$  nm,  $E_{IB}$  – energy cutoff of the interband transitions.

	$\hbar\Omega_p, eV$	Damping rate $\gamma, eV$	$\varepsilon''$ at $\lambda = 520$ nm	$E_{IB}, eV$
Au	8.8 [33]	0.071 [35]	2.58	2.45 [37]
	8.6 [34]	0.026 [33]		2.5 [35]
		0.018 [36]		
Ag	9.2 [38]	0.021 [35]	0.33	3.9 [38]
	9.6 [34]	0.018 [38]		
Cu	9.3 [38]	0.019 [38]	6.16	2.1 [38]
	10.8 [34]	0.095 [35]		2.0 [33]
Ni	10.0 [36]	0.045 [41]	12.65	4.8 [44]
	5.2 [39,40]	0.235 [42]		4.7 [39]
		0.034 [43]		
Al	12.7 [45]	0.129 [45]	5.20	1.5 [45]
	12.5 [46]	0.062 [46]		
	15.8 [34]	0.598 [47]		
		0.549 [48]		

Noble metals (Au, Ag, Cu) are typically considered as “good” plasmonic materials. Thanks to a high density of states (*d*-bands) under the Fermi level, and also hybridization of the conduction *sp*-bands with the valence *d*-bands, a large amount of *sp*-intra-band transitions can be excited to high-energy levels with respect to the Fermi level. Moreover, low DOS of the *sp*-bands leaves lower options for the excited electron to dissipate its energy and, therefore, significantly extends its lifetime. Despite different configuration of the band structure, Al also shows an excellent plasmonic response, and due to higher amount of free conduction electrons (3 per atom) compared to noble metals (1 per atom), is able to generate plasmons with higher energy.

However, interband transition in gold is located in the visible light range, which causes additional losses at optical frequencies and makes it unsuitable for many applications, which demand low losses. On the other hand, many other abundant group VIII transition metals (Ni, Ru, Rh) can demonstrate plasmonic properties, however, with a much lower lifetime [49,50]. From Figure 1.7 it can be seen that the losses for nickel are at least an order of magnitude higher than the one for silver. Damping of the plasmon in transition metals is especially large due to the high density of states at the Fermi level.

Nickel is considered to be a good candidate as an alternative plasmonic material [49]. Unlike many other metals, interband transitions in nickel are highly localized (at 4.7-4.8 eV, [39,51,52]), and are very unlikely to interfere with the optical phenomena happening at the visible range. Although its optical properties suggest a strong damping due to high losses, nickel possesses a great ability to generate heat under resonant illumination [53]. According to the studies, the electron thermalization (due to electron-electron collision) in nickel happens in 80 fs, and the electron-phonon relaxation time is 0.3-0.4 ps [54].

Plasmonic metals are most widely used in surface-enhanced Raman spectroscopy (SERS) [55]. A strong EM field of dipoles, created by the surface charge oscillations, can enhance the Raman spectra intensity of molecules adsorbed on the surface of a plasmonic material up to  $10^{14}$ . Thus, plasmonic nanoparticles with a high plasmon lifetime can be used as gas and bio sensors. Their ability to effectively scatter light allows their application as a back-scattering layer in solar cells, significantly improving their efficiency. Transition plasmonic nanostructures, such as Ni, are extensively used for magneto-optical applications [56–61]. Lastly, plasmon-induced catalysis is a hot emerging field, opening a wide range of materials for energy-efficient selective and environmentally friendly catalysis.

### 1.3.2. Surface plasmon polariton

Surface plasmon polariton (SPP) is a propagating wave, which occurs at the metal-dielectric interface, and consists partially from the electromagnetic wave in the dielectric media, and partially from the longitudinal charge oscillation on the metallic surface (Figure 1.8).

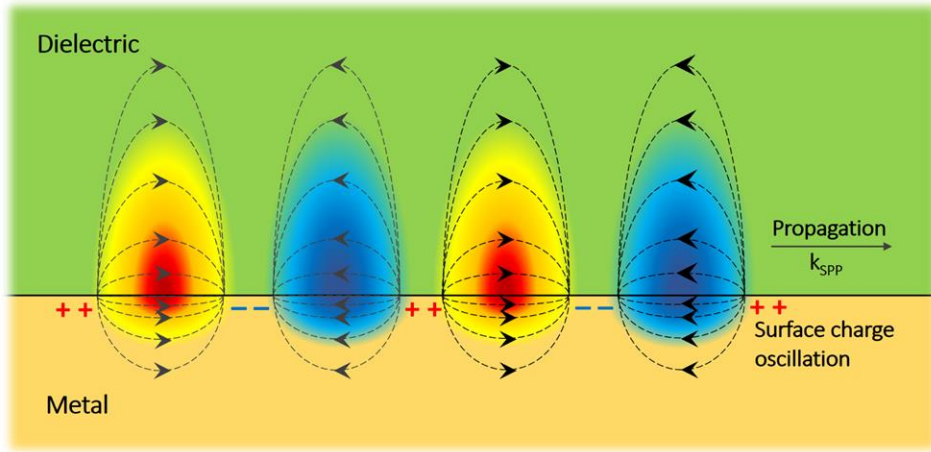


**Figure 1.8.** Surface plasmon polariton.

SPP is a non-radiative plasmon, whose electromagnetic fields exhibit an exponential decay perpendicular to the surface and becomes very localized, when the frequency of the incident light coincides with the resonant surface plasmon polariton frequency:

$$\Omega_{SPP} = \frac{\Omega_P}{\sqrt{\epsilon_m^\infty + \epsilon_d^\infty}}, \quad (1.6)$$

Which is usually simplified to:

$$\Omega_{SPP} = \frac{\Omega_P}{\sqrt{2}}. \quad (1.7)$$

The condition of the surface resonance is  $\epsilon_m = -\epsilon_d$ , and  $\kappa_m = \kappa_d$ , which basically results in the zero group velocity of the polariton.

Solution of the Maxwell's equations assuming the continuity condition at the metal-dielectric interface leads to the following dispersion relation for SPP:

$$k_{SPP} = \frac{\omega}{c} \sqrt{\frac{\epsilon_m \epsilon_d}{\epsilon_m + \epsilon_d}} \quad (1.8)$$

Where  $\epsilon_m$  is the dielectric function of the metal,  $\epsilon_d$  – the corresponding function of the dielectric, and  $c$  is the speed of light.

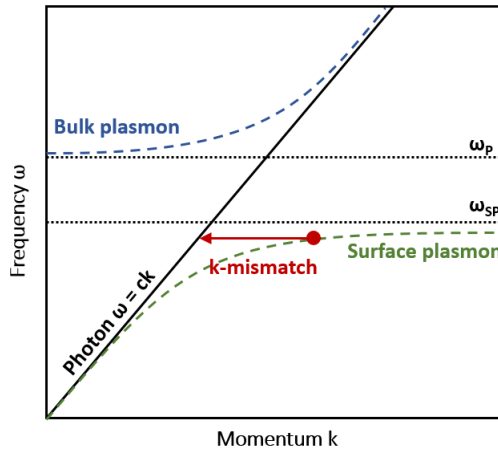


**Figure 1.9.** Dispersion diagram of bulk and surface plasmons and light in vacuum.

In Figure 1.9 it can be seen that the dispersion curve of the surface plasmon does not cross the dispersion line of light in vacuum (air). This means, that the SPP on the plain metal surface cannot be excited by plane waves due to the conservation law of the momentum vector. The parallel to the interface component of the SPP momentum is always larger than the wavevector momentum of the radiative light coming from the dielectric medium, making it impossible to excite the plasmon unless the momentum is matched by use of additional techniques. One approach lies in a setup in which light gains the lacking momentum by passing through a glass prism. Two slightly different configurations of this approach were introduced by Kretschmann [62] and Otto [63]. In Kretschmann's configuration the light passes through a glass prism and penetrates into a deposited on the bottom of the prism thin metal film, exciting the surface plasmons. In Otto's configuration the metal film is kept at a small distance from the bottom of the prism, and the SPP is excited by the evanescent wave of the light beam, which passes through the prism and is fully internally reflected from its bottom. It is also worth noting that in non-magnetic materials SPP can be excited only by a TM-polarized (p-polarized) wave. Another method to excite surface plasmon in the metal is to add an in-plane momentum to the incident wavevector by introducing gratings on the metallic surface [64] or

creating a highly ordered array of voids in a thin film, so-called nanohole array (NHA) [65–70].

SPP in a non-transparent metallic grating is usually determined by a minimum in the reflection spectrum [71]. However, NHAs exhibit non-zero transmittance, which can be used to characterize the plasmonic modes due to simplicity of the measurements. If the NHA is located on a dielectric substrate (e.g. glass), the dielectric media at its two surfaces is different. The surface modes, created at the lower surface can tune to the top one and be scattered back, contributing to the overall transmittance. This effect is called extraordinary optical transmission (EOT) and is determined as maxima on the transmission spectra of the NHAs.

Besides surface plasmons, the NHAs are also characterized by a Wood's (or Rayleigh-Wood's) anomaly [72]. It occurs at specific wavelengths due to an in-plane diffraction of light by the grating and can be detected by a sudden drop in the reflection or transmission spectrum of the NHA. The Wood's anomaly, unlike SPP, has a geometrical origin and does not depend on the optical properties of the metal. Coupling of Wood's anomaly with SPP can result in narrowing and intensifying of the EOT [73].

As the surface plasmon resonance condition depends on the in-plane momentum value of incident irradiation, the resonant wavelength will change with variation of the incident angle. Shift of the resonance depends on its order and can be both red and blue directed. Similar angular dependency also applies to the Wood's anomaly, as this spectral feature obeys the Bragg's law of diffraction.

Highly ordered nanohole arrays (NHA) are a promising type of materials that allow their wide use in sensing, optical and optoelectronic applications. The ability of the hole to scatter light more efficiently than a disk of the same size makes them an excellent back-scatter electrode in solar cells [74]. They also make excellent SERS detectors thanks to the strongly enhanced EM field in the voids [66]. Spectrally tunable EOT allows to use them as color-filter devices [75]. Finally, they can be applied as photo-active electrodes for catalytic reactions [76].

### **1.3.3. Localized surface plasmons**

On a small nanoparticle ( $d \ll \lambda$ ), the electric field of the incident light is nearly constant over the whole nanoparticle, implying a quasi-static approximation regime. In this case the plasmon becomes confined, and results in periodic non-propagating

oscillation of the electron density across the nanoparticles (Figure 1.10). Such plasmon is called localized, and can be excited with a resonant frequency:

$$\Omega_{LSPR} = \frac{\Omega_P}{\sqrt{3}}. \quad (1.9)$$

Plasmonic nanoparticles efficiently scatter and absorb light, and have extinction cross-sections exceeding the diameter of the nanoparticle [77]. Unlike the SPP, localized surface plasmon in metallic nanoparticles can be excited by an incident electromagnetic wave, causing electron density oscillations.

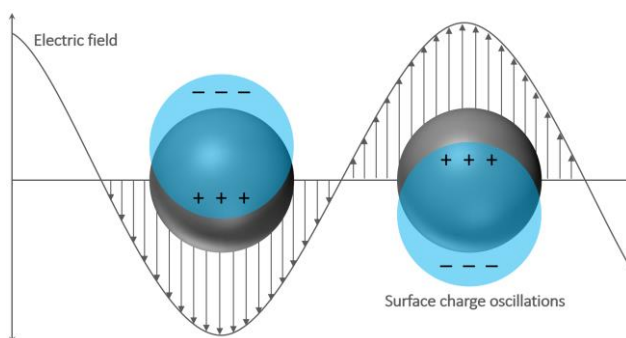


**Figure 1.10.** Surface charge and electric field oscillations in a metallic nanoparticle as a result of LSPR.

Localized surface plasmon resonance depends on the optical properties of the material and on the size and shape of the nanoparticle, which define the boundary conditions for the electromagnetic field. It should be noted, that the quasi-static approximation applies only to the nanoparticles with the diameters essentially smaller than the incident wavelength. When the size of the nanoparticle is increased, the quasi-static approximation is not completely valid anymore. As the charges in the nanoparticle become more spatially separated with the NP size, the dynamic depolarization of the resonance becomes stronger and red-shifts the resonance position [78].

Advanced colloidal chemistry allows synthesis of differently shaped nanoparticles, especially from noble metals, such as nanorods [79,80], nanostars [81–83] or nanotriangles [84,85]. Change in the nanoparticle shape was shown to have a drastic impact on the resonance position, due to the complex nature of the electric field oscillation [86]. Moreover, anisotropic particles can demonstrate several dipolar resonances. For example, metallic nanorods present two resonances: transversal and longitudinal, corresponding to the short and long axis in the particle. It has been demonstrated, that increase in the aspect ratio of the nanoparticle red-shifts the resonant wavelength [87]. Therefore, synthesis of various metallic nanopartilces

offers excellent tunability of their resonances through control of their size, shape and aspect ratio.

When two or more plasmonic nanoparticles approach each other up to the distance which is less than the diameter of one particle, their plasmons couple [88]. This leads to hybridization of the individual nanoparticle resonance bands, which also significantly affects the resonant frequency. Depending on the distance and, therefore, the strength of the coupling, the plasmon resonance can be red-shifted or blue-shifted.

One should note that the surface plasmon is a surface effect, which happens on the interface between metal and dielectric. For this reason, the LSPR effect, observed for metallic nanoparticles can as well be observed for the voids in the metallic films [89]. Thus, the developed theory for LSPR can be also applied to the void resonance, keeping in mind that the dipole moments in nanoparticles and nanoholes show opposite orientations.

Finally, highly ordered nanoholes can induce both SPP and LSPR effects. Coupling of the localized plasmon in the void with the surface polariton may cause significant shifts in the resonant wavelengths. Unlike SPP, LSPR does not depend on the incident light angle, but depends on the size and shape of the hole.

#### **1.3.4. Mechanisms of plasmon decay**

In a real system, the plasmon is damped [90–94] through two possible channels: radiative or non-radiative. Radiative losses result in scattering of the incident light through its re-radiation in the outer space, while non-radiative, or ohmic, losses are responsible for the light absorption by the metallic nanoparticle. One of the most common non-radiative damping mechanisms happens during the energy transfer between free electrons and the plasmon wave, and is called Landau damping. Landau damping happens in a timescale of 1-100 fs and leads to a non-equilibrium charge distribution, resulting in charge carriers with high energy relative to the Fermi level, so-called “hot electrons” or “hot holes”. These charge carriers can be injected into a supporting semiconductor [95], directly participate in a chemical reaction on the surface of the nanoparticle [96] or be transferred to a counter electrode in order to generate useful current [94]. Another non-radiative way of plasmon damping is a plasmon-induced resonant energy transfer (PIRET) from the excited nanoparticle to the support through dipole-dipole interaction [97]. The resonant energy transfer can directly excite an electron-hole pair in a semiconductor below the plasmonic nanoparticle, which can contribute to the photocurrent or

participate in a chemical reaction. Similar process can happen when a molecule is adsorbed directly on the metallic nanoparticle and is called chemical interface damping (CID) [98]. In this case, the hot electrons are directly generated in the unoccupied orbitals of the molecule and participate in its further transformation. Within the next 10 ps, the electrons that were not transferred are relaxed due to electron-electron interaction, contributing to the overall temperature increase. The rest of the oscillating free electrons are relaxed through the electron-phonon interaction, resulting in the complete damping of the plasmon and strong increase of the local temperature after  $\approx 10$  ns from the moment the plasmon was excited. All of the described decay mechanisms and the corresponding timeline is schematically shown in Figure 1.11.

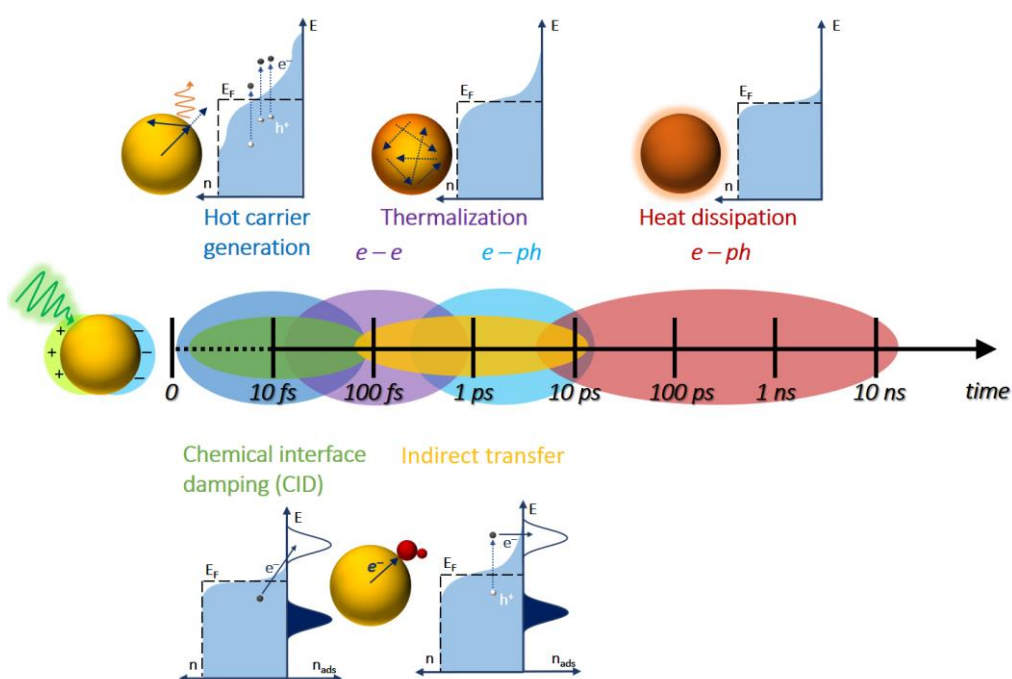


**Figure 1.11.** Timeline and mechanisms of the LSPR damping in metallic nanoparticles.

Most of the LSPR applications require a long lifetime of the plasmon in the nanoparticle, which would have a higher probability of the plasmon to result in a strong EM field enhancement at the particle surface, or at least to generate hot charge carriers that would contribute to the electronic processes. For these purposes, noble metals with small losses in the optical region are more desirable as materials for nanoplasmonic devices. However, a rising interest to the photothermal application of plasmonic materials allows us to choose from a wider spectrum of metals, including transition metals. Despite their high ohmic losses originated from



the high density of states at the Fermi level, which rules them out from “good plasmonic materials” as potential candidates for sensing applications, these materials can effectively transform the energy of photons to localized heat, thus serving in a numerous amount of applications, such as biomedicine [99], seawater desalination [100–102] and catalysis [103].

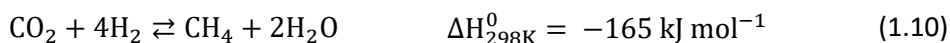
## 1.4. Catalytic reactions for renewable fuels

As it was mentioned in section 1.1, two main catalytic reactions, required in P2G technology are CO<sub>2</sub> methanation and water reduction reactions. In this section the reaction overview, state of the art and main mechanisms are discussed.

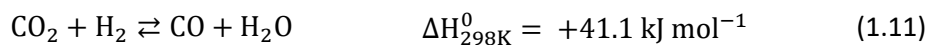
### 1.4.1. CO<sub>2</sub> methanation

#### 1.4.1.1. Description and state of the art

CO<sub>2</sub> methanation, or Sabatier reaction is a highly exothermic reversible reaction [104], requiring the transfer of eight electrons for the full reaction to happen:



Typically, this reaction is performed thermocatalytically under stoichiometric gas ratio (H<sub>2</sub>:CO<sub>2</sub> = 4:1) at temperatures from 200°C to 450°C, which depends on the catalyst and other ambient conditions (pressure and gas flow). At higher temperatures, a competing reaction starts to take place, named reverse water gas shift reaction (RWGS), limiting the methanation reaction yield:



Due to the high demand for renewable methane it is extremely important to find an efficient and at the same time non-expensive catalyst for carbon dioxide methanation. The most typical candidates for these catalysts are transition metals, such as nickel (Ni), iron (Fe), cobalt (Co), rhodium (Rh), ruthenium (Ru) etc. The advantage of transition metals as methanation reaction catalysts lies in the partially occupied d-orbitals, which take an active part in the hydrogen molecule dissociation for the further CO<sub>2</sub> molecule hydrogenation. Besides, the atoms of these metals can have multiple oxidation states, which opens a variety of reaction pathways. In the work of Gao et al. [105] for the first time a comparison of the VIII-group metal activities was made as the methanation catalysts. Among transition metals, Ni and Ru have the highest selectivity to methane [106], in general due to the high adsorption energy of the CO<sub>2</sub> on the metal atoms. This feature allows the intermediate products (such as CO, HCOOH, etc.) to not desorb from the catalyst surface, but hydrogenate completely until CH<sub>4</sub> formation. Given the fact that nickel, compared to ruthenium, is an abundant and non-toxic material [107], its utilization as an industrial catalyst is the most promising from the economical point of view.

The catalyst efficiency directly depends on the amount of the active sites, where some of the reaction steps take place. These sites are located on the surface of the material, and are in the direct contact with the reactant. Therefore, the amount of catalytic reactions per time unit, and, correspondingly, the catalyst activity is increased with increase of the its surface. Large catalyst effective surface can be achieved in dispersed metal catalysts, where metal-oxide supports are used as a substrate for the metallic nanoparticles, dispersed in their surface. As nanoparticles have a high surface-to-mass ratio, they can assure greater catalyst activity at lower mass of resources spent, which determines the economic benefits of their use on an industrial scale. In their turn, the inorganic substrates can possess a complicated porous structure, and, as a result, a large open surface area. It allows to place more metallic nanoparticles on their surface, and thus increase the catalyst efficiency without changing its volume. However, except for their morphological advantages, the metal-oxide supports can also have a number of reaction-promoting properties.

Zeolites and metal oxides ( $\text{SiO}_2$ ,  $\text{Al}_2\text{O}_3$ ,  $\text{SiO}_2\text{-Al}_2\text{O}_3$ ,  $\text{TiO}_2$ , etc.) are most frequently used as industrial catalyst supports. Aziz et al. [108] performed a comparative study of different metal-oxide supports and their influence on methane yield and selectivity revealed that the nickel-based catalyst with cerium oxide support showed the best catalytic properties, far ahead of other metal-oxide promoters. Later, a Ni-Co-based catalyst with  $\text{CeO}_2\text{-ZrO}_2$  support demonstrated 95% conversion of  $\text{CO}_2$  to methane at  $400^\circ\text{C}$  with selectivity 99% [109].

Cerium oxide has a high ionic conductivity, which is due to the low bond energy of its lattice oxygen [110]. As a result, these materials has a high concentration of bulk and, importantly, surface oxygen vacancies, which leads to an increased concentration of  $\text{CO}_2$  adsorption active sites. During oxygen vacancy formation, so-called basic sites are formed, which possess free electron density, needed for chemisorption and activation of the  $\text{CO}_2$  molecule on the surface of the oxide. Besides, high oxygen vacancy mobility in the cerium oxide hinders the metal nanoparticle oxidation, but facilitates their efficient reduction.

It has also been seen, that small-sized nickel nanoclusters result in higher activity and methane selectivity [111]. In this regard, the mass fraction of nickel to the support mass is a critical parameter in the design of the catalyst. A low mass fraction of nickel leads to low concentration of the active sites, and, therefore, low catalyst activity as a result of the amount of reactions per time unit. On the other hand, a too high mass fraction results in increase of the metal cluster size and decrease of the surface-to-volume ratio, which in its turn also leads to the low number of active sites. Besides, as the size of the clusters decreases, the perimeter of the interface

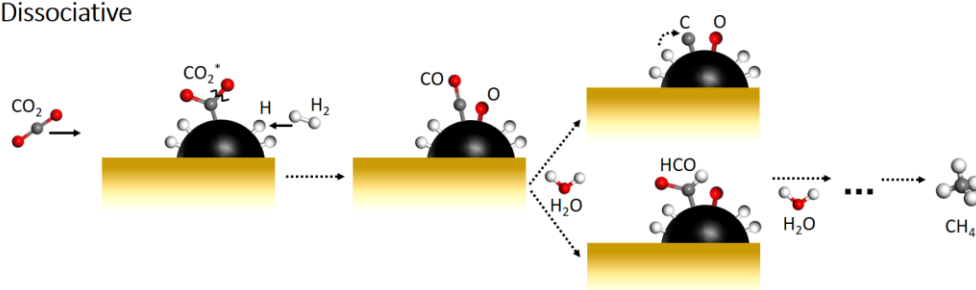
between the nickel clusters and the substrate becomes larger, which, according to numerous works, often plays a key role in the effective course of the methanation reaction [112,113].

The main bottleneck for the use of nickel as an industrial catalyst lies in its tendency to deactivate with time [114]. In particular, carbon atoms, which are present on the nickel surface during the reaction, can become nuclei for long carbon chain (coke) formation [115]. Such structures poison the catalyst, strongly bonding on its surface and depriving it of active sites for hydrogen dissociation. Besides, under long reaction time and high operation temperatures nickel nanoclusters tend to sinter, significantly impairing the distribution of the catalyst on the substrate surface and reducing the number of active sites [116]. These problems are often addressed by adding a second metal to the active phase [117], or by changing the  $\text{CO}_2/\text{H}_2$  ratio [118], which results in the regeneration of the catalyst surface by competing adsorption of additional carbon dioxide.

#### 1.4.1.2. Mechanisms of $\text{CO}_2$ methanation

The two most accepted mechanisms of Ni-based catalytic carbon dioxide methanation are considered to be the dissociative and associative mechanisms [105,112,119]. The reaction goes along one or another pathway depending, particularly, on the characteristics of the support, as well as on the ambient conditions, such as inlet gas ratio, temperature and pressure.

Dissociative



Associative

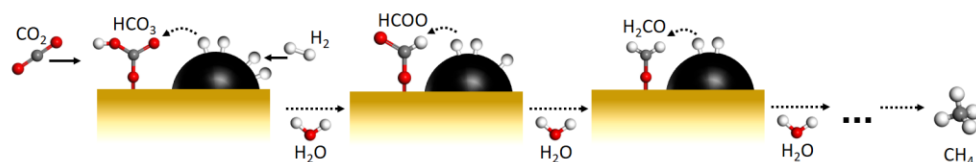


**Figure 1.12.** Mechanisms of  $\text{CO}_2$  methanation over Ni-based catalyst.

Both mechanisms involve Ni surface atoms as active sites for hydrogen molecule adsorption and dissociation, as well as spill-over of hydrogen atoms on the nickel-support interface (Figure 1.12). Nickel, like all transition metals, has a reduced activation barrier of hydrogen molecule dissociation, mainly due to the presence of semi-occupied *d*-orbitals, which extend for a considerable distance from the surface. However, the methanation mechanism depends on the CO<sub>2</sub> molecule activation.

The dissociative mechanism can be described as follows: the carbon dioxide molecule is adsorbed on the active site (nickel or support surface) and dissociated into the oxygen atom and a carbonyl radical (CO<sub>ads</sub>), which according to numerous studies [112,120,121] is bonded with the metallic nanoparticles. Due to the high adsorption energy of carbonyls on nickel, this radical is not desorbed as a CO molecule, but further hydrogenated to methane either directly through formyl intermediates (HCO<sub>ads</sub>) [122], or by dissociation into C<sub>ads</sub> and O<sub>ads</sub> species and subsequent hydrogenation of adsorbed carbon [123].

The key to the associative mechanism lies in adsorption of the CO<sub>2</sub> molecule as carbonates and bicarbonates (COO<sup>-</sup>, HCO<sub>3</sub>) as a result of high concentration of basic sites (due to oxygen vacancies formation) or randomly present OH<sup>-</sup> groups on the surface of the support [124]. Oxygen atoms of adsorbed carbonate species are subsequently replaced by atomic hydrogen, supplied by the metallic clusters, taking the route through formate intermediates (HCOO<sup>-</sup>) to methane [125].

Despite the strong bonding of carbonyls with surface Ni atoms, at higher temperatures CO desorption becomes more favorable, which opens a pathway for the RWGS reaction, thus decreasing the selectivity to methane [126].

## 1.4.2. Hydrogen evolution reaction (HER)

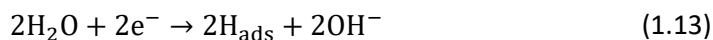
### 1.4.2.1. Description and state of the art

The water splitting reaction is a non-spontaneous reaction that requires energy to break water into hydrogen and oxygen. The theoretical minimum energy to break the water molecule is defined by its Gibbs free energy. In electrochemical conditions, this energy corresponds to the minimal thermodynamic water splitting potential: 1.23 V. However, in a real system, due to different types of losses, the applied potential needed to perform the reaction is usually larger than the theoretical one by the value  $\eta$ , which is called *overpotential*. This value depends on

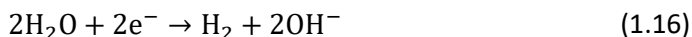
the catalyst and electrolyte properties, as well as the cell setup. So the minimum required voltage for water splitting can be written down as following:

$$V = 1.23 \text{ V} + \eta \quad (1.12)$$

The hydrogen evolution reaction (HER) requires two electrons to reduce the water molecules to a hydrogen [127]. The HER in alkaline media takes place in two steps: i) Volmer water dissociation, consisting in chemisorption of the water molecule on the catalyst surface and its dissociation which results in the formation of two adsorbed protons (Equation 1.12), and one of the two following steps: ii) Tafel chemical hydrogen desorption reaction (Equation 1.13) or iii) Heyrovsky electrochemical hydrogen desorption, which happens with an additional electron transfer (Equation 1.14).



The overall reaction would look like following:



The absolute potential value, required for HER depends on the electrolyte media according to the Nernst equation, and in the alkaline media (pH = 14) is equal to  $E^0 = -0.826 \text{ eV vs. RHE}$ .

As HER is happening at the cathode of the EC cell, a compensating oxidation reaction must happen at the anode. Mostly, it is oxygen evolution reaction (OER), but other oxidation reactions can take place.

Sabatier principle, which states that for efficient reaction the adsorption energy of the reactant on the catalyst should be neither too large nor too small, can be also applied to HER. Therefore, candidate materials for HER catalyst should follow a typical volcano plot [128], with the optimal materials at the top of the volcano. According to the numerous studies, Pt is considered to be the best single-metal material for HER. However, due to high cost of this rare metal, search for better candidates has been still relevant. Moreover, exchange current density for platinum catalyst, being high at acidic conditions, drastically decreases in alkaline media [129]. Out of other single metals, nickel turned out to be the optimal material

for HER in the alkaline media thanks to its high hydrogen generation activity, excellent corrosion resistance, high conductivity and cheapness [130].

However, recent advances have shown that Ni-containing transition metal bimetallic and trimetallic materials (NiMo [131–133], NiFe [134–136], NiCo [137], CoNiMo [138], CoNiFe [139], NiFeMo [140] etc.) are the benchmark catalysts for HER. One of the lowest overpotentials was reported on the MoNi<sub>4</sub> catalyst supported by MoO<sub>2</sub> cuboids on a nickel foam [141]. MoS<sub>2</sub> is considered a promising low-cost catalyst with an almost optimal binding energy with hydrogen (0.08 eV) [142]. Also, transition metal carbides (TMC) [143,144] and transition metal phosphides (TMP) [145–147] have received a lot of attention recently owing to their high catalytic activity and stability in both acid and alkaline media.

Photoelectrochemical hydrogen evolution requires photo-active corrosion-resistive electrodes, which are most commonly represented by semiconductors [148]. They should also have proper band alignment with respect to the water reduction potential. Thus, the following materials meet the criteria stated above and are most abundantly used as photocathodes for HER: Cu<sub>2</sub>O [149], GaP [150], GaInP [23,151], CuGaSe<sub>2</sub> [152], CIGS [153], CaFe<sub>2</sub>O<sub>4</sub> [154] etc. The following photocathode materials Sb<sub>2</sub>Se<sub>3</sub> photocathode recently demonstrated benchmark performance in solar hydrogen production [155].

Finally, plasmonic approach allows to combine excellent catalytic properties of noble and transition metal catalysis with their ability to harvest solar light for photoelectrochemical water splitting application.

#### **1.4.2.2. Electron scavengers and hole scavengers**

In order to facilitate either of the water-splitting half-reactions (hydrogen or oxygen evolution reaction), special sacrificial chemical compounds are used, which react easily with one of the carrier types. This significantly lowers the energetic barrier for the other half-reaction and also prevents the generated charge carriers from recombination in case of photocatalytic materials [19]. Specifically, hole scavengers consume generated holes and are used to improve water reduction, when the electron scavengers are excellent electron acceptors and are used to study oxygen evolution reaction. These compounds must have lower corresponding redox potentials compared to water redox potentials, making their reaction favorable in the aqueous environment. Iodates (KIO<sub>3</sub> and NaIO<sub>3</sub>) were reported as excellent electron scavengers [156,157], while also other reagents (AgNO<sub>3</sub>, Na<sub>2</sub>S<sub>2</sub>O<sub>8</sub>) can be used [158,159].

## 1.5. Plasmon-enhanced catalysis

Owing to different decay mechanisms, surface plasmons in catalytic materials offer several main ways of improving chemical reactions: through hot-carrier generation, local field enhancement, energy transfer and heating. Although all four consequences of the plasmon damping can boost the reaction, only non-thermal decay pathways can result in altering of the reaction mechanism, while the photothermal one can only affect the reaction rate [160].

Often plasmonic nanoparticles are combined with semiconductor supports [161,162]. Depending on the relative position of the energy levels in the combined system, several scenarios can be developed. On the one hand, the semiconductor can act as a trap for hot carriers, generated as a result of a localized plasmon decay in metallic nanoparticles and transferred to the support, and use them further in the redox reactions [95]. On the other hand, the metallic nanoparticles can be used as a drain for photo-excited charge carriers, generated in the semiconductor due to direct absorption of a photon [163]. Also, the excited LSPR in the metallic NP can cause an electron-hole pair generation through a plasmon-induced resonant energy transfer (PIRET) via dipole-dipole interaction [97]. Finally, a novel mechanism consisting in direct metal-semiconductor charge transfer has been recently discovered [96].

Plasmon heating is a widely accepted consequence of the LSPR damping in plasmonic nanoparticles. As was mentioned before, transition metals are more popular in the photothermal catalytic applications than noble metals due to higher damping and significant ability to generate heat. Moreover, transition metals possess a broad absorption band, which in some cases almost perfectly matches the solar irradiation spectrum [164]. Among others, Ni was proven to demonstrate excellent ability to effectively absorb solar light and convert it to heat [165].

Two main drawbacks of the photothermal enhancement of the catalytic reactions are its inability to improve selectivity to one chemical product or another by activating a new reaction pathway and inevitability of overall catalyst heating and its possible subsequent thermal degradation.

### 1.5.1. Plasmon-enhanced CO<sub>2</sub> methanation

As was discussed above, standard thermocatalytic approach for CO<sub>2</sub> methanation requires relatively high temperatures (150-500°C) [166], which gives rise to a number of alternative approaches to replace or assist thermochemical



catalysis [108,167–169]. Utilization of solar light as an additional energy source for CO<sub>2</sub> hydrogenation to methane has been massively reported [170–174]. Among other light-involving approaches, plasmon-assisted catalysis is a rapidly emerging field in CO<sub>2</sub> reduction [175].

To avoid losses and ensure hot-carrier excitation at the active sites, noble metals were used in plasmon-assisted CO<sub>2</sub> conversion into value-added products [176,177]. W. Hou et al. reported 24-fold enhancement of CO<sub>2</sub> conversion to methane by Au/TiO<sub>2</sub> catalyst under visible light through PIRET mechanism compared to pure TiO<sub>2</sub> or Au phase [178]. Effective charge separation and consequently improved photocatalytic methanation of CO<sub>2</sub> was also observed for Au nanoparticles sandwiched between CuTiP nanosheets [179].

However, noble catalysts are known for their low conversion rates and poor selectivity to methane. This has stimulated intensive research on plasmon-enhanced methanation over transition metal catalysts. Due to severe damping of the plasmon in transition metals, many studies have focused on exploiting the photothermal effect of the plasmon decay [180,181]. Remarkable photothermal properties of group VIII nanocatalysts were reported and discussed in the framework of their applications in CO<sub>2</sub> hydrogenation [182]. Moreover, a fully solar-driven CO<sub>2</sub> reforming of CH<sub>4</sub> was demonstrated over a Ni nanoclusters-based catalyst with excellent photothermal conversion values [183].

Another common approach lies in combining noble plasmonic nanoparticles with transition metal catalyst. Liu et al. have utilized the visible light to excite the plasmon resonance in Au nanoparticles in order to increase the reaction rate of Rh/SBA-15 catalyst in the dry reforming of CO<sub>2</sub> to syngas [184], later confirming a similar effect in the Pt-Au/SiO<sub>2</sub> coupled catalyst [185]. A bimetallic Ni-Au catalyst was reported in the work [186], showing excellent synergetic effect between the two components under visible light irradiation.

Nevertheless, multiple studies have shown that transition metals can induce non-thermal effects on the CO<sub>2</sub> reduction [187–190]. Light-assisted CO<sub>2</sub> reduction with methane was studied for plasmonic Ni/Al<sub>2</sub>O<sub>3</sub> catalyst where non-thermal reaction improvement was claimed [191,192]. Same conclusion was withdrawn for SiO<sub>2</sub>-encapsulated Ni nanoclusters [193]. Mateo et al. used a Ni-BTO photothermal catalyst for CO<sub>2</sub> methanation and suggested that the reaction was driven by a non-thermal hot-electron mechanism [194]. Finally, CO<sub>2</sub> methanation with Ni modified low-crystalline Ni–Ge containing hydroxide was significantly enhanced owing to the improved absorption ability of the catalyst and hot-electron contribution [195]. Besides the increase in the reaction rate, the plasmonic catalysts were proven to affect the selectivity to methane by altering the reaction pathway [196].

### 1.5.2. Plasmon-enhanced electrochemical reactions

Plasmon-driven electrochemical reactions form another uprising field of light-assisted catalysis, and are widely investigated in photoelectrochemical cells [162].

The major part of the studies is focused on the hot-carrier-induced enhancement of the reactions through hot electron transfer from a plasmonic nanoparticle to a semiconductor [197]. Same as in photocatalysis, Au/TiO<sub>2</sub> is the most studied combination of materials for PEC. Qian et al. showed that size of Au plasmonic nanoparticles plays a crucial role in the hot electron transfer to TiO<sub>2</sub> under visible light illumination ( $\lambda > 435$  nm) during HER, where large NPs stimulate the electron injection, while the small ones accumulate charge and impede the reaction [25].

SPP-based photoelectrodes were used in water splitting. Au nanohole array with incorporated hematite nanorods have shown a tenfold increase in the photocurrent at  $E_w = 0.23$  vs. Ag/AgCl [76]. The excellent performance at the energies below the band gap of hematite was attributed to SPR-induced local field enhancement and generating additional photocurrent in hematite nanorods through PIRET mechanism.

Photothermal consequence of the plasmon resonance has been observed for a variety of different materials [103]. Wu et al. reported significant enhancement of the HER caused by a combined thermoplasmonic and hot electron effect in MXenes [198]. In another work, Ag-based encapsulated plasmonic catalyst demonstrated excellent photothermal solar-to-heat conversion for H<sub>2</sub> production from seawater and its simultaneous desalination [199].

Very few works were published on plasmonic Ni-based materials for PEC water splitting. Pawar et al. reported more than double production of hydrogen by using Ni-decorated LaFeO<sub>3</sub> electrode compared to the plain one [200]. Yalavarthi et al. have applied a periodic array of CdS-coated Ni/Pt nanopillars as a plasmonic photocathode for photoelectrochemical water splitting [201]. They observed almost threefold increase in the photocurrent and attributed it to PIRET due to strong field enhancement from the hybridized photonic/plasmonic modes.

Other nickel-containing materials have also proved themselves as excellent candidates for photothermally-boosted electrochemical catalysts. Nickel phosphide catalyst with broadband solar light absorption and thermal insulation demonstrated the ability to perform HER at overpotentials as low as 218 mV while delivering 100 mA cm<sup>-2</sup> current density [202].

### 1.5.3. Disentangling photothermal and charge-induced catalytic enhancements

Usually, photothermal and charge-carrier-induced effects in a plasmonic catalyst happen simultaneously, and its catalytic response to illumination contains both contributions. Distinguishing them is a nontrivial problem, which is typically approached by temperature control [203–205]. However, it requires highly accurate measurements of the surface temperature, and is hardly achievable in regular set-ups. Zhang et al. made an attempt to measure the gradient of the temperature in the catalyst by using two thermocouples, showing a clear difference in the top and bottom surfaces [188]. Recently, Baffou et al. [206] have provided a series of experimental procedures that would help to disentangle these effects, including variation of light intensity, wavelength, polarization and beam size.

Photoelectrochemical techniques are often used to separate thermal and electronic effects. In the work of Zhan et al. [207], the two phenomena are distinguished by separating the plasmonic photocurrent into two contributions: rapid response current (RRC) and slow response current (SRC). The thermal contribution was also confirmed using a thermodynamic model, based on the shape of the electrochemical response. An important issue has to be considered when applying photoelectrochemical approach is to control the temperature of the electrolyte, when comparing dark and light measurements [208].

Untangling thermal and non-thermal effects for CO<sub>2</sub> methanation over Rh/TiO<sub>2</sub> catalyst was studied by Zhang et al [188]. By measuring the temperature gradient of the Rh/TiO<sub>2</sub> catalyst bed and total reaction rate they have evaluated an effective thermal reaction rate and calculated the non-thermal term. Later, Li et al. have proven nonthermal effects in CO<sub>2</sub> methanation over the same catalyst by applying indirect illumination along with precise temperature profile monitoring [187]. They have also observed a linear dependence of the non-thermal reaction rate on surface temperature, while the thermal catalysts demonstrate exponential behavior. It should be noted that light-driven non-thermal mechanisms in transition metal catalysts with an active support may also originate from the photocatalytic properties of the metal-oxide support. Thus, Quan et al. have attributed the non-thermal part of the light-induced methanation enhancement to the CeO<sub>2</sub> photocatalytic response, rather than to hot-electron effect on Ru [209].

## 1.6. Objectives of the thesis

In summary, the rapidly emerging field of plasmonic catalysis offers numerous ways of enhancing catalytic reactions, vital for the development of innovative technologies to solve some of the environmental challenges that currently face our society. Despite the obvious advantages of noble metals in plasmonic applications, transition metals exhibit a variety of attractive features, such as broad visible-light absorption, high reactivity and excellent photothermal properties. Considering that nickel is an abundant transition metal with appropriate catalytic properties for renewable fuel synthesis, it was selected as a target material in our work. Therefore, this thesis is focused on applying solar light to Ni-based plasmonic catalysts for the enhancement of catalytic reactions for renewable synthetic fuels. The main objectives of the thesis can be stated as follows:

- Design Ni-based plasmonic catalysts for renewable fuels reactions (CO<sub>2</sub> methanation and HER);
- Identify optimal reaction conditions by optical characterization of the catalyst;
- Quantify the reaction gain and compare the results;
- Define mechanisms of reaction enhancement and discern between thermal and non-thermal contributions.

In relation with the objectives stated above, the thesis is organized as follows.

- Chapter 2 is focused on synthesis, characterization and application of high-surface-area plasmonic Ni/CeO<sub>2</sub> catalyst for light-assisted CO<sub>2</sub> methanation. The catalytic activity of the catalyst is studied with and without illumination, revealing the combined effect of solar light on the reaction boost. Mechanism of the light-assisted reaction is identified by in-situ spectroscopy and high resolution microscopy techniques, and the evaluations of energy consumption gains are presented.
- Chapter 3 presents development of plasmonic photothermal Ni nanoparticles catalyst for HER and its incorporation as a photocathode in the electrochemical cell. Dark and irradiation studies were made to demonstrate the difference between heat-induced and photothermal approaches, showing a clear difference in the electrochemical response. Periodic pulsed illumination was used to define the mechanism of reaction enhancement.
- Chapter 4 shows a study on a Ni nanohole array plasmonic structure used as a photocathode for electrochemical reduction reaction. The NHA was used as a model structure to identify surface and localized plasmons in nickel and emphasize the role of nanohole ordering. The electrochemical activity of the Ni NHA photocathode was studied with pulsed laser-assisted irradiation, allowing

to investigate wavelength-dependent electrochemical response as well as the mechanism of plasmon-induced reaction improvement.

Finally, the main conclusions and future outlook are summarized in Chapter 5. In addition, Appendices to the Chapters 2-4, containing additional experimental and theoretical data, are provided at the end of the manuscript.

## 1.7. References

- [1] UNITED NATIONS DEVELOPMENT PROGRAMME, *Human Development Data Center*, <https://hdr.undp.org/en/data>.
- [2] N. S. Ouedraogo, *Energy Consumption and Human Development: Evidence from a Panel Cointegration and Error Correction Model*, *Energy* **63**, 28 (2013).
- [3] British Petroleum, *Statistical Review of World Energy*, 2021.
- [4] *Global Monitoring Laboratory*, <https://gml.noaa.gov/ccgg/>.
- [5] D. R. Lide, *CRC Handbook of Chemistry and Physics, Internet Version 2005* (CRC Press, Boca Raton, FL, 2005).
- [6] International Energy Agency, *Key World Energy Statistics*, 2021.
- [7] M. Perez and R. Perez, *Update 2022 – A Fundamental Look at Supply Side Energy Reserves for the Planet*, *Sol. Energy Adv.* **2**, 100014 (2022).
- [8] B.P., *Statistical Review of World Energy*, 2020.
- [9] International Energy Agency and OECD Nuclear Energy Agency, *Projected Costs of Generating Electricity*, 2020.
- [10] IRNEA, *Renewable Power Generation Costs in 2020*, 2020.
- [11] M. Specht, J. Brellocks, V. Frick, B. Stürmer, U. Zuberbühler, M. Sterner, and G. Waldstein, *Speicherung von Bioenergie Und Erneuerbarem Strom Im Erdgasnetz*, *Erdoel Erdgas Kohle* **126**, 342 (2010).
- [12] A. Ajanovic and R. Haas, *On the Long-Term Prospects of Power-to-Gas Technologies*, *Wiley Interdiscip. Rev. Energy Environ.* **8**, 1 (2019).
- [13] M. A. Scibioh and B. Viswanathan, *CO<sub>2</sub> Conversion—Relevance and Importance*, *Carbon Dioxide to Chem. Fuels* **1** (2018).
- [14] H. Chen, R. Shi, and T. Zhang, *Nanostructured Photothermal Materials for Environmental and Catalytic Applications*, *Molecules* **26**, 7552 (2021).
- [15] C. Jiang, S. J. A. Moniz, A. Wang, T. Zhang, and J. Tang, *Photoelectrochemical Devices for Solar Water Splitting-Materials and Challenges*, *Chem. Soc. Rev.* **46**, 4645 (2017).
- [16] L. Ye and K. Xie, *High-Temperature Electrocatalysis and Key Materials in Solid Oxide Electrolysis Cells*, *J. Energy Chem.* **54**, 736 (2021).
- [17] S. Cestellos-Blanco, H. Zhang, J. M. Kim, Y. xiao Shen, and P. Yang, *Photosynthetic Semiconductor Biohybrids for Solar-Driven Biocatalysis*, *Nat. Catal.* **3**, 245 (2020).
- [18] R. Snoeckx and A. Bogaerts, *Plasma Technology-a Novel Solution for CO<sub>2</sub> Conversion?*, *Chem. Soc. Rev.* **46**, 5805 (2017).
- [19] D. Kong, Y. Zheng, M. Kobielski, Y. Wang, Z. Bai, W. Macyk, X. Wang, and J. Tang, *Recent Advances in Visible Light-Driven Water Oxidation and Reduction in Suspension Systems*, *Mater. Today* **21**, 897 (2018).

- [20] W. N. Wang, W. J. An, B. Ramalingam, S. Mukherjee, D. M. Niedzwiedzki, S. Gangopadhyay, and P. Biswas, *Size and Structure Matter: Enhanced CO<sub>2</sub> Photoreduction Efficiency by Size-Resolved Ultrafine Pt Nanoparticles on TiO<sub>2</sub> Single Crystals*, *J. Am. Chem. Soc.* **134**, 11276 (2012).
- [21] O. Ola and M. Mercedes Maroto-Valer, *Role of Catalyst Carriers in CO<sub>2</sub> Photoreduction over Nanocrystalline Nickel Loaded TiO<sub>2</sub>-Based Photocatalysts*, *J. Catal.* **309**, 308 (2014).
- [22] M. T. Winkler, C. R. Cox, D. G. Nocera, and T. Buonassisi, *Modeling Integrated Photovoltaic-Electrochemical Devices Using Steady-State Equivalent Circuits*, *Proc. Natl. Acad. Sci. U. S. A.* **110**, E1076 (2013).
- [23] H. Lim, J. L. Young, J. F. Geisz, D. J. Friedman, T. G. Deutsch, and J. Yoon, *High Performance III-V Photoelectrodes for Solar Water Splitting via Synergistically Tailored Structure and Stoichiometry*, *Nat. Commun.* **10**, 3388 (2019).
- [24] J. M. Chem, *Plasmon-Dominated Photoelectrodes for Solar Water Splitting*, *J. Mater. Chem. A* **5**, 4233 (2017).
- [25] K. Qian, B. C. Sweeny, A. C. Johnston-peck, W. Niu, J. O. Graham, J. S. Duchene, J. Qiu, Y. Wang, M. H. Engelhard, D. Su, E. A. Stach, and W. D. Wei, *Surface Plasmon-Driven Water Reduction: Gold Nanoparticle Size Matters*, *J. Am. Chem. Soc.* **136**, 9842 (2014).
- [26] T. G. U. Ghobadi, A. Ghobadi, E. Ozbay, and F. Karadas, *Strategies for Plasmonic Hot-Electron-Driven Photoelectrochemical Water Splitting*, *ChemPhotoChem* **2**, 161 (2018).
- [27] P. Peerakiatkhajohn, T. Butburee, J. Yun, H. Chen, R. M. Richards, and L. Wang, *A Hybrid Photoelectrode with Plasmonic Au@TiO<sub>2</sub> Nanoparticles for Enhanced Photoelectrochemical Water Splitting*, **3**, (2015).
- [28] K. Ueno, Y. Mor, and T. Osh, *Plasmon-Enhanced Water Splitting Utilizing the Heterojunction Synergistic Effect between SrTiO<sub>3</sub> and Rutile-TiO<sub>2</sub>*, *Chem. Lett.* **44**, 618 (2015).
- [29] A. Kudo, *Z-Scheme Photocatalyst Systems for Water Splitting under Visible Light Irradiation*, *MRS Bull.* **36**, 32 (2011).
- [30] F. Urbain, *Multijunction Si Photocathodes with Tunable Photovoltages from 2.0 V to 2.8 V for Light Induced Water Splitting*, *Energy Environ. Sci.* **9**, 145 (2016).
- [31] P. Drude, *Zur Elektronentheorie Der Metalle*, *Ann. Phys.* (1900).
- [32] M. Polyanskiy, *RefractiveIndex.INFO*, <https://refractiveindex.info/>.
- [33] B. R. Cooper, H. Ehrenreich, and H. R. Philipp, *Optical Properties of Noble Metals. II*, *Phys. Rev.* **138**, A494 (1965).
- [34] C. Noguez and C. E. Román-Velázquez, *Dispersive Force between Dissimilar Materials: Geometrical Effects*, *Phys. Rev. B - Condens. Matter Mater. Phys.* **70**, 1 (2004).
- [35] P. B. Johnson and R. W. Christy, *Optical Constant of the Noble Metals*, *Phys. Rev. B* **6**, 4370 (1972).
- [36] J. H. Weaver and H. P. R. Frederikse, *Optical Properties of Selected Elements*, 82nd ed. (CRC Press, Boca Raton, FL, 2001).
- [37] R. Rosei, F. Antonangeli, and U. M. Grassano, *D Bands Position and Width in Gold From Very Low Temperature Thermomodulation Measurements*, *Surf. Sci.* **37**, 689 (1973).

- [38] H. Ehrenreich and H. R. Philipp, Optical Properties of Ag and Cu, *Phys. Rev.* **128**, 1622 (1962).
- [39] M. Gadenne and J. Lafait, *Optical Properties of Ni from 0.03 to 6 eV*, *J. Phys.* **47**, 1405 (1986).
- [40] D. W. Lynch, R. Rosei, and J. H. Weaver, *Infrared and Visible Optical Properties of Single Crystal Ni at 4K*, *Solid State Commun.* **9**, 2195 (1971).
- [41] D. Gall, *Electron Mean Free Path in Elemental Metals*, *J. Appl. Phys.* **119**, 1 (2016).
- [42] V. K. Kamineni, M. Raymond, E. J. Bersch, B. B. Doris, and A. C. Diebold, *Optical Metrology of Ni and NiSi Thin Films Used in the Self-Aligned Silicidation Process*, *J. Appl. Phys.* **107**, (2010).
- [43] A. S. Siddiqui and D. M. Treherne, *Optical Properties of Some Transition Metals at Infrared Frequencies*, *Infrared Phys.* **17**, 33 (1977).
- [44] P. B. Johnson and R. W. Christy, *Optical Constants of Transition Metals*, *Phys. Rev. B* **9**, 5056 (1974).
- [45] H. Ehrenreich, H. R. Philipp, and B. Segall, *Optical Properties of Aluminum*, *Phys. Rev.* **132**, 1918 (1963).
- [46] D. Y. Smith and B. Segall, *Intraband and Interband Processes in the Infrared Spectrum of Metallic Aluminum*, *Phys. Rev. B* **34**, 5191 (1986).
- [47] R. LaVilla and H. Mendlowitz, *Optical Constants of Aluminum in Vacuum Ultraviolet*, *Phys. Rev. Lett.* **9**, 149 (1962).
- [48] G. Hass and J. . Waylonis, *Optical Constants and Reflectance and Transmittance of Evaporated Aluminum in the Visible and Ultraviolet*, *J. Opt. Soc. Am.* **51**, 719 (1961).
- [49] P. R. West, S. Ishii, G. V. Naik, N. K. Emani, V. M. Shalaev, and A. Boltasseva, *Searching for Better Plasmonic Materials*, *Laser Photonics Rev.* **4**, 795 (2010).
- [50] G. V. Naik, V. M. Shalaev, and A. Boltasseva, *Alternative Plasmonic Materials: Beyond Gold and Silver*, *Adv. Mater.* **25**, 3264 (2013).
- [51] T. Pakizeh, *Optical Absorption of Nanoparticles Described by an Electronic Local Interband Transition*, *J. Opt. (United Kingdom)* **15**, (2013).
- [52] S. Schuermans, T. Maurer, J. Martin, J.-B. Moussy, and J. Plain, *Plasmon / Interband Transitions Coupling in the UV from Large Scale Nanostructured Ni Films*, *Opt. Mater. Express* **7**, 1787 (2017).
- [53] A. Lalisse, G. Tessier, J. Plain, and G. Baffou, *Quantifying the Efficiency of Plasmonic Materials for Near-Field Enhancement and Photothermal Conversion*, *J. Phys. Chem. C* **119**, 25518 (2015).
- [54] M. Van Kampen, J. T. Kohlhepp, W. J. M. De Jonge, B. Koopmans, and R. Coehoorn, *Sub-Picosecond Electron and Phonon Dynamics in Nickel*, *J. Phys. Condens. Matter* **17**, 6823 (2005).
- [55] X. Wang, S. C. Huang, S. Hu, S. Yan, and B. Ren, *Fundamental Understanding and Applications of Plasmon-Enhanced Raman Spectroscopy*, *Nat. Rev. Phys.* **2**, 253 (2020).
- [56] J. Chen, P. Albella, Z. Pirzadeh, P. Alonso-González, F. Huth, S. Bonetti, V. Bonanni, J. Åkerman, J. Nogués, P. Vavassori, A. Dmitriev, J. Aizpurua, and R. Hillenbrand, *Plasmonic Nickel Nanoantennas*, *Small* **7**, 2341 (2011).
- [57] Z. Pirzadeh, T. Pakizeh, V. Miljkovic, C. Langhammer, and A. Dmitriev, *Plasmon-Interband*



- Coupling in Nickel Nanoantennas*, ACS Photonics **1**, 158 (2014).
- [58] A. A. Grunin, A. G. Zhdanov, A. A. Ezhov, E. A. Ganshina, and A. A. Fedyanin, *Surface-Plasmon-Induced Enhancement of Magneto-Optical Kerr Effect in All-Nickel Subwavelength Nanogratings*, Appl. Phys. Lett. **97**, 2010 (2010).
- [59] E. T. Papaioannou, V. Kapaklis, E. Melander, B. Hjörvarsson, S. D. Pappas, P. Patoka, M. Giersig, P. Fumagalli, A. Garcia-Martin, and G. Ctistis, *Surface Plasmons and Magneto-Optic Activity in Hexagonal Ni Anti-Dot Arrays*, Opt. Express **19**, 23867 (2011).
- [60] M. Salaheldeen, M. Méndez, V. Vega, A. Fernández, and V. M. Prida, *Tuning Nanohole Sizes in Ni Hexagonal Antidot Arrays: Large Perpendicular Magnetic Anisotropy for Spintronic Applications*, ACS Appl. Nano Mater. **2**, 1866 (2019).
- [61] H. Fang, B. Caballero, E. M. Akinoglu, E. T. Papaioannou, A. García-Martín, J. C. Cuevas, M. Giersig, and P. Fumagalli, *Observation of a Hole-Size-Dependent Energy Shift of the Surface-Plasmon Resonance in Ni Antidot Thin Films*, Appl. Phys. Lett. **106**, (2015).
- [62] E. Kretschmann and H. Raether, *Radiative Decay of Non Radiative Surface Plasmons Excited by Light*, Zeitschrift Fur Naturforsch. - Sect. A J. Phys. Sci. **23**, 2135 (1968).
- [63] A. Otto, *Excitation of Nonradiative Surface Plasma Waves in Silver by the Method of Frustrated Total Reflection*, Zeitschrift Für Phys. **216**, 398 (1968).
- [64] H. Raether, *Surface Plasmons on Smooth and Rough Surfaces and on Gratings*, Vol. 111 (Springer-Verlag, Berlin, 1988).
- [65] M. Najiminaini, F. Vasefi, B. Kaminska, and J. J. L. Carson, *Nano-Hole Array Structure with Improved Surface Plasmon Energy Matching Characteristics*, Appl. Phys. Lett. **100**, (2012).
- [66] P. Zheng, S. K. Cushing, S. Suri, and N. Wu, *Tailoring Plasmonic Properties of Gold Nanohole Arrays for Surface-Enhanced Raman Scattering*, Phys. Chem. Chem. Phys. **17**, 21211 (2015).
- [67] B. Malani S and P. Viswanath, *Impact of Ordering of Gold Nanohole Arrays on Refractive Index Sensing*, J. Opt. Soc. Am. B **35**, 2501 (2018).
- [68] M. Tavakoli, Y. S. Jalili, and S. M. Elahi, *Rayleigh-Wood Anomaly Approximation with FDTD Simulation of Plasmonic Gold Nanohole Array for Determination of Optimum Extraordinary Optical Transmission Characteristics*, Superlattices Microstruct. **130**, 454 (2019).
- [69] J. P. Monteiro, L. B. Carneiro, M. M. Rahman, A. G. Brolo, M. J. L. Santos, J. Ferreira, and E. M. Girotto, *Effect of Periodicity on the Performance of Surface Plasmon Resonance Sensors Based on Subwavelength Nanohole Arrays*, Sensors Actuators, B Chem. **178**, 366 (2013).
- [70] T. Ohno, C. Wadell, S. Inagaki, J. Shi, Y. Nakamura, and T. Sannomiya, *Hole-Size Tuning and Sensing Performance of Hexagonal Plasmonic Nanohole Arrays*, **6**, 1594 (2016).
- [71] V. M. Agranovich and D. L. Mills, *Surface Polaritons: Electromagnetic Waves at Surfaces and Interfaces* (North-Holland, Amsterdam, 1982).
- [72] R. W. Wood, *On a Remarkable Case of Uneven Distribution of Light in a Diffraction Grating Spectrum*, Proc. Phys. Soc. London **18**, 269 (1901).
- [73] H. Gao, J. M. McMahon, M. H. Lee, J. Henzie, S. K. Gray, G. C. Schatz, and T. W. Odom, *Rayleigh Anomaly-Surface Plasmon Polariton Resonances in Palladium and Gold Subwavelength Hole Arrays*, Opt. Express **17**, 2334 (2009).

- [74] H. A. Atwater and A. Polman, *Plasmonics for Improved Photovoltaic Devices*, *Nat. Mater.* **9**, 865 (2010).
- [75] L. B. Sun, X. L. Hu, B. Zeng, L. S. Wang, S. M. Yang, R. Z. Tai, H. J. Fecht, D. X. Zhang, and J. Z. Jiang, *Effect of Relative Nanohole Position on Colour Purity of Ultrathin Plasmonic Subtractive Colour Filters*, *Nanotechnology* **26**, 305204 (2015).
- [76] J. Li, S. K. Cushing, P. Zheng, F. Meng, D. Chu, and N. Wu, *Plasmon-Induced Photonic and Energy-Transfer Enhancement of Solar Water Splitting by a Hematite Nanorod Array*, *Nat. Commun.* **4**, 2651 (2013).
- [77] C. F. Bohren, *How Can a Particle Absorb More than the Light Incident on It?*, *Am. J. Phys.* **51**, 323 (1983).
- [78] E. A. Coronado, E. R. Encina, and F. D. Stefani, *Optical Properties of Metallic Nanoparticles: Manipulating Light, Heat and Forces at the Nanoscale*, *Nanoscale* **3**, 4042 (2011).
- [79] T. K. Sau, C. J. Murphy, and M. L. H. C. Commun, *Seeded High Yield Synthesis of Short Au Nanorods in Aqueous Solution*, *Langmuir* **20**, 6414 (2004).
- [80] B. X. Xu and M. B. Cortie, *Shape Change and Color Gamut in Gold Nanorods, Dumbbells, and Dog Bones*, *Adv. Funct. Mater.* **16**, 2170 (2006).
- [81] M. Yamamoto, Y. Kashiwagi, T. Sakata, H. Mori, and M. Nakamoto, *Synthesis and Morphology of Star-Shaped Gold Nanoplates Protected by Poly( N -Vinyl-2-Pyrrolidone)*, **17**, 2003 (2005).
- [82] J. L. Burt, J. L. Elechiguerra, J. Reyes-gasga, J. M. Montejano-carrizales, and M. Jose-yacaman, *Beyond Archimedean Solids : Star Polyhedral Gold Nanocrystals*, **285**, 681 (2005).
- [83] C. L. Nehl, H. Liao, and J. H. Hafner, *Optical Properties of Star-Shaped Gold Nanoparticles*, *Nano Lett.* **6**, 683 (2006).
- [84] L. Scarabelli, M. Coronado-Puchau, J. J. Giner-Casares, J. Langer, and L. M. Liz-Marzán, *Monodisperse Gold Nanotriangles: Size Control, Large-Scale Self-Assembly, and Performance in Surface-Enhanced Raman Scattering*, *ACS Nano* **8**, 5833 (2014).
- [85] C. Kuttner, M. Mayer, M. Dulle, A. Moscoso, J. M. López-Romero, S. Förster, A. Fery, J. Pérez-Juste, and R. Contreras-Cáceres, *Seeded Growth Synthesis of Gold Nanotriangles: Size Control, SAXS Analysis, and SERS Performance*, *ACS Appl. Mater. Interfaces* **10**, 11152 (2018).
- [86] C. L. Nehl and J. H. Hafner, *Shape-Dependent Plasmon Resonances of Gold Nanoparticles*, *J. Mater. Chem.* **18**, 2415 (2008).
- [87] S. Eustis and M. A. El-Sayed, *Why Gold Nanoparticles Are More Precious than Pretty Gold: Noble Metal Surface Plasmon Resonance and Its Enhancement of the Radiative and Nonradiative Properties of Nanocrystals of Different Shapes*, *Chem. Soc. Rev.* **35**, 209 (2006).
- [88] P. K. Jain, W. Huang, and M. A. El-Sayed, *On the Universal Scaling Behavior of the Distance Decay of Plasmon Coupling in Metal Nanoparticle Pairs: A Plasmon Ruler Equation*, *Nano Lett.* **7**, 2080 (2007).
- [89] B. Sepúlveda, Y. Alaverdyan, J. Alegret, M. Käll, and P. Johansson, *Shape Effects in the Localized Surface Plasmon Resonance of Single Nanoholes in Thin Metal Films*, **16**, 3909 (2008).
- [90] A. Guglielmelli, F. Pierini, N. Tabiryan, C. Umeton, T. J. Bunning, and L. De Sio, *Thermoplasmonics with Gold Nanoparticles: A New Weapon in Modern Optics and Biomedicine*, *Adv. Photonics Res.* **2**, 2000198 (2021).

- [91] B. Palpant, *Gold Nanoparticles for Physics, Chemistry and Biology* (Imperial College Press, London, 2012).
- [92] G. V. Hartland, *Optical Studies of Dynamics in Noble Metal Nanostructures*, Chem. Rev. **111**, 3858 (2011).
- [93] H. P. Paudel, A. Safaei, and M. N. Leuenberger, *Nanoplasmonics in Metallic Nanostructures and Dirac Systems, in Nanoplasmonics - Fundamentals and Applications* (2017).
- [94] M. L. Brongersma, N. J. Halas, and P. Nordlander, *Plasmon-Induced Hot Carrier Science and Technology*, Nat. Nanotechnol. **10**, 25 (2015).
- [95] J. S. Pelli Cresi, M. C. Spadaro, S. D'Addato, S. Valeri, S. Benedetti, A. Di Bona, D. Catone, L. Di Mario, P. O'Keeffe, A. Paladini, G. Bertoni, and P. Luches, *Highly Efficient Plasmon-Mediated Electron Injection into Cerium Oxide from Embedded Silver Nanoparticles*, Nanoscale **11**, 10282 (2019).
- [96] K. Wu, J. Chen, J. R. McBride, and T. Lian, *Efficient Hot-Electron Transfer by a Plasmon-Induced Interfacial Charge-Transfer Transition*, Science **349**, 632 (2015).
- [97] S. K. Cushing, J. Li, F. Meng, T. R. Senty, S. Suri, M. Zhi, M. Li, A. D. Bristow, and N. Wu, *Photocatalytic Activity Enhanced by Plasmonic Resonant Energy Transfer from Metal to Semiconductor*, J. Am. Chem. Soc. **134**, 15033 (2012).
- [98] Y. Zhang, S. He, W. Guo, Y. Hu, J. Huang, J. R. Mulcahy, and W. D. Wei, *Surface-Plasmon-Driven Hot Electron Photochemistry*, Chem. Rev. **118**, 2927 (2018).
- [99] L. Jauffred, A. Samadi, H. Klingberg, P. M. Bendix, and L. B. Oddershede, *Plasmonic Heating of Nanostructures*, Chem. Rev. **119**, 8087 (2019).
- [100] L. Zhang, J. Xing, X. Wen, J. Chai, S. Wang, and Q. Xiong, *Plasmonic Heating from Indium Nanoparticles on a Floating Microporous Membrane for Enhanced Solar Seawater Desalination*, Nanoscale **9**, 12843 (2017).
- [101] T. Liu and Y. Li, *Photocatalysis: Plasmonic Solar Desalination*, Nat. Photonics **10**, 361 (2016).
- [102] M. U. Farid, J. A. Kharraz, P. Wang, and A. K. An, *High-Efficiency Solar-Driven Water Desalination Using a Thermally Isolated Plasmonic Membrane*, J. Clean. Prod. **271**, 122684 (2020).
- [103] S. Luo, X. Ren, H. Lin, H. Song, and J. Ye, *Plasmonic Photothermal Catalysis for Solar-to-Fuel Conversion: Current Status and Prospects*, Chem. Sci. **12**, 5701 (2021).
- [104] C. E. Verostko and R. K. Forsythe, *A Study of the Sabatier-Methanation Reaction*, SAE Technical Paper 740933 (1974).
- [105] J. Gao, Q. Liu, F. Gu, B. Liu, Z. Zhong, and F. Su, *Recent Advances in Methanation Catalysts for the Production of Synthetic Natural Gas*, RSC Advances **5**, 22759 (2015).
- [106] S. Tada, T. Shimizu, H. Kameyama, T. Haneda, and R. Kikuchi, *Ni/CeO<sub>2</sub> Catalysts with High CO<sub>2</sub> Methanation Activity and High CH<sub>4</sub> Selectivity at Low Temperatures*, Int. J. Hydrogen Energy **37**, 5527 (2012).
- [107] G. B. Haxel, J. B. Hedrick, and G. J. Orris, *Rare Earth Elements — Critical Resources for High Technology*, USGS Fact Sheet **087-02**, 1 (2002).
- [108] M. A. A. Aziz, A. A. Jalil, S. Triwahyono, and A. Ahmad, *CO<sub>2</sub> Methanation over Heterogeneous*

- Catalysts: Recent Progress and Future Prospects*, Green Chemistry **17**, 2647 (2015).
- [109] R. Razzaq, H. Zhu, L. Jiang, U. Muhammad, C. Li, and S. Zhang, *Catalytic Methanation of CO and CO<sub>2</sub> in Coke Oven Gas over Ni-Co/ZrO<sub>2</sub>-CeO<sub>2</sub>*, Ind. Eng. Chem. Res. **52**, 2247 (2013).
- [110] R. C. Maher, G. Kerherve, D. J. Payne, X. Yue, P. A. Connor, and J. Irvine, *The Reduction Properties of M-Doped (M = Zr, Gd) CeO<sub>2</sub>/YSZ Scaffolds Co-Infiltrated with Nickel*, Energy Technol. **6**, 2045 (2018).
- [111] Y. Yu, Y. M. Chan, Z. Bian, F. Song, J. Wang, Q. Zhong, and S. Kawi, *Enhanced Performance and Selectivity of CO<sub>2</sub> Methanation over g-C<sub>3</sub>N<sub>4</sub> Assisted Synthesis of Ni-CeO<sub>2</sub> Catalyst: Kinetics and DRIFTS Studies*, Int. J. Hydrogen Energy **43**, 15191 (2018).
- [112] B. Miao, S. S. K. Ma, X. Wang, H. Su, and S. H. Chan, *Catalysis Mechanisms of CO<sub>2</sub> and CO Methanation*, Catal. Sci. Technol. **6**, 4048 (2016).
- [113] A. Cárdenas-Arenas, A. Quindimil, A. Davó-Quiñonero, E. Bailón-García, D. Lozano-Castelló, U. De-La-Torre, B. Pereda-Ayo, J. A. González-Marcos, J. R. González-Velasco, and A. Bueno-López, *Isotopic and in Situ DRIFTS Study of the CO<sub>2</sub> Methanation Mechanism Using Ni/CeO<sub>2</sub> and Ni/Al<sub>2</sub>O<sub>3</sub> Catalysts*, Appl. Catal. B Environ. **265**, 118538 (2020).
- [114] S. Abelló, C. Berruero, and D. Montané, *High-Loaded Nickel-Alumina Catalyst for Direct CO<sub>2</sub> Hydrogenation into Synthetic Natural Gas (SNG)*, Fuel **113**, 598 (2013).
- [115] C. H. Bartholomew, *Carbon Deposition in Steam Reforming and Methanation*, Catal. Rev. Sci. Eng. **24**, 67 (1982).
- [116] S. Ewald, M. Kolbeck, T. Kratky, M. Wolf, and O. Hinrichsen, *On the Deactivation of Ni-Al Catalysts in CO<sub>2</sub> Methanation*, Appl. Catal. A Gen. **570**, 376 (2019).
- [117] A. I. Tsiotsias, N. D. Charisiou, I. V. Yentekakis, and M. A. Goula, *Bimetallic Ni-Based Catalysts for CO<sub>2</sub> Methanation: A Review*, Nanomaterials **11**, 1 (2021).
- [118] T. Inui, T. Hagiwara, and Y. Takegami, *Prevention of Catalyst Deactivation Caused by Coke Formation in the Methanation of Carbon Oxides*, Fuel **61**, 537 (1982).
- [119] P. Panagiotopoulou, D. I. Kondarides, and X. E. Verykios, *Mechanistic Aspects of the Selective Methanation of CO over Ru/TiO<sub>2</sub> Catalyst*, Catal. Today **181**, 138 (2012).
- [120] Y. Yu, Z. Bian, Z. Wang, J. Wang, W. Tan, Q. Zhong, and S. Kawi, *CO<sub>2</sub> Methanation on Ni-Ce<sub>0.8</sub>Mo<sub>0.2</sub>O<sub>2</sub> (M=Zr, Sn or Ti) Catalyst: Suppression of CO via Formation of Bridging Carbonyls on Nickel*, Catal. Today **2**, (2020).
- [121] H. Muroyama, Y. Tsuda, T. Asakoshi, H. Masitah, T. Okanishi, T. Matsui, and K. Eguchi, *Carbon Dioxide Methanation over Ni Catalysts Supported on Various Metal Oxides*, J. Catal. **343**, 178 (2016).
- [122] S. Eckle, H. G. Anfang, and R. J. Behm, *Reaction Intermediates and Side Products in the Methanation of CO and CO<sub>2</sub> over Supported Ru Catalysts in H<sub>2</sub>-Rich Reformate Gases*, J. Phys. Chem. C **115**, 1361 (2011).
- [123] S. ichiro Fujita, M. Nakamura, T. Doi, and N. Takezawa, *Mechanisms of Methanation of Carbon Dioxide and Carbon Monoxide over Nickel/Alumina Catalysts*, Appl. Catal. A, Gen. **104**, 87 (1993).
- [124] D. C. Upham, A. R. Derk, S. Sharma, H. Metiu, and E. W. McFarland, *CO<sub>2</sub> Methanation by Ru-Doped Ceria: The Role of the Oxidation State of the Surface*, Catal. Sci. Technol. **5**, 1783 (2015).

- [125] C. Schild, A. Wokaun, R. A. Koepfel, and A. Baiker, *CO<sub>2</sub> Hydrogenation over Nickel/Zirconia Catalysts from Amorphous Precursors: On the Mechanism of Methane Formation*, *J. Phys. Chem.* **95**, 6341 (1991).
- [126] P. A. U. Aldana, F. Ocampo, K. Kobl, B. Louis, F. Thibault-Starzyk, M. Daturi, P. Bazin, S. Thomas, and A. C. Roger, *Catalytic CO<sub>2</sub> Valorization into CH<sub>4</sub> on Ni-Based Ceria-Zirconia. Reaction Mechanism by Operando IR Spectroscopy*, *Catal. Today* **215**, 201 (2013).
- [127] A. Lasia, *Hydrogen Evolution Reaction*, in *Handbook of Fuel Cells – Fundamentals, Technology and Applications*, edited by W. Vielstich, A. Lamm, and H. A. Gasteiger (John Wiley & Sons, Ltd, Chichester, 2003), pp. 416–440.
- [128] S. Trasatti, *Work Function, Electronegativity, and Electrochemical Behaviour of Metals. III. Electrolytic Hydrogen Evolution in Acid Solutions*, *J. Electroanal. Chem.* **39**, 163 (1972).
- [129] W. Sheng, H. A. Gasteiger, and Y. Shao-Horn, *Hydrogen Oxidation and Evolution Reaction Kinetics on Platinum: Acid vs Alkaline Electrolytes*, *J. Electrochem. Soc.* **157**, B1529 (2010).
- [130] K. Zeng and D. Zhang, *Recent Progress in Alkaline Water Electrolysis for Hydrogen Production and Applications*, *Prog. Energy Combust. Sci.* **36**, 307 (2010).
- [131] F. Bao, E. Kemppainen, I. Dorbandt, R. Bors, F. Xi, R. Schlattmann, R. van de Krol, and S. Calnan, *Understanding the Hydrogen Evolution Reaction Kinetics of Electrodeposited Nickel-Molybdenum in Acidic, Near-Neutral, and Alkaline Conditions*, *ChemElectroChem* **8**, 195 (2021).
- [132] C. González-Buch, I. Herraiz-Cardona, E. Ortega, J. García-Antón, and V. Pérez-Herranz, *Study of the Catalytic Activity of 3D Macroporous Ni and NiMo Cathodes for Hydrogen Production by Alkaline Water Electrolysis*, *J. Appl. Electrochem.* **46**, 791 (2016).
- [133] E. Navarro-Flores, Z. Chong, and S. Omanovic, *Characterization of Ni, NiMo, NiW and NiFe Electroactive Coatings as Electrocatalysts for Hydrogen Evolution in an Acidic Medium*, *J. Mol. Catal. A Chem.* **226**, 179 (2005).
- [134] R. Solmaz and G. Kardaş, *Electrochemical Deposition and Characterization of NiFe Coatings as Electrocatalytic Materials for Alkaline Water Electrolysis*, *Electrochim. Acta* **54**, 3726 (2009).
- [135] H. Song, S. Oh, H. Yoon, K. H. Kim, S. Ryu, and J. Oh, *Bifunctional NiFe Inverse Opal Electrocatalysts with Heterojunction Si Solar Cells for 9.54%-Efficient Unassisted Solar Water Splitting*, *Nano Energy* **42**, 1 (2017).
- [136] A. Alobaid, C. Wang, and R. A. Adomaitis, *Mechanism and Kinetics of HER and OER on NiFe LDH Films in an Alkaline Electrolyte*, *J. Electrochem. Soc.* **165**, J3395 (2018).
- [137] J. Dong, T. Sun, Y. Zhang, H. Zhang, S. Lu, D. Hu, J. Chen, and L. Xu, *Mesoporous NiCo Alloy/Reduced Graphene Oxide Nanocomposites as Efficient Hydrogen Evolution Catalysts*, *J. Colloid Interface Sci.* **599**, 603 (2021).
- [138] W. Sheng, A. P. Bivens, M. Myint, Z. Zhuang, R. V. Forest, Q. Fang, J. G. Chen, and Y. Yan, *Non-Precious Metal Electrocatalyst with High Activity for Hydrogen Oxidation Reaction in Alkaline Electrolytes*, *Energy Environ. Sci.* **00**, 1 (2013).
- [139] J. Yao, D. Xu, X. Ma, J. Xiao, M. Zhang, and H. Gao, *Trimetallic CoNiFe-Layered Double Hydroxides: Electronic Coupling Effect and Oxygen Vacancy for Boosting Water Splitting*, *J. Power Sources* **524**, 231068 (2022).
- [140] F. Qin, Z. Zhao, M. K. Alam, Y. Ni, F. Robles-Hernandez, L. Yu, S. Chen, Z. Ren, Z. Wang, and J.

- Bao, *Trimetallic NiFeMo for Overall Electrochemical Water Splitting with a Low Cell Voltage*, ACS Energy Lett. **3**, 546 (2018).
- [141] J. Zhang, T. Wang, P. Liu, Z. Liao, S. Liu, X. Zhuang, M. Chen, E. Zschech, and X. Feng, *Efficient Hydrogen Production on MoNi<sub>4</sub> Electrocatalysts with Fast Water Dissociation Kinetics*, Nat. Commun. **8**, 1 (2017).
- [142] M. He, F. Kong, G. Yin, Z. Lv, X. Sun, H. Shi, and B. Gao, *Enhanced Hydrogen Evolution Reaction Activity of Hydrogen-Annealed Vertical MoS<sub>2</sub> Nanosheets*, RSC Adv. **8**, 14369 (2018).
- [143] J. R. Kitchin, J. K. Nørskov, M. A. Barteau, and J. G. Chen, *Trends in the Chemical Properties of Early Transition Metal Carbide Surfaces: A Density Functional Study*, Catal. Today **105**, 66 (2005).
- [144] H. Vrubel and X. Hu, *Molybdenum Boride and Carbide Catalyze Hydrogen Evolution in Both Acidic and Basic Solutions*, Angew. Chemie - Int. Ed. **51**, 12703 (2012).
- [145] E. J. Popczun, J. R. McKone, C. G. Read, A. J. Biacchi, A. M. Wiltrot, N. S. Lewis, and R. E. Schaak, *Nanostructured Nickel Phosphide as an Electrocatalyst for the Hydrogen Evolution Reaction*, J. Am. Chem. Soc. **135**, 9267 (2013).
- [146] R. Zhang, X. Wang, S. Yu, T. Wen, X. Zhu, F. Yang, X. Sun, X. Wang, and W. Hu, *Ternary NiCo<sub>2</sub>P<sub>x</sub> Nanowires as PH-Universal Electrocatalysts for Highly Efficient Hydrogen Evolution Reaction*, Adv. Mater. **29**, (2017).
- [147] C. G. Read, J. F. Callejas, C. F. Holder, and R. E. Schaak, *General Strategy for the Synthesis of Transition Metal Phosphide Films for Electrocatalytic Hydrogen and Oxygen Evolution*, ACS Appl. Mater. Interfaces **8**, 12798 (2016).
- [148] Q. Huang, Z. Ye, and X. Xiao, *Recent Progress in Photocathodes for Hydrogen Evolution*, J. Mater. Chem. A **3**, 15824 (2015).
- [149] R. Wick and S. D. Tilley, *Photovoltaic and Photoelectrochemical Solar Energy Conversion with Cu<sub>2</sub>O*, J. Phys. Chem. C **119**, 26243 (2015).
- [150] M. Malizia, B. Seger, I. Chorkendorff, and P. C. K. Vesborg, *Formation of a p-n Heterojunction on GaP Photocathodes for H<sub>2</sub> Production Providing an Open-Circuit Voltage of 710 mV*, J. Mater. Chem. A **2**, 6847 (2014).
- [151] W. Yu, J. L. Young, T. G. Deutsch, and N. S. Lewis, *Understanding the Stability of Etched or Platinized P-GaInP Photocathodes for Solar-Driven H<sub>2</sub> Evolution*, ACS Appl. Mater. Interfaces **13**, 57350 (2021).
- [152] B. Mahmoudi, F. Caddeo, T. Lindenberg, T. Schneider, T. Hölscher, R. Scheer, and A. W. Maijenburg, *Photoelectrochemical Properties of Cu-Ga-Se Photocathodes with Compositions Ranging from CuGaSe<sub>2</sub> to CuGa<sub>3</sub>Se<sub>5</sub>*, Electrochim. Acta **367**, (2021).
- [153] M. G. Mali, H. Yoon, B. N. Joshi, H. Park, S. S. Al-Deyab, D. C. Lim, S. J. Ahn, C. Nervi, and S. S. Yoon, *Enhanced Photoelectrochemical Solar Water Splitting Using a Platinum-Decorated CIGS/CdS/ZnO Photocathode*, ACS Appl. Mater. Interfaces **7**, 21619 (2015).
- [154] S. Ida, K. Yamada, T. Matsunaga, H. Hagiwara, Y. Matsumoto, and T. Ishihara, *Preparation of P-Type CaFe<sub>2</sub>O<sub>4</sub> Photocathodes for Producing Hydrogen from Water*, J. Am. Chem. Soc. **132**, 17343 (2010).
- [155] W. Yang, J. H. Kim, O. S. Hutter, L. J. Phillips, J. Tan, J. Park, H. Lee, J. D. Major, J. S. Lee, and J. Moon, *Benchmark Performance of Low-Cost Sb<sub>2</sub>Se<sub>3</sub> Photocathodes for Unassisted Solar*

- Overall Water Splitting*, Nat. Commun. **11**, (2020).
- [156] B. Wang, S. Shen, and L. Guo, *SrTiO<sub>3</sub> Single Crystals with High-Indexed {023} Facets and {001} Facets for Photocatalytic Hydrogen and Oxygen Evolution*, Appl. Catal. B, Environ. **166–167**, 320 (2015).
- [157] R. Li, H. Han, F. Zhang, D. Wang, and C. Li, *Highly Efficient Photocatalysts Constructed by Rational Assembly of Dual-Cocatalysts Separately on Different Facets of BiVO<sub>4</sub>*, Energy Environ. Sci. **7**, 1369 (2014).
- [158] F. A. Frame, T. K. Townsend, R. L. Chamousis, E. M. Sabio, T. Dittrich, N. D. Browning, and F. E. Osterloh, *Photocatalytic Water Oxidation with Nonsensitized IrO<sub>2</sub> Nanocrystals under Visible and UV Light*, J. Am. Chem. Soc. **133**, 7264 (2011).
- [159] X. Xu, C. Randorn, P. Efstathiou, and J. T. S. Irvine, *A Red Metallic Oxide Photocatalyst*, Nat. Mater. **11**, 9 (2012).
- [160] L. Mascaretti and A. Naldoni, *Hot Electron and Thermal Effects in Plasmonic Photocatalysis*, J. Appl. Phys. (2020).
- [161] M. M. Abouelela, G. Kawamura, and A. Matsuda, *A Review on Plasmonic Nanoparticle-Semiconductor Photocatalysts for Water Splitting*, J. Clean. Prod. **294**, 126200 (2021).
- [162] N. Wu, *Plasmonic Metal-Semiconductor Photocatalysts and Photoelectrochemical Cells: A Review*, Nanoscale **10**, 2679 (2018).
- [163] J. Low, B. Cheng, and J. Yu, *Surface Modification and Enhanced Photocatalytic CO<sub>2</sub> Reduction Performance of TiO<sub>2</sub>: A Review*, Appl. Surf. Sci. **392**, 658 (2017).
- [164] G. E. Jonsson, V. Miljkovic, and A. Dmitriev, *Nanoplasmon-Enabled Macroscopic Thermal Management*, Sci. Rep. **4**, 5111 (2014).
- [165] J. Chen, Y. Zhou, R. Li, X. Wang, and G. Z. Chen, *Highly-Dispersed Nickel Nanoparticles Decorated Titanium Dioxide Nanotube Array for Enhanced Solar Light Absorption*, Appl. Surf. Sci. **464**, 716 (2019).
- [166] M. Younas, L. Loong Kong, M. J. K. Bashir, H. Nadeem, A. Shehzad, and S. Sethupathi, *Recent Advancements, Fundamental Challenges, and Opportunities in Catalytic Methanation of CO<sub>2</sub>*, Energy and Fuels **30**, 8815 (2016).
- [167] J. Wu, Y. Huang, W. Ye, and Y. Li, *CO<sub>2</sub> Reduction: From the Electrochemical to Photochemical Approach*, Adv. Sci. **4**, 1700194 (2017).
- [168] R. P. Ye, J. Ding, W. Gong, M. D. Argyle, Q. Zhong, Y. Wang, C. K. Russell, Z. Xu, A. G. Russell, Q. Li, M. Fan, and Y. G. Yao, *CO<sub>2</sub> Hydrogenation to High-Value Products via Heterogeneous Catalysis*, Nat. Commun. **10**, 5698 (2019).
- [169] K. Manthiram, B. J. Beberwyck, and A. P. Alivisatos, *Enhanced Electrochemical Methanation of Carbon Dioxide with a Dispersible Nanoscale Copper Catalyst*, J. Am. Chem. Soc. **136**, 13319 (2014).
- [170] X. Dai and Y. Sun, *Reduction of Carbon Dioxide on Photoexcited Nanoparticles of VIII Group Metals*, Nanoscale **11**, 16723 (2019).
- [171] U. Ulmer, T. Dingle, P. N. Duchesne, R. H. Morris, A. Tavasoli, T. Wood, and G. A. Ozin, *Fundamentals and Applications of Photocatalytic CO<sub>2</sub> Methanation*, Nat. Commun. **10**, 3169 (2019).

- [172] P. G. O'Brien, A. Sandhel, T. E. Wood, A. A. Jelle, L. B. Hoch, D. D. Perovic, C. A. Mims, and G. A. Ozin, *Photomethanation of Gaseous CO<sub>2</sub> over Ru/Silicon Nanowire Catalysts with Visible and near-Infrared Photons*, *Adv. Sci.* **1**, 1400001 (2014).
- [173] Ş. Neatu, J. A. Maciá-Agulló, P. Concepció, and H. Garcia, *Gold-Copper Nanoalloys Supported on TiO<sub>2</sub> as Photocatalysts for CO<sub>2</sub> Reduction by Water*, *J. Am. Chem. Soc.* **136**, 15969 (2014).
- [174] F. Sastre, A. V. Puga, L. Liu, A. Corma, and H. García, *Complete Photocatalytic Reduction of CO<sub>2</sub> to Methane by H<sub>2</sub> under Solar Light Irradiation*, *J. Am. Chem. Soc.* **136**, 6798 (2014).
- [175] P. Wang, B. Huang, Y. Dai, and M. H. Whangbo, *Plasmonic Photocatalysts: Harvesting Visible Light with Noble Metal Nanoparticles*, *Phys. Chem. Chem. Phys.* **14**, 9813 (2012).
- [176] G. Kumari, X. Zhang, D. Devasia, J. Heo, and P. K. Jain, *Watching Visible Light-Driven CO<sub>2</sub> Reduction on a Plasmonic Nanoparticle Catalyst*, *ACS Nano* **12**, 8330 (2018).
- [177] C. Wang, O. Ranasingha, S. Natesakhawat, P. R. Ohodnicki, M. Andio, J. P. Lewis, and C. Matranga, *Visible Light Plasmonic Heating of Au-ZnO for the Catalytic Reduction of CO<sub>2</sub>*, *Nanoscale* **5**, 6968 (2013).
- [178] W. Hou, W. H. Hung, P. Pavaskar, A. Goepfert, M. Aykol, and S. B. Cronin, *Photocatalytic Conversion of CO<sub>2</sub> to Hydrocarbon Fuels via Plasmon-Enhanced Absorption and Metallic Interband Transitions*, *ACS Catal.* **1**, 929 (2011).
- [179] J. Y. Do, N. Son, R. K. Chava, K. K. Mandari, S. Pandey, V. Kumaravel, T. S. Senthil, S. W. Joo, and M. Kang, *Plasmon-Induced Hot Electron Amplification and Effective Charge Separation by Au Nanoparticles Sandwiched between Copper Titanium Phosphate Nanosheets and Improved Carbon Dioxide Conversion to Methane*, *ACS Sustain. Chem. Eng.* **8**, 18646 (2020).
- [180] J. Ren, S. Ouyang, H. Xu, X. Meng, T. Wang, D. Wang, and J. Ye, *Targeting Activation of CO<sub>2</sub> and H<sub>2</sub> over Ru-Loaded Ultrathin Layered Double Hydroxides to Achieve Efficient Photothermal CO<sub>2</sub> Methanation in Flow-Type System*, *Adv. Energy Mater.* 1601657 (2017).
- [181] S. Jantarang, E. C. Lovell, T. H. Tan, J. Scott, and R. Amal, *Role of Support in Photothermal Carbon Dioxide Hydrogenation Catalysed by Ni/Ce<sub>x</sub>Ti<sub>y</sub>O<sub>2</sub>*, *Prog. Nat. Sci. Mater. Int.* **28**, 168 (2018).
- [182] X. Meng, T. Wang, L. Liu, S. Ouyang, P. Li, H. Hu, T. Kako, H. Iwai, A. Tanaka, and J. Ye, *Photothermal Conversion of CO<sub>2</sub> into CH<sub>4</sub> with H<sub>2</sub> over Group VIII Nanocatalysts: An Alternative Approach for Solar Fuel Production*, *Angew. Chemie* **53**, 11478 (2014).
- [183] H. Huang, M. Mao, Q. Zhang, Y. Li, J. Bai, Y. Yang, M. Zeng, and X. Zhao, *Solar-Light-Driven CO<sub>2</sub> Reduction by CH<sub>4</sub> on Silica-Cluster-Modified Ni Nanocrystals with a High Solar-to-Fuel Efficiency and Excellent Durability*, *Adv. Energy Mater.* **8**, (2018).
- [184] H. Liu, X. Meng, T. D. Dao, H. Zhang, P. Li, K. Chang, T. Wang, M. Li, T. Nagao, and J. Ye, *Conversion of Carbon Dioxide by Methane Reforming under Visible-Light Irradiation: Surface-Plasmon-Mediated Nonpolar Molecule Activation*, *Angew. Chemie* **54**, 11545 (2015).
- [185] H. Song, X. Meng, T. D. Dao, W. Zhou, H. Liu, L. Shi, H. Zhang, T. Nagao, T. Kako, and J. Ye, *Light-Enhanced Carbon Dioxide Activation and Conversion by Effective Plasmonic Coupling Effect of Pt and Au Nanoparticles*, *ACS Appl. Mater. Interfaces* **10**, (2018).
- [186] J. N. G. Stanley, I. García-García, T. Perfrement, E. C. Lovell, T. W. Schmidt, J. Scott, and R. Amal, *Plasmonic Effects on CO<sub>2</sub> Reduction over Bimetallic Ni-Au Catalysts*, *Chem. Eng. Sci.* **194**, 94 (2019).



- [187] X. Li, H. O. Everitt, and J. Liu, *Confirming Nonthermal Plasmonic Effects Enhance CO<sub>2</sub> Methanation on Rh/TiO<sub>2</sub> Catalysts*, *Nano Res.* **12**, 1906 (2019).
- [188] X. Zhang, X. Li, M. E. Reish, D. Zhang, N. Q. Su, Y. Gutiérrez, F. Moreno, W. Yang, H. O. Everitt, and J. Liu, *Plasmon-Enhanced Catalysis: Distinguishing Thermal and Nonthermal Effects*, *Nano Lett.* **18**, 1714 (2018).
- [189] D. Takami, Y. Ito, S. Kawaharasaki, A. Yamamoto, and H. Yoshida, *Low Temperature Dry Reforming of Methane over Plasmonic Ni Photocatalysts under Visible Light Irradiation*, *Sustain. Energy Fuels* **3**, 2968 (2019).
- [190] C. Kim, S. Hyeon, J. Lee, W. D. Kim, D. C. Lee, J. Kim, and H. Lee, *Energy-Efficient CO<sub>2</sub> Hydrogenation with Fast Response Using Photoexcitation of CO<sub>2</sub> Adsorbed on Metal Catalysts*, *Nat. Commun.* **9**, (2018).
- [191] H. Liu, T. D. Dao, L. Liu, X. Meng, T. Nagao, and J. Ye, *Light Assisted CO<sub>2</sub> Reduction with Methane over Group VIII Metals: Universality of Metal Localized Surface Plasmon Resonance in Reactant Activation*, *Appl. Catal. B Environ.* **209**, 183 (2017).
- [192] H. Liu, H. Song, X. Meng, L. Yang, and J. Ye, *Light Irradiation Enhanced CO<sub>2</sub> Reduction with Methane: A Case Study in Size-Dependent Optical Property of Ni Nanoparticles*, *Catal. Today* **335**, 187 (2019).
- [193] H. Liu, X. Meng, T. D. Dao, L. Liu, P. Li, G. Zhao, T. Nagao, L. Yang, and J. Ye, *Light Assisted CO<sub>2</sub> Reduction with Methane over SiO<sub>2</sub> Encapsulated Ni Nanocatalysts for Boosted Activity and Stability*, *J. Mater. Chem. A* **5**, 10567 (2017).
- [194] D. Mateo, N. Morlanes, P. Maity, G. Shterk, O. F. Mohammed, and J. Gascon, *Efficient Visible-Light Driven Photothermal Conversion of CO<sub>2</sub> to Methane by Nickel Nanoparticles Supported on Barium Titanate*, *Adv. Funct. Mater.* **31**, 1 (2021).
- [195] Z. Xin, L. Lu, B. Wang, X. Wang, K. Zhu, Z. Xu, Z. Yu, S. Yan, and Z. Zou, *Lewis Acid Activated CO<sub>2</sub> Reduction over a Ni Modified Ni-Ge Hydroxide Driven by Visible-Infrared Light*, *Dalt. Trans.* **48**, 1672 (2019).
- [196] X. Zhang, X. Li, D. Zhang, N. Q. Su, W. Yang, H. O. Everitt, and J. Liu, *Product Selectivity in Plasmonic Photocatalysis for Carbon Dioxide Hydrogenation*, *Nat. Commun.* **8**, 14542 (2017).
- [197] I. I. Nedrygailov, S. Y. Moon, and J. Y. Park, *Hot Electron-Driven Electrocatalytic Hydrogen Evolution Reaction on Metal–Semiconductor Nanodiode Electrodes*, *Sci. Rep.* **9**, 1 (2019).
- [198] X. Wu, J. Wang, Z. Wang, F. Sun, Y. Liu, K. Wu, X. Meng, and J. Qiu, *Boosting the Electrocatalysis of MXenes by Plasmon-Induced Thermalization and Hot-Electron Injection*, *Angew. Chemie* **133**, 9502 (2021).
- [199] M. Gao, P. K. N. Connor, and G. W. Ho, *Plasmonic Photothermic Directed Broadband Sunlight Harnessing for Seawater Catalysis and Desalination*, *Energy Environ. Sci.* **9**, 3151 (2016).
- [200] G. S. Pawar, A. Elikkottil, B. Pesala, A. A. Tahir, and T. K. Mallick, *Plasmonic Nickel Nanoparticles Decorated on to LaFeO<sub>3</sub> Photocathode for Enhanced Solar Hydrogen Generation*, *Int. J. Hydrogen Energy* **44**, 578 (2019).
- [201] R. Yalavarthi, L. Mascaretti, Z. A. Kudyshev, A. Dutta, S. Kalytchuk, R. Zbořil, P. Schmuki, V. M. Shalaev, Š. Kment, A. Boltasseva, and A. Naldoni, *Enhancing Photoelectrochemical Energy Storage by Large-Area CdS-Coated Nickel Nanoantenna Arrays*, *ACS Appl. Energy Mater.* **4**, 11367 (2021).

- [202] L. Ai, N. Li, M. Chen, H. Jiang, and J. Jiang, *Photothermally Boosted Water Splitting Electrocatalysis by Broadband Solar Harvesting Nickel Phosphide within a Quasi-MOF*, *J. Mater. Chem. A* **9**, 16479 (2021).
- [203] H. Yang, L. Q. He, Y. W. Hu, X. Lu, G. R. Li, B. Liu, B. Ren, Y. Tong, and P. P. Fang, *Quantitative Detection of Photothermal and Photoelectrocatalytic Effects Induced by SPR from Au@Pt Nanoparticles*, *Angew. Chemie - Int. Ed.* **54**, 11462 (2015).
- [204] Y. Yu, V. Sundaresan, and K. A. Willets, *Hot Carriers versus Thermal Effects: Resolving the Enhancement Mechanisms for Plasmon-Mediated Photoelectrochemical Reactions*, *J. Phys. Chem. C* **122**, 5040 (2018).
- [205] L. Zhou, D. F. Swearer, H. Robotjazi, A. Alabastri, P. Christopher, E. A. Carter, P. Nordlander, and N. J. Halas, *Quantifying Hot Carrier and Thermal Contributions in Plasmonic Photocatalysis*, *Science* **364**, 69 (2019).
- [206] G. Baffou, I. Bordacchini, A. Baldi, and R. Quidant, *Simple Experimental Procedures to Distinguish Photothermal from Hot-Carrier Processes in Plasmonics*, *Light Sci. Appl.* **9**, 108 (2020).
- [207] C. Zhan, B. W. Liu, Y. F. Huang, S. Hu, B. Ren, M. Moskovits, and Z. Q. Tian, *Disentangling Charge Carrier from Photothermal Effects in Plasmonic Metal Nanostructures*, *Nat. Commun.* **10**, 2671 (2019).
- [208] E. R. Corson, E. B. Creel, R. Kostecki, B. D. McCloskey, and J. J. Urban, *Important Considerations in Plasmon-Enhanced Electrochemical Conversion at Voltage-Biased Electrodes*, *IScience* **23**, 100911 (2020).
- [209] F. Quan, G. Zhan, C. Mao, Z. Ai, F. Jia, L. Zhang, H. Gu, and S. Liu, *Efficient Light-Driven CO<sub>2</sub> Hydrogenation on Ru/CeO<sub>2</sub> Catalysts*, *Catal. Sci. Technol.* **8**, 6503 (2018).



## Chapter 2

# Plasmonic Ni/CeO<sub>2</sub>-based catalyst for light-assisted thermal methanation of CO<sub>2</sub>

The results presented in chapter 2 are mainly published in Applied Catalysis B: Environmental as “*Effects of solar irradiation on thermally driven CO<sub>2</sub> methanation using Ni/CeO<sub>2</sub>-based catalyst*” by V. Golovanova, M. C. Spadaro, J. Arbiol, V. Golovanov, T. T. Rantala, T. Andreu, and J. R. Morante (Appl. Catal. B Environ. **291**, 120038 (2021)).

HRTEM/EELS data were obtained in collaboration with EMAT research group of Prof. Sara Bals from University of Antwerp and Advanced Electron Nanoscopy group of Prof. Jordi Arbiol from ICN2.

## 2.1. Introduction

This chapter is focused on the fundamental study of plasmonic Ni/CeO<sub>2</sub> catalyst for thermally-driven CO<sub>2</sub> methanation under light-assisted conditions.

As it has been stated in chapter 1, few works have emphasized the importance of the catalytic performance enhancement of the Ni-based catalysts due to plasmon-induced self-heating of nickel nanoparticles followed by a dissipation of heat to the oxide matrix. Due to the excellent photothermal properties of Ni nanoparticles [1–4], this effect in many cases can be considered as the main consequence of the plasmon excitation in Ni-based catalysts as compared with direct hot electrons interface transfer.

Enlarging of the specific surface area of heterogeneous catalysts is one of the key components on the way to increase their activity for gas-phase reactions. The surface area of the catalyst active phase can be increased by introducing a high-surface-area support, or by modifying the geometry of the promoter/active phase at the nanoscale level. One of the approaches of nanostructuring inorganic materials is by increasing their porosity, with a pore size large enough to allow gas diffusion. Various metal oxide materials were synthesized using surfactants through self-assembly into liquid crystals [5,6]. However, they presented low thermal stability and higher variability. Another way is known as hard template method, and lies in introducing the metal salt precursors into the mesoporous host structure, their mineralization and subsequent removal of the sacrificial template in order to obtain a high-surface-area mesostructure [7–9]. This method is more controllable, predictable and topologically stable than the soft template approach, making it an attractive route to create an efficient nanostructured catalyst. Out of numerous sacrificial templates, SBA-15 mesoporous silica is one of the most frequently used templates for synthesis of the replica catalyst material [10–13]. It is a highly porous, mechanically stable material with exceptionally controllable pore size. Its preparation procedure is described below.

The optimal relative amount of the active phase lies between two extremes. A low value of the nickel material in the catalyst leads to few active sites needed for hydrogen dissociation, which is a crucial step in the CO<sub>2</sub> methanation reaction. On the other hand, high loading of nickel results in large Ni particles, surface-to-volume ratio of which is drastically decreasing with increasing of their size. This leads to the reduction of nickel active sites exposed to the gas phase, thus decreasing the catalytic activity. The optimal nickel loading, corresponding to the highest catalytic activity, was optimized previously in the group and was equal to 15 wt.% of the whole catalyst weight.

In section 2.2, a hard template synthesis method to obtain high-surface-area plasmonic Ni/CeO<sub>2</sub> catalyst for CO<sub>2</sub> methanation is described. In addition, this section focuses on the design of the reactor to perform the photothermal catalytic reaction as well as methods for numerical evaluation of the catalyst efficiency. Lastly, all the characterization techniques used in this chapter are listed briefly describing their operating conditions.

Physicochemical and functional characterization of the designed catalyst is provided in the section 2.3. The catalyst was studied by a number of different techniques, revealing its surface area, morphology and crystal structure. Particular attention was paid to the optical and photothermal properties of the prepared plasmonic catalyst. The sample was tested in various operating conditions to evaluate its catalytic activity in dark and light-assisted setups. The reaction mechanism was investigated by in-situ diffuse reflectance infrared spectroscopy, determining the intermediate species in the CO<sub>2</sub> methanation reaction process over the Ni/CeO<sub>2</sub> catalyst with and without external illumination.

In section 2.4, on the basis of in-situ characterization results, the mechanism of light-assisted methanation reaction over Ni/CeO<sub>2</sub> catalyst is proposed. The effect of solar illumination on the Ni/CeO<sub>2</sub> catalyst was studied with respect to both metallic and semiconductor phases. The optimal conditions for the plasmon-assisted methanation reaction were found, and the reduction of the power needed for the reaction due to solar illumination was evaluated (section 2.5). Finally, the conclusions of chapter 2 were withdrawn in section 2.6.

## 2.2. Experimental methodology

### 2.2.1. Catalyst preparation

#### 2.2.1.1. Preparation of the SBA-15 template

SBA-15 mesoporous silica templates were synthesized by the following process, based on the one described in a previous work [14] and illustrated in Figure 2.1: 9 g of Pluronic® P123 (polyethylene glycol-block-polypropylene glycol-block-polyethylene glycol, average  $M_n \sim 5,800$ , Sigma-Aldrich) was mixed with 90 g of diluted HCl (50 wt.%) and 245 g of Milli-Q water and stirred at 38°C until full dissolution to obtain polymeric micelles of cylindrical shape (steps 1 and 2), which were self-organized into liquid crystals with hexagonal symmetry (step 3). 18.7 g of TEOS (tetraethyl orthosilicate, 98%, Sigma-Aldrich) was added as a silica precursor (step 4). The reaction was held for another 24 hours at 100°C, after which the mixture was filtered, washed with Milli-Q water, dried at 60°C for 10 hours and eventually calcined at 550°C for 5 hours (step 5).

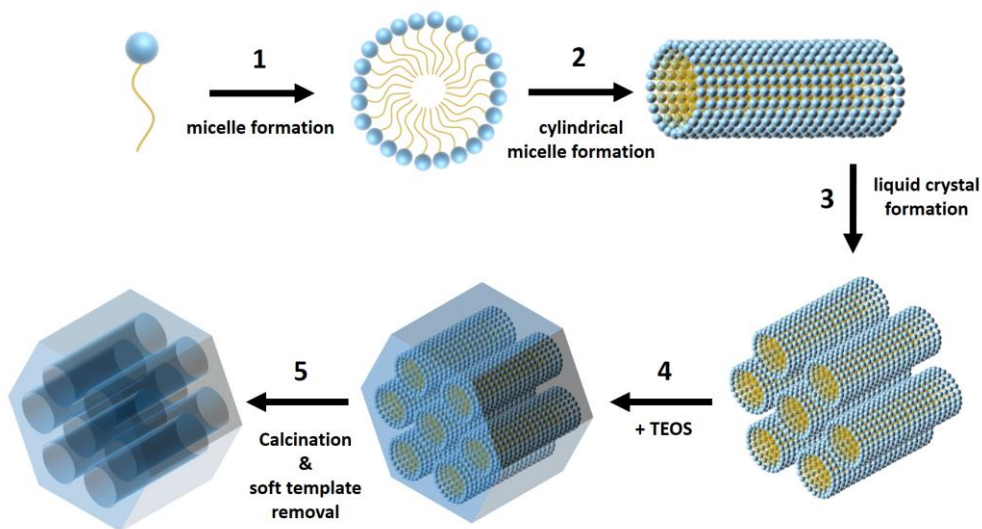


**Figure 2.1.** Scheme of the SBA-15 template synthesis.

### 2.2.1.2. Synthesis of the Ni/CeO<sub>2</sub> catalyst

The Ni/CeO<sub>2</sub> catalyst was prepared by simultaneous impregnation of SBA-15 templates (1.05 g) with 6.5 ml of 0.6 M cerium (III) nitrate hexahydrate (Sigma-Aldrich) and 3 ml of 0.6 M nickel (II) nitrate hexahydrate (Sigma-Aldrich). The Ni/Ce ratio was chosen in such a way that the estimated Ni weight concentration in the final product would be 15%. The reaction was held in two steps, to achieve a high degree of impregnation [14,15]: first with impregnation of the solutions to the mesoporous silica and annealing at 350°C for the preliminary precursor decomposition and a second impregnation with half of the initial amounts, followed by annealing of the sample at 800°C. The silica template was further dissolved in 2 M NaOH for 12 hours at 70°C with constant stirring. The obtained NiO/CeO<sub>2</sub> powder was further reduced in hydrogen atmosphere (5% H<sub>2</sub> and 95% Ar) for 7 hours at 450°C to get the Ni/CeO<sub>2</sub> catalyst. The scheme of the process is depicted on the figure 2.2.

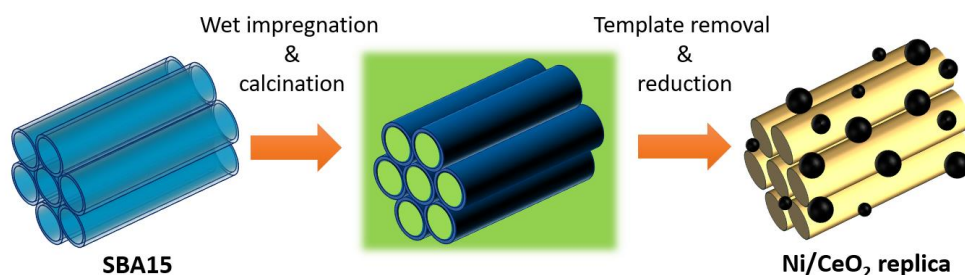


Figure 2.2. Ni/CeO<sub>2</sub> catalyst fabrication process.

For comparison, samples without Ni were also prepared using the same template impregnation technique. 6.5 ml of 0.6 M cerium nitrate hexahydrate was added to 0.9 g of SBA-15, and the same two-step procedure was applied for calcination and second impregnation of silica template.

## 2.2.2. Reactor setup

### 2.2.2.1. Planar reactor for photothermocatalytical characterization

A custom-made flow-type gas reactor (Figure 2.3) was created in order to allow simultaneous heating and illumination of the catalyst. The reactor was equipped with a ceramic heater (HT19R, Thorlabs), connected to a controllable power supply.

The catalyst was spread uniformly over an aluminum support, placed on top of the heater. The temperature of the catalyst was constantly measured by a K-type thermocouple, introduced into the reactor alongside with the heater. An intimate contact was preserved throughout the reaction in order to measure directly the changes in the catalyst temperature.

The reactor was also equipped with a quartz window, transparent for solar illumination. As a source of illumination, we used a 300 W solar simulator (Xe lamp, AM1.5G filter) with a variable illumination power. The power density was measured by a laser powermeter (Gentec-EO UNO) containing a calibrated reference silicon cell. Bandpass filters (FGL400S, FGS900S, ThorLabs) were introduced to the system between the illumination source and the reactor to cut a part of the spectrum as shown in Figure 2.3. Transmission spectra of the quartz window and filters used in this setup can be found in Appendix 2.2.

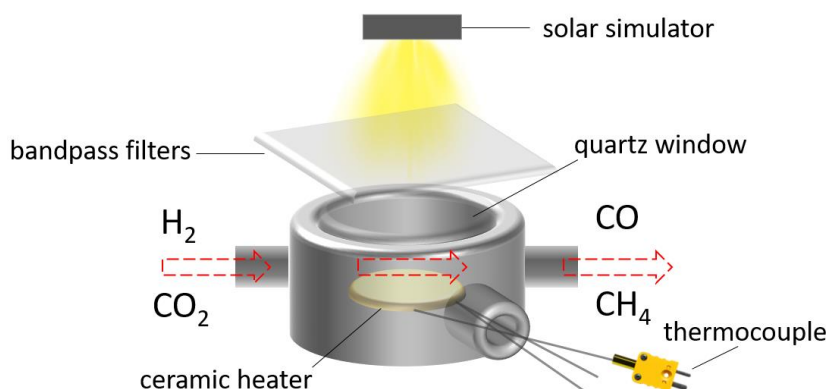


**Figure 2.3.** Scheme of the planar reactor for photothermocatalytic characterization.

For every reaction, 50 mg of the catalyst was preliminarily reduced in hydrogen atmosphere (5% H<sub>2</sub> and 95% Ar) for 7 hours at 450°C under a flow of 150 ml/min and spread over the aluminum support in the reactor. The methanation reaction was held under a constant flow of 80% H<sub>2</sub> and 20% CO<sub>2</sub> gas mixture (99.999%, Linde) at a rate of 20 ml min<sup>-1</sup>. The outlet gas flow passed through a cold liquid-gas separator (5°C) for water condensation, and was measured by a mass flow meter (MF, Bronkhorst). The gas products (CH<sub>4</sub>, CO, CO<sub>2</sub> and H<sub>2</sub>) were analyzed using a 490 microGC gas chromatograph (Agilent Technologies).



### 2.2.2.2. Tubular reactor for high-flow measurements

Functional characterization and stability measurements were performed in the tubular-type fixed-bed flow reactor, which consisted of two coaxial quartz tubes (Figure 2.4). The catalyst was placed between the tubes on a quartz wool bed, and the gas mixture was allowed to flow through the catalyst. The catalyst was preliminary reduced under the same conditions described above. Some tests were also made with the catalyst which was reduced in-situ under 150 ml min<sup>-1</sup> flow of 5% H<sub>2</sub>/95% Ar gas at 450°C. This reactor allowed us to study the CO<sub>2</sub> conversion at higher gas flows and higher loadings of the catalyst. These conditions, along with the particular configuration of the reactor (specifically flowing of the gas through the catalyst) helped us to avoid water condensation issues, discussed in section 2.4.

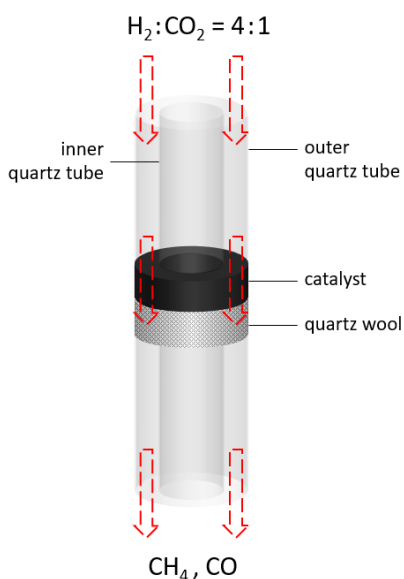


**Figure 2.4.** Scheme of the tubular reactor used in this work.

### 2.2.3. Evaluation of catalytic properties

The methane yield ( $Y_{CH_4}$ ) was calculated according to the equation:

$$Y_{CH_4}(\%) = \frac{X_{CO_2}(\%) \times S_{CH_4}(\%)}{100\%} \quad (2.1)$$

Where  $X_{CO_2}$  is the conversion of CO<sub>2</sub> and  $S_{CH_4}$  is the selectivity to methane:

$$X_{CO_2}(\%) = \frac{\Phi_{CO_2,in} - \Phi_{CO_2,out}}{\Phi_{CO_2,in}} \quad (2.2)$$

$$S_{CH_4}(\%) = \frac{\Phi_{CH_4,out}}{\Phi_{CO_2,in} - \Phi_{CO_2,out}} \quad (2.3)$$

$\Phi_{CO_2,in}$ ,  $\Phi_{CO_2,out}$  are the CO<sub>2</sub> molar flows in the inlet and in the outlet, respectively, and  $\Phi_{CH_4,out}$  is the CH<sub>4</sub> molar flow in the outlet. The catalytic activity was then evaluated from the following equation:

$$k = \frac{\Phi}{m} \times \frac{Y_{CH_4}(\%)}{100\%} \quad (2.4)$$

The reported data were the average values, taken from five measurements for each temperature point, with the measurement error less than 3%. Carbon mass balance was closed within the accuracy of  $\pm 7\%$ .

Provided that methanation is an exothermic reaction, the temperature was allowed to reach a stable value in all of the studied conditions before any illumination was introduced.

## 2.2.4. Characterization techniques

A number of techniques were used to characterize the prepared catalyst and evaluate its physical, chemical and optical properties. The techniques used in this section are listed and described below.

- **XRD spectra** were recorded on a Bruker type XRD D8 diffraction-meter (CuK $\alpha$  radiation,  $\lambda = 1.5418 \text{ \AA}$ , 40kV, 40mA) with a scanning range of  $2\theta$  from  $20^\circ$  to  $80^\circ$  and step size of  $0.05^\circ 3s^{-1}$ . The average crystalline sizes of metallic nanoparticles were derived from the Scherrer's equation  $D = \frac{K\lambda}{\beta \cos \theta}$ , where  $\theta$  is the Bragg angle,  $K$  is the shape factor,  $\lambda$  is the X-ray wavelength and  $\beta$  is the full width of the diffraction peak at half maximum (FWHM).
- **Scanning electron microscope (SEM)**, Zeiss Auriga 60) was used to study the morphology of the samples. The composition of the synthesized catalyst

was studied by energy dispersive X-ray spectroscopy (EDX, Oxford Inca Energy).

- **N<sub>2</sub>-physisorption analysis** was conducted in TriStar II 3020-Micrometrics equipment at liquid nitrogen temperature. Before the measurements, the samples were degassed under vacuum conditions at 90°C for 1 h and then at 250°C for 3 h. Brunauer-Emmett-Teller (BET) method was applied for calculation of the BET surface area for a relative pressure ( $P/P_0$ ) range of 0.1-0.3. The total pore volume and the average pore size were determined by applying Barrett-Joyner-Halenda (BJH) method to desorption branch of the isotherms at the value  $P/P_0 = 0.95$ .
- **H<sub>2</sub>-TPR** (hydrogen temperature programmed reduction) and **CO-chemisorption** were carried out using an automated chemisorption analyzer (Autochem HP-Micrometrics). In case of H<sub>2</sub>-TPR measurements 100 mg of powder sample was kept under constant 5% H<sub>2</sub>/Ar flow, while the temperature was increased from 25°C to 800°C with a heating ramp of 10°C min<sup>-1</sup>. The consumed H<sub>2</sub> was measured using a thermal conductivity detector (TCD). The CO-chemisorption measurements were held at 35°C under the flow of 10% CO/He over the samples, which were pre-reduced at 450°C under 5% H<sub>2</sub>/Ar flow for 7 h. Pulses of CO were periodically introduced until full saturation of the system. Active metal surface area and metal dispersion were calculated assuming the stoichiometric ratio CO/Ni equal to 1, Ni atomic weight to 58.71, its atomic cross-sectional area to 0.0649 nm<sup>2</sup> and density to 8.9 g cm<sup>-3</sup>.
- **UV-visible light absorption spectra** were measured using the Perkin Elmer Lambda 35 UV-visible spectrometer in the diffuse reflectance mode. Absorption of the samples was calculated according to the equation:  $A = 1 - R$ , as no transmission was observed.
- **High-resolution transmission electron microscopy (HRTEM)** together with **scanning TEM (STEM)** investigation was performed on a field emission gun FEI Tecnai F20 microscope. **High angle annular dark-field (HAADF) STEM** was combined with **electron energy loss spectroscopy (EELS)** in the Tecnai microscope by using a GATAN QUANTUM filter. The configuration of in-situ HRTEM chamber allowed filling it with different ambient gases and simultaneous temperature control. The oxidation state of Ce was withdrawn from the EELS spectra and was defined by the ratio of M<sub>4</sub> and M<sub>5</sub> ionization peaks, as was demonstrated previously [1].  $M_5/M_4 < 1$  corresponds to fully oxidized Ce<sup>4+</sup> oxidation state, while  $M_5/M_4 < 1$  is attributed to reduced Ce<sup>3+</sup>.
- **In-situ diffuse reflectance infrared Fourier transform spectroscopy (DRIFTS)** was used in order to study the nature of intermediate species

formed during the methanation reaction over the Ni/CeO<sub>2</sub> catalyst under dark and light-assisted reaction conditions. The spectra were recorded using Bruker-Vertex70 spectrophotometer equipped with a high-temperature reaction control cell with two ZnSe windows, one quartz window and a catalytic bed. The catalyst was pre-reduced at 450°C under 5% H<sub>2</sub>/He flow of 50 ml min<sup>-1</sup> for 1 hour, then purged in He gas for 40 min to remove the residual H<sub>2</sub> from the cell and finally cooled down to desired temperature. The background spectrum was recorded in He at room temperature. CO<sub>2</sub> methanation reaction was performed in 20 ml min<sup>-1</sup> of gas mixture (75% of stoichiometric H<sub>2</sub>/CO<sub>2</sub> ratio = 4 and 25% of He balance) at 100°C, 150°C, 200°C, 225°C and 250°C. Each measurement was recorded after 30 min in isothermal conditions, and followed by purging in He for 30 min to remove the excess water molecules. Spectra were recorded from 4200 cm<sup>-1</sup> to 1000 cm<sup>-1</sup> with a step of 1 cm<sup>-1</sup>. Thermal analyzer Thermostat was used to control the product stream by their molecular weights (m/z ratios). The illumination (5 suns) during the DRIFTS measurement was applied through the quartz window from the solar simulator used during the functional characterization.

## 2.3. Ni/CeO<sub>2</sub> hybrid catalyst characterization

### 2.3.1. Physical characterization of the catalyst

SEM and TEM images (Figure 2.5) show that the obtained catalyst consists of CeO<sub>2</sub> nanofibers support (with a diameter of ~10nm) and well-distributed Ni nanoclusters with the size distribution approximately from 5 to 50 nm. The EDX analysis shows the presence of 12 wt.% Ni, which is in a good proximity with the initial estimations. Some residual silicon was spotted, which supposedly comes from the non-dissolved SBA-15 template, but its amount was as low as 1% of the catalyst mass.

The ceria support, shown in Figure 2.5(d), has a typical channel shape due to the SBA-15 template where each channel is 8 nm distant to the closest. This configuration of the support leads to its mesoporous properties and allows the small Ni clusters to penetrate inside the ceria structure.

HRTEM study has shown that the used synthesis procedure is suitable to create a ceria-supported catalyst with a presence of highly distributed small Ni nanoparticles (~5 nm) which have a strong interaction with the ceria support (Figure 2.6). They are mostly located in the voids between the ceria rods. CO<sub>2</sub> methanation over Ni/CeO<sub>2</sub> is a complex reaction, requiring simultaneous H<sub>2</sub> and CO<sub>2</sub> activation. The former occurs on the metallic Ni sites and the latter on the basic sites of CeO<sub>2</sub> [16]. The challenge of the catalyst design is that products of these two reaction steps (H\* and CO<sub>x</sub>) are separated by a spatial constraint, which has to be minimized in order to achieve better catalytic performance. From this point of view, highly distributed Ni nanoclusters embedded in the mesoporous CeO<sub>2</sub> (Figure 2.5(d)) represent the optimal catalyst configuration for CO<sub>2</sub> methanation. We assume that the high exposure of the boundary phase Ni/CeO<sub>2</sub> to the gas is responsible for the significant CO<sub>2</sub> conversion.

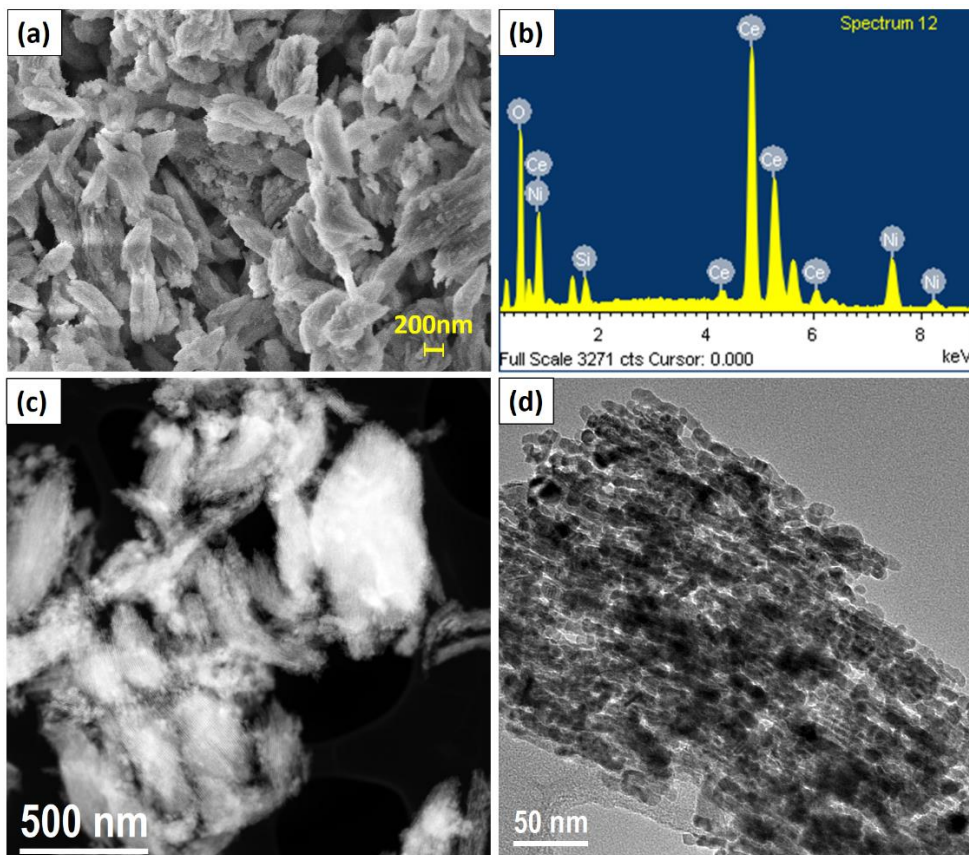
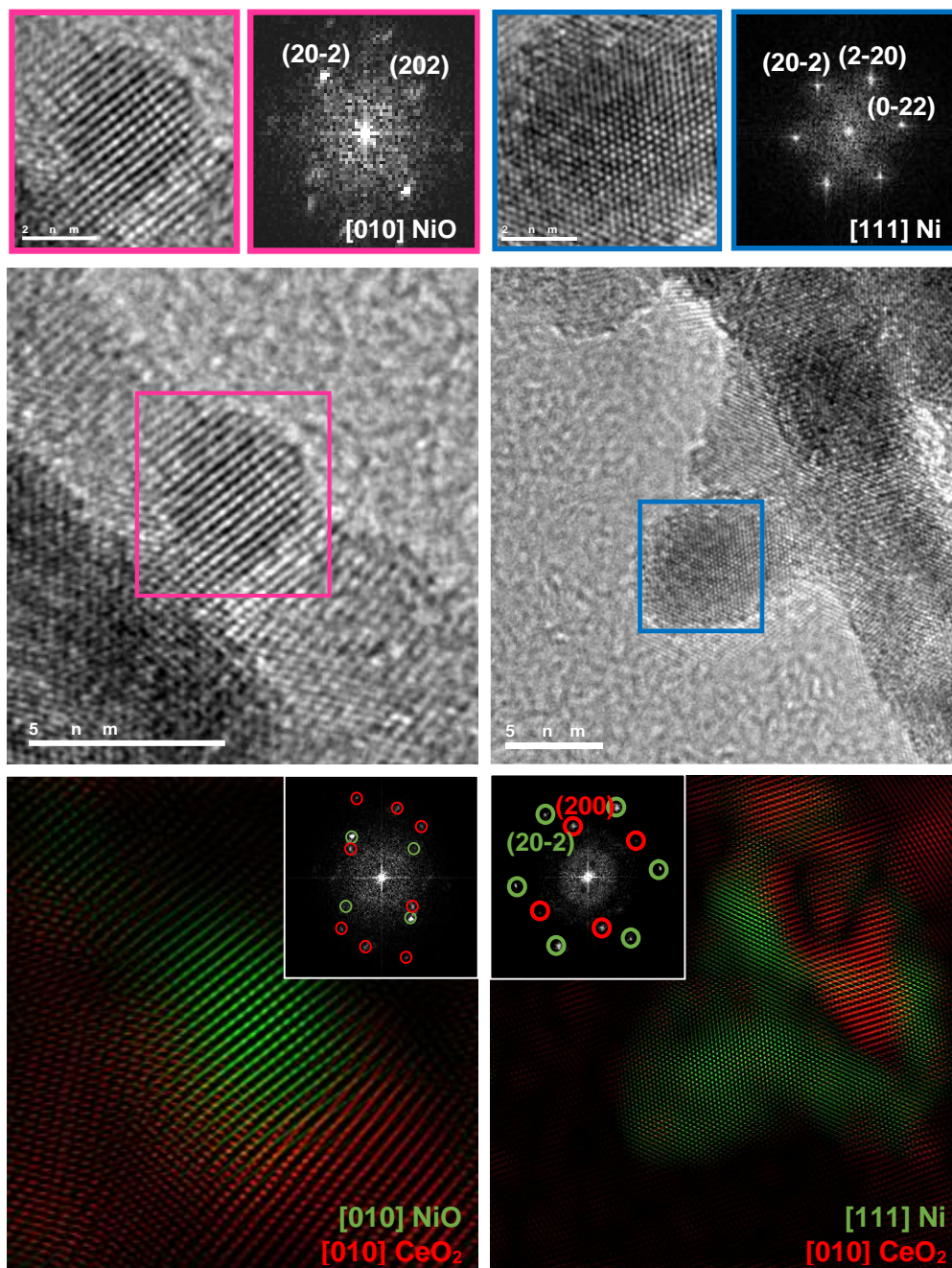


**Figure 2.5.** SEM image of the Ni/CeO<sub>2</sub> catalyst (a) and the corresponding EDX spectrum (b); HAADF STEM (c) and TEM (d) general view images of the sample at low magnification.

From the low-magnification images (Figure. 2.5(d); Appendix A.1.1, Ni panel) we can also see the presence of bigger Ni clusters (~20-50 nm). They are located mostly on the surface of the catalyst and therefore play the major role in the solar light absorption and scattering. Relatively high distribution of the sizes of nanoclusters is responsible for broadening of the plasmonic extinction peak and black coloring of the reduced powder.



S

**Figure 2.6.** HRTEM micrographs of a detail of the non-reduced NiO/CeO<sub>2</sub> (left) and reduced Ni/CeO<sub>2</sub> (right) nanostructures. In the top panel we report the magnification in the squared area and the corresponding indexed power spectra. In the bottom panel, we report the frequency filtered maps evidencing NiO, Ni and CeO<sub>2</sub> planes with different colors.

The N<sub>2</sub>-physorption analysis of the silica SBA-15 template, CeO<sub>2</sub> and Ni/CeO<sub>2</sub> replica has shown that the obtained powders possess a mesoporous structure with a high BET surface area. The surface areas and pore dimensions of pure CeO<sub>2</sub> support and Ni/CeO<sub>2</sub> catalyst used in this study are quite similar, which indicates that Ni impregnation has not influenced the mesoporous morphology of the ceria support. Moreover, the Ni/CeO<sub>2</sub> catalyst exhibits a good dispersion of Ni nanoparticles with high metal surface area, which was derived from CO-chemisorption analysis (Table 2.1).

**Table 2.1.** N<sub>2</sub>-physorption and CO-chemisorption analysis data of the Ni/CeO<sub>2</sub> catalyst, pure CeO<sub>2</sub> support and SBA-15 mesoporous silica template

Sample	Surface area, m <sup>2</sup> g <sup>-1</sup>	Micropore volume, cm <sup>3</sup> g <sup>-1</sup>	Pore size, nm	Ni dispersion, %	Active metal surface area, m <sup>2</sup> g <sup>-1</sup> <sub>Ni</sub>
SBA-15	866.2	0.99	6.6	--	--
CeO <sub>2</sub>	121.1	0.21	3.3	--	--
Ni/CeO <sub>2</sub>	103.5	0.20	2.9	1.3	8.6

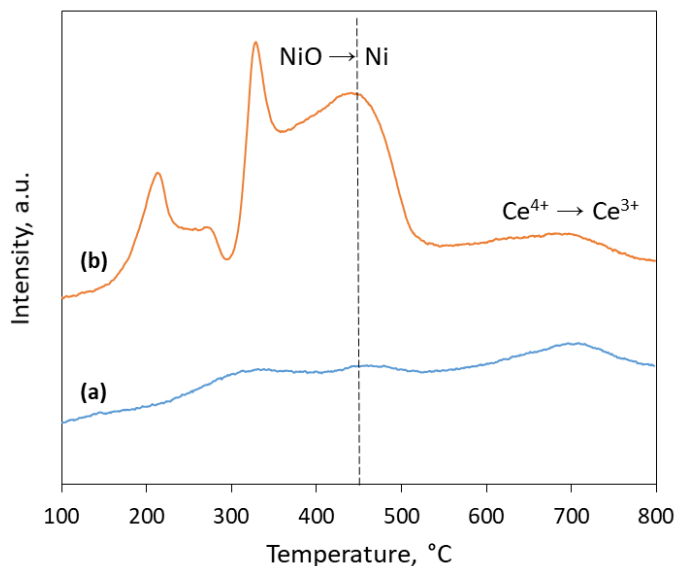


**Figure 2.7.** H<sub>2</sub>-TPR profile of the CeO<sub>2</sub> support (a) and Ni/CeO<sub>2</sub> catalyst (b).

H<sub>2</sub>-TPR analysis was used to study reduction properties of the obtained catalyst (Figure 2.7). The Ni/CeO<sub>2</sub> sample presents a strong peak at T = 328°C and two smaller ones at T = 213°C and T = 271°C, attributed to the reduction of the weakly bound NiO species on the CeO<sub>2</sub> surface [17]. The more intensive one is related to the



reduction of smaller nanoparticles, whereas the low-temperature peaks are due to the large NiO particles on the CeO<sub>2</sub> support. The peak at  $T = 442^{\circ}\text{C}$  was assigned to the reduction of strongly bound NiO [18], and the high-temperature process at  $T = 697^{\circ}\text{C}$  was attributed to the  $\text{Ce}^{4+}$  to  $\text{Ce}^{3+}$  reduction in CeO<sub>2</sub> [19].

The H<sub>2</sub>-TPR analysis confirmed that the reduction temperature of  $450^{\circ}\text{C}$  (dashed line on Figure 2.7), chosen for NiO/CeO<sub>2</sub> catalyst is sufficient to reduce all the types of NiO clusters. EELS chemical composition maps prove that the Ni present in the reduced sample is mostly metallic (Appendix A.1.1).

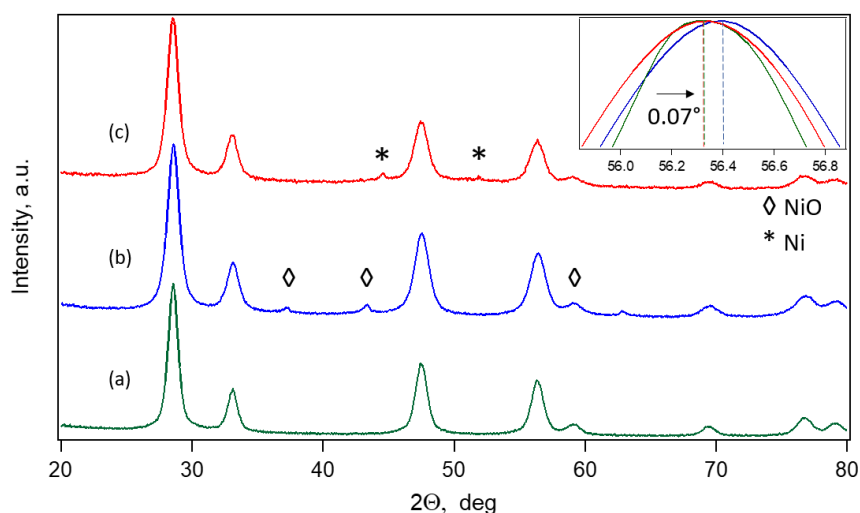


**Figure 2.8.** XRD spectra of the CeO<sub>2</sub> support (a), non-reduced (b) and reduced (c) Ni/CeO<sub>2</sub> catalyst. The inset shows the shift of the  $56.335^{\circ}$  CeO<sub>2</sub> diffraction peak in the non-reduced Ni/CeO<sub>2</sub> catalyst with respect to the reduced one and the pure CeO<sub>2</sub> support.

Figure 2.8 shows XRD spectra of the as-prepared samples and reduced under H<sub>2</sub> atmosphere (5% H<sub>2</sub> in Ar, 7h,  $450^{\circ}\text{C}$ ). As we can see from the figure, NiO phase, that was present in the as-prepared catalyst, disappears completely in favor of metallic Ni. The peaks attributed to CeO<sub>2</sub> are shifted with respect to the clear CeO<sub>2</sub> phase in case of the non-reduced samples, which indicates the incorporation of Ni atoms and nanoclusters to CeO<sub>2</sub>, expanding the lattice [20]. This shift can be clearly seen on the inset of Figure 2.8, where the CeO<sub>2</sub> diffraction peak ( $56.34^{\circ}$ ) present in both pure CeO<sub>2</sub> and reduced Ni/CeO<sub>2</sub> samples, is shifted to  $56.41^{\circ}$  in the case of non-reduced NiO/CeO<sub>2</sub>. After reducing, all Ni is removed from the CeO<sub>2</sub> lattice, which results in shifting of the peaks back to the positions of the CeO<sub>2</sub> phase. It is also worth noticing, that the peak is broadened with respect to the pure CeO<sub>2</sub> support, which indicates the non-uniform strain caused by the presence of Ni nanoclusters in close contact

with the CeO<sub>2</sub> rods. The crystallite sizes of Ni particles were estimated by Sherrer's equation using the peak of  $2\theta=44.51^\circ$ . The average size was found to be 27.9 nm, which is in accordance with the nanoparticle dimensions extracted from the TEM data.

In order to analyze the possible strain influence of the Ni nanoparticles embedded in the CeO<sub>2</sub> mesoporous channels, we used the Geometrical Phase Analysis (GPA) routines in the Digital Micrograph software [21]. Our GPA analyses showed a relative compression of the CeO<sub>2</sub> lattice planes when they are close to a Ni nanoparticle (Figure 2.9). The profile obtained along the dark blue arrow pointed out in the figure corroborates that the CeO<sub>2</sub> {111} planes suffer a 4-5% compression close to the Ni nanoparticle, which is in line with the previous XRD analysis.

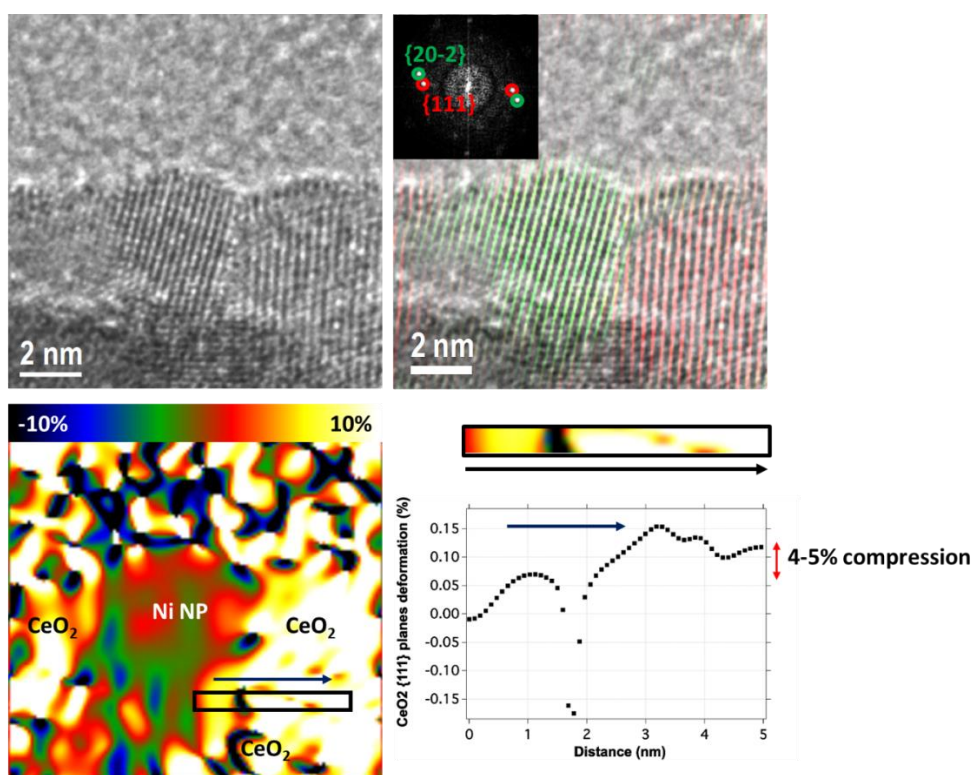


**Figure 2.9.** HRTEM image of the CeO<sub>2</sub> support in one of the channels composing a mesoporous aggregate with a Ni nanoparticle embedded on it (top left). A frequency filter was applied to the HRTEM image in order to obtain the position of the CeO<sub>2</sub> {111} planes (red) and those corresponding to the Ni {20-2} planes (green) (top right). A GPA map was obtained in the same area (bottom left). The profile obtained along the dark blue arrow pointed out in the figure corroborates that the CeO<sub>2</sub> {111} planes suffer a 4-5% compression close to the Ni nanoparticle (bottom right). This compression may differ depending on the relative epitaxial relationship (rotation) of the Ni nanoparticle vs the CeO<sub>2</sub> support.

### 2.3.2. Ni/CeO<sub>2</sub> catalytic performance in the CO<sub>2</sub> methanation reaction

We performed functional characterization of the synthesized catalyst in the tubular-type reactor in dark conditions, configuration of which was discussed in section 2.2.2.2. The measured catalytic activity at different reaction temperatures is shown on the Figure 2.10(a). We found that CO<sub>2</sub> conversion reaches 80% at 300°C, and the selectivity to methane was as high as 95%.

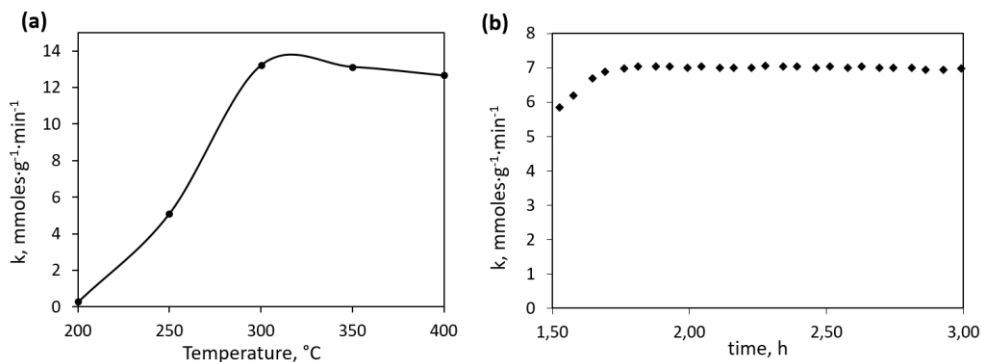


**Figure 2.10.** (a) Temperature dependence of the Ni/CeO<sub>2</sub> catalytic activity in dark conditions; (b) Stability test of the Ni/CeO<sub>2</sub> catalyst.

Due to its high surface area the catalytic activity of Ni/CeO<sub>2</sub> catalyst used in this work is comparable to the activity of the other Ni/CeO<sub>2</sub> catalysts reported previously [22,23].

We have also carried out a stability test which has revealed a high stability of the catalyst under constant reaction conditions at  $T = 270^\circ\text{C}$  (Figure 2.10(b)).

### 2.3.3. Photothermal effects

UV-visible spectroscopy was used to measure the reflectance of bare CeO<sub>2</sub> and Ni/CeO<sub>2</sub> samples. The obtained data were transformed into absorption as no transmittance was observed. As it can be seen from the Figure 2.11(a), bare cerium oxide powder does not absorb under IR and visible illumination, but starts absorbing strongly starting from 430 nm, which corresponds to the reported band gap of oxygen vacancy-enriched CeO<sub>2</sub> nanoparticles (2.87 eV) [24]. In contrast, samples with Ni nanoparticles exhibit an extraordinary high absorption over all of the measured illumination range. We attribute this significant rise in the visible and IR light absorption to the localized surface plasmon resonance of the Ni nanoparticles,

which is known to have a broad band in the IR-vis range, as was previously reported [25–27].

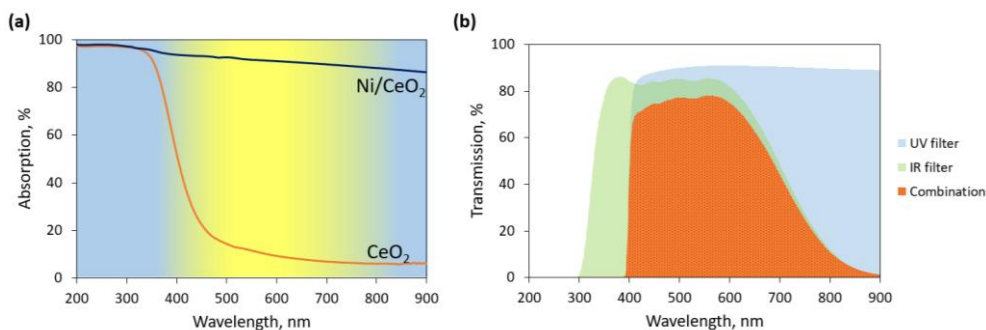


**Figure 2.11.** (a) Reflectance absorption spectra of the bare CeO<sub>2</sub> and Ni/CeO<sub>2</sub> samples. Background yellow color represents the visible irradiation band used in this work. (b) Transmission spectra of the bandpass filters used in this work.

To take advantage of the extra light absorption of the catalyst used in this work, we performed a series of CO<sub>2</sub> methanation tests under solar illumination. We observed a significant increase in the CH<sub>4</sub> yield under illumination, which was concomitant with a temperature increase in the reactor.

Although the plasmonic Ni nanoparticles have a higher damping factor comparing to frequently used Au or Ag nanoparticles, the overlap of their absorption spectrum with the solar one is much better [28]. This ensures an effective absorption of the solar illumination and transforming it to heat. The strong increase in the temperature under solar illumination for Ni-decorated catalyst in comparison to bare CeO<sub>2</sub> support is demonstrated in Appendix, Figure A.1.2.

We have used three different light intensities and operated at three different starting temperatures in order to study the effects related to the photoinduced catalytic activity. Also, in order to investigate the nature of the activity enhancement, we performed wavelength-dependent tests by introducing bandpass filters into the experimental setup. UV filter ( $\lambda > 400\text{nm}$ ) was used to cut off the UV part of the solar spectrum, while the IR filter ( $\lambda < 800\text{nm}$ ) removed the near-IR and IR photons. Transmission spectra of the used filters are shown on the Figure 2.11(b). We have used the combination of two bandpass filters in order to study the pure effect of visible light on the CO<sub>2</sub> conversion. It is worth noting that introducing of the UV filter solely does not affect the catalytic performance of the Ni/CeO<sub>2</sub> catalyst, indicating that the absorption of light by CeO<sub>2</sub> is not responsible for the increase in the catalytic activity.

Figure 2.12(a) sums up the changes in catalytic activity that occur in the catalyst under solar light illumination at different temperatures, light intensities and illumination ranges. As it can be seen from the graph, introducing of visible light has a notable effect on the reaction rate, while the full solar spectrum induces an even higher increase to the catalytic activity. As it was stated previously, cutting off the UV part of the solar spectrum ( $h\nu > 3.1$  eV) does not affect the reaction rate, thus neglecting the role of band-band electron transitions in ceria in the methane production enhancement. Eventually, the illumination of the catalyst may increase the rate of the methanation reaction as high as 2.4 times under suitable reaction conditions (Figure 2.12(b)).

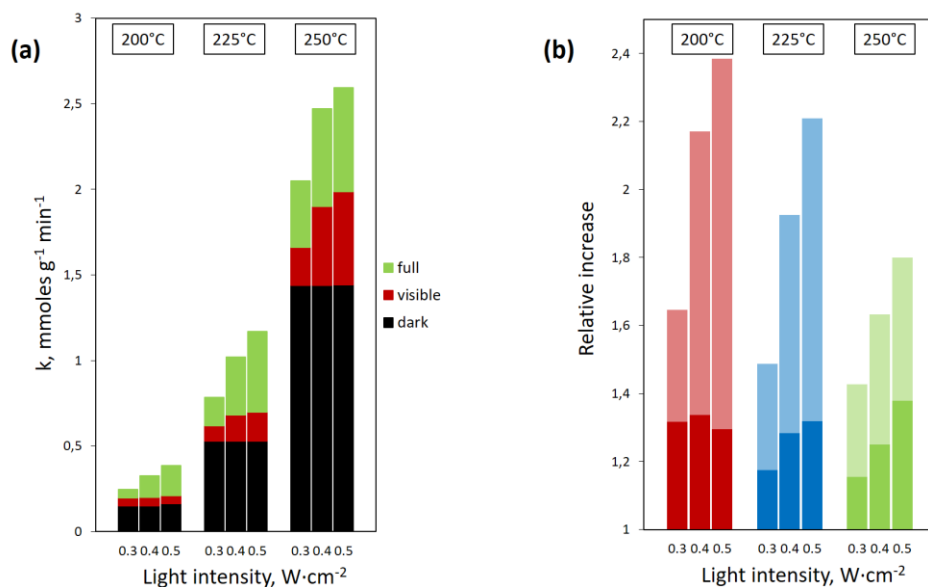


**Figure 2.12.** Catalytic activity of the Ni/CeO<sub>2</sub> catalyst under visible light and full solar illumination of 3 to 5 suns at three different starting temperature points (200°C, 225°C and 250°C) (a); Relative increase of the catalytic activity under illumination with respect to the dark reaction at the corresponding conditions (b). Solid bars correspond to the visible illumination, whereas the full bar corresponds to the full solar illumination. The light intensities correspond to the ones measured before introducing of the filters.

### 2.3.4. DRIFTS characterization

To study the effect of illumination on the intermediate steps of the reaction, we have performed in-situ DRIFTS experiments at different starting temperatures. The measurements were held both in dark conditions and under solar illumination. The corresponding spectra are shown on the Figures 2.13, 2.14 except the band at 2350 cm<sup>-1</sup> corresponding to gas phase CO<sub>2</sub>.

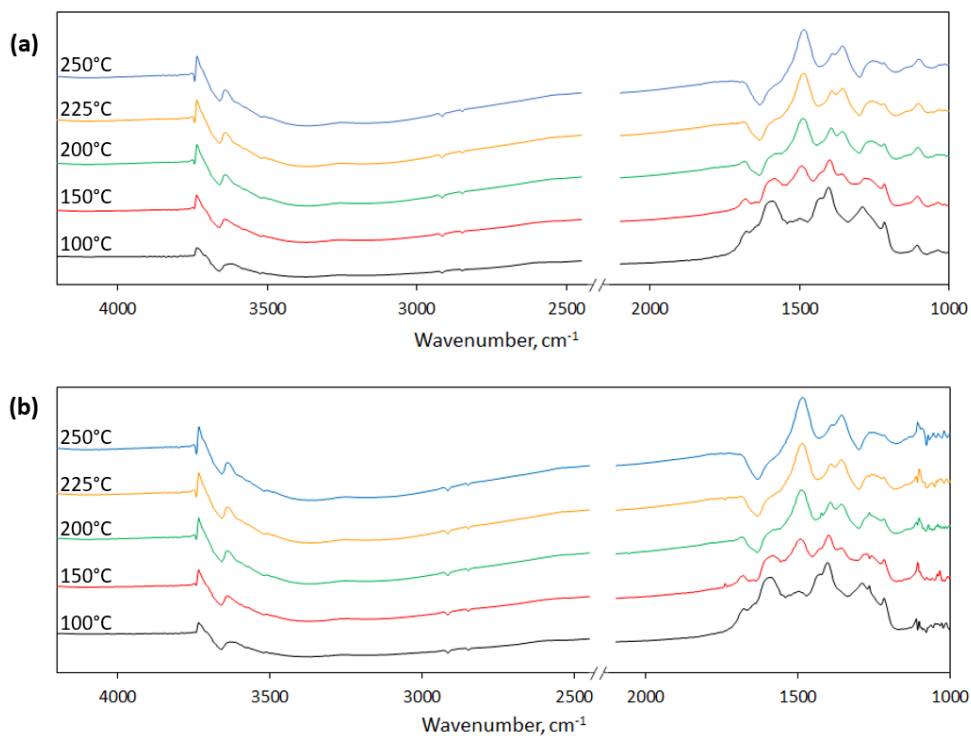


**Figure 2.13.** In-situ DRIFTS spectra during CO<sub>2</sub> methanation over the CeO<sub>2</sub> support in dark conditions (a); under solar illumination (5 suns) (b).

The pure CeO<sub>2</sub> samples without Ni nanoclusters show presence of hydroxyl groups with vibrations  $\nu(\text{OH})$  identified at 3725-3560 cm<sup>-1</sup> and carbonate species only (Figure 2.13). At 100°C the surface is covered by bidentate carbonates (1586, 1300 cm<sup>-1</sup>), bridged carbonates (1646, 1120 cm<sup>-1</sup>) and hydrogen carbonates (1681, 1630, 1422, 1392 and 1212 cm<sup>-1</sup>), presumably formed over OH groups on the CeO<sub>2</sub> surface. The temperature increase stimulates transformation of these carbonates into more stable mono- and polydentate carbonates (1483-1500, 1357 and

1150 cm<sup>-1</sup>). In the absence of Ni<sup>0</sup> the dissociation of the H<sub>2</sub> molecule is not favored, and, therefore, formates are not formed on pure CeO<sub>2</sub> surface.

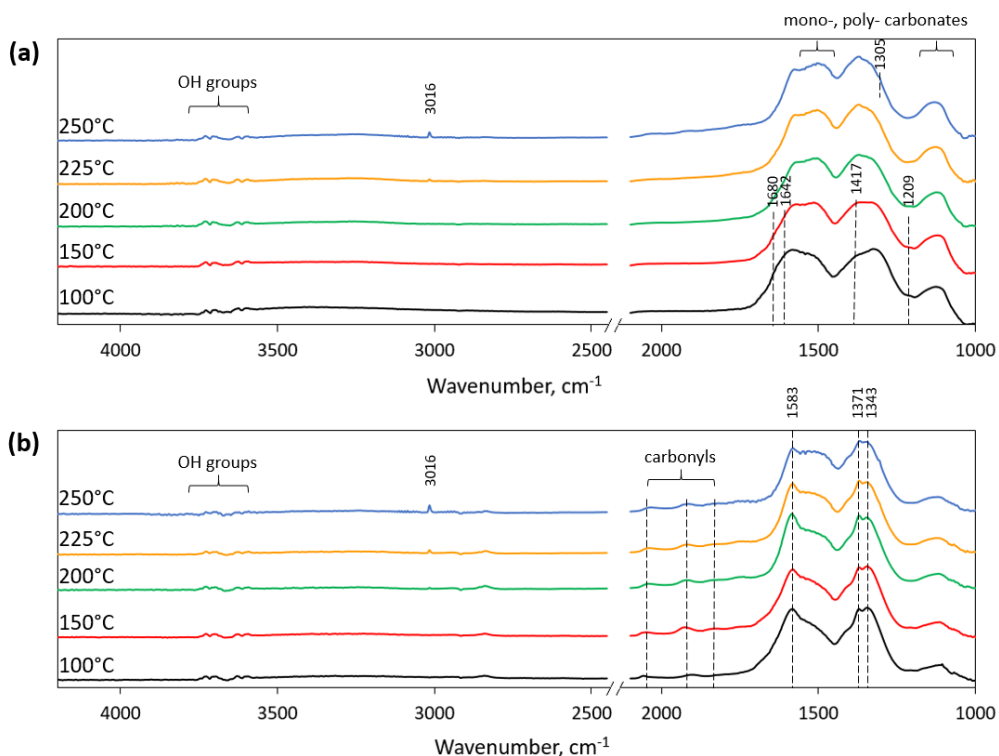


**Figure 2.14.** In-situ DRIFTS spectra measured during CO<sub>2</sub> methanation over the Ni/CeO<sub>2</sub> catalyst (a) in dark conditions; (b) under solar illumination (5 suns).

For Ni/CeO<sub>2</sub> catalyst at 100°C no methane is produced, and CO<sub>2</sub> is mainly adsorbed on the basic Ce<sup>3+</sup> sites [29,30], forming carbonate and hydrogen carbonates species, which are known as precursor for creation of formates. The bands at 1680 cm<sup>-1</sup>, 1417 cm<sup>-1</sup> and 1209 cm<sup>-1</sup> were attributed to hydrogen carbonates vibrations, and the peak at 1642 cm<sup>-1</sup> was assigned to bridged carbonates. The broad band (1472-1530 cm<sup>-1</sup>) and a peak at 1150 cm<sup>-1</sup> were attributed to mono- and polydentate carbonates. At 150°C the weakly bound bridged carbonates are being transformed into mono- and polydentate carbonates and a new bands (1583, 1371 and 1343 cm<sup>-1</sup>) attributed to formates begin to grow [31]. Starting from 200°C a band attributed to production of methane appears at 3016 cm<sup>-1</sup>. It grows further with the temperature increase, while the intensity of the formate peaks is being diminished. On the other hand, the band, attributed to mono- and polydentate carbonates, continuously grows with the temperature increase. This testifies that formates are the precursor in the methane

formation, while the mono- and polydentate carbonates species do not take significant part in the reaction.

Under illumination, the DRIFTS spectra undergo some qualitative changes. At 100°C the peaks at 1583 and 1371 cm<sup>-1</sup>, attributed to vibration of monodentate formate ( $\nu_{\text{asym}}(\text{COO})$ ) become much more pronounced, while the peaks related to hydrogen carbonate species (1680, 1417 or 1209 cm<sup>-1</sup>) are distinctly decreased.

Another significant feature of the DRIFTS spectra, recorded under illumination is appearance of the carbonyl species on the Ni surface, identified at 2041 cm<sup>-1</sup> (monocarbonyl), 1927 cm<sup>-1</sup> (bridged carbonyl) and 1830 cm<sup>-1</sup> (two-fold bridged carbonyl). These bands are growing with temperature increase up to 200°C and afterwards turn to decrease along with formation of methane. This evidently indicates that carbonyls take part in the process of CO<sub>2</sub> hydrogenation to methane. The formation of carbonyls on the Ni surface may occur either through the direct dissociation of CO<sub>2</sub> or through decomposition of formate species.

### 2.3.5. In-situ HRTEM/EELS study

In order to better understand morphological and chemical properties of the Ni/CeO<sub>2</sub> catalyst under operation conditions, we employed in-situ HRTEM/EELS characterization at various temperatures and ambient gases. In this work, the sample was subjected to high vacuum, pure He and a mixture of gases He:CO<sub>2</sub>:H<sub>2</sub> (70:24:6) to simulate stoichiometric methanation reaction conditions, under the range of temperatures from 120°C to 400°C. As ceria support can play a key role in CO<sub>2</sub> coordination and activation, it is crucial to investigate the nature of its active sites, which are mostly defined by the oxidation state of Ce cations in the CeO<sub>2</sub> support lattice.

Reduced Ce<sup>3+</sup> states are formed in CeO<sub>2</sub> lattice as a result of oxygen vacancy formation. Oxygen vacancy releases two electrons, which are captured by Ce<sup>4+</sup> ions and reduce them to Ce<sup>3+</sup> [2]. Therefore, the concentration of Ce<sup>3+</sup> active sites should be tightly related to the temperature and ambient atmosphere.

In vacuum environment, the catalyst heating from 120°C to 350°C induces a slight change in the Ce<sup>3+</sup>/Ce<sup>4+</sup> ratio, related to oxygen vacancy formation under temperature increase (Figure A.3.1). However, the variation in Ce<sup>3+</sup> states is negligibly small, which is explained by a high-temperature Ce<sup>4+</sup>/Ce<sup>3+</sup> reduction peak demonstrated during the TPR measurement (Figure 2.7).



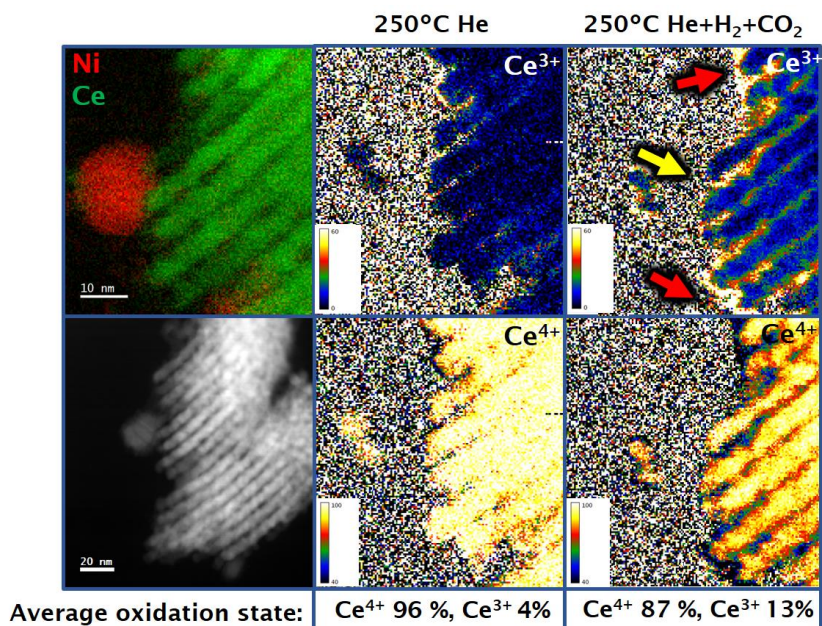


**Figure 2.15.** STEM EELS composition map (top) and HAADF STEM image of Ni/CeO<sub>2</sub> catalyst (bottom). EELS oxidation state maps for Ce under He and He:CO<sub>2</sub>:H<sub>2</sub> gas mixture at 250°C are shown on the middle and right panels. Red arrows show the zones of high Ce<sup>3+</sup> concentration, and the yellow arrow points to the zone where Ni NP resides.

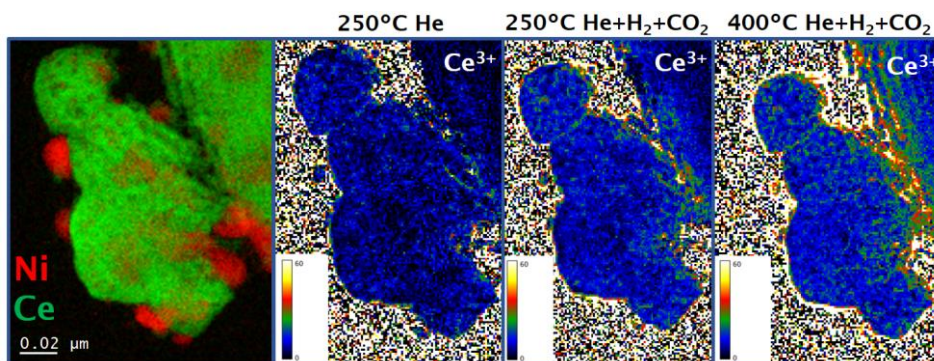


**Figure 2.16.** STEM EELS composition map of Ni/CeO<sub>2</sub> catalyst (left) and its corresponding Ce<sup>3+</sup> mapping under different ambient gases and temperatures (right panels).

In presence of helium at the operating temperature of 250°C, the predominant oxidation state remains Ce<sup>4+</sup> in the content of 95±1%, whereas Ce<sup>3+</sup> makes up 5±1%. However, the situation is drastically changed when the reactant gases are introduced into the chamber. In Figure 2.15 it can be seen that the average concentration of reduced cerium states is increased from 4 to 13% in the bulk CeO<sub>2</sub>. As the CO<sub>2</sub> molecule is at its maximum oxidation state and cannot be responsible for

CeO<sub>2</sub> reduction, Ce<sup>3+</sup> formation is attributed to the presence of H<sub>2</sub> in the gas mixture. In particular, the hydrogen gas is adsorbed and dissociated on the nickel nanoparticles, providing protons which can react with the ceria support, generating water molecules and leaving oxygen vacancies behind. It is worth noting that the distribution of Ce<sup>3+</sup> after introducing the CO<sub>2</sub>/H<sub>2</sub> gas mixture is clearly inhomogeneous and directly depends on the Ni nanoparticle location. In Figure 2.15 we can see that under CO<sub>2</sub>/H<sub>2</sub> atmosphere the formation of reduced Ce<sup>3+</sup> states is suppressed directly under the Ni nanoparticle (yellow arrow), but is highly evident in the areas next to the NP (red arrows). Mapping of other zones of the same sample has shown a similar tendency (Figure A.3.2). This tendency confirms the assumption of hydrogen-driven ceria reduction. The dissociated hydrogen is migrated to the surface of CeO<sub>2</sub> in the close proximity to the Ni nanoparticle, which is called “spillover”. However, hydrogen migration on the CeO<sub>2</sub> surface is kinetically limited, which results in the areas close to the Ni NP being more reduced than the further located zones. CeO<sub>2</sub>, situated under the Ni nanoparticle, is not exposed to hydrogen and, therefore, is significantly less reduced.

Moreover, when the temperature is increased up to 400°C, the amount of Ce<sup>3+</sup> sites grows as a result of higher rate of hydrogen dissociation and, correspondingly, higher amount of protons provided for CeO<sub>2</sub> reduction (Figure 2.16).

To better localize the reduced Ce<sup>3+</sup> states, we have performed a linescan of the oxidation state intensity along the perpendicular direction to the elongated ceria nanorods. An oxidation state intensity profile has shown a periodic shape, where the concentration of Ce<sup>3+</sup> is low in the “bulk” of the 7 nm-thick nanorods and increased at their surface, exposing a core-shell type of a structure. This indicates a higher concentration of oxygen vacancies at the surface of the rods, when exposed to CO<sub>2</sub>/H<sub>2</sub> gas mixture at the reaction temperature. The profile also shows a clear tendency in the Ce<sup>3+</sup> states concentration growth up to 45% when approaching the Ni nanoparticle (Figure 2.17). The same trend is confirmed by oxidation state mapping, done over two zones in the sample, in the bulk and in close proximity to the nickel nanoparticle (marked by orange and blue boxes in Figure 2.17, respectively). The results show a significant increase in the Ce<sup>3+</sup> concentration from 13 to 23% when CeO<sub>2</sub> is put into contact with Ni, confirming the previous results.

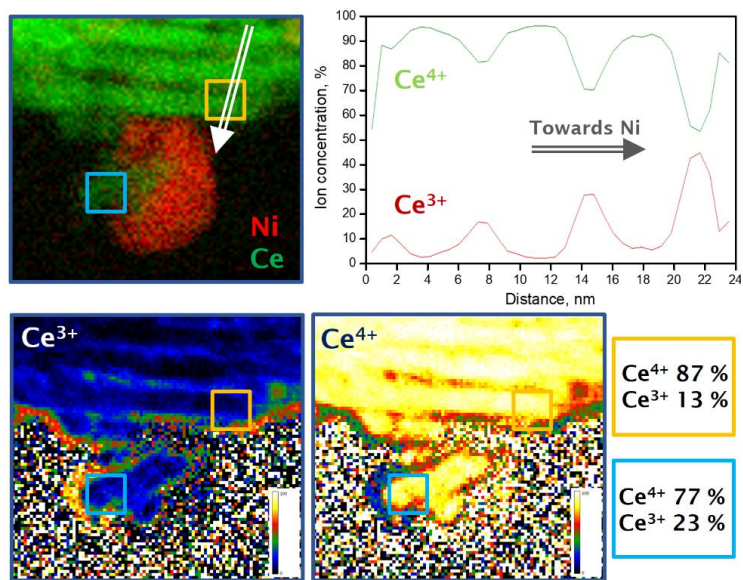


**Figure 2.17.** STEM EELS composition map of Ni/CeO<sub>2</sub> catalyst, corresponding Ce oxidation state mapping and oxidation state profile, calculated along the direction shown with a white arrow. The average oxidation state concentrations of the orange and blue box zones are presented correspondingly.

## 2.4. Mechanism of photothermal CO<sub>2</sub> methanation

Typically, CO<sub>2</sub> hydrogenation on the Ni-based catalysts with inactive support, such as Al<sub>2</sub>O<sub>3</sub> or SiO<sub>2</sub> occurs through the dissociative mechanism, i.e. formation of carbonyl or formate intermediates on the Ni<sup>0</sup> active sites [16]. On the other hand, Ni/CeO<sub>2</sub> catalysts were found to favor the associative mechanism of CO<sub>2</sub> methanation [32–34]. It means that the CO<sub>2</sub> molecules are chemisorbed as monodentate or bidentate carbonates on the reduced active sites of CeO<sub>2</sub>, mostly present at the Ni/CeO<sub>2</sub> interface. At the same time, H<sub>2</sub> molecules dissociate on the metallic Ni clusters, facilitate C=O double-bond breaking and creation of the formates followed by their step-by-step hydrogenation to CH<sub>4</sub>. This mechanism of CO<sub>2</sub> activation is energetically more favorable than the route through CO formation, and is ensured by high mobility of the oxygen vacancies in ceria. The latter allows partial reduction of the CeO<sub>2</sub> material by H<sub>2</sub> at the Ni/CeO<sub>2</sub> interface with subsequent formation of water molecules, while keeping the active sites reduced, as was shown by in-situ HRTEM/EELS study.

In dark conditions, the DRIFTS data recorded from our samples are in agreement with described above associative mechanism, indicating that stable bridged formate species serve as a main precursor for CO<sub>2</sub> hydrogenation to methane, probably through formation of formaldehyde and methoxy adsorbates. However, when the samples are illuminated, we observe immediate changes in the DRIFTS spectra. In particular, variations of the peaks suggest that hydrogen carbonates are more likely transformed to formates. Besides, we detect the appearance of carbonyl species, which may be formed through dissociation of excessive formates [35].

Based on the obtained results, we suggest that illumination has a two-fold effect on the operational performance of the Ni/CeO<sub>2</sub> catalyst. First, visible and IR irradiations excite LSPR in Ni nanoparticles. Although plasmons in Ni are effectively damped, they result in strong local heating of the nickel nanoclusters with following heat dissipation to the surrounding oxide matrix. Such a plasmon-induced increase of the temperature facilitates the principal reaction channel at the Ni/CeO<sub>2</sub> interface.

On the other hand, the illumination is changing the surface chemistry of the catalyst as a result of photoelectronic processes. The obtained changes in the DRIFTS spectra indicate that illumination is promoting the stabilization of formate species from less stable hydrogen carbonates.

As the illumination of the catalyst is followed by the temperature increase (summarized in Appendix, Table A.1.1), we have further analyzed the data from Figure 2.12 in order to find out the nature of the improved catalytic activity. A

thermally activated methanation reaction follows an exponential trend, i.e.  $k \sim e^{-\frac{E_a}{kT}}$ , where  $E_a$  is the activation energy of the reaction, or the rate-limiting step [36]. Therefore,  $\ln(k) \sim -\frac{1}{T}$  for the process that is fully controlled by the temperature. We have plotted a natural logarithm of the measured catalytic activities in all of the applied conditions versus the inverse temperature (Figure 2.18). Remarkably, all the light-assisted measurements of the catalytic activity at low conversion rates were followed the same linear trend, indicating that the solar light illumination of the Ni/CeO<sub>2</sub> catalyst caused an increase of the catalytic activity due to the local temperature changes induced by plasmonic heating of the Ni nanoparticles.

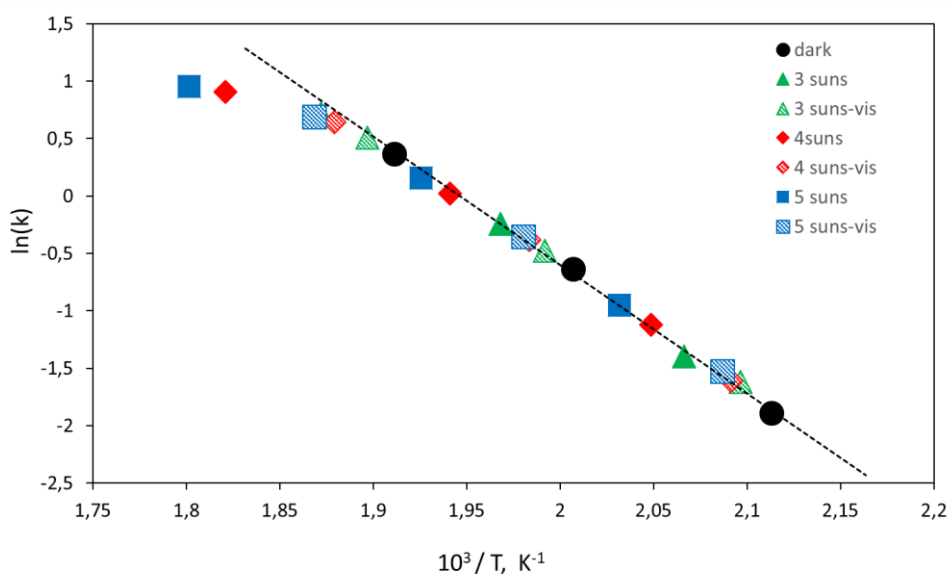


**Figure 2.18.** Arrhenius slope of the temperature activated methanation reaction. The y axis indicates the natural logarithm of catalytic activity under different reaction conditions.

From the Figure 2.18 we have evaluated the Arrhenius slope for the methanation reaction (dashed line), with the activation energy of 0.96 eV. As discussed above, we attribute this energy to the methanation pathway that takes place through hydrogenation of the formates on ceria, presumably to the dissociation of formalin to formaldehyde, as it was shown in [37]. The light-induced increase in the concentration of formates, seen from the DRIFTS data, does not affect the main reaction channel, the latter being totally controlled by temperature. However, we have found that with increase of the illumination intensity the formate and carbonyl peaks on the DRIFTS spectra become more pronounced. We applied Gaussian multi-

peak fitting to the spectra measured under dark conditions, 3 and 5 suns illumination in order to quantify the contribution of the formate intermediates depending on the intensity of the photon flux (Figure 2.19). We found that the amount of adsorbed species is proportional to the power of the applied illumination, which indicates that the electronic effect of the solar illumination can be much more noticeable when higher light intensities are applied.

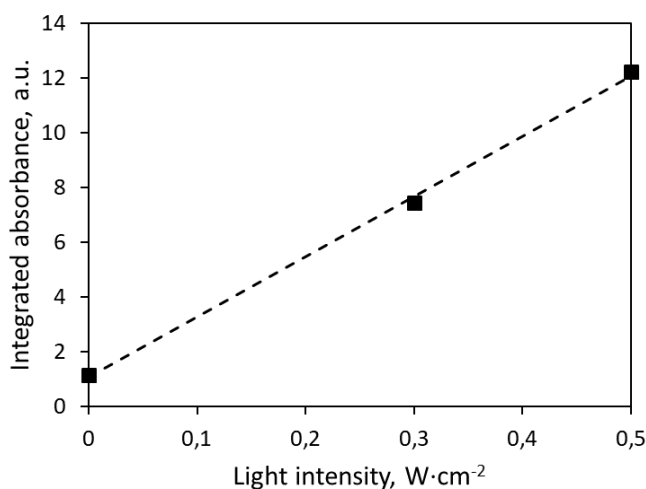


**Figure 2.19.** Dependence of the monodentate formate integrated absorbance on the illumination intensity. The data is obtained from the Gaussian fitting of the 1583 cm<sup>-1</sup> peak from the DRIFTS spectra of Ni/CeO<sub>2</sub> catalyst.

However, when reaching higher temperatures, one can observe a strong deviation from the linear trend towards lower catalytic activities, which points out on a new rate-limiting process that occurs at higher temperatures. As the selectivity to methane was not altered upon the temperature increase (see Appendix, Table A.1.2), this deviation cannot be explained by the activation of a side reaction, i.e. producing of carbon monoxide (reverse water gas-shift reaction), which is enabled at higher temperatures [38]. It is well known that the main deactivation pathways for the Ni-based catalysts are sintering of the Ni nanoparticles and coke formation [39]. However, these processes are also taking place at higher operation temperatures. On the other hand, Cárdenas-Arenas et al. conducted isotopic experiments on Ni/CeO<sub>2</sub> catalyst and showed that water desorption is the slowest step of the methanation mechanism [34]. As it was mentioned before, the light-assisted reaction was held in a custom-designed planar-type reactor under low gas flows. Apparently, at higher CO<sub>2</sub> conversion values the physisorbed water molecules, formed in big amounts during the reaction, are not efficiently removed from the reactor and block the active sites of the catalyst. Thus, in our case,

desorption of water becomes a new rate-limiting step in the methanation process at high conversion rates. We assume that changing of the reactor design to being suitable for high-flow operation conditions will allow to examine the effect of strong illumination on methanation reaction rate with no limitations due to poisoning of the active sites by water molecules.

To understand the effect of different wavelengths on the catalyst we performed a series of DRIFTS experiments under solar illumination with different optical filters. The dark spectra were subtracted from the ones recorded under illumination in order to obtain differential data (Figure 2.20). The results show that the UV part of the solar spectrum has the largest effect on the growth of formate and carbonyl peaks, while the visible light has a much weaker influence on the formate concentration. In the Appendix, Table A.1.3 we have summarized the relative amounts of incident light intensities, used in this work. The intensity of transmitted light with the energy sufficient to excite band-to-band transitions in CeO<sub>2</sub> (250-400 nm) sums up to 10.5% of the total solar spectrum, which results in a non-negligible amount of photogenerated carriers in the ceria support.

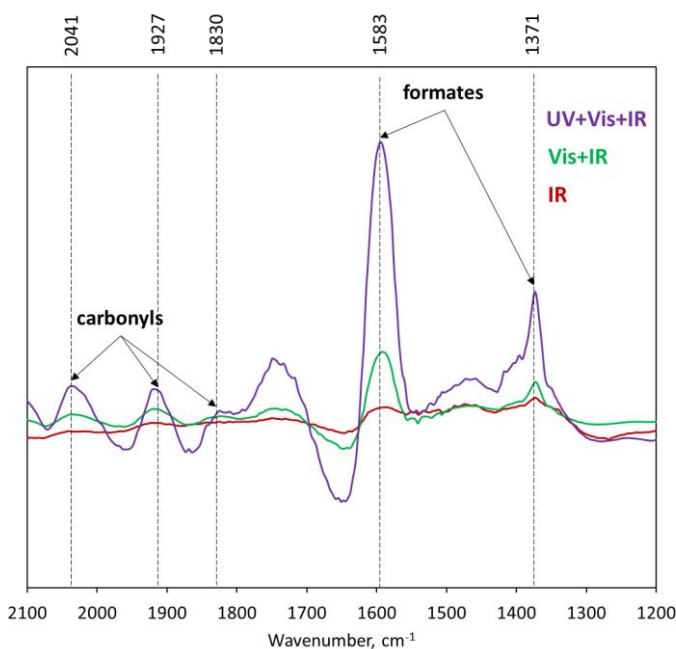


**Figure 2.20.** Differential DRIFTS spectra of the Ni/CeO<sub>2</sub> catalyst measured at starting temperature of 200°C under different wavelength illumination.

It should be noted that the real temperature of the illuminated catalyst is higher than the nominal value of the starting point. To ensure that the DRIFTS changes do not occur due to temperature-induced effects, caused by the heating of the catalyst

under solar light, we have compared DRIFTS spectra of the catalyst under illumination with spectra recorded at elevated temperature in dark conditions (Figure 2.21). The differential graph exhibits the same features as in the Figure 2.20, which proves the non-thermal nature of the light-induced changes on the catalyst surface.

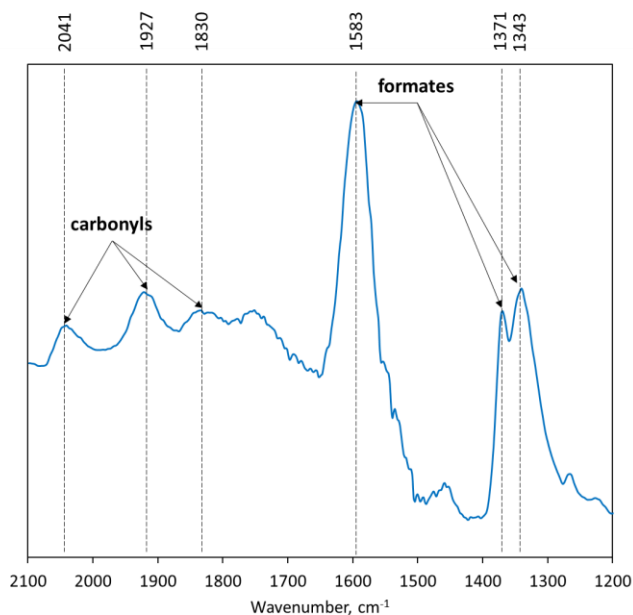


**Figure 2.21.** Difference of the Ni/CeO<sub>2</sub> catalyst DRIFTS spectra measured at 200°C under solar illumination (5 suns, full spectrum) and at 225°C under dark conditions.

According to DRIFTS data, solar light promotes stabilization of the formate species on ceria surface. The increased concentration of formates, however, does not facilitate the overall methane production at the Ni/CeO<sub>2</sub> interface, which follows the Arrhenius slope (Figure 2.18).

According to the in-situ microscopy study, the surface of CeO<sub>2</sub> is enriched with reduced Ce<sup>3+</sup> states, and, therefore, with oxygen vacancies, especially at the Ni/CeO<sub>2</sub> interface due to efficient reduction of ceria by dissociated hydrogen. It is known that oxygen vacancies can trap photogenerated electrons under UV light excitation [40,41]. Furthermore, it was reported that chemisorption of CO<sub>2</sub> becomes favorable on the reduced CeO<sub>2</sub> surface with abundance of additional charge [30,42]. Therefore, it is plausible that UV and blue light illumination, present



in the solar spectrum, can generate electron-hole pairs in ceria that activate surface vacancy sites and enhance sorption processes at CeO<sub>2</sub> surface. Photogenerated carriers facilitate transformation of the carbonate species to the more energetically stable formates, which is reflected in the corresponding changes of DRIFTS spectra. The concentration of formates is increased throughout the ceria support, including the sites apart from the Ni/CeO<sub>2</sub> interface. On the other hand, hydrogenation of formates, being the rate-limiting step of the methanation reaction, requires active hydrogen atoms, which are abundant at the interface with nickel nanoparticles. Thus, the formates adsorbed on ceria surface apart from the interface are lacking hydrogens and do not contribute effectively to the overall methane production.

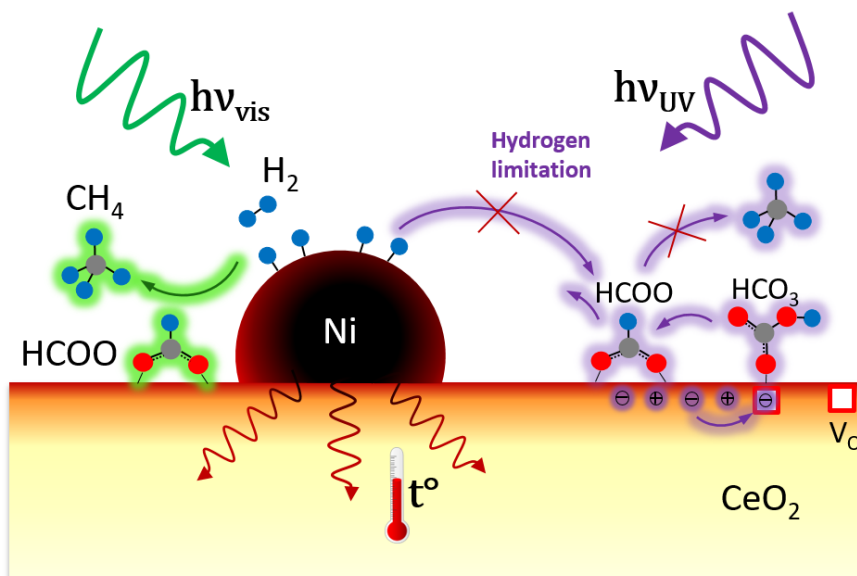


**Figure 2.22.** Proposed mechanism of CO<sub>2</sub> methanation under solar illumination.

The suggested mechanism of CO<sub>2</sub> methanation on the Ni/CeO<sub>2</sub> catalyst is schematically shown on Figure 2.22 and can be described as follows. In dark conditions, CO<sub>2</sub> is adsorbed on the active sites at Ni/CeO<sub>2</sub> interface as bridged carbonates or hydrogen carbonates, which are further transformed to formates and monodentate carbonates. Under constant supply of hydrogen atoms from Ni nanoclusters, the formates at the interface are hydrogenated to methane. Solar illumination has a two-fold effect on the reaction. First, Ni nanoparticles exhibit a rapid local heating due to the strongly damped localized surface plasmons generated on Ni. This leads to an increase of the average temperature of the catalyst and to the overall increase of the methane production. Secondly, UV and visible illumination is enhancing photocatalytic properties of ceria. Photoinduced charge

carriers facilitate transformation of hydrogen carbonates to formates, giving rise to the corresponding peak on the DRIFTS spectra. However, the newly formed species adsorbed apart from the Ni/CeO<sub>2</sub> interface do not contribute to the methanation due to the limited hydrogen supply.

The specific configuration of the Ni/CeO<sub>2</sub> catalyst suggests its use as a plasmonic nanoreactor (PNR): a reactor with plasmonic properties which allows encapsulating the reactant molecules in a confined space at the nanoscale in order to facilitate their chemical interaction and shield the reaction from external effects [43]. This significantly increases the conversion rate and allows tuning of the catalyst selectivity, improving its overall performance. Mesoporous structure of CeO<sub>2</sub> support with high distribution of Ni nanoparticles in the pores of the material can be considered as a combination of nanoreactors, making Ni/CeO<sub>2</sub> a promising catalyst for highly controlled nanoscale CO<sub>2</sub> methanation.

A plasmonic nanoreactor uses LSPR of metallic nanoparticles embedded into the mesoporous structure of the support material to induce charge transfer or local temperature increase as a result of plasmonic heating [44,45]. In our case, plasmonic Ni nanoparticles can be used as a source of local heat upon external illumination, avoiding the excessive energy loss under total heating of the material by lowering the overall temperature. The increased temperature improves the reaction kinetics and, along with the hydrogen spillover effect, activates the CeO<sub>2</sub> support at the interface with Ni nanoparticles due to reduction of Ce<sup>4+</sup> to Ce<sup>3+</sup> states.

## 2.5. Energy consumption evaluation

One of the effective ways of exploiting the plasmon-induced photothermal effect of the Ni/CeO<sub>2</sub> catalyst for CO<sub>2</sub> methanation is to maintain the constant temperature of the reaction, by controlling the power supplied to the reactor. After compensation of the increased temperature to the initial value by reducing the power consumption, no improvement in the reaction rate was observed, which confirms that the photothermal effect of the illumination on the main reaction pathway is dominant at low temperatures and light intensities. However, we have measured the power, supplied to the reactor in the dark conditions ( $P_{dark}$ ), and the corresponding power under illumination ( $P_{light}$ ), reduced in order to maintain the working temperature at its initial value. Then, the reduced power consumption (RPC) for all of the experimental conditions used in this work was calculated according to the following formula:

$$RPC = \frac{P_{dark} - P_{light}}{P_{dark}} \cdot 100\% \quad (2.5)$$

The results are presented in the Figure 2.23.

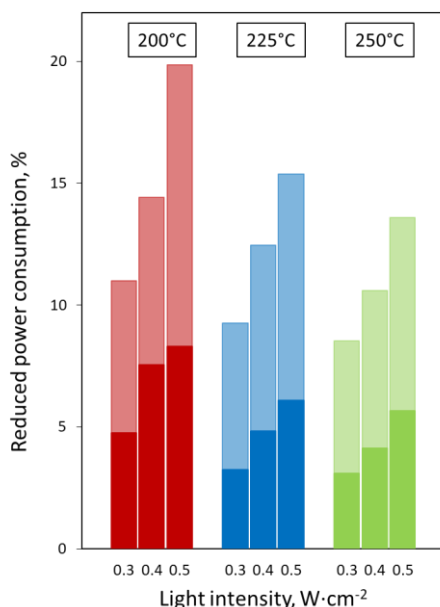


**Figure 2.23.** Power consumption savings under visible light and full solar illumination of 3 to 5 suns at three different temperatures: 200°C, 225°C and 250°C. Solid bars correspond to the visible illumination, whereas the full bar corresponds to the full solar illumination.

We can see that using concentrated sun illumination we are able to save up to 20% of power applied for the conventional thermocatalytical approach to CO<sub>2</sub> methanation. Utilization of renewable solar energy source and an earth-abundant material with plasmonic properties for facilitation of effective thermal-driven CO<sub>2</sub> methanation allowed us to gain energy for further lowering of the cost, scalability and industrialization of the process.

## 2.6. Conclusions

In this chapter, we have demonstrated that the catalytic activity of the methanation reaction can be improved by the photothermal effect due to localized surface plasmonic properties of the Ni nanoparticles in the Ni/CeO<sub>2</sub> catalyst under visible and infrared light illumination. Using of the mesoporous SBA-15 silica template allowed us to synthesize large-surface-area Ni/CeO<sub>2</sub> catalyst, which ensures highly stable and efficient conversion of CO<sub>2</sub> (80%) with high selectivity to methane (95%). The obtained catalyst exhibits up to a 2.4-fold increase in the reaction rate under solar light illumination, which allowed us to decrease the power consumption by 20% with respect to the dark conditions.

In-situ HRTEM/EELS and DRIFTS analysis revealed the mechanism of the CO<sub>2</sub> methanation in dark and light-assisted conditions. In dark conditions the CO<sub>2</sub> methanation is following the associative route through formate hydrogenation on CeO<sub>2</sub>, using Ni<sup>0</sup> active sites only for H<sub>2</sub> dissociation and spillover to CeO<sub>2</sub> support, increasing the concentration of reduced Ce<sup>3+</sup> sites, used for CO<sub>2</sub> activation. When illuminating the catalyst with solar light, two main effects were observed. On the one hand, the visible and IR illumination results in a strong photothermal plasmon-induced effect, followed by local heating and enhanced methane production. On the other hand, UV and blue light induced photogenerated free carriers in CeO<sub>2</sub> can improve the CO<sub>2</sub> coordination and promote the creation of formates. However, their further hydrogenation remains fully controlled by the photothermally activated process due to the limited hydrogen supply to the formate species. Investigation of the rate-limiting step by means of the first-principles calculations will be the subject of the future work.

At high conversion rates, the activity of the Ni/CeO<sub>2</sub> catalyst in the current reactor design is damped by the slow water desorption process from the active Ni<sup>0</sup> sites. Therefore, we have utilized the plasmon-induced photothermal effect of the Ni/CeO<sub>2</sub> catalyst for CO<sub>2</sub> methanation by operating at low reaction temperatures, reducing the power supplied to the reactor. Nevertheless, we believe that new reactor design may open a possibility of a thorough study and exploitation of the new light-induced methanation route at higher illumination intensities and conversion rates, thus further reducing the power consumed by the reactor.

The obtained results emphasize the two-fold effect of solar illumination on the plasmonic Ni-based catalysts: photothermal and electronic. Hence, the combined photo- and thermocatalytical approach is expected to provide a promising pathway for Ni-based heterogeneous catalysts for green CO<sub>2</sub> hydrogenation.

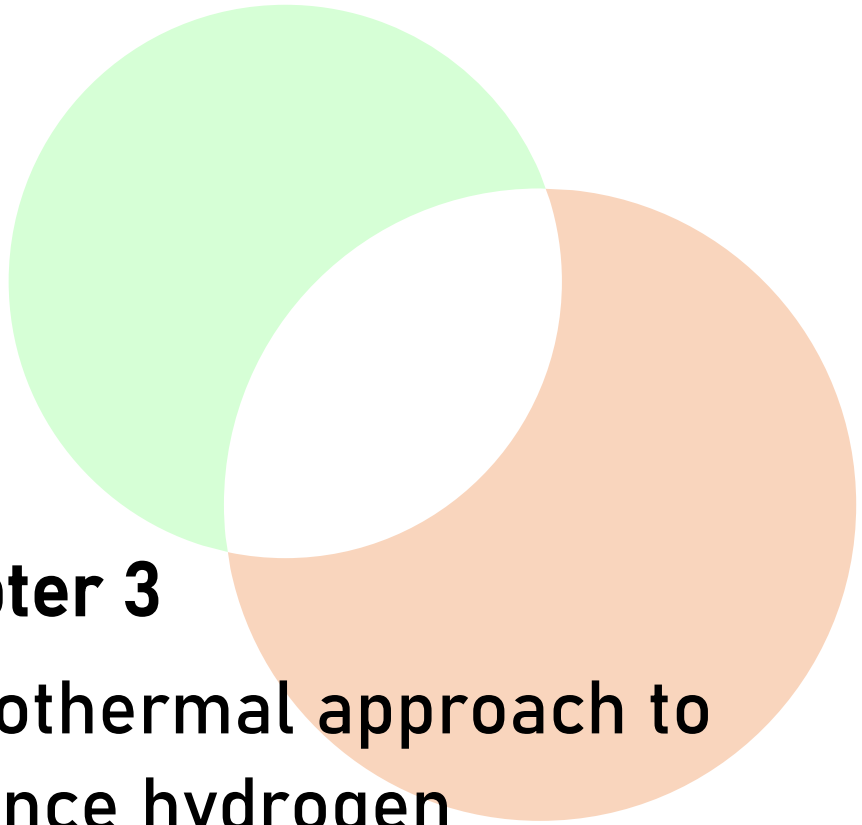
## 2.7. References

- [1] J. Chen, Y. Zhou, R. Li, X. Wang, and G. Z. Chen, *Highly-Dispersed Nickel Nanoparticles Decorated Titanium Dioxide Nanotube Array for Enhanced Solar Light Absorption*, Appl. Surf. Sci. **464**, 716 (2019).
- [2] Q. Zhang, M. Mao, Y. Li, Y. Yang, H. Huang, Z. Jiang, Q. Hu, S. Wu, and X. Zhao, *Novel Photoactivation Promoted Light-Driven CO<sub>2</sub> Reduction by CH<sub>4</sub> on Ni/CeO<sub>2</sub> Nanocomposite with High Light-to-Fuel Efficiency and Enhanced Stability*, Appl. Catal. B Environ. **239**, 555 (2018).
- [3] J. Albero, H. Garcia, and A. Corma, *Temperature Dependence of Solar Light Assisted CO<sub>2</sub> Reduction on Ni Based Photocatalyst*, Top. Catal. **59**, 787 (2016).
- [4] X. Meng, T. Wang, L. Liu, S. Ouyang, P. Li, H. Hu, T. Kako, H. Iwai, A. Tanaka, and J. Ye, *Photothermal Conversion of CO<sub>2</sub> into CH<sub>4</sub> with H<sub>2</sub> over Group VIII Nanocatalysts: An Alternative Approach for Solar Fuel Production*, Angew. Chemie **53**, 11478 (2014).
- [5] R. R. Poolakkandy and M. M. Menampambath, *Soft-Template-Assisted Synthesis: A Promising Approach for the Fabrication of Transition Metal Oxides*, Nanoscale Adv. **2**, 5015 (2020).
- [6] N. D. Hoa, N. Van Duy, and N. Van Hieu, *Crystalline Mesoporous Tungsten Oxide Nanoplate Monoliths Synthesized by Directed Soft Template Method for Highly Sensitive NO<sub>2</sub> Gas Sensor Applications*, Mater. Res. Bull. **48**, 440 (2013).
- [7] B. Tian, X. Liu, L. A. Solovyov, Z. Liu, H. Yang, Z. Zhang, S. Xie, F. Zhang, B. Tu, C. Yu, O. Terasaki, and D. Zhao, *Facile Synthesis and Characterization of Novel Mesoporous and Mesorelief Oxides with Gyroidal Structures*, J. Am. Chem. Soc. **126**, 865 (2004).
- [8] Y. J. Han, J. M. Kim, and G. D. Stucky, *Preparation of Noble Metal Nanowires Using Hexagonal Mesoporous Silica SBA-15*, Chem. Mater. **12**, 2068 (2000).
- [9] H. Yang, Q. Shi, B. Tian, Q. Lu, F. Gao, S. Xie, J. Fan, C. Yu, B. Tu, and D. Zhao, *One-Step Nanocasting Synthesis of Highly Ordered Single Crystalline Indium Oxide Nanowire Arrays from Mesostructured Frameworks*, J. Am. Chem. Soc. **125**, 4724 (2003).
- [10] X. F. Guo and G. J. Kim, *Synthesis of Ordered Mesoporous Manganese Oxides by Double Replication for Use as an Electrode Material*, Bull. Korean Chem. Soc. **32**, 186 (2011).
- [11] H. Yen, Y. Seo, R. Guillet-Nicolas, S. Kaliaguine, and F. Kleitz, *One-Step-Impregnation Hard Templating Synthesis of High-Surface-Area Nanostructured Mixed Metal Oxides (NiFe<sub>2</sub>O<sub>4</sub>, CuFe<sub>2</sub>O<sub>4</sub> and Cu/CeO<sub>2</sub>)*, Chem. Commun. **47**, 10473 (2011).
- [12] A. Galarneau, H. Cambon, F. Di Renzo, R. Ryoo, M. Choi, and F. Fajula, *Microporosity and Connections between Pores in SBA-15 Mesostructured Silicas as a Function of the Temperature of Synthesis*, New J. Chem. **27**, 73 (2003).
- [13] P. Janus, R. Janus, B. Dudek, M. Drozdek, A. Silvestre-Albero, F. Rodríguez-Reinoso, and P. Kuśtrowski, *On Mechanism of Formation of SBA-15/Furfuryl Alcohol-Derived Mesoporous Carbon Replicas and Its Relationship with Catalytic Activity in Oxidative Dehydrogenation of Ethylbenzene*, Microporous Mesoporous Mater. **299**, 110118 (2020).
- [14] E. Rossinyol, J. Arbiol, F. Peiró, A. Cornet, J. R. Morante, B. Tian, T. Bo, and D. Zhao, *Nanostructured Metal Oxides Synthesized by Hard Template Method for Gas Sensing Applications*, Sensors Actuators, B Chem. **109**, 57 (2005).

- [15] L. Almar, T. Andreu, A. Morata, M. Torrell, L. Yedra, S. Estradé, F. Peiró, and A. Tarancón, *High-Surface-Area Ordered Mesoporous Oxides for Continuous Operation in High Temperature Energy Applications*, *J. Mater. Chem. A* **2**, 3134 (2014).
- [16] B. Miao, S. S. K. Ma, X. Wang, H. Su, and S. H. Chan, *Catalysis Mechanisms of CO<sub>2</sub> and CO Methanation*, *Catal. Sci. Technol.* **6**, 4048 (2016).
- [17] V. La Parola, G. Pantaleo, and A. Venezia, *Effects of Synthesis on the Structural Properties and Methane Partial Oxidation Activity of Ni/CeO<sub>2</sub> Catalyst*, *Catalysts* **8**, 220 (2018).
- [18] S. Xu and X. Wang, *Highly Active and Coking Resistant Ni/CeO<sub>2</sub>-ZrO<sub>2</sub> Catalyst for Partial Oxidation of Methane*, *Fuel* **84**, 563 (2005).
- [19] D. He, D. Chen, H. Hao, J. Yu, J. Liu, J. Lu, F. Liu, G. Wan, S. He, and Y. Luo, *Structural/Surface Characterization and Catalytic Evaluation of Rare-Earth (Y, Sm and La) Doped Ceria Composite Oxides for CH<sub>3</sub>SH Catalytic Decomposition*, *Appl. Surf. Sci.* **390**, 959 (2016).
- [20] R. Murugan, G. Vijayaprasath, T. Mahalingam, and G. Ravi, *Enhancement of Room Temperature Ferromagnetic Behavior of Rf Sputtered Ni-CeO<sub>2</sub> Thin Films*, *Appl. Surf. Sci.* **390**, 583 (2016).
- [21] M. J. Hÿtch, E. Snoeck, and R. Kilaas, *Quantitative Measurement of Displacement and Strain Fields from HREM Micrographs*, *Ultramicroscopy* **74**, 131 (1998).
- [22] S. Tada, T. Shimizu, H. Kameyama, T. Haneda, and R. Kikuchi, *Ni/CeO<sub>2</sub> Catalysts with High CO<sub>2</sub> Methanation Activity and High CH<sub>4</sub> Selectivity at Low Temperatures*, *Int. J. Hydrogen Energy* **37**, 5527 (2012).
- [23] G. Zhou, H. Liu, K. Cui, A. Jia, G. Hu, Z. Jiao, Y. Liu, and X. Zhang, *Role of Surface Ni and Ce Species of Ni/CeO<sub>2</sub> Catalyst in CO<sub>2</sub> Methanation*, *Appl. Surf. Sci.* **383**, 248 (2016).
- [24] S. Soni, S. Kumar, B. Dalela, S. Kumar, P. A. Alvi, and S. Dalela, *Defects and Oxygen Vacancies Tailored Structural and Optical Properties in CeO<sub>2</sub> Nanoparticles Doped with Sm<sup>3+</sup> Cation*, *J. Alloys Compd.* **752**, 520 (2018).
- [25] H. Liu, T. D. Dao, L. Liu, X. Meng, T. Nagao, and J. Ye, *Light Assisted CO<sub>2</sub> Reduction with Methane over Group VIII Metals: Universality of Metal Localized Surface Plasmon Resonance in Reactant Activation*, *Appl. Catal. B Environ.* **209**, 183 (2017).
- [26] Z. Xin, L. Lu, B. Wang, X. Wang, K. Zhu, Z. Xu, Z. Yu, S. Yan, and Z. Zou, *Lewis Acid Activated CO<sub>2</sub> Reduction over a Ni Modified Ni-Ge Hydroxide Driven by Visible-Infrared Light*, *Dalt. Trans.* **48**, 1672 (2019).
- [27] H. Liu, H. Song, X. Meng, L. Yang, and J. Ye, *Light Irradiation Enhanced CO<sub>2</sub> Reduction with Methane: A Case Study in Size-Dependent Optical Property of Ni Nanoparticles*, *Catal. Today* **335**, 187 (2019).
- [28] G. E. Jonsson, V. Miljkovic, and A. Dmitriev, *Nanoplasmon-Enabled Macroscopic Thermal Management*, *Sci. Rep.* **4**, 5111 (2014).
- [29] N. M. Martin, F. Hemmingsson, A. Schaefer, M. Ek, L. R. Merte, U. Hejral, J. Gustafson, M. Skoglundh, A. C. Dippel, O. Gutowski, M. Bauer, and P. A. Carlsson, *Structure-Function Relationship for CO<sub>2</sub> Methanation over Ceria Supported Rh and Ni Catalysts under Atmospheric Pressure Conditions*, *Catal. Sci. Technol.* **9**, 1644 (2019).
- [30] F. Wang, S. He, H. Chen, B. Wang, L. Zheng, M. Wei, D. G. Evans, and X. Duan, *Active Site Dependent Reaction Mechanism over Ru/CeO<sub>2</sub> Catalyst toward CO<sub>2</sub> Methanation*, *J. Am.*

- Chem. Soc. **138**, 6298 (2016).
- [31] Y. Yang, C. A. Mims, R. S. Disselkamp, J. H. Kwak, C. H. F. Peden, and C. T. Campbell, *(Non)Formation of Methanol by Direct Hydrogenation of Formate on Copper Catalysts*, J. Phys. Chem. C **114**, 17205 (2010).
- [32] P. A. U. Aldana, F. Ocampo, K. Kobl, B. Louis, F. Thibault-Starzyk, M. Daturi, P. Bazin, S. Thomas, and A. C. Roger, *Catalytic CO<sub>2</sub> Valorization into CH<sub>4</sub> on Ni-Based Ceria-Zirconia. Reaction Mechanism by Operando IR Spectroscopy*, Catal. Today **215**, 201 (2013).
- [33] S. M. Lee, Y. H. Lee, D. H. Moon, J. Y. Ahn, D. D. Nguyen, S. W. Chang, and S. S. Kim, *Reaction Mechanism and Catalytic Impact of Ni/CeO<sub>2-x</sub> Catalyst for Low-Temperature CO<sub>2</sub> Methanation*, Ind. Eng. Chem. Res. **58**, 8656 (2019).
- [34] A. Cárdenas-Arenas, A. Quindimil, A. Davó-Quiñonero, E. Bailón-García, D. Lozano-Castelló, U. De-La-Torre, B. Pereda-Ayo, J. A. González-Marcos, J. R. González-Velasco, and A. Bueno-López, *Isotopic and in Situ DRIFTS Study of the CO<sub>2</sub> Methanation Mechanism Using Ni/CeO<sub>2</sub> and Ni/Al<sub>2</sub>O<sub>3</sub> Catalysts*, Appl. Catal. B Environ. **265**, 118538 (2020).
- [35] A. Westermann, B. Azambre, M. C. Bacariza, I. Graça, M. F. Ribeiro, J. M. Lopes, and C. Henriques, *The Promoting Effect of Ce in the CO<sub>2</sub> Methanation Performances on NiUSY Zeolite: A FTIR In Situ/Operando Study*, Catal. Today **283**, 74 (2017).
- [36] C. E. Verostko and R. K. Forsythe, *A Study of the Sabatier-Methanation Reaction*, SAE Technical Paper 740933 (1974).
- [37] Z. Cheng and C. S. Lo, *Mechanistic and Microkinetic Analysis of CO<sub>2</sub> Hydrogenation on Ceria*, Phys. Chem. Chem. Phys. **18**, 7987 (2016).
- [38] L. Pastor-Pérez, F. Baibars, E. Le Sache, H. Arellano-García, S. Gu, and T. R. Reina, *CO<sub>2</sub> Valorisation via Reverse Water-Gas Shift Reaction Using Advanced Cs Doped Fe-Cu/Al<sub>2</sub>O<sub>3</sub> Catalysts*, J. CO<sub>2</sub> Util. **21**, 423 (2017).
- [39] S. Abelló, C. Berruenco, and D. Montané, *High-Loaded Nickel-Alumina Catalyst for Direct CO<sub>2</sub> Hydrogenation into Synthetic Natural Gas (SNG)*, Fuel **113**, 598 (2013).
- [40] B. Choudhury, P. Chetri, and A. Choudhury, *Oxygen Defects and Formation of Ce<sup>3+</sup> Affecting the Photocatalytic Performance of CeO<sub>2</sub> Nanoparticles*, RSC Adv. **4**, 4663 (2014).
- [41] C. Yang, J. Yang, X. Duan, G. Hu, Q. Liu, S. Ren, J. Li, and M. Kong, *Roles of Photo-Generated Holes and Oxygen Vacancies in Enhancing Photocatalytic Performance over CeO<sub>2</sub> Prepared by Molten Salt Method*, Adv. Powder Technol. **31**, 4072 (2020).
- [42] K. R. Hahn, M. Iannuzzi, A. P. Seitsonen, and J. Hutter, *Coverage Effect of the CO<sub>2</sub> Adsorption Mechanisms on CeO<sub>2</sub>(111) by First Principles Analysis*, J. Phys. Chem. C **117**, 1701 (2013).
- [43] R. Syah, M. Zahar, and E. Kianfar, *Nanoreactors: Properties, Applications and Characterization*, Int. J. Chem. React. Eng. **19**, 981 (2021).
- [44] B. Han, L. Wu, J. Li, X. Wang, Q. Peng, N. Wang, and X. Li, *A Nanoreactor Based on SrTiO<sub>3</sub> Coupled TiO<sub>2</sub> Nanotubes Confined Au Nanoparticles for Photocatalytic Hydrogen Evolution*, Int. J. Hydrogen Energy **5**, 1 (2019).
- [45] C. Zhan, Q. X. Wang, J. Yi, L. Chen, D. Y. Wu, Y. Wang, Z. X. Xie, M. Moskovits, and Z. Q. Tian, *Plasmonic Nanoreactors Regulating Selective Oxidation by Energetic Electrons and Nanoconfined Thermal Fields*, Sci. Adv. **7**, 1 (2021).





## **Chapter 3**

**Photothermal approach to  
enhance hydrogen  
production via water splitting**

### 3.1. Introduction

This chapter is dedicated to the investigation of a photothermal effect in plasmonic nickel nanoparticles for the production of hydrogen from water splitting.

The promising approach to enhance the hydrogen evolution reaction (HER) is to use electrocatalysts based on nanoparticles that have a large electrochemically active area. In particular, the nickel nanoparticles are widely used for hydrogen evolution reaction in alkaline media, as they are highly active, stable and earth-abundant. On the other hand, the well-known method for acceleration the reaction kinetics is based on the increasing of the working temperature in the electrochemical cell [1–4]. The combination of both features may serve as a key for efficient hydrogen production.

As it was discussed in chapter 1, photoactive catalyst with the resonance in the visible light range is of special interest for the solar light assisted applications. However, nickel nanoparticles of various sizes are often reported to have a plasmonic peak in the UV part of the spectrum [5,6]. On the other hand, it was mentioned in chapter 1 that the shape of the nanoparticles drastically affects their optical properties. According to the previous experimental and theoretical studies, the most pronounced light absorption in the visible range is due to the plasmon resonance at the nickel nanoparticles that happens when they exhibit a specific morphology [7–9]. The most common shapes of Ni nanoparticles that can be found in the literature are disks, stars and rods [10–12]. However, there is a big difficulty in the synthesis of Ni NPs with a complex morphology due to their easy spontaneous oxidation.

Wetness impregnation method, described in this section is a robust and facile approach, when comparing to the soft chemistry methods. The shape of the nanoparticles is determined by the pore shape of the mesoporous template and does not depend on the subtle reaction conditions. Using of the SBA-15 mesoporous silica allows to obtain elongated nickel nanoparticles, defined by the shape of the pores of the template. The synthesis procedure is described in the section 3.2, as well as the experimental setup for photoelectrochemical characterization of the catalyst. The characterization techniques used in this chapter are the same as in the chapter 2 and are described in the section 2.2.4.

Section 3.3 is focused on the characterization of the synthesized nanoparticles to investigate their morphology, optical and photothermal properties. The effects of solar irradiation on the plasmonic Ni-based electrode are investigated using a heating-cooling cycle under dark and light conditions and discussed in section 3.4.

Then, the light pulses were applied under galvanostatic conditions in order to study transient processes of the electrochemical behavior, and the shape of the overpotential response curve was analyzed in the several time spans. Variation of light intensity and illumination range were used to delve into the study of the photothermal response. Based on the transient characterization analysis, a mechanism of photothermally enhanced HER is proposed and discussed (section 3.5). Section 3.6 is dedicated to determining optimal electrochemical parameters to observe the strongest response of the system to the solar irradiation, and to evaluating the boost of the HER under corresponding conditions. Lastly, conclusions of the chapter 3 were made in section 3.7.

## 3.2. Experimental methods

### 3.2.1. Synthesis of the Ni/SBA-15 nanoparticles

In order to obtain elongated Ni nanoparticles, mesoporous SBA-15 silica template was synthesized as reported in section 2.2.1.1, dried at 85°C in vacuum and infiltrated by a highly concentrated nickel nitrate solution (6.7 M). 1.25 ml of 6.7 M  $\text{Ni}(\text{NO}_3)_2 \cdot 6\text{H}_2\text{O}$  solution was added dropwise to 0.55 g of SBA-15 powder. The impregnated matrix was dried in a rotary evaporator in vacuum conditions at 75°C during 2 h and 95°C during 1 h. Then, the powder was calcined at 550°C for 4 h to obtain crystalline NiO inside of the ordered mesoporous silica template. In order to preserve the elongated morphology of the catalyst, NiO was reduced under a flow of 5%  $\text{H}_2/\text{Ar}$  (150 ml  $\text{min}^{-1}$ ) at 450°C for 5 h inside of the SBA-15 matrix. After reduction, silica template was dissolved by washing the powder in 5% (w.t.) hydrofluoric acid in order to avoid the re-oxidation of nickel. The synthesis process is depicted in Figure 3.1.

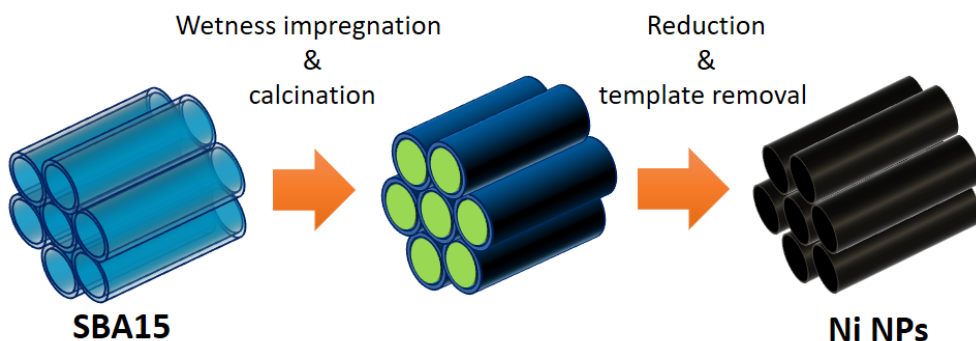


Figure 3.1. Scheme of the Ni NPs wetness impregnation synthesis.

### 3.2.2. Electrode preparation

In order to evaluate photothermal and photoelectrocatalytic properties of the synthesized material, we have deposited the Ni nanoparticles over the transparent conducting FTO substrate by drop casting 2.5 mg of Ni nanopowder on the 1 cm × 1 cm FTO plate. As references, we used commercial Ni nanoparticles (65 nm, Nanografi), deposited on the FTO in the similar manner, a piece of nickel foil and a bare FTO substrate.

### 3.2.2. Photoelectrochemical characterization setup

Electrochemical characterization was performed in a three-electrode system with a quartz cell with 80 ml of 1 M KOH electrolyte using a Hg/HgO reference electrode ( $E^0 = 0.098$  V vs. RHE) and Pt mesh as a counter electrode. The electrochemical measurements were performed using a BioLogic VMP-300 potentiostat. Potentiostatic electrochemical impedance spectroscopy was obtained by scanning from 1 MHz to 1 Hz with amplitude of 10 mV.

A 300 W solar simulator (Xe lamp, AM1.5 G filter) with a variable illumination power was applied as a source of solar illumination. The power density was measured by a laser powermeter (Gentec-EO UNO) containing a calibrated reference silicon cell. Bandpass filters (FGL400S, FGS900S, ThorLabs) were introduced to the system to cut out a part of the spectrum. The temperature data of the catalyst in air were obtained using a thermal camera FLIR One Pro, while the temperature of the electrolyte in the cell was measured *in-situ* using a K-type thermocouple, located 2 cm away from the working electrode. The temperature-dependent measurements were performed by placing of the electrochemical cell on the hot plate with constant stirring. The full scheme of the setup is depicted on the Figure 3.2.

The transient response overpotential curves were measured under galvanostatic conditions using chopped solar illumination with duration of the pulses equal to 12s or 40s.

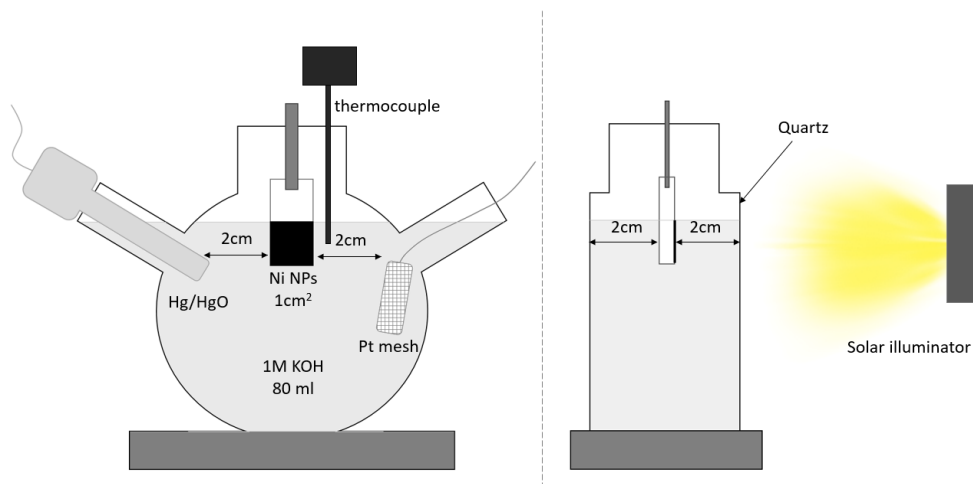


**Figure 3.2.** Scheme of the electrochemical cell used for photoelectrochemical characterization (front and side view).

### 3.3. Characterization of the plasmonic Ni/SBA-15 nanoparticles

#### 3.3.1. Physicochemical characterization

After reducing the NiO powder and removing the silica template, the obtained Ni nanoparticles appeared to have mixed morphology, containing both big Ni particles (50-200nm) and bunches of elongated Ni nanorods ( $\approx 10 \times 100 \text{ nm}$ ), corresponding to the reciprocal structure of the SBA-15 template (Figure 3.3, Figure 3.4(a)).

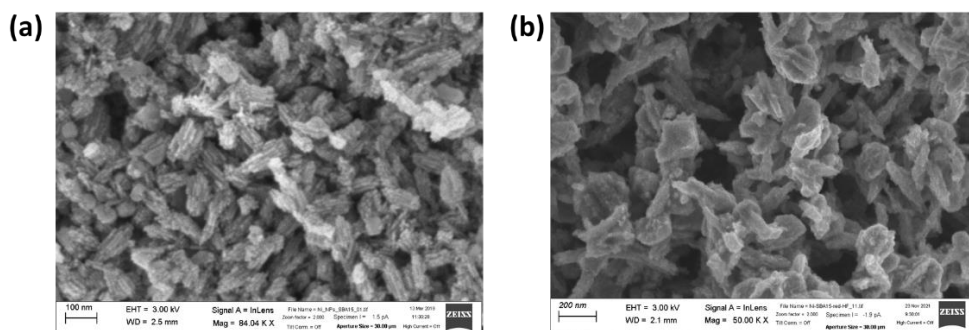


**Figure 3.3.** SEM images of (a) as-calcined NiO and (b) reduced Ni catalyst.

XRD characterization has shown that the synthesized Ni nanoparticles possess a highly crystalline structure, which can be indexed as a cubic phase (JCPDS-00-001-1260), with the (111) plane most pronounced (Appendix, Figure B.1.1). The UV-vis absorption spectrum of the synthesized particles shows a peak at 280 nm (Figure 3.4(b)), corresponding to the interband transition in Ni, and a broad band in the visible range, attributed to a plasmonic mode.

Yu *et al.* [13] have developed an analytical model, which describes the shape-dependent optical response of plasmonic nanoparticles. It consists in a strict solution of Maxwell's equations in an extended electrostatic limit with incorporated retardation corrections due to the finite size of the particle. In order to simulate the optical response (extinction spectra, plasmon frequency, scattering cross-sections etc.) the model uses complex dielectric permittivity of the material and a small set of parameters, tabulated for each individual morphology. We have applied this model, implemented in a widget [14], to the most representative shapes and sizes of the synthesized Ni nanoparticles, and extracted their corresponding extinction spectra. As it can be seen from Figure 3.4, the position of the plasmonic peak drastically depends on the aspect ratio of the nanoparticles. Due to a large distribution of sizes and proportions of the Ni nanoparticles in the synthesized

catalyst, the plasmonic peaks are overlaid in the visible range, justifying the experimentally measured broad absorption band.

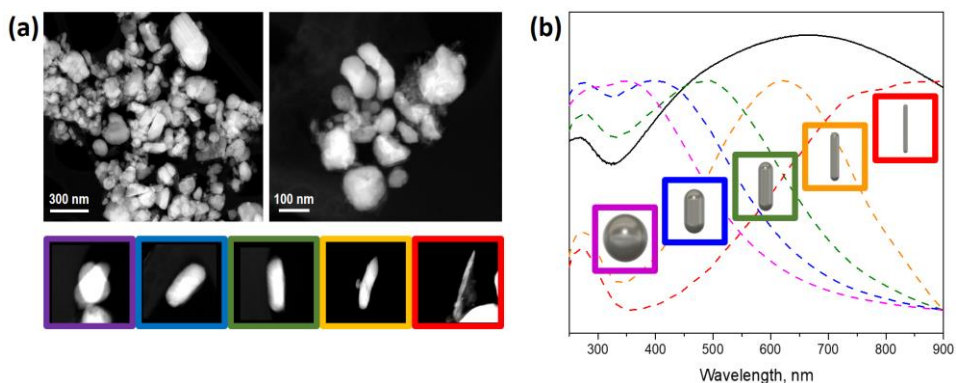


**Figure 3.4.** (a) HAADF-STEM images of reduced Ni catalyst. The most representative shapes of the elongated Ni nanoparticles are shown in the colored boxes; (b) UV-vis extinction spectrum of the Ni plasmonic catalyst and simulated extinction spectra of 100nm Ni nanoparticles with different aspect ratio: from 1:1 to 1:10.

### 3.3.2. Photothermal characterization of the Ni nanoparticles

The temperature of the samples was measured after 5 minutes of exposure to the concentrated solar light illumination in air (Figure 3.5). Due to direct heating of the material by infrared waves of the solar light, a bare FTO substrate, as well as a piece of Ni foil undergoes a temperature increase in the range of 10-15°C. However, the temperature of the substrate, decorated by synthesized Ni nanoparticles increases up to 93°C, thus showing remarkable photothermal properties. It is worth noting, that, despite the similar average size and apparent color of commercial Ni nanoparticles, they heat up only to 72°C, which can be explained by the absence of the strong plasmonic absorption of the nanoparticles in the visible range in comparison with the elongated Ni nanoparticles, discussed in this chapter.

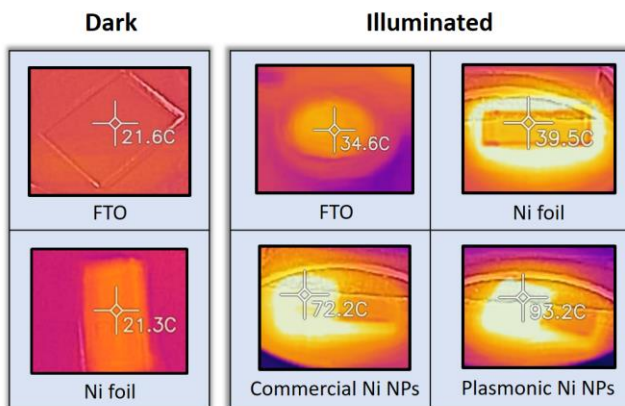


**Figure 3.5.** IR-camera measured temperature of different samples under dark conditions and under solar light irradiation ( $0.5 \text{ W cm}^{-2}$ ) during 5 minutes.

When immersed in the electrolyte, the illuminated nanoparticles start to dissipate the formed heat to the surrounding media, thus increasing the temperature of the electrolyte. In Figure 3.6 it can be seen that after 40 minutes of constant illumination of the Ni/SBA-15 electrode under 5 sun power density, the electrolyte temperature reaches  $48^\circ\text{C}$ , while the bare FTO substrate can heat the cell only up to  $38^\circ\text{C}$ . Assuming similar mass to be heated and similar specific heat coefficient, this behavior points out that in the case of the Ni nanoparticles-decorated electrode there is almost a 60% more absorption of energy compared to a bare FTO.

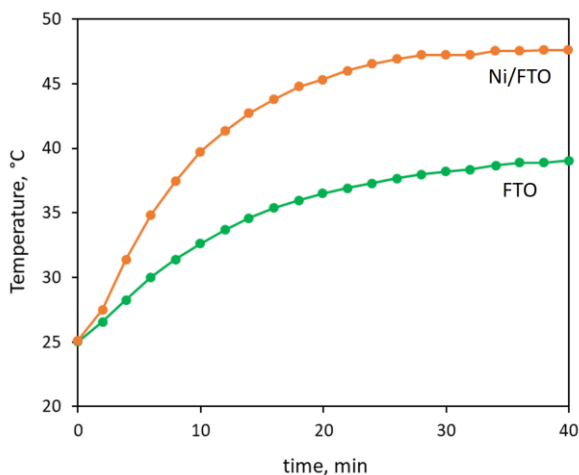


**Figure 3.6.** Temperature of the electrolyte depending on the illumination time for bare FTO substrate and Ni/FTO electrode (power density was fixed to  $0.5 \text{ W cm}^{-2}$ ).



### 3.4. Photothermal effects on HER

To study the effect caused by the visible light absorption of the Ni nanoparticles on their electrochemical properties, we performed a set of experiments under concentrated solar illumination. First of all, among the experiments carried out, it is necessary to distinguish between:

- i) No irradiation: Experiments carried out in the dark by applying an external heating system using a hot plate;
- ii) Constant irradiation: Experiments carried out under solar illumination, using the energy of photons absorbed by the nickel nanoparticles as a source of heat;
- iii) Pulsed irradiation: Experiments under the application of chopped illumination to be able to study the transient effects.

We have started by comparing the behavior of the electrode overpotential under external heating without irradiation with the corresponding behavior under constant solar irradiation. In order to see the difference between the light-induced heating from the conventional heating of the cell, we have performed a heating-cooling cycle for the both approaches.

In the first case we were controlling the temperature of the cell by a conventional hot plate, taking the values of the electrolyte temperature and corresponding working potential. In the other cases we have performed the same measurement, but now the heating of the system was induced by the illumination of the electrode. For all these measurements, the temperature of the electrolyte was recorded with the thermocouple immersed in the electrolyte. The cooling was natural although accelerated by applying an ice bath. As it can be seen from Figure 3.7(a), the rate of temperature variation obtained under applied experimental conditions is very similar in both cases at least during the first 15 °C of the heating process. With time, the rate becomes different due to the stabilization of the final temperature value in the case of heating obtained under irradiation. Similar behavior is seen for the cooling process.

As it can be seen from Figure 3.7(b), in the dark conditions, the working potential of the electrode linearly depends on the temperature of the electrolyte. However, when the sample is illuminated with no external heating applied, the working potential is having a hysteresis-like behavior on the measured electrolyte temperature. During the first seconds, the working potential is undergoing a jump, while the further illumination results in a linear overpotential shift, like in the case

without irradiation. Similar process is happening when the illumination is turned off: the working potential value drops drastically, although the cell temperature is changing only a few degrees. Under further cooling, the overpotential values return back to their original ones, following the same cooling branch, as the during the first case.

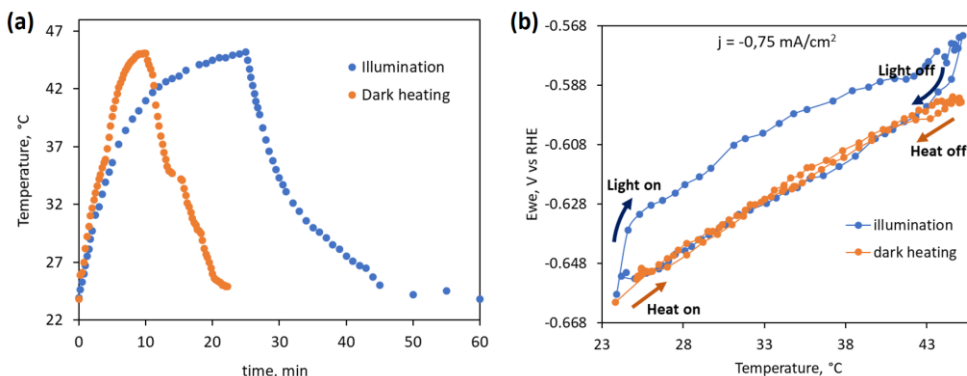


**Figure 3.7.** (a) Electrolyte temperature dependence with time and (b) variation of the electrode working potential under galvanostatic conditions ( $j = -0.75 \text{ mA cm}^{-2}$ ) on the change of the temperature, caused by conventional heating (orange) and photothermal effect (blue).

The obtained results prove the importance of the local plasmonic effects in the nickel nanoparticles and shows the clear difference of the light-induced heating over conventional one. At room temperature, a thermal equilibrium is established at the nickel/electrolyte interface. When the cell is heated by the hot plate, the electrolyte temperature is averaged due to stirring, and as the electrolyte temperature is raised slowly, the nickel/electrolyte interface is reaching a thermal equilibrium in every moment of time. Therefore, the temperature increase is, as expected, enhancing the reaction kinetics according to the law of chemical reaction controlled by an energy barrier,  $\sim \exp(-E_{\text{barrier}}/kT)$ . Accordingly, the working potential of the electrode is linearly depending on the temperature as can be seen from the following equation [15]:

$$E = E^0 + \frac{\Delta S}{nF}(T - T_0) - \frac{RT}{nF} \ln \left( \frac{a(\text{H}_2)a(\text{O}_2)^{1/2}}{a(\text{H}_2\text{O})} \right) \quad (3.1)$$

On the contrary, in the case of the irradiation, the initial behavior is totally different. In the beginning, there is a sudden variation in the overpotential corresponding to a decrease of the charge transfer resistance. When the photons are absorbed by

plasmonic Ni nanoparticles, the excited plasmons are efficiently damped due to high losses in nickel as a consequence of its optical properties, resulting in strong local heating in the timescale of under 10 ns. This leads to thermalized electrons being more susceptible to be transferred from the hot electrode surface to the adsorbates, stimulating the reaction. The ionic subsystem of the nickel/electrolyte interface is, however, reacting slower to the photon-induced heating, leading to prevalence of the adsorption processes over desorption. As the irradiation continues, the heat from the electrode is slowly diffused to the electrolyte, thus gradually increasing the nickel/electrolyte temperature, resulting in the linear shift of the overpotential, similar to the conventional heating case. As the irradiation is switched off, the nickel nanoparticles are rapidly cooled down and their electrons quickly come into balance with the electrode, while the ions react with delay [16]. The disturbed equilibrium at the nickel/electrolyte interface is reflected in the drastic rise of the overpotential after switching the light off, indicating the prevailing of the desorption processes over adsorption. In a while, the electrolyte comes into a new thermal balance with the electrode, which is gradually altered with time as the cell is cooled down. This is followed by a linear shift of the working potential, as the electrochemical reaction after the first seconds is being controlled solely by the thermal equilibrium at the nickel/electrolyte interface. Therefore, the orange and blue curves coincide in the cooling part of the cycle. So, the significant and relevant change in the overpotential in the first moments of illumination, leading to more efficient hydrogen production, can be explained by interaction of photons with plasmonic Ni nanoparticles which give rise to a significant difference between the catalyst surface temperature and the electrolyte bulk one. The non-equilibrium state of the electrode results in the availability of the thermally excited electrons, enhancing the hydrogen evolution reaction.

### 3.5. Mechanism of photothermal HER enhancement

#### 3.5.1. Pulsed illumination

As it has been seen from Figure 3.7, constant illumination leads to strong heating of the cell, which can mask the effects, directly happening at the catalyst surface. To avoid the overall heating, and study the mechanism of reaction enhancement, we have applied pulsed illumination, with duration of the pulses equal to 12 s, to the photoelectrochemical cell in both potentiostatic and galvanostatic conditions.

In order to be able to detect the reaction kinetics, it is important to consider working at relatively low current densities, corresponding to a low reaction rate. This way, the mechanisms, originated from the plasmonic properties of nickel nanoparticles, are less masked by the initially high activity of the electrode.

The typical shape of the overpotential variation under chopped illumination of 12 s is shown in the Figure 3.8(a). After switching the light on, the response can be separated into three stages: rapid decrease of the overpotential (1), followed by a deceleration zone (2), and a quasi-linear region (3) (Figure 3.8(b)).

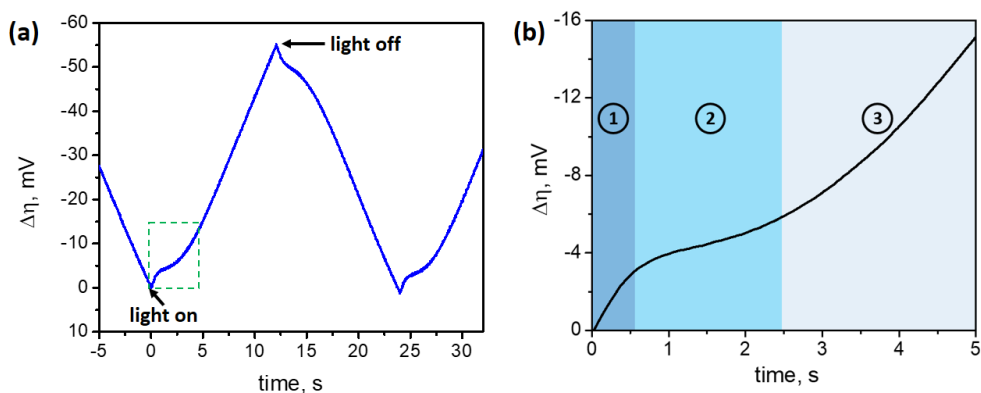


**Figure 3.8.** (a) Typical shape of the 12 s light pulse induced working potential variation. The zoomed-in part of the curve highlighted by a dashed green rectangle is shown on (b).

The application of chopped illumination allowed us to analyze the influence of the light power on the overpotential variation. The response strongly depends on the power density of the incident light in a non-linear manner, as shown in the Figure 3.9(a). According to the previous studies [18], the exponential dependence of the electrochemical response to the intensity of the illumination points out a photothermal nature of the observed enhancement. We also studied the effect of the incident illumination spectral range on the overpotential variation. Figure 3.9(b)

shows that illuminating the electrode with infrared light has little influence on the reaction rate. Moreover, absence of UV illumination does not significantly affect the intensity of the pulse variation, making visible range the key contributor to the studied effect.

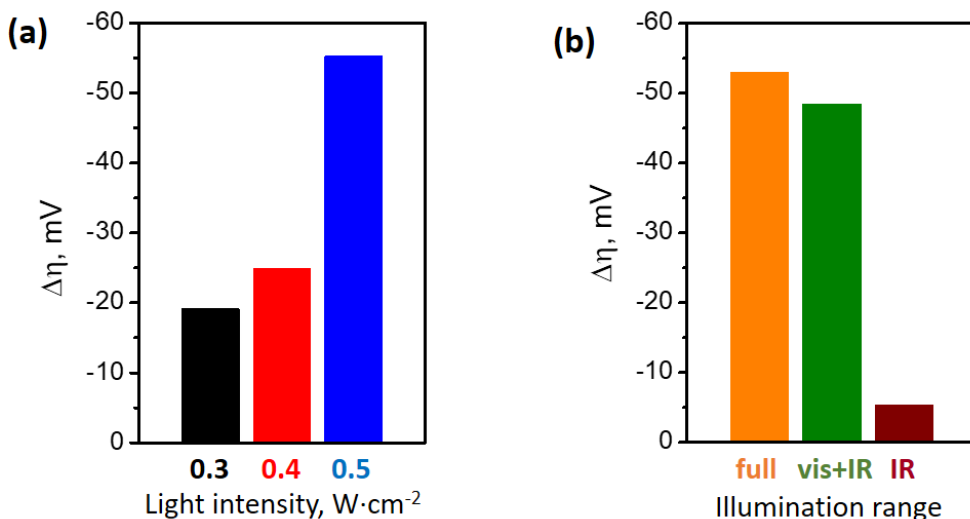


**Figure 3.9.** Peak overpotential variation value under the 12 s light pulses depending (a) on the light intensity; (b) on the illumination range. The latter values were corrected on the transmittance of the filters used to cut the light range.

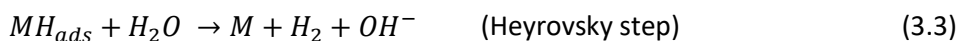
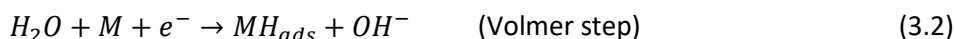
One of the problems in the photoelectrocatalytic materials with the application in electrochemical reactions is formation of gas bubbles as a result of the reaction, which cause the scattering of the light and, thus, impede the proper illumination of the catalyst surface. One of the ways to avoid this problem in order to correctly characterize the effect of light on the studied material is the use of a transparent conducting substrate, such as FTO. Despite the strong absorption in the UV region, the FTO is highly transparent in the visible and IR range. Nevertheless, to account for the possible impact of UV light we have also performed the same tests using both front and back illumination. The results reveal no significant effect of UV photons on the electrochemical response and are shown in the Figure B.1.3.

Another way to analyze the shape of the overpotential response to illumination is to plot the derivative of the overpotential with time (Figure B.1.4). As it can be seen, a high value of the overpotential derivative is followed by a minimum and a lower constant value. It points out the three main stages in the electrochemical response of the electrode to the illumination, as was earlier shown in the Figure 3.8(b).

Electrochemical impedance spectroscopy (EIS) was conducted in order to investigate the photothermally enhanced electrochemical behavior of the Ni electrode upon solar irradiation. The EIS curves and the corresponding fitting in dark and light conditions are shown in the Figure B.1.5. The illuminated sample exhibits much smaller charge transfer resistance, which points out faster charge transfer between the nickel electrode and adsorbates on its surface, owed to the thermalized electrons as the result of plasmonic heating. The exposure to solar light also affects the LSV of the electrode, shifting the HER branch to lower overpotentials (Figure B.1.6).

### 3.5.2. Mechanism

In the alkaline conditions the HER is usually described by Volmer-Heyrovsky-Tafel mechanism and can be written down using the following equations [19]:



It should be noted, that Heyrovsky and Tafel processes can take place simultaneously, however they both require adsorption of hydrogen atoms through Volmer mechanism. It has also been reported, that both Heyrovsky and Tafel processes are considered to be the rate-limiting steps in the hydrogen evolution reaction [20]. However, under very low current densities, the electron transfer is slow and can become the limiting process in the overall hydrogen evolution reaction, leading to Volmer step being the rate-determining one [21,22]. Thus, when the catalyst is illuminated, the photons are immediately absorbed by plasmonic Ni nanoparticles, and excite the plasmon, which is transformed into heat due to strong damping mechanisms during the characteristic times  $\tau < 10$  ns. The electron subsystem then almost immediately comes into balance with the hot Ni nanoparticles, resulting in thermalized electrons, which efficiently participate in dissociation of the water molecules and adsorption of H atoms, disturbing the equilibrium at the nickel/electrolyte interface towards adsorption predominance (stage 1). As the electron transfer is no more limiting the reaction, the hydrogen desorption becomes the rate-determining step. This results in a non-equilibrium concentration of the H atoms on the catalyst surface, followed by the deceleration stage in the overpotential response curve (stage 2). However, with time the thermal diffusion from the electrode to the electrolyte takes place, leading to a new balance

between the electronic and ionic subsystems, which results in the linear shift of the overpotential controlled by the new nickel/electrolyte interface equilibrium (stage 3). The corresponding mechanism is schematically depicted in Figure 3.10.

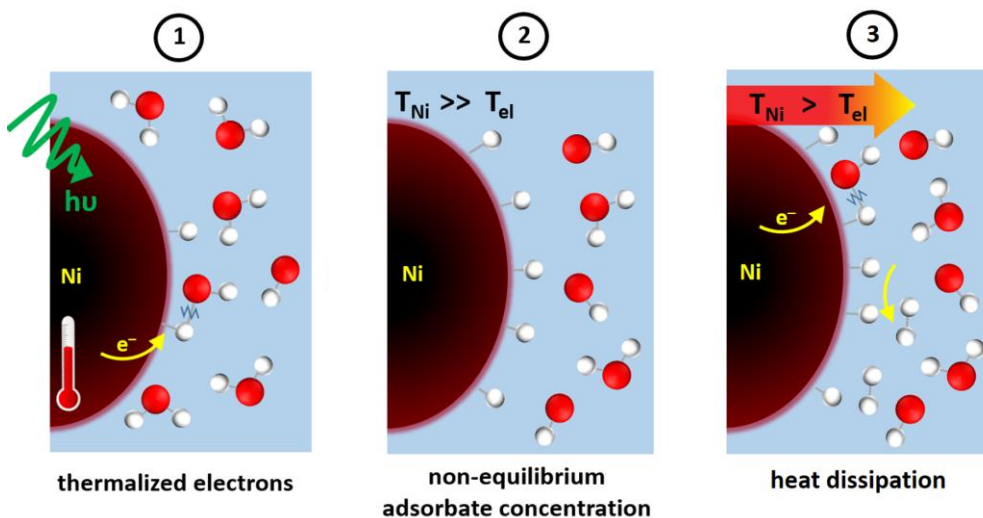


**Figure 3.10.** Schematic description of the overpotential response to the pulsed illumination. At the stage (1) the thermalized electrons of the plasmonic Ni nanoparticles are efficiently used in the dissociation of water molecules and adsorption of H atoms. During stage (2) the H atoms are not yet desorbed as hydrogen molecules, blocking the active sites for the reaction. At stage (3) the heat is dissipated to the electrolyte, resulting in a new nickel/electrolyte equilibrium.

The suggested mechanism can be summarized as follows. When the photons are absorbed by the Ni plasmonic nanoparticles, the generated plasmon is quickly damped and transformed into heat during the period of time which is below the detection limit of the potentiostat. The localized increase of temperature is breaking the thermal balance on the catalyst surface, and is resulting in a non-equilibrium occupation of the surface states by adsorbed hydrogen atoms. After a certain time, due to the heat diffusion processes from the electrode to the electrolyte, a new nickel/electrolyte equilibrium is reached, which is gradually changed while the illumination is on.

### 3.6. Evaluation of the HER enhancement

In addition to the selection of the excitation spectral range and the energy density, it is necessary to select the optimal operating point ( $J$ ,  $V$ ) of the electrode. Taking into account the relationship between intensity and overpotential, at low current values the overpotential variations will be small as it is proportional to the current value. However, at large current values, the variation of the overpotential is also smaller, as the number of thermalized electrons due to local temperature increase is insignificant compared to the total number of electrons with energy enough to overcome the reaction barrier. In other words, the additional effect from plasmonic heating of the Ni nanoparticles is masked by the initially large current values. This allowed us to find the optimal current density that corresponds to the highest overpotential response, which according to the experimental results shown in Figure 3.11 is equal to  $-0.15 \text{ mA cm}^{-2}$ .

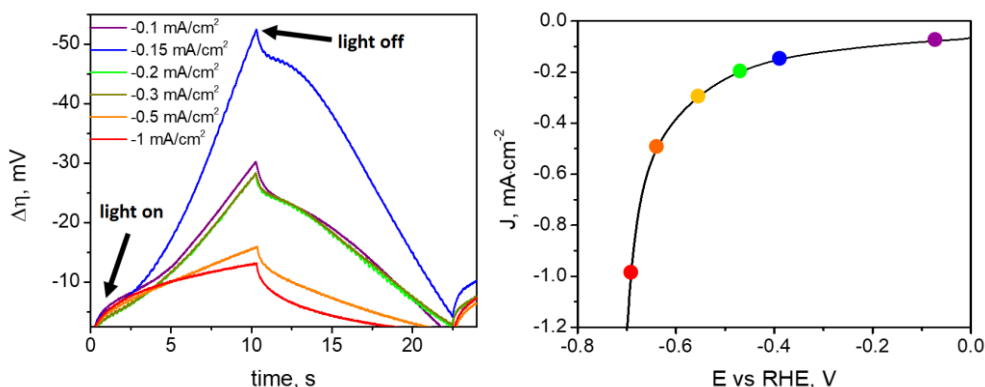


**Figure 3.11.** Left: change of the overpotential under short light pulses (12s) depending on the applied current density (light intensity  $0.5 \text{ W cm}^{-2}$ ; right: corresponding current densities marked on LSV.

Moreover, as current density increases, the three-stage response to irradiation disappears. This is explained by a more facile electron transfer from the electrode to the adsorbates due to higher working potentials. At low current densities the reaction is mostly controlled by the electron transfer from the electrode to the adsorbates. In this case, a strong photothermal response of Ni nanoparticles to illumination, which results in non-equilibrium surface hydrogen due to thermalized electrons, is clearly seen on the response curve, as the reaction is relatively slow. However, at high current densities, and, correspondingly, at high overpotentials, the reaction rate is higher, as more electrons have enough energy to overcome the reaction barrier. For this reason, the light-induced changes in the electron subsystem, i.e. the contribution of the thermalized electrons to the adsorption



process, which causes the three-stage response curve at low current densities, is too insignificant relative to the high current density value and cannot be detected by the measurement system, resulting in a simple exponential response.

After finding the optimal conditions, by increasing the light pulse up to 40 s we were able to reduce the overpotential of the cell by 185 mV without overall heating of the cell (Figure 3.12(a)). The temperature variation of the bulk electrolyte was less than 3 K during every pulse, which is not negligible, but too small to be responsible for such a strong change in the overpotential. It proves that the local heating of the electrode plays the key role in reducing of the overpotential, compared to the overall heating of the electrolyte.

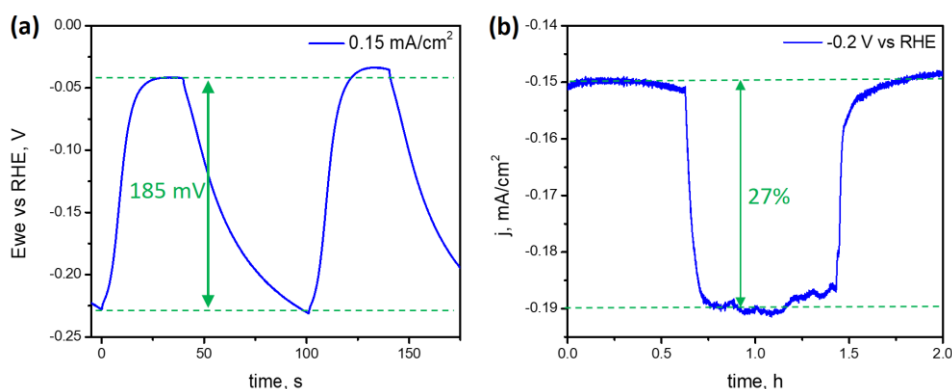


**Figure 3.12.** (a) Change in the working potential under 40s light pulses with 60s relaxation time ( $I = -0.15 \text{ mA cm}^{-2}$ ); (b) Change in the cathodic current under solar light illumination for 50 min ( $E_{we} = -0.2 \text{ V vs. RHE}$ ). Light intensity in both cases is equal to  $0.5 \text{ W cm}^{-2}$ .

Moreover, we studied the static illumination effect on the Ni electrode by applying constant solar irradiation under potentiostatic conditions until the stabilization of the current density value. We applied the working potential  $E_w = -0.2 \text{ V vs. RHE}$ , as the one corresponding to the optimal current density ( $0.15 \text{ mA cm}^{-2}$ ). In less than 8 minutes the increase in the current density value reached 27%, which in average was maintained until the illumination was off (Figure 3.12(b)). Temperature variation in this case was 21 K. Provided the input conditions, electrolyte and working potentials, hydrogen evolution reaction is the only reaction happening in the cell. Therefore, increase in the current density is directly proportional to the increase in the hydrogen production under solar light illumination.

### 3.7. Conclusions

We have proved that plasmonic Ni nanoparticles exhibit a photothermal effect under solar light illumination due to their strong absorption in the visible range. Illumination of the catalyst under cathodic potentiostatic conditions allowed us to improve the reaction rate of hydrogen evolution reaction, which is followed by a 27% enhancement in the hydrogen gas production. On the other side, by applying galvanostatic conditions to the electrode we were able to decrease the overpotential needed for the hydrogen formation.

A set of experiments, including conventional heating, constant and pulsed illumination, has allowed us to investigate the mechanism of the HER enhancement under low current densities. We have distinguished two main processes, related to enhanced electron transfer due to strong plasmonic heating, and to the thermal diffusion from the electrode to the electrolyte. After beginning of the illumination, the adsorbed photons are immediately (under the timescale of 100 ps-10 ns) relaxed to phonons, i.e. to the heating of the nanoparticles. The electron subsystem is quickly reacting to the new temperature state, resulting in thermalized electrons, which are used to dissociate water molecules and adsorb hydrogen atoms. This results in a non-equilibrium concentration of the hydrogen atoms, slowing the reaction down. After 1-2 s heat diffusion takes place, leading to the reaction fully controlled by the nickel/electrolyte temperature.

Based on the obtained results, we have shown that the illumination of the nanostructured nickel catalyst with solar light can lead to the enhanced HER rate, and, as a result, to improved hydrogen production. We expect the LSPR photothermal approach to pave way to a more efficient photoelectrochemical water splitting process, taking advantage of visible and near-IR illumination.

### 3.8. References

- [1] B. Pierozynski and T. Mikolajczyk, *On the Temperature Dependence of Hydrogen Evolution Reaction at Nickel Foam and Pd-Modified Nickel Foam Catalysts*, *Electrocatalysis* **6**, 51 (2014).
- [2] N. M. Marković, B. N. Grgur, and P. N. Ross, *Temperature-Dependent Hydrogen Electrochemistry on Platinum Low-Index Single-Crystal Surfaces in Acid Solutions*, *J. Phys. Chem. B* **101**, 5405 (1997).
- [3] T. J. Schmidt, P. N. Ross, and N. M. Markovic, *Temperature Dependent Surface Electrochemistry on Pt Single Crystals in Alkaline Electrolytes: Part 2. The Hydrogen Evolution/Oxidation Reaction*, *J. Electroanal. Chem.* **524–525**, 252 (2002).
- [4] A. R. Madram, A. F. Zonouz, and H. R. Pouretedal, *Effect of Temperature on Kinetics of the Hydrogen Evolution Reaction on Ni-P-C Cathodes in Alkaline Solution*, *Iran. J. Hydrog. Fuel Cell* **4**, 215 (2015).
- [5] S. Schuermans, T. Maurer, J. Martin, J.-B. Moussy, and J. Plain, *Plasmon / Interband Transitions Coupling in the UV from Large Scale Nanostructured Ni Films*, *Opt. Mater. Express* **7**, 1787 (2017).
- [6] V. Sharma, C. Chotia, Tarachand, V. Ganesan, and G. S. Okram, *Influence of Particle Size and Dielectric Environment on the Dispersion Behaviour and Surface Plasmon in Nickel Nanoparticles*, *Phys. Chem. Chem. Phys.* **19**, 14096 (2017).
- [7] J. Chen, P. Albella, Z. Pirzadeh, P. Alonso-González, F. Huth, S. Bonetti, V. Bonanni, J. Åkerman, J. Nogués, P. Vavassori, A. Dmitriev, J. Aizpurua, and R. Hillenbrand, *Plasmonic Nickel Nanoantennas*, *Small* **7**, 2341 (2011).
- [8] G. E. Jonsson, V. Miljkovic, and A. Dmitriev, *Nanoplasmon-Enabled Macroscopic Thermal Management*, *Sci. Rep.* **4**, 5111 (2014).
- [9] D. A. Perry, R. L. Borchers, J. W. Golden, A. R. Owen, A. S. Price, W. A. Henry, F. Watanabe, and A. S. Biris, *Surface-Enhanced Infrared Absorption on Elongated Nickel Nanostructures*, *J. Phys. Chem. Lett.* **4**, 3945 (2013).
- [10] Z. Libor and Q. Zhang, *The Synthesis of Nickel Nanoparticles with Controlled Morphology and SiO<sub>2</sub>/Ni Core-Shell Structures*, *Mater. Chem. Phys.* **114**, 902 (2009).
- [11] E. A. Kwizera, E. Chaffin, X. Shen, J. Chen, Q. Zou, Z. Wu, Z. Gai, S. Bhana, R. Oconnor, L. Wang, H. Adhikari, S. R. Mishra, Y. Wang, and X. Huang, *Size- and Shape-Controlled Synthesis and Properties of Magnetic-Plasmonic Core-Shell Nanoparticles*, *J. Phys. Chem. C* **120**, 10530 (2016).
- [12] C. Kim, C. Kim, K. Lee, and H. Lee, *Shaped Ni Nanoparticles with an Unconventional Hcp Crystalline Structure*, *Chem. Commun.* **50**, 6353 (2014).
- [13] R. Yu, L. M. Liz-Marzán, and F. J. García De Abajo, *Universal Analytical Modeling of Plasmonic Nanoparticles*, *Chem. Soc. Rev.* **46**, 6710 (2017).
- [14] F. J. Garcia de Abajo, *Extinction, Elastic-Scattering, and Absorption Cross-Sections for Selected Nanoparticle Morphologies*, <http://widgets.nanophotonics.es/nanoplasmons/index.html>.
- [15] R. O'Hayre, S.-W. Cha, W. Colella, and F. B. Prinz, *Fuel Cell Fundamentals*, 3rd ed. (Wiley, New Jersey, 2016).

- [16] V. Golovanov and V. Smytyna, *Interaction between Collective and Local Subsystems in Semiconductor Surface-Active Structures*, *Sensors Actuators B. Chem.* **25**, 647 (1995).
- [17] G. Baffou, I. Bordacchini, A. Baldi, and R. Quidant, *Simple Experimental Procedures to Distinguish Photothermal from Hot-Carrier Processes in Plasmonics*, *Light Sci. Appl.* **9**, (2020).
- [18] N. Krstajić, M. Popović, B. Grgur, M. Vojnović, and D. Šepa, *On the Kinetics of the Hydrogen Evolution Reaction on Nickel in Alkaline Solution - Part I. The Mechanism*, *J. Electroanal. Chem.* **512**, 16 (2001).
- [19] N. M. Marković, S. T. Sarraf, H. A. Gasteiger, and P. N. Ross, *Hydrogen Electrochemistry on Platinum Low-Index Single-Crystal Surfaces in Alkaline Solution*, *J. Chem. Soc. Faraday Trans.* **92**, 3719 (1996).
- [20] S. Bajracharya, A. ElMekawy, S. Srikanth, and D. Pant, *Cathodes for Microbial Fuel Cells*, in *Microbial Electrochemical and Fuel Cells: Fundamentals and Applications* (Elsevier Ltd., 2016), pp. 179–213.
- [21] K. Zeng and D. Zhang, *Recent Progress in Alkaline Water Electrolysis for Hydrogen Production and Applications*, *Prog. Energy Combust. Sci.* **36**, 307 (2010).



## **Chapter 4**

# **Nanostructured plasmonic nickel films for electrochemical applications**

The results presented in chapter 4 were obtained in collaboration with the SOC&SAM group of University of Barcelona and Organic Nanostructured Photovoltaics group at ICFO.

## 4.1. Introduction

An electromagnetic phenomenon, called surface plasmon polariton (SPP) can be observed at the interface between a thin metallic film and a dielectric when illuminated with light of a resonant wavelength. However, SPP can only be excited when the momentum of light is matching the longitudinal oscillations at the interface, which can be achieved by modifying the incident light by a Kretschmann configuration [1] or introducing a two-dimensional grating on the metallic film [2]. In case of thin films, the grating is turned into a periodically perforated metallic film, which is also commonly referred to as nanohole array (NHA).

Usually, the highly ordered metallic nanohole structures are obtained by means of photolithography techniques, which are expensive and problematic to scale up [3,4]. However, some alternative less costly methods have been proposed [5]. Out of them, the nanosphere lithography (NSL) is the most appealing approach due to its flexibility, simplicity and, most importantly, possibility of tuning the geometrical parameters without the need of fabricating a new expensive mask [6–9]. This method consists in the self-assembly of polystyrene (PS) or silica nanospheres into a sacrificial hexagonal closed pack (HCP) monolayer which are used as a mask during metal deposition and are removed afterwards in order to obtain a highly-ordered perforated metallic film.

Under thermodynamic equilibrium, the spherical colloid particles tend to self-assemble in ordered HCP arrays at the liquid-air interface due to the interplay of capillary forces, gravity and electrostatic interactions [10–12]. In this context, the most used approaches to obtain colloid crystals are controlled evaporation [13–15], dip-coating [16,17], spin-coating [18,19], centrifugation [20] and electrophoretic assembly [21,22]. However, these methods operate a significant number of parameters, which require a thorough optimization: temperature, humidity, colloid concentration, deposition speed, etc. The need to control many parameters at the same time leads to poor reproducibility of the self-assembled films, and also to the possibility of multi-layer formation instead of a perfect monolayer. One of the simplest and highly reproducible approaches for monolayer formation is the Langmuir-Blodgett (LB) technique [23]. It has also been used in NSL, but is still not very common as it requires a specific device [24,25]. However, this technique allows to assemble and deposit monolayers of relatively high areas (in the order of  $10 \times 10 \text{ cm}^2$ ) by controlling only one parameter, being the surface tension. Moreover, using low-concentrated and well-dispersed colloids can practically guarantee the absence of multilayers in the resulting film.

The typical transmission spectra of metallic NHAs exhibit sharp minima followed by the maxima. Although in some works [26,27], the typical profile of the metallic NHA transmission spectra was attributed to the Fano resonance, being a superposition of a discrete state and a continuous background, it is widely accepted that the maxima represent the extraordinary transmission (EOT) bands and correspond to the SPP modes, while the minima are attributed to the Wood's anomalies – effect, happening due to the diffraction of the light in parallel with the surface of the NHA.

In this chapter, metallic NHAs were synthesized according to procedure described in section 4.2. The section also explores the techniques used in this chapter and the setup for photoelectrochemical characterization of the obtained NHAs, as well as theoretical background used to describe the optical features of the structures. The LB process was optimized in order to achieve well-ordered HCP monolayers of PS spheres (section 4.3). Morphology of the NHAs with tunes hole diameters for different materials (Ag and Ni) was discussed in section 4.4. The optical transmission spectra were measured and compared for the silver and nickel NHAs of several hole diameters and film thicknesses, defining the SPP bands and discussing their origin (section 4.5). The Ni NHAs were then used as photo-active cathodes, and their wavelength-resolved light-induced electrochemical response was measured and compared between NHAs with different periodicity and flat films (section 4.6). Finally, the mechanism of the reaction enhancement was discussed in section 4.7, and conclusions of chapter 4 made in section 4.8.

## 4.2. Experimental methods

### 4.2.1. Synthesis of metallic NHAs

In order to obtain the periodic array of Ni nanoholes we applied the method of masked lithography, using polystyrene (PS) spheres as a sacrificial layer which is removed after metal deposition. In this chapter, PS spheres of two different diameters, 0.46  $\mu\text{m}$  and 0.6  $\mu\text{m}$  were purchased from Sigma-Aldrich to compare different periodicity of the NHAs.

Langmuir-Blodgett technique was applied to create a self-assembled monolayer of PS spheres. A Langmuir deposition system consisted of a small trough (364  $\times$  75  $\text{mm}^2$ ) and allowed constant compression of the surface with two barriers of controllable speed. The surface pressure was measured throughout the compression with a Wilhelmy plate (1  $\times$  2  $\text{cm}^2$ ) made of filter paper. The horizontal deposition, or Langmuir-Schaefer approach, was applied using a home-made 3D printed holder (Figure 4.1). Glass microscope slides were cut into 8  $\times$  12  $\text{mm}^2$  pieces and sonicated in acetone, Milli-Q water and ethanol successively before using as a substrate.

The commercial PS spheres were diluted with  $\text{H}_2\text{O}:\text{EtOH}$  (1:1) solution, which resulted in the following concentrations: 11  $\text{g l}^{-1}$ , 22  $\text{g l}^{-1}$  and 44  $\text{g l}^{-1}$ . Despite the high polarity of ethanol and, therefore, its high ability of mixing with water, it allowed better dispersion of the beads due to their hydrophobicity, and also faster evaporation of the solvent from the trough surface than the PS spheres dispersed in 100% water.

The Langmuir process of self-assembly consisted of the following steps:

1. The trough was cleaned and filled with Milli-Q water, making sure that the level of the water exceeds the edges of the trough.
2. The glass substrate was fixed on the home-made holder for horizontal deposition and dipped under the water surface.
3. The water surface was thoroughly cleaned using a pump and a paster pipette.
4. After the surface was free of dust particles, the surface pressure was adjusted to zero, and 1.5 ml of PS spheres suspension was distributed dropwise on the surface of Milli-Q water, ensuring a good coverage of the surface.



5. The barriers were allowed to compress with the speed  $v_b=2\text{mm min}^{-1}$ , while measuring the surface pressure value.
6. At the target surface pressure, the glass plate was lifted up with a constant speed  $v_d=5\text{mm min}^{-1}$  to ensure a good film transfer to the glass substrate.

For disordered structure synthesis, the PS spheres were dispersed on the water surface in a beaker, and the film was transferred to the glass substrate by “fishing” with the help of tweezers.

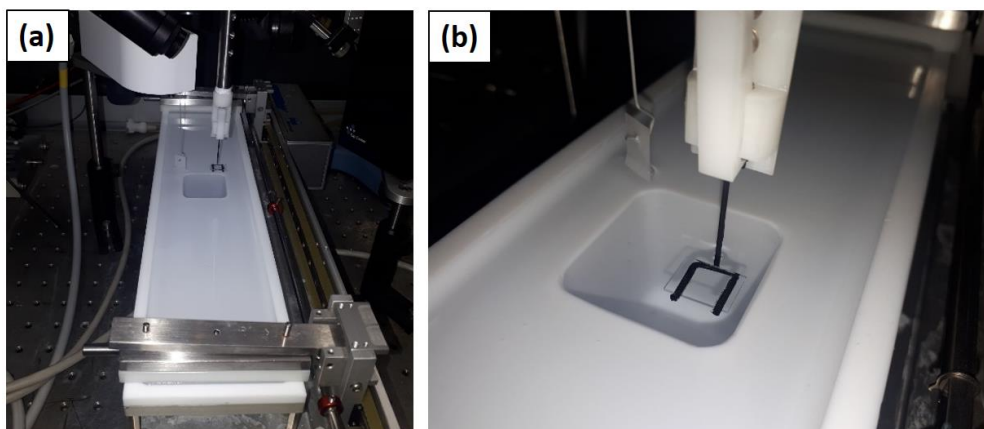


**Figure 4.1.** Photographs of the Langmuir-Blodgett setup (a) and the home-made holder for the horizontal deposition (b).

The metal NHA were obtained using the procedure depicted in the Figure 4.2. Firstly, the PS spheres monolayer film was obtained using LB approach. Secondly, the spheres were etched in the oxygen plasma atmosphere for a fixed time (5 min, 10 min and 15 min) at the  $\text{O}_2$  flow of  $15\text{ ml min}^{-1}$  using PE-50 Plasma Etch system to tune their size. Then, a metallic film of desired thickness was deposited over the prepared mask. Silver films were thermally evaporated with the rate of  $0.5\text{ \AA s}^{-1}$ , and nickel films were fabricated by magnetron sputtering (Aja International) with the rate of  $1\text{ \AA s}^{-1}$ . Finally, the PS spheres were removed from the substrate by sonication of the films in acetone for 30 min. It is worth noting, that if the diameter of the spheres was decreased to values, comparable with deposition thicknesses, the removal of the spheres was hindered because of their full coverage with the metallic layer and, therefore, poor exposure to the solvent.

The average diameter of the holes and periodicity of each NHA sample was determined as the mean value of 20 measurements from the SEM images of the samples at 30,000X magnification.

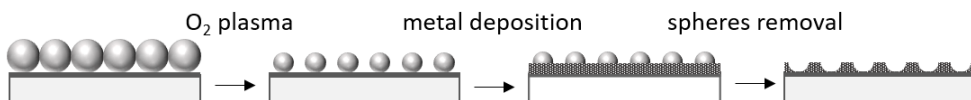


**Figure 4.2.** Scheme of the NHA synthesis.

#### 4.2.2. Photoelectrochemical and optical characterization setup

In order to study the effect of wavelength on the catalytic response of nickel nanohole arrays, we used four different laser lines with wavelengths of 400 nm, 532 nm, 633 nm and 800 nm, to which we will also refer as blue, green, red and IR lines, respectively.

Laser spot area depended on the laser wavelength, and the area of the sample was limited to the smallest laser spot out of all the available lines: 0.5 mm<sup>2</sup> (633 nm red line). The spot areas of other lines were equalized to 0.5 mm<sup>2</sup> by introducing of an iris diaphragm between the laser source and the sample. This ensured a full irradiation of the catalyst in all of the used wavelengths. In order to homogenize the irradiation power, a continuously variable density filter (NDC-100C, Thorlabs) was introduced into the measurement system. The filter was turned to adjust the output intensity, which allowed to equalize the power to  $P = 1.7$  mW regardless of the irradiation wavelength. The laser spot profile was ignored, as it was similar in all of the laser lines, and only the average power density was used as the equalization value. The optical setup is schematically shown in Figure 4.3.

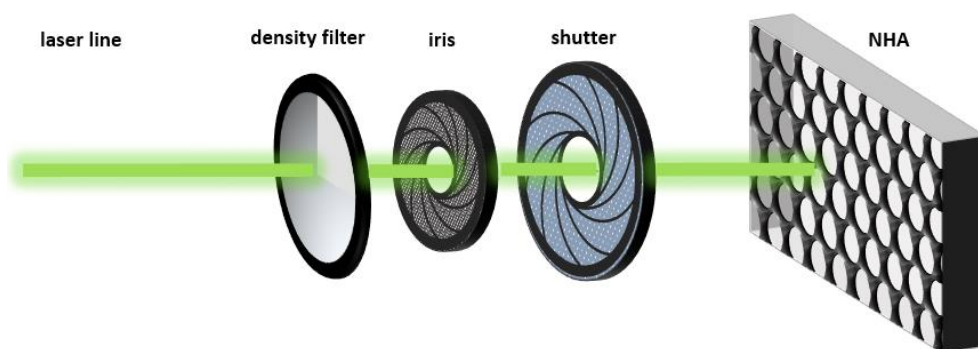


**Figure 4.3.** Scheme of the laser setup for comparable photoelectrochemical characterization of the metallic NHAs.

Electrochemical characterization was performed using a three-electrode system in a home-made cell with a quartz window. 0.1 M phosphate buffer (KPi) electrolyte (pH=12) was used to perform the electrochemical reaction, with Ag/AgCl (1M KCl) as a reference electrode ( $E^0 = 0.222$  V vs. RHE) and Pt wire as a counter electrode. 1 mg of electron scavenger,  $KIO_3$  (Sigma-Aldrich,  $\geq 99.0\%$ ), was added to the electrolyte to avoid hydrogen formation. The electrochemical measurements were performed using a BioLogic VMP-300 potentiostat. In order to ensure a better contact with the working electrode, 50 nm of gold was sputtered over the top ( $8 \times 3$  mm<sup>2</sup>) area of the NHA. The area of the exposed catalyst was limited to 5 mm<sup>2</sup> in order to make sure that all of the area is irradiated by the laser spot. The electrochemical surface area (ECSA) of the samples was compared by estimating the electrochemical double-layer capacitance, as the area is proportional to the capacitance value with a factor of specific capacitance. The double-layer capacitance was calculated from the CV data of the samples with 20 mm<sup>2</sup> of exposed geometrical area, measured in a small potential window (from -0.2 to 0.2 V vs. Ag/AgCl (1M KCl)) at different scan rates (10 to 300 mV s<sup>-1</sup>). For  $C_{DL}$ , the following relation is true:

$$\Delta j = vC_{DL}, \quad (4.1)$$

where  $\Delta j = \frac{j_a - j_c}{2}$ ,  $j_a$  being the anodic current density,  $j_c$  – the cathodic one, and  $v$  is the scan rate. Therefore,  $C_{DL}$  was defined as the slope of the  $\Delta j(v)$  plot.

The transmittance and reflectance spectra of the samples were taken on the PerkinElmer Lambda 35 UV-vis spectrophotometer with an integrating sphere module. The absorption of the samples was calculated according to the following equation:  $A + R + T = 1$ . The angle-dependent transmission measurements were conducted using a home-made rotating stage which was placed into the spectrophotometer and ensured tuning of the incidence angle. AFM measurements were performed using Park Systems XE-100 with platinum conductive cantilevers.

### 4.2.3. Theoretical calculations

As it was discussed in chapter 1, the momentum of incident light is less than the momentum needed to excite a surface plasmon in a metallic film. However, a periodic grating can provide additional in-plane momentum to the incident photons. In other words, in order for the surface plasmon to be excited, the momentum conservation law has to be satisfied:

$$\vec{k}_{SPP} = \vec{k}_x \pm i\vec{G}_x \pm j\vec{G}_y \quad (4.2)$$

Where  $\vec{k}_x = |\vec{k}_0| \sin \theta \cos \varphi \vec{x} + |\vec{k}_0| \sin \theta \sin \varphi \vec{y}$ ,  $\theta$  being the incident angle and  $\varphi$  being the azimuthal angle between the incidence plane and lattice orientation (Figure 4.4).

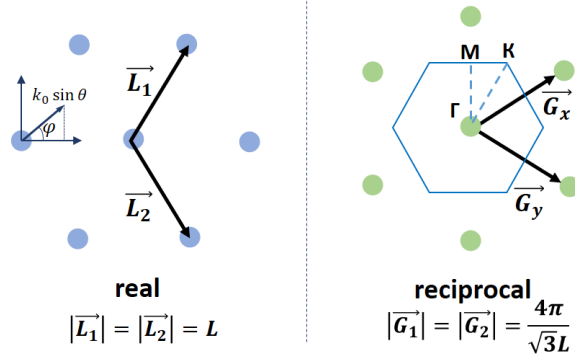


**Figure 4.4.** Scheme of the real and reciprocal hexagonal lattice with the primitive lattice vectors and azimuthal angle definition.

The SPP modes can be generated under the Bragg coupling conditions:

$$|\vec{k}_{SPP}| = \text{Re} \left[ |\vec{k}_0| \sqrt{\frac{\epsilon_d \epsilon_m(\lambda)}{\epsilon_d + \epsilon_m(\lambda)}} \right] \quad (4.3)$$

$\vec{G}_x$  and  $\vec{G}_y$  are the hexagonal lattice reciprocal vectors with the length  $|\vec{G}_x| = |\vec{G}_y| = \frac{4\pi}{\sqrt{3}L}$ , and  $|\vec{k}_0| = \frac{2\pi}{\lambda}$ .

For the light, coming normally to the surface of the hexagonal NHA ( $\sin \theta = 0$ ), the SPP coupling condition can be met for the following wavelength:

$$\lambda = \text{Re} \left[ \frac{L}{\sqrt{\frac{4}{3}(i^2 + ij + j^2)}} \sqrt{\frac{\epsilon_d \epsilon_m(\lambda)}{\epsilon_d + \epsilon_m(\lambda)}} \right] \quad (4.4)$$

This is an implicit equation, which allows only numerical solution. The resonant wavelength corresponds to the EOT, which appears as a maximum of the transmission spectrum. Two different solutions may exist for the metallic NHA: at the metal-glass and at the metal-air interfaces. The minima correspond to the Wood's anomalies, which can be found using the following equation:

$$\lambda = \frac{L}{\sqrt{\frac{4}{3}(i^2 + ij + j^2)}} \sqrt{\epsilon_d} \quad (4.5)$$

These minima positions do not depend on the metal type, but only on the dielectric material.

These equations are modified if the light is coming to the surface of the NHA under an incident angle  $\theta > 0$ . Following the calculations provided in Appendix 4.1, the angular dependence of the resonant wavelengths can be derived.

The corresponding equations were encoded and solved using MatLab software. The optical constants of nickel and silver were taken from [28] and [29], respectively.

### 4.3. Langmuir PS films

The monolayers of PS spheres were deposited on glass substrates at different target pressures, ranging from  $10 \text{ mN m}^{-1}$  to  $40 \text{ mN m}^{-1}$ . The typical isotherm surface-pressure curves are shown in the Figure 4.5. Unlike the isotherms for molecular monolayers, the curves don't have a clear liquid-solid phase transition [23], and breaking the monolayer into a multi-layer system was not necessarily followed by a surface pressure dip. The quality of the films was controlled by SEM imaging, with a focus on periodicity of the structure and presence of defects (holes, agglomerations of spheres, etc.). The best films were achieved when deposited at the target pressure values in the region of the linear ascending part of the isotherm.

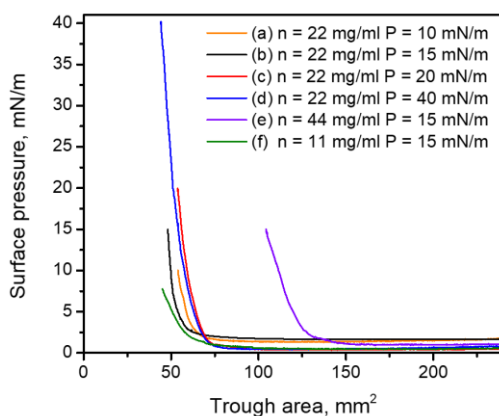


**Figure 4.5.** LB isotherms of PS spheres monolayers deposited at different target pressures and initial concentrations.

Another important factor influencing the film quality was the initial concentration of the PS spheres dispersion. High initial nanospheres concentration resulted in their agglomerations, whereas low concentration required too much volume to achieve the target pressure (isotherms (e) and (f) in the Figure 4.4). After comparing the film integrity and defects, the optimal parameters for PS spheres LS deposition were fixed to: target pressure  $P = 15 \text{ mN m}^{-1}$ ; concentration of PS spheres  $n = 22 \text{ g l}^{-1}$  in  $\text{H}_2\text{O}:\text{EtOH} (1:1)$ .

At the optimal pressure ( $15 \text{ mN m}^{-1}$ ) the LB procedure resulted in compact PS sphere films with minor defects (Figure 4.6). Due to the close pack of the PS nanospheres and their softness, they were squeezed compared to their initial size ( $460 \text{ nm}$ ) and formed a periodic structure with periodicity  $p = 420 \text{ nm}$ .

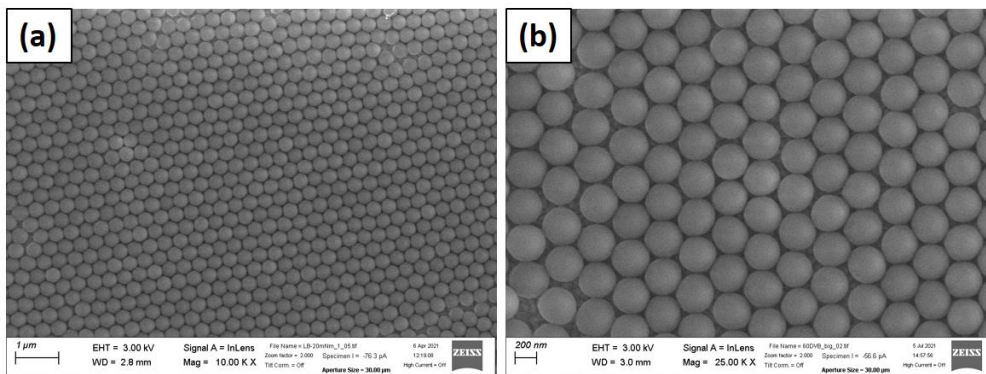


**Figure 4.6.** LB monolayer of PS spheres deposited under surface pressure  $P = 15 \text{ mN m}^{-1}$  at different magnifications: (a) 10,000X; (b) 25,000X.

To tune the size of masking spheres, while keeping the periodicity constant, the LB films were etched in  $\text{O}_2$  plasma, which resulted in homogenous reducing of the sphere size. By varying the time of exposure, we obtained samples with several different average sphere diameters (Figure 4.7).

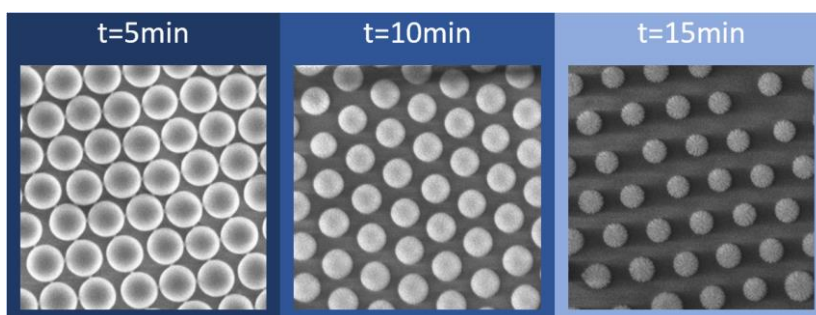


**Figure 4.7.** LB films of PS spheres (initial diameter  $d = 460 \text{ nm}$ ) after 5 min, 10 min and 15 min of  $\text{O}_2$  plasma treatment. The corresponding average sphere diameter was equal to 360 nm, 300 nm and 240 nm, respectively.

#### 4.4. Morphology of metallic NHAs

The main parameters, considered in this study, were periodicity ( $p$ ), inner hole diameter ( $\varnothing$ ) and thickness of the metallic film ( $d$ ). The periodicity was determined by choosing different initial PS spheres sizes for the monolayer deposition and was equal to 420 nm and 620 nm, being the periodicity of the obtained LB monolayers from PS spheres of different diameters used in this work. The hole diameter was varied by etching the PS spheres monolayers in  $O_2$  plasma for a controlled amount of time. The change in the hole size did not affect the periodicity, as the spheres were etched homogeneously from all sides. Lastly, the thickness of the film was defined by the deposition parameters, which were optimized for thermal evaporation of silver and sputtering of nickel previously and controlled by AFM.

The SEM images of the silver and nickel NHAs with different geometrical parameters is shown in Figure 4.8.

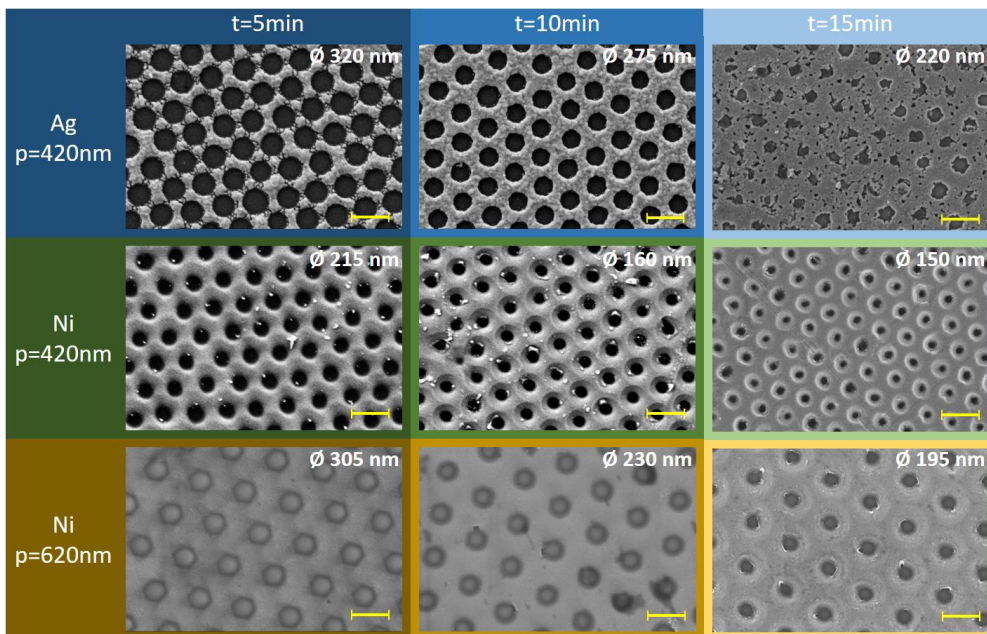


**Figure 4.8.** SEM images of the metallic NHAs ( $d = 100$  nm). The rows define the metal type and the periodicity, and the columns – the time of plasma treatment. Scale bar is 500 nm. The value on each image corresponds to the average diameter of the holes of each sample.

Due to the different methods of synthesis, the geometrical structure of the voids in the NHAs is different for the nickel and silver films. In case of thermal evaporation of Ag films, the holes have a cylindrical shape, while the sputtering of nickel led to



the conical configuration of the voids. The low-magnification SEM images of the NHA structures are shown in Figure C.2.2 and demonstrate good long-range periodicity.

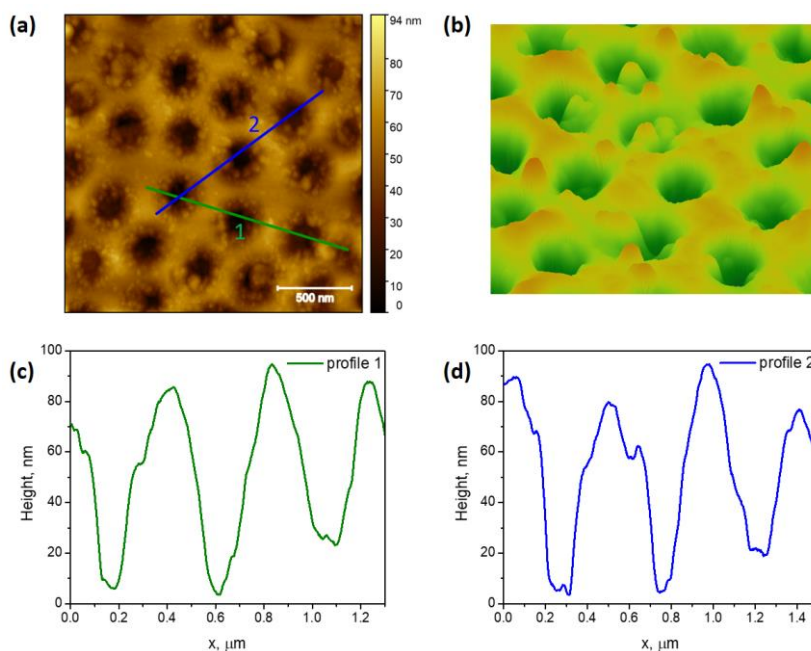


**Figure 4.9.** (a) AFM image of the 100 nm thick Ni NHA; (b) 3D reconstruction of the Ni NHA surface from the AFM image; (c-d) height profiles, corresponding to the directions 1 and 2 marked on the AFM image (a).

The AFM characterization revealed a nanohole topography with minor defects on the surface (Figure 4.9(a)). The height profile of the voids is shown in Figure 4.9(c-d). It exhibits a relatively periodical structure and revealed a curved shape of the voids. The average depth of the holes was found to be  $85 \pm 11$  nm, which is less than was expected according to the deposition conditions. However, the correct determination of the depth by the AFM profile method is not precise due to the non-contact measurement method, which doesn't allow full penetration of the tip to the bottom of the sample. The 3D reconstruction of the surface is demonstrated on the Figure 4.9(b).

XRD analysis has revealed a crystalline cubic structure of the Ni NHA film (JCPDS-00-001-1260) with a well-defined (111) diffraction peak. Absence of diffraction from (200) and (220) planes indicated a preferred [111] orientation (Appendix, Figure C.2.3).

## 4.5. Optical properties of metallic nanohole arrays

### 4.5.1. General characterization

The transmission spectra exhibit a number of maxima and minima, attributed to SPP modes and Wood's anomalies, correspondingly [30]. The latter one occurs when the diffracted wave propagated tangentially to the plane of the grating, and is determined only by the geometrical parameters of the NHA. The SPP modes, on the other hand, are represented as the extraordinary transmission (EOT) bands.

The transmission spectrum of silver NHA shows strong optical features, presenting two EOT bands at 775 nm and 515 nm (Figure 4.10). It can be seen that nickel also possesses plasmonic bands at 845 nm and 484 nm which are, however, much less explicit due to the strong damping of the plasmon. The plasmonic band at 484 nm is masked by the overall absorbance of the Ni film, whereas the 845 nm resonance is visible. The Wood's anomalies are located at 404 nm and 605 nm for Ag, and 431 nm and 636 nm for Ni.

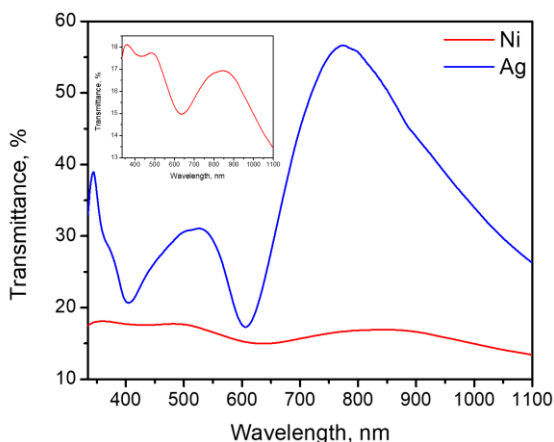


**Figure 4.10.** Transmission spectra of silver and nickel NHAs. The thickness and periodicity of the both NHAs are  $d=100$  nm and  $p=420$  nm, respectively, and the hole diameter is  $\varnothing = 275$  nm for Ag and  $\varnothing = 160$  nm for Ni NHAs. The inset shows the transmission spectrum of Ni NHA zoomed in along the y-axis.

The metallic films of the same thickness were almost non-transparent ( $T < 1\%$ ). Provided that the geometrical area of the holes was 42% in the case of Ag NHA ( $p=420$ nm,  $d=100$ nm,  $\varnothing=275$ nm), the peak transmittance of 57% indicates the existence of the EOT in silver nanostructured films. In the similar way, Ni NHA ( $p=420$ nm,  $d=100$ nm,  $\varnothing=160$ nm) possesses the peak transmittance maxima at

≈18%, which is more than the transmittance that could have been provided by the open area of the holes (14%).

A clear distinction between the NHA with different periodicity can be seen in the Figure 4.11(a). By choosing the initial size of the sacrificial PS spheres in the beginning of the synthesis process we were able to tune the position of the SPP resonance modes within the visible light range. While the most intensive SPP band for Ni NHA  $p = 420$  nm are located at 485 nm and 845 nm, the SPP maximum for the Ni NHA  $p = 620$  nm is found at 675 nm.

In order to excite the surface plasmon we need to add the lacking part of the momentum to the momentum of incident light. For this we need to have a periodic structure on the surface which would have a reciprocal lattice. Thus, due to its periodicity, the ordered array of nanoholes possesses features which are not present in the non-ordered array. To clarify the effect of periodicity we synthesized Ni nanohole arrays using the above-described procedure but without the LB ordering of the spheres. Instead, the monolayers of PS spheres were obtained by “fishing” of the self-assembled spheres with the glass substrate after their drop casting on the water surface (Appendix, Figure C.2.4). The corresponding transmission spectra for the ordered and disordered nanohole arrays are compared in Figure 4.11(b). As it can be seen from the figure, the disordered NHA does not possess the features, inherent to the periodic structure. In particular, the SPP band at 845 nm is not present in the disordered grating, as well as the Wood’s anomaly at 636 nm. The band at 485 nm is weaker than in the ordered NHA, as is probably originated from the short-range order of the nanoholes which happens due to self-organizing of the PS nanospheres on the water surface in small hexagonal close-packed structures even without the additional ordering.

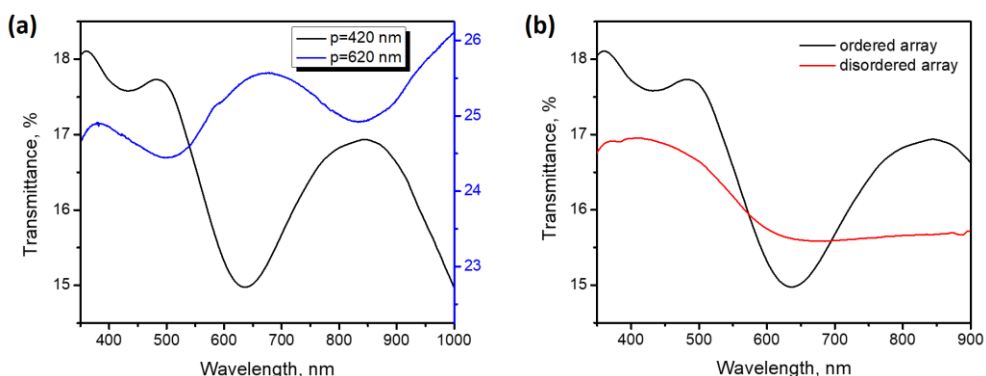


**Figure 4.11.** (a) Transmission spectra for Ni NHA with different periodicity:  $p = 420$  nm and  $p = 620$  nm; (b) transmission spectra for ordered and disordered Ni NHAs with the same sacrificial PS spheres used for their synthesis.

With the deviation of the incident angle from the normal, the degeneracy of the  $(\pm i, \pm j)$  SPP modes is broken. Depending on the sign of the  $i$  and  $j$  indices, the SPP mode can be shifted both to the shorter and longer wavelengths with increase of the angle (Figure 4.12). The angle-dependent modes are also non-invariant with respect to the permutation of the indices. The slight broadness of the peak can be explained by further breaking of the SPP state degeneracy under higher incident angles.

Upon the angle increase, there start to appear some perturbations in the transmission spectrum at 512 nm and 462 nm, whose intensity depends on the incident angle, but the position remains constant. These peaks are attributed to the interference effects between the transmitted light and the one double reflected from the outer glass surface and the metal film, which become much more prominent when the incident angle is higher and more light is passing through the glass substrate.

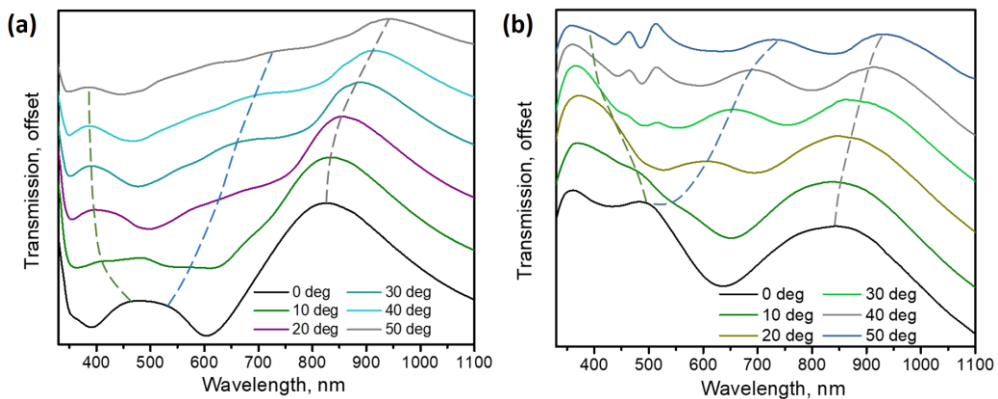


**Figure 4.12.** Angular dependence of the (a) Ag NHA ( $p = 420$  nm,  $\varnothing = 275$  nm,  $d = 100$  nm) and (b) Ni NHA ( $p = 420$  nm,  $\varnothing = 160$  nm,  $d = 100$  nm) transmission spectra. The dashed lines show the shift of the SPP modes with increase of the incident angle.

To understand the origin of these plasmonic bands, we applied the theoretical model described in section 4.2.3 to the Ni and Ag NHAs with periodicity  $p = 420$  nm and  $p = 620$  nm. We estimated the SPP and Wood's anomaly positions using the Equations 4.4 and 4.5, for metal/glass and metal/air interfaces, considering only the resonant modes, falling into the visible light range. According to the Equation 4.5, the calculated positions for the Wood's anomalies of the NHAs with the periodicity  $p = 420$  nm, regardless of the metal type, were found to be 546 nm for  $(0, \pm 1)_{\text{metal/glass}}$  mode and 364 nm for  $(0, \pm 1)_{\text{metal/air}}$  mode.

Surface plasmon bands, unlike Wood's anomalies, also depend on the dielectric properties of the metal. The SPP resonant modes calculated for Ag NHA ( $p = 420$  nm)

in the visible range were limited to three resonances:  $(0, \pm 1)_{\text{Ag/glass}}$  at 596 nm,  $(0, \pm 1)_{\text{Ag/air}}$  at 412 nm and  $(1, 1)_{\text{Ag/glass}}$  at 363 nm. The experimentally observed Ag band at 515 nm can be originated from the overlap of the  $(0, \pm 1)_{\text{Ag/air}}$  and  $(1, 1)_{\text{Ag/glass}}$  modes.

Visible maxima estimated for surface plasmons in Ni NHA with periodicity  $p = 420$  nm were found to be  $(0, \pm 1)_{\text{Ni/glass}}$  at 563 nm and  $(0, \pm 1)_{\text{Ni/air}}$  at 369 nm, while the SPP modes for Ni NHA with periodicity  $p = 620$  nm were  $(0, \pm 1)_{\text{Ni/glass}}$  at 825 nm,  $(0, \pm 1)_{\text{Ni/air}}$  at 545 nm and  $(1, 1)_{\text{Ni/glass}}$  at 481 nm.

While the experimentally measured EOT band at 485 nm for Ni NHA ( $p = 420$  nm) can be explained by overlapping of the  $(0, \pm 1)_{\text{Ni/glass}}$  and  $(0, \pm 1)_{\text{Ni/air}}$  modes, which also justifies the broadness of the band, the origin of  $\sim 845$  nm band cannot be explained by the Equation 4.4, as the least energy mode ( $(0, \pm 1)_{\text{Ni/glass}}$  SPP) corresponds to the wavelength  $\lambda_{\text{SPP}} = 564$  nm. However, according to the angular-dependent transmittance data, the low-energy band is also shifting with the change of the incident angle, proving the SPP nature of the peak. It can be originated from a coupling of the localized plasmon inside the holes with a surface propagating plasmon, owed to the periodical structure. Another explanation of the low-energy plasmonic band at 800 nm can be obtained in case we consider a spontaneous metal-oxide film on the surface of the nickel nanohole array, when exposed to air for a while. The nickel oxide might act as another dielectric in contact with the nickel grating, creating a new metal-dielectric interface. Considering the dielectric constant of NiO to be  $\epsilon \approx 5$  in the visible light range [31], the Equation 4.4 gives the SPP resonance wavelength value for the  $(0, \pm 1)_{\text{Ni/NiO}}$  SPP mode being equal to 852 nm. However, the NiO layer is too thin to be detected by XRD spectra, which might indicate that there is not enough material on the surface of the nickel nanohole array to possess dielectric properties of a NiO thin film and be responsible for the surface plasmon polariton on the Ni/NiO interface.

The discrepancies between the calculated and experimentally found SPP modes and Wood's anomalies positions can be understood considering imperfect long-range periodicity (varying from 410 to 460 nm), multiple defects on the surface and imperfection of the applied model. However, these simple estimations allowed us to observe and explain the tendencies of the SPP shifts with the change of the angle, justifying both the blue and red shifts with the increase in the incidence angle (Figure 4.12, Figures C.3.1–C.3.3).

### 4.5.2. Effect of geometric parameters on the NHA optical properties

The resonance positions do not shift significantly with changes in the thickness of the metal film (Figure 4.13). However, the relative intensity of the EOT bands can be tuned by changing the thickness due to improving of the coupling. In case of the Ag films, reducing the thickness from 150 nm to 100 nm without changing the hole diameter, drastically improves the EOT, and, therefore, the plasmonic response. Among the different thicknesses of Ni NHAs, 100 nm leads to the most intensive band as the SPP intensity strongly depends on the geometrical parameters of the grating, particularly the depth of the holes [32].

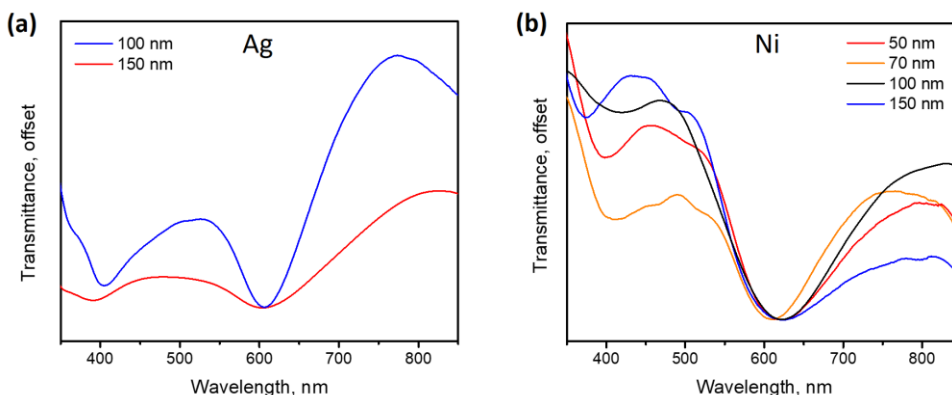


**Figure 4.13.** Dependence of the transmission spectra on the deposited film thickness of (a) silver and (b) nickel NHAs. The spectra are shown in their absolute values (%) but shifted in the y-direction so that the minimum of the transmittance is the same for all the thicknesses for easier comprehension.

On the other hand, the transmission spectra exhibit a slight dependence on the hole diameter of the structures. With the change of the hole size, the maximum transmission peak is distinctly displaced due to the change in the resonant frequency (Figure 4.14). As SPP and Wood's anomaly depend solely on the periodicity of the grating, and should not depend on the hole diameter, we may conclude that the SPP resonances are coupled to the LSPR happening in the void. However, the oversimplified model, described in section 4.2.3, does not account for the hole size and, therefore, cannot explain the observed effect.

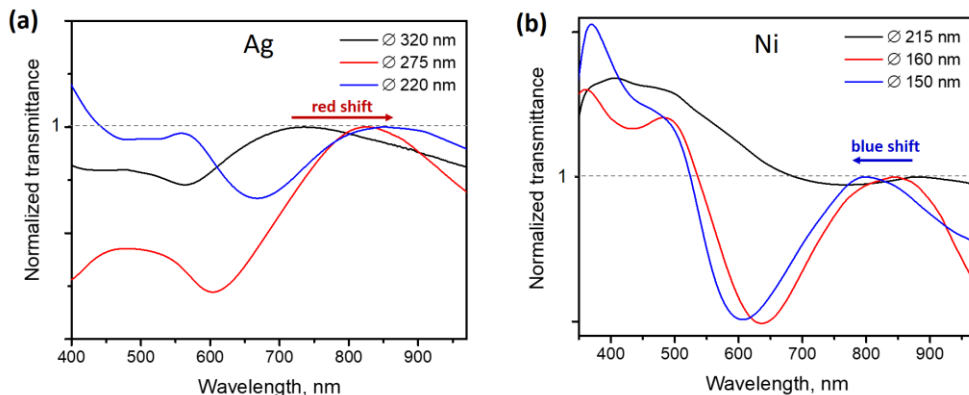


**Figure 4.14.** Dependence of the transmission spectra on hole diameter for (a) silver and (b) nickel NHAs ( $p = 420$  nm). The spectra were normalized on the maximum of the red EOT band for easier comprehension.

To improve the model we have introduced an effective dielectric constant of the medium, as it was done in the work of Fang et al. [33]:

$$\varepsilon_{eff} = f * \varepsilon_m + (1 - f) * \varepsilon_{air} \quad (4.6)$$

Here, the filling factor  $f$  stands for the relative amount of metal in the perforated film, and the larger is the factor, the smaller are the holes in the NHA. Despite the fact that in the work [33] this expression was used to explain the red shift of the SPP peak with decreasing of the hole diameter, our calculations show that with increasing of the factor  $f$  (i.e. increasing of the nickel share in the perforated film and, consequently, decreasing of the hole size), the SPP peak from Equation 4.4 exhibits a non-monotonous behavior. The corresponding dependence of the  $(0,+1)_{Ni/glass}$  resonance on the filling factor  $f$  is shown in Appendix, Figure C.3.4. For the low values of the filling factor ( $f < 0.4$ ), the SPP mode is red-shifted, while for the larger values ( $f > 0.4$ ) it shifts to the lower wavelengths. However, the real  $f$ -values, corresponding to the NHAs, discussed in this chapter, were in the range of 0.7-0.9 for Ni NHA. Therefore, for the studied structures, the introduction of the effective dielectric constant is enough to explain the blue-shift of the SPP mode with decreasing of the hole size. The blue shift of the SPP peak was also reported for golden nanohole arrays [34].

Remarkably, when decreasing the hole diameter, the EOT peak in silver nanohole arrays undergoes a red shift, while the EOT bands in the nickel nanohole arrays shift to the lower wavelengths. In the case of silver, the  $f$ -values of the real NHAs were in the range of 0.4-0.75. However, according to the calculations, introduction of the effective dielectric constant predicts a blue-shift of the SPP mode with decreasing of the hole size (Figure C.3.4).

The red shift of the SPP bands was commonly reported elsewhere and explained mostly by the strong coupling with the LSPR modes. The latter tend to red shift with decreasing of the hole size due to the relation of the holes and particles as complementary structures:  $\omega_{hole}^2 + \omega_{particle}^2 = \omega_p^2$  [9,35], where  $\omega_p$  is the bulk plasma frequency.

In the work of [36], the array of narrow holes were made in the golden and silver films. There, due to the small diameter of the holes, the SPP is creating a standing wave in the hole due to the strong coupling of the charges on the opposite sides of the walls. This creates a coupling of the SPP with the localized standing wave, which results a strong dependence of the resonant wavelength with the hole diameter. However, with increased hole diameter, this coupling is smaller due to less interaction of the charge in this structure.

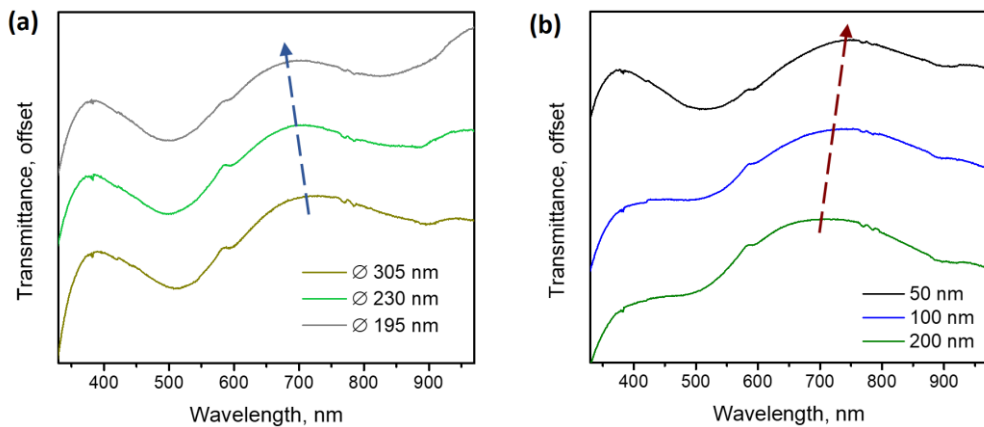


**Figure 4.15.** Transmission spectra of Ni NHAs ( $p = 620$  nm) depending on the (a) change in the hole diameter; (b) change in the film thickness.

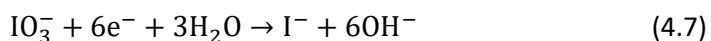
It should be noted, that in case of the Ni NHA with periodicity  $p = 620$  nm, decrease of the hole diameter results in the similar blue shift as in the case of Ni NHA  $p = 420$  nm, proving that this phenomenon depends on the type of the material and does not depend on the periodicity (Figure 4.15). However, with increase in the thickness of the Ni film, the position of the SPP mode is much more significantly affected than in case of the lower periodicity.



## 4.6. Electrochemical measurements

The characterized Ni NHAs were first used as a photoactive cathode for hydrogen evolution reaction (HER). The poor adhesion of silver to the glass substrate impeded the non-destructive use of silver nanohole arrays as electrodes for electrochemical measurements, so the study was limited to application of nickel NHAs to light-assisted electrochemical reduction.

Restricted by the laser spot size, the area of the exposed catalyst was limited to 5 mm<sup>2</sup> in order to make sure that all of the area is irradiated by the laser. Over the course of the water reduction reaction, the potentiostatic measurements over the exposed area of the catalyst were followed by a large noise, making it almost impossible to study the irradiation effects (Appendix, Figure C.2.6). Hydrogen evolution reaction results in formation of hydrogen gas bubbles, which can severely interfere with the measurement process. Particularly, when the bubble is formed on the surface of the catalyst, it impedes electrolyte from reaching the surface and hinders the reaction on the catalyst under the bubble. Another common problem when irradiating the catalyst is scattering of light on the gas/liquid interface due to the curvature of the bubble which impacts the amount of light reaching the surface. This effect is especially significant when the area of the catalyst is small, which leads to a large noise in the baseline. Due to the reasons stated above, it was decided to study the effect of Ni catalyst illumination on another reduction reaction, namely reduction of the IO<sub>3</sub><sup>-</sup> ion to iodide (I<sup>-</sup>) with the redox potential +1.086 V vs. RHE [37]:



This reaction is also a reduction reaction, which happens at higher potentials than HER and, therefore, is more favorable (Figure C.2.7), acting as electron scavenger.

The chopped illumination resulted in pulsed variation of the current density, which increased when the illumination was on, and returned to the baseline, when the light was turned off. The baseline was subtracted from the experimental values of the current density, and the intensity of the current density variation was compared for different samples and illumination wavelengths.

In the Figure 4.16(a) we have shown typical pulsed variations of the measured current density under chopped laser illumination with the duration of 60 s. It can be also seen, that with time the baseline linearly shifts to higher values, pointing out that the electrolyte temperature is slightly increased upon irradiation.

In order to see the advantage of the nanostructured nickel we compared a flat Ni film with the nickel nanohole arrays of different periodicity  $p = 420$  nm and

$p = 620$  nm. To facilitate the comparison of electrochemical response to illumination pulses, we have measured the electrochemically active surface area (ECSA) of the three samples and used it to normalize the response. ECSA can be calculated from the electrochemical double-layer capacitance at the catalyst-electrolyte interface. The latter is obtained from the non-Faradaic capacitive current of the electrode close to the open-circuit potential, determined from the cyclic voltammograms measured at different scan rates. From the data, shown in the Figure 4.16(b), we can deduce the values of the double-layer capacitance for the five samples compared in this study. The results are provided in Table 4.1.

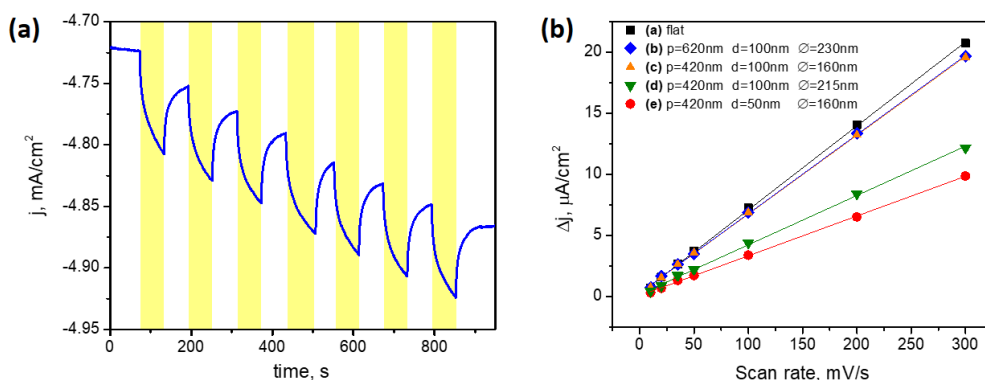


**Figure 4.16.** (a) Current density variation under chopped laser illumination ( $\lambda=532$ nm, pulse duration  $t=60$ s,  $E_{we} = -1$  V vs. Ag/AgCl); (b) capacitive currents with a scan rate 10, 20, 35, 50, 100, 200 and 300  $\text{mV s}^{-1}$  for Ni NHAs with different geometrical parameters.

**Table 4.1.** Double-layer capacitance values for the Ni NHAs with different periodicity ( $p$ ), thickness ( $d$ ), diameter ( $\varnothing$ ) and a flat Ni film.

Sample	$p$ , nm	$d$ , nm	$\varnothing$ , nm	$C_{DL}$ , $\mu\text{F}$
(a)	--	70	--	68.7
(b)	620	100	230	64.7
(c)	420	50	160	64.5
(d)	420	100	160	40.3
(e)	420	100	215	32.5

The three selected samples appeared to have similar electrochemical active surface area (a-c), unlike samples with bigger holes (d) or lower thickness (e). Despite the morphology differences in the flat and nanostructured samples, in the NHA the absence of nickel sites (holes) are compensated by the material on the “walls” of the holes, resulting in the similar values of ECSA. However, when the hole diameter is too big, or the thickness of the sample is too small, the surface areas of “holes”

and “walls” are not compensating each other anymore and result in a lower total active surface area of the catalyst.

Another important factor to consider before comparing the current density variation during illumination is the absorbance of different samples. The ability of a film to absorb light may significantly affect the resulting temperature and become a crucial factor in the current density response to the illumination. For this reason, in order to compare the flat and nanostructured plasmonic nickel electrodes, we need to ensure similar absorbance at the excitation wavelength. Moreover, we chose the flat samples with slightly higher absorbance than the NHAs to demonstrate the advantage of Ni NHAs over the flat nickel film in the photoresponse. Thus, we compared the current density variation of two pairs of electrodes to the illumination of different wavelengths: Ni NHA ( $p = 420$  nm,  $d = 100$  nm) to flat Ni ( $d = 70$  nm) (Figure 4.17(a)) and Ni NHA ( $p = 620$  nm,  $d = 100$  nm) to flat Ni ( $d = 50$  nm) (Figure 4.17(b)). The corresponding absorption spectra are also shown in the figure. It is also worth noting, that the active surface area of the flat samples is not changing with the thickness. As it can be seen from the Figure 4.17, the response of the current density for the Ni NHAs is higher than for the flat samples, despite the higher absorbance of the latter. The gain in current density over the flat samples was quantified to be  $24 \pm 6\%$  and  $26 \pm 9\%$  for the Ni NHA with periodicity  $p = 420$  nm and  $p = 620$  nm, respectively.

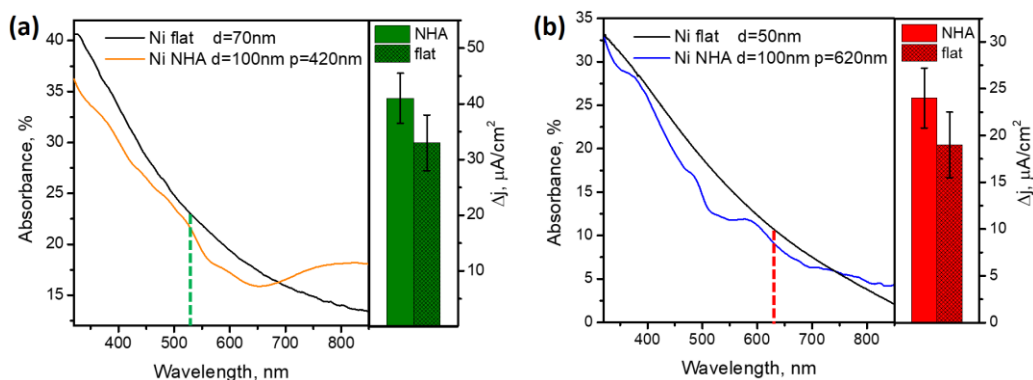


**Figure 4.17.** Absorption spectra of the Ni NHAs with thickness  $d = 100$  nm and periodicity (a)  $p = 420$  nm and (b)  $p = 620$  nm compared to the spectra of flat Ni films with thickness (a)  $d = 50$  nm and (b)  $70$  nm, and the corresponding photoelectrochemical response of the NHA and flat samples with the excitation wavelength (a)  $\lambda = 532$  nm and (b)  $\lambda = 633$  nm. The dashed lines on the optical spectra indicate the position of the excitation wavelengths.

The correlation of the electrochemical response to the pulses of different laser lines is shown on Figure 4.18 for Ni NHA with periodicity equal to (a)  $420$  nm and (b)  $620$  nm. As it can be seen from the figure, the current density variation under

irradiation with different wavelengths follows the transmission spectra of the corresponding Ni NHAs, showing higher response at the EOT bands of the structures.

The blue illumination causes the biggest response of the current density. As the light power was equalized due to the specific setup configuration, these results are comparable with the response to the other wavelengths. The deviation from the transmission spectrum can be clearly explained by the absorption spectrum of Ni NHA, where the absorbance is increasing towards the higher frequency (Figure 4.17).

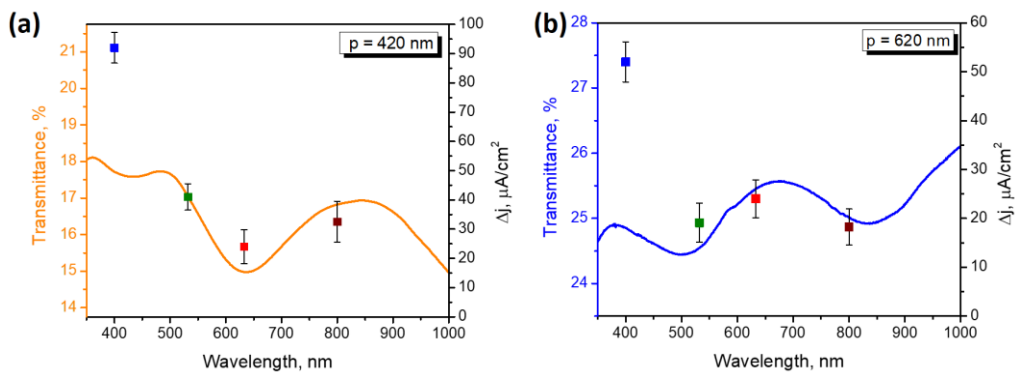


**Figure 4.18.** Current density variation under chopped laser illumination (pulse duration  $t=60$ s,  $E_{we} = -1$  V vs. Ag/AgCl) for different excitation wavelengths:  $\lambda=800$  nm, 633 nm, 532 nm and 400 nm (wine, red, green and blue dot colors, respectively) and the corresponding transmission spectra for Ni NHAs with (a)  $p = 420$  nm and (b)  $p = 620$  nm.

## 4.7. Mechanism of the reaction enhancement

The origin of the redox reaction enhancement needs further investigation. However, the analysis of the curve shape of the current density pulses allowed to draw conclusions about the nature of the observed effects.

For the system operated at the constant light intensity, the following expression for the system temperature can be derived on the basis of linear non-equilibrium thermodynamics [38]:

$$T = Ae^{-\frac{ak}{Cl}t} + \frac{Pl}{ak} + T_0 \quad (4.8)$$

Here  $P$  is the power density of the incident illumination,  $k$  – thermal conductivity of nickel,  $C$  – heat capacity of the system,  $a$  – area of the electrode,  $l$  – thickness of the thermal diffusion layer where the temperature changes linearly,  $T_0$  – temperature of the surrounding media, and  $t$  is time.  $A$  is a constant, which can be derived from the boundary conditions.

From the Figure 4.19(a) we can deduce the linear dependence of the current density on the temperature:

$$j = A_0T + D \quad (4.9)$$

and state the following expression for the photothermally-enhanced current density:

$$j = Be^{-\frac{ak}{Cl}t} + \text{const} \quad (4.10)$$

According to the fitting results (Figure 4.19(b)), the biggest part of the curve is well-described by the exponential decay:

$$y = y_0 + Ae^{-x/t} \quad (4.11)$$

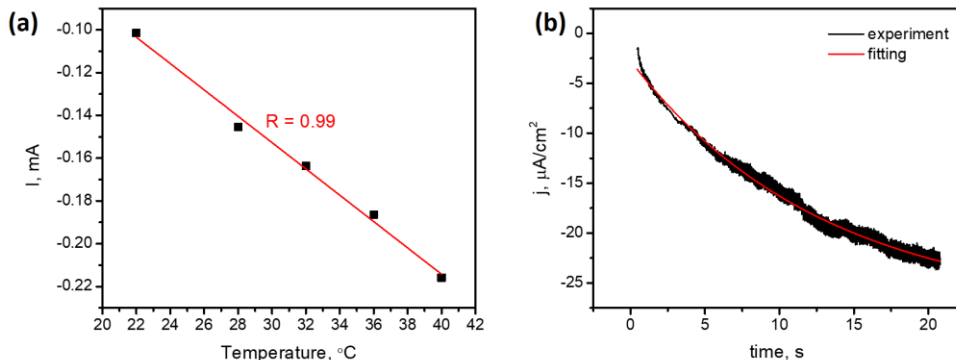


**Figure 4.19.** (a) Temperature dependence of the current at working potential  $E = -0.9 \text{ V vs. Ag/AgCl}$ ; (b) fitting of the current density pulse with an exponential decay function.

From the analysis performed above we can deduce mostly thermal origin of the observed enhancement of the reaction. In other words, the light, absorbed by the electrode is transformed into heat, which affects the reaction rate on its surface. The enhanced response of the nanostructured nickel electrodes compared to flat films is probably due to excitement of surface plasmon at the Ni/glass interface and its subsequent decay to extra heat, which is responsible for the additional current density, observed under laser illumination.

At higher potentials “fast effects” are present, such as those observed in chapter 3 (Figure C.2.8). In the beginning of the light pulse, there is a rapid increase in the current density, followed by a slowdown. After a couple of seconds, the pulse gets back its typical exponential shape, until the light is turned off. Then the current density undergoes the similar behavior in the opposite direction. This leads us to the conclusion that the mechanism of the reaction enhancement might be similar to the HER improvement under plasmonic nickel photoresponse. In other words, the sudden irradiation of the sample results in the break of the equilibrium at the catalyst-electrolyte interface due to the instant heating of the catalyst surface. The rapid temperature increase leads to activation of the electronic subsystem of the catalyst, tending the reaction towards adsorption. The ionic subsystem is reacting with delay, resulting in deceleration of the current density upon the illumination pulse. When the electrolyte begins to heat up, a new quasi-equilibrium is set, resulting in a purely exponential behavior of the current density, pointing out the thermal nature of the process.

## 4.8. Conclusions

In this chapter, periodic metallic nanohole arrays were obtained with the use of the LB-deposited monolayer of PS spheres in order to study the surface plasmon effects on electrochemical reduction reaction. Horizontal deposition was applied to the LB setup with optimized parameters to obtain a homogeneous hexagonal monolayer of PS spheres over a glass substrate with minimal defects. Various depositions of nickel and silver thin films over the treated PS mask with the subsequent spheres removal resulted in a set of samples with different geometrical parameters and dielectric properties, that allowed us to determine SPP bands in the nanohole arrays and discuss their coupling with the localized surface plasmons in the voids as well as their angular dependence. The shift of the SPP modes with the hole size depends on the material, and exhibits an opposite behavior for Ag and Ni films due to the stronger SPP-LSPR coupling of the former.

Photoelectrochemical response of the synthesized Ni NHA electrodes was compared to the one of the thin films, demonstrating a clear advantage of the nanostructured samples over the flat ones, with an average gain in the current density of 25%. The plasmonic origin of the enhanced reduction reaction was corroborated by studying the electrochemical response to the irradiation of the NHA surface with lasers of different wavelengths. Fitting of the current density pulsed variation allowed us to attribute the nature of the reaction improvement to the photothermal effect of the surface plasmon. The reason of the delayed response in the reduction reaction was suggested to be of the same origin as the photothermal enhancement of the Ni nanoparticles discussed in chapter 3.

## 4.9. References

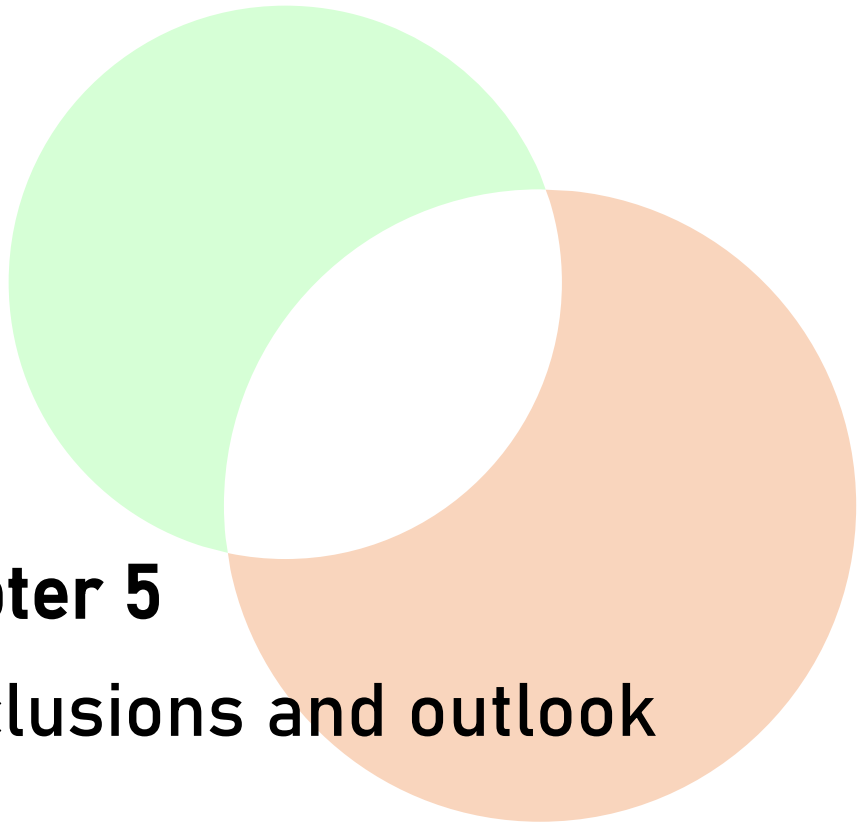
- [1] E. Kretschmann and H. Raether, *Radiative Decay of Non Radiative Surface Plasmons Excited by Light*, Zeitschrift Fur Naturforsch. - Sect. A J. Phys. Sci. **23**, 2135 (1968).
- [2] H. Raether, *Surface Plasmons on Smooth and Rough Surfaces and on Gratings*, Vol. 111 (Springer-Verlag, Berlin, 1988).
- [3] Z. Sun and H. K. Kim, *Growth of Ordered, Single-Domain, Alumina Nanopore Arrays with Holographically Patterned Aluminum Films*, Appl. Phys. Lett. **81**, 3458 (2002).
- [4] C. Y. Liu, A. Datta, and Y. L. Wang, *Ordered Anodic Alumina Nanochannels on Focused-Ion-Beam-Prepatterned Aluminum Surfaces*, Appl. Phys. Lett. **78**, 120 (2001).
- [5] D. Navas, M. Hernández-Vlez, M. Vázquez, W. Lee, and K. Nielsch, *Ordered Ni Nanohole Arrays with Engineered Geometrical Aspects and Magnetic Anisotropy*, Appl. Phys. Lett. **90**, 1 (2007).
- [6] K. W. A. Chee, W. Guo, J. R. Wang, Y. Wang, Y. e. Chen, and J. Ye, *Tuning Photonic Crystal Fabrication by Nanosphere Lithography and Surface Treatment of AlGaIn-Based Ultraviolet Light-Emitting Diodes*, Mater. Des. **160**, 661 (2018).
- [7] G. H. Chan, J. Zhao, E. M. Hicks, G. C. Schatz, and R. P. Van Duyne, *Plasmonic Properties of Copper Nanoparticles Fabricated by Nanosphere Lithography*, Nano Lett. **7**, 1947 (2007).
- [8] C. C. Ho, K. Zhao, and T. Y. Lee, *Quasi-3D Gold Nanoring Cavity Arrays with High-Density Hot-Spots for SERS Applications via Nanosphere Lithography*, Nanoscale **6**, 8606 (2014).
- [9] P. Zheng, S. K. Cushing, S. Suri, and N. Wu, *Tailoring Plasmonic Properties of Gold Nanohole Arrays for Surface-Enhanced Raman Scattering*, Phys. Chem. Chem. Phys. **17**, 21211 (2015).
- [10] D. J. Norris, E. G. Arlinghaus, L. Meng, R. Heiny, and L. E. Scriven, *Opaline Photonic Crystals: How Does Self-Assembly Work?*, Adv. Mater. **16**, 1393 (2004).
- [11] C. Zhang, S. Cvetanovic, and J. M. Pearce, *Fabricating Ordered 2-D Nano-Structured Arrays Using Nanosphere Lithography*, MethodsX **4**, 229 (2017).
- [12] S. Portal-Marco, M. À. Vallvé, O. Arteaga, J. Ignés-Mullol, C. Corbella, and E. Bertran, *Structure and Physical Properties of Colloidal Crystals Made of Silica Particles*, Colloids Surfaces A Physicochem. Eng. Asp. **401**, 38 (2012).
- [13] Z. Zhou and X. S. Zhao, *Flow-Controlled Vertical Deposition Method for the Fabrication of Photonic Crystals*, Langmuir **20**, 1524 (2004).
- [14] Y. Fu, Z. Jin, G. Liu, and Y. Yin, *Self-Assembly of Polystyrene Sphere Colloidal Crystals by in Situ Solvent Evaporation Method*, Synth. Met. **159**, 1744 (2009).
- [15] S. H. Im and O. O. Park, *Effect of Evaporation Temperature on the Quality of Colloidal Crystals at the Water-Air Interface*, Langmuir **18**, 9642 (2002).
- [16] D. Nagao, R. Kameyama, Y. Kobayashi, and M. Konno, *Multiformity of Particle Arrays Assembled with a Simple Dip-Coating*, Colloids Surfaces A Physicochem. Eng. Asp. **311**, 26 (2007).
- [17] Y. Fu, Z. Jin, Z. Liu, and W. Li, *Preparation of Ordered Porous SnO<sub>2</sub> Films by Dip-Drawing Method with PS Colloid Crystal Templates*, J. Eur. Ceram. Soc. **27**, 2223 (2007).



- [18] T. Ogi, L. B. Modesto-Lopez, F. Iskandar, and K. Okuyama, *Fabrication of a Large Area Monolayer of Silica Particles on a Sapphire Substrate by a Spin Coating Method*, *Colloids Surfaces A Physicochem. Eng. Asp.* **297**, 71 (2007).
- [19] S. S. Shinde and S. Park, *Oriented Colloidal-Crystal Thin Films of Polystyrene Spheres via Spin Coating*, *J. Semicond.* **36**, 023001 (2015).
- [20] J. Ballato and A. James, *Ceramic Photonic Crystal Temperature Sensor*, *J. Am. Ceram. Soc.* **82**, 2273 (1999).
- [21] Y. W. Chung, I. C. Leu, J. H. Lee, and M. H. Hon, *Fabrication and Characterization of Photonic Crystals from Colloidal Processes*, *J. Cryst. Growth* **275**, 2389 (2005).
- [22] Z. Z. Gu, S. Hayami, S. Kubo, Q. B. Meng, Y. Einaga, D. A. Tryk, A. Fujishima, and O. Sato, *Fabrication of Structured Porous Film by Electrophoresis*, *J. Am. Chem. Soc.* **123**, 175 (2001).
- [23] J. D. Swalen, *Langmuir-Blodgett Films*, 1st ed. (Springer, New York, 1990).
- [24] M. S. L. Technique, R. Wei-dong, L. Zhi-cheng, J. I. Nan, W. Chun-xu, Z. Bing, and Z. Jun-hu, *Facile Fabrication of Large Area Polystyrene Colloidal Crystal*, *Chem. Res. Chinese* **6**, 712 (2007).
- [25] M. Bardosova, M. E. Pemble, I. M. Povey, and R. H. Tredgold, *The Langmuir-Blodgett Approach to Making Colloidal Photonic Crystals from Silica Spheres.*, *Adv. Mater.* **22**, 3104 (2010).
- [26] S.-H. Chang, S. K. Gray, and G. C. Schatz, *Surface Plasmon Generation and Light Transmission by Isolated Nanoholes and Arrays of Nanoholes in Thin Metal Films*, *Opt. Express* **13**, 3150 (2005).
- [27] M. Pellarin, M. Broyer, J. Lermé, M. A. Lebeault, J. Ramade, and E. Cottancin, *Plasmon Resonances Tailored by Fano Profiles in Silver-Based Core-Shell Nanoparticles*, *Phys. Chem. Chem. Phys.* **18**, 4121 (2016).
- [28] P. B. Johnson and R. W. Christy, *Optical Constants of Transition Metals*, *Phys. Rev. B* **9**, 5056 (1974).
- [29] P. B. Johnson and R. W. Christy, *Optical Constant of the Nobel Metals*, *Phys. Rev. B* **6**, 4370 (1972).
- [30] H. Ghaemi, T. Thio, D. Grupp, and T. Ebbesen, *Surface Plasmons Enhance Optical Transmission through Subwavelength Holes*, *Phys. Rev. B - Condens. Matter Mater. Phys.* **58**, 6779 (1998).
- [31] J. W. Park, K. N. Choi, S. H. Baek, K. S. Chung, and L. E. E. Hosun, *Optical Properties of NiO Thin Films Grown by Using Sputtering Deposition and Studied with Spectroscopic Ellipsometry*, *J. Korean Phys. Soc.* **52**, 1868 (2008).
- [32] A. Degiron, H. J. Lezec, W. L. Barnes, and T. W. Ebbesen, *Effects of Hole Depth on Enhanced Light Transmission through Subwavelength Hole Arrays*, *Appl. Phys. Lett.* **81**, 4327 (2002).
- [33] H. Fang, B. Caballero, E. M. Akinoglu, E. T. Papaioannou, A. García-Martín, J. C. Cuevas, M. Giersig, and P. Fumagalli, *Observation of a Hole-Size-Dependent Energy Shift of the Surface-Plasmon Resonance in Ni Antidot Thin Films*, *Appl. Phys. Lett.* **106**, (2015).
- [34] T. Ohno, C. Wadell, S. Inagaki, J. Shi, Y. Nakamura, and T. Sannomiya, *Hole-Size Tuning and Sensing Performance of Hexagonal Plasmonic Nanohole Arrays*, **6**, 1594 (2016).
- [35] Z. Zuo, Y. Wen, and S. Zhang, *Interface-Induced Nucleation and Growth: A New Route for*

*Fabricating Ordered Silver Nanohole Arrays*, *Nanoscale* **10**, 14039 (2018).

- [36] A. Dhawan, M. Canva, and T. Vo-Dinh, *Narrow Groove Plasmonic Nano-Gratings for Surface Plasmon Resonance Sensing*, *Opt. Express* **19**, 787 (2011).
- [37] Y. Miseki, S. Fujiyoshi, T. Gunji, and K. Sayama, *Photocatalytic Water Splitting under Visible Light Utilizing  $I_3^-/I^-$  and  $IO_3^-/I^-$  Redox Mediators by Z-Scheme System Using Surface Treated  $PtO_x/WO_3$  as  $O_2$  Evolution Photocatalyst*, *Catal. Sci. Technol.* **3**, 1750 (2013).
- [38] C. Zhan, B. W. Liu, Y. F. Huang, S. Hu, B. Ren, M. Moskovits, and Z. Q. Tian, *Disentangling Charge Carrier from Photothermal Effects in Plasmonic Metal Nanostructures*, *Nat. Commun.* **10**, (2019).



## **Chapter 5**

### **Conclusions and outlook**

## 5.1. Conclusions

This thesis was focused on the synthesis and fundamental study of Ni-based catalysts for plasmon-assisted chemical reactions for a more efficient production of renewable fuels. First at all, we have been centered on the processes taking place in a light-assisted thermochemical reaction for methane synthesis. Secondly, we have paid our attention to the processes occurring under illumination during the electrochemical hydrogen production. Finally, we have highlighted the role played by the nanostructured configuration of the plasmonic Ni-based catalyst.

Thereby, the work covered the following issues: i) synthesis and use of Ni/CeO<sub>2</sub> catalyst for light-assisted CO<sub>2</sub> methanation reaction; ii) fabrication and application of Ni nanoparticle-based photoactive cathode for hydrogen evolution reaction; iii) optimization and optical characterization of Ni nanohole arrays and their utilization in laser-assisted iodate electrochemical reduction. Accordingly, the main conclusions of the thesis are divided into the corresponding sections and can be summarized as follows:

### I.

- Ni/CeO<sub>2</sub> catalyst, obtained by replication of mesoporous SBA-15 silica template demonstrated excellent catalytic properties with 80% CO<sub>2</sub> conversion and 95% selectivity to methane. The catalyst consisted from high-surface-area CeO<sub>2</sub> support with highly dispersed Ni nanoparticles, which facilitated the CO<sub>2</sub> methanation due to large Ni/CeO<sub>2</sub> interface. The specific morphology promoted reduction of the CeO<sub>2</sub> support and increased the amount of Ce<sup>3+</sup> active sites for CO<sub>2</sub> coordination and activation.
- The catalyst showed excellent photothermal properties due to strong absorption in the visible and IR range of the solar spectrum as a consequence of a plasmon resonance in Ni nanoparticles. Under solar light illumination the methanation reaction rate was increased up to 2.4 times compared to the dark conditions at the initial operation temperature of 200°C. On the other hand, the increase in the catalytic activity under irradiation has led to decrease in the power consumption by 20%.
- In-situ DRIFTS and HRTEM/EELS analysis revealed that the mechanism of CO<sub>2</sub> methanation was associative, occurring through the coordination of CO<sub>2</sub> on ceria support which is further

hydrogenated to methane by hydrogen, previously dissociated on the Ni nanoparticles. Further in-situ HRTEM/EELS investigation has demonstrated the importance of high Ni nanoparticles dispersion due to key role of Ni/CeO<sub>2</sub> interface in the CO<sub>2</sub> hydrogenation.

- It has been proved that solar light had a dual effect on the Ni/CeO<sub>2</sub> catalyst: i) the visible part of the solar spectrum excited LSPR in the Ni nanoparticles, which was quickly damped and resulted in strong local heating; ii) the blue and UV light activated the ceria support, exciting electrons and providing them to the active sites of ceria. This promoted the creation of formates, being intermediates for methane production. Despite the electronic effect of light, the methanation reaction was fully controlled by the photothermal process due to limited supply of hydrogen atoms.

## II.

- Wetness impregnation of mesoporous SBA-15 silica template allowed to obtain elongated Ni nanoparticles with several ratios which demonstrated a broad plasmon mode in the visible light range. The Ni NPs deposited over an FTO electrode showed a strong photothermal effect under concentrated solar illumination, reaching 93°C after 5 min under incident power of 0.5 W cm<sup>-2</sup>.
- Pulsed illumination has revealed two main processes in the mechanism of light-induced reaction enhancement at low current densities: i) enhanced electron transfer due to strong plasmonic heating and ii) thermal energy dissipation from the electrode to the electrolyte. At the initial stage of the illumination, the excited plasmons were efficiently damped, in the timescale up to 10 ns, resulting in a strong local heating of the nanoparticles. This led to prevalence of the H atoms adsorption on the Ni surface due to facile electron transfer, and resulted in deceleration of the reaction, changing the rate-limiting step to hydrogen desorption. With time, the heat diffusion to the electrolyte created a new nickel/electrolyte equilibrium, which controlled the overpotential value under further illumination.
- Irradiation of the Ni-NPs cathode with concentrated solar light (0.5 W cm<sup>-2</sup>) has led to a 27% increase in the current density at the working potential E<sub>w</sub> = 0.2 V vs. RHE. Moreover, a 40 s pulse of light in galvanostatic conditions (j = 0.15 mA cm<sup>-2</sup>) resulted in decrease of the overpotential by 185 mV with negligibly small overall heating of the cell.

### III.

- Langmuir-Blodgett procedure was successfully employed to produce ordered arrays of polystyrene nanosphere films, used as a mask for Ni and Ag NHA synthesis. Geometrical parameters of the periodic structure (periodicity, nanohole diameter and metal layer thickness) were tuned to achieve distinguished SPP modes in the visible light range. Angle-dependent measurements confirmed the plasmonic nature of the extraordinary transmission peaks.
- The blue shift of SPP modes in Ni NHAs with decreasing of the hole size is explained by introducing the effective dielectric permittivity of the perforated metallic film. On contrary, the SPP mode in Ag NHAs is red-shifted, which is attributed to the strong coupling of SPP with LSPR modes in the nanoholes.
- The Ni NHAs were used as a photoactive cathode in electrochemical reduction of iodate ion to iodine under pulsed laser illumination. The comparison of Ni NHAs with flat samples with similar absorption and active surface area revealed improved catalytic activity under laser irradiation with resonant wavelength, demonstrating an average gain in the current density of 25%. Moreover, the current density response depended on the incident wavelength and matched the optical spectra of the Ni NHAs, confirming the plasmonic nature of the reaction enhancement. Analysis of the current density variation under pulsed illumination indicated photothermal effect of the surface plasmon on the electrochemical reaction.

To summarize, this work has shown that plasmonic properties of Ni can advantageously complement its excellent catalytic activity and significantly enhance chemical reactions by applying solar light as a renewable energy source, reducing the cost of supplied energy. Photothermal effect was found to be the main consequence of the plasmon resonance in Ni nanostructures, which, although often considered detrimental, was used as a driving force in the improvement of catalytic reactions. The results, obtained in this work, emphasize the benefits of Ni utilization as an alternative plasmonic material in catalysis and open a new pathway for combined approaches to catalytic reactions for renewable fuels.

## 5.2. Outlook and future work

Plasmon-assisted catalysis based on transition metals is an emerging field, which requires further investigation of the enhancement mechanisms and optimization of the catalysts and operating reactors, suitable for the combined photo-thermal and photoelectrochemical approaches. Based on the results obtained in this work, the following objectives are to be addressed in future research:

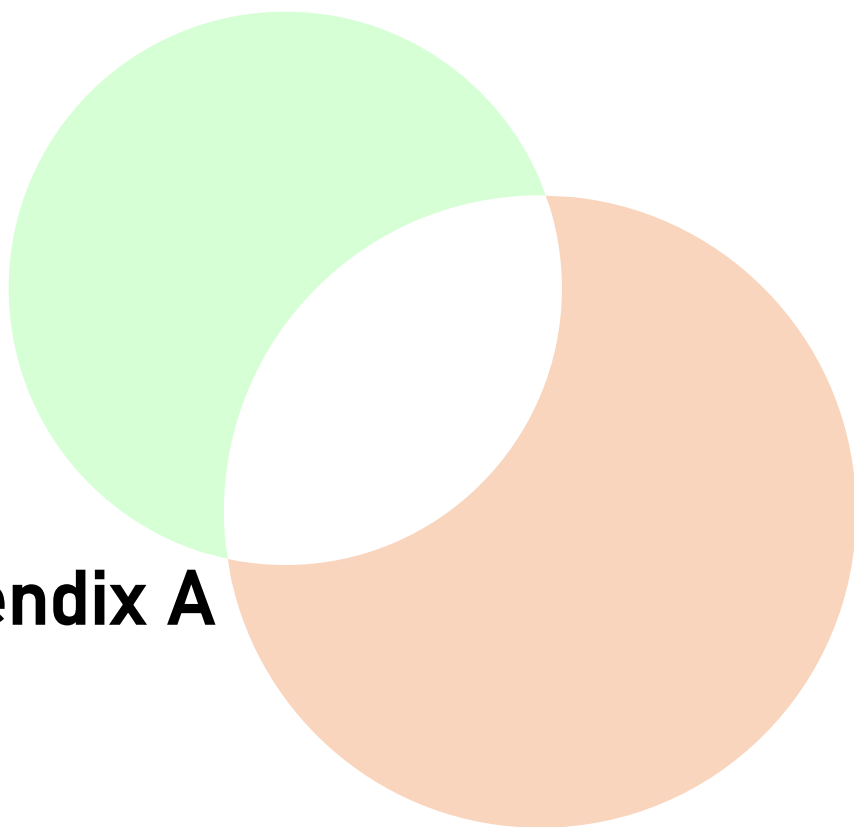
- Further optimization of the Ni-based plasmonic catalysts needs to be done keeping in mind three main goals: i) higher dispersion of Ni nanoparticles to ensure better interaction between the nanoparticles and support; ii) better size and shape control over the Ni nanoparticles in order to tune the resonant frequency of the LSPR; iii) combination of Ni active phase with other metals to take advantage of both hot-electron and photothermal plasmon consequences. Likewise, the obtained knowledge should be extended to the use of other non-ideal plasmonic materials with high catalytic activities.
- A more detailed study of the fundamental processes in plasmonic catalysts will reveal pathways for their nanostructured optimization. Thus, first-principle calculations for investigation of the CO<sub>2</sub> methanation and HER rate-determining steps under photon excitation are crucial to confirm and understand the reaction mechanisms. Finite element method (FEM) and finite-difference time-domain (FDTD) approaches to Maxwell equations solution should be performed to simulate the light-matter interaction in Ni nanostructures of various sizes and shapes.
- Apart from the catalyst, the reactor design plays a key role in the efficiency of the plasmon-assisted reactions. An optimized flow-type reactor is necessary to avoid slow water desorption in order to exploit the new light-induced CO<sub>2</sub> methanation route at higher illumination intensities and conversion rates. Similarly, an optimized electrochemical cell with precise temperature control can facilitate the distinction between photothermal and charge-induced processes.
- Moreover, in order to fully optimize the P2G cycle, one needs to address the most energy demanding part of the process: oxygen evolution reaction. In the future work, plasmonic Ni nanoparticles and/or Ni NHAs could be combined with a semiconductor photoactive material in a complex

photoanode to achieve synergetic effects of enhanced solar light absorption and improved catalytic activity.

- Finally, to prove feasibility of the developed catalytic systems the photoactive Ni catalyst needs to be implemented in a full stand-alone electrolyzer for photo-assisted water splitting. The produced hydrogen can be further mixed with preliminarily captured carbon dioxide and forwarded to a built-in methanation reactor. Also, at device level, light and heat management should be optimized with innovative designs.



# Appendix A



## Appendix A.1. Supplementary catalyst characterization

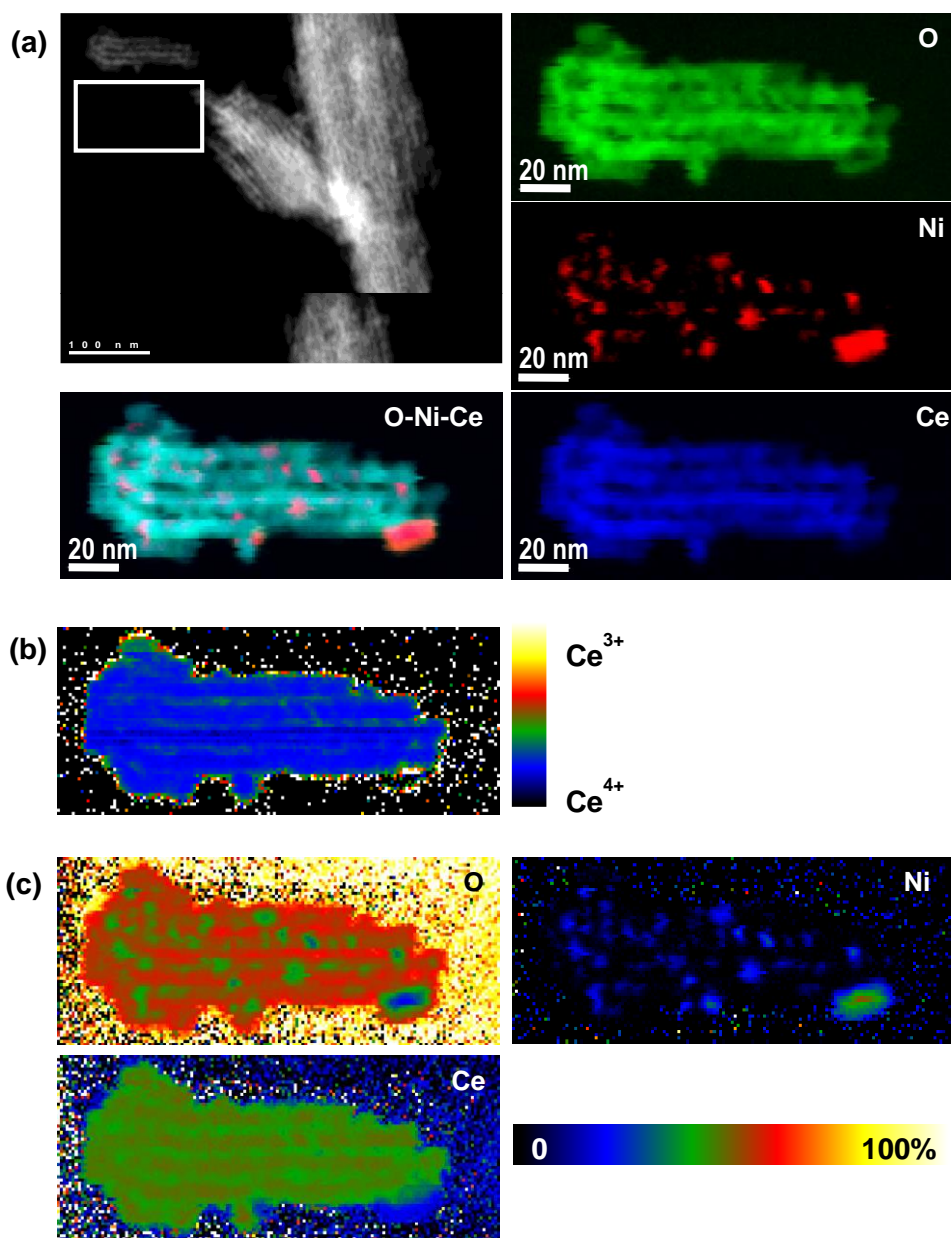


**Figure A.1.1.** (a) HAADF STEM image of the sample and STEM-EELS elemental maps obtained on the selected areas as indicated in the white box. The maps shown in the Spectrum Images have been obtained by using: O k-edge at 532 eV (green), Ni L-edge at 855 eV (red) and Ce M-edge at 883 eV (blue), as well as composites of O-Ni-Ce. Scale bar = 20 nm. (b) Ce M<sub>5</sub>/M<sub>4</sub> intensity ratio map. (c) Relative intensity maps of the different elements.

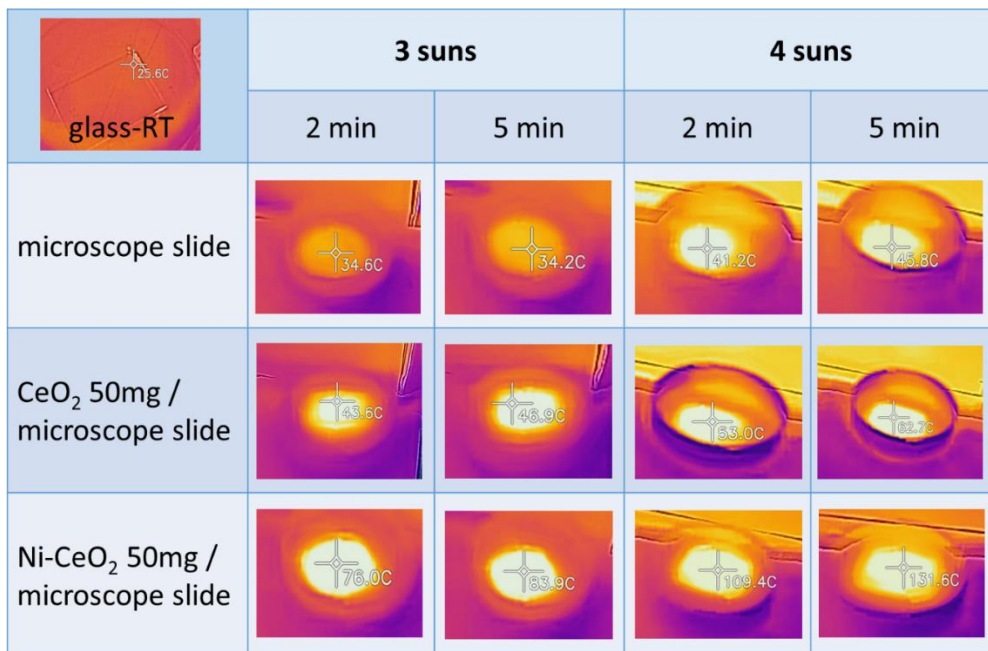


**Figure A.1.2.** IR-camera measured temperature of 50 mg of bare CeO<sub>2</sub> powder and Ni/CeO<sub>2</sub> catalyst under solar light irradiation (0.3 and 0.4 W cm<sup>-2</sup>) starting from room temperature during 2 and 5 minutes. The temperature change of the microscope slide as well as its reference room temperature is given for comparison.

**Table A.1.1.** Temperature increase of the Ni/CeO<sub>2</sub> catalyst under various illumination intensities and ranges at different starting temperature points

Starting temperature, °C	Light intensity, W cm <sup>-2</sup>	Illumination range	Temperature increase, °C
200	0.3	visible	4
200	0.3	full	10
200	0.4	visible	5
200	0.4	full	15
200	0.5	visible	6
200	0.5	full	19
225	0.3	visible	4
225	0.3	full	10
225	0.4	visible	6
225	0.4	full	17
225	0.5	visible	7
225	0.5	full	21
250	0.3	visible	4
250	0.3	full	11

250	0.4	visible	9
250	0.4	full	26
250	0.5	visible	12
250	0.5	full	32

**Table A.1.2.** CO<sub>2</sub> conversion and CH<sub>4</sub> selectivity for different operation conditions

Operation conditions	CO <sub>2</sub> conversion, %	CH <sub>4</sub> selectivity, %
200°C	1.6	95.2
200°C+3suns-vis	1.9	95.8
200°C+3suns	2.4	95.8
200°C+4suns-vis	2.0	95.0
200°C+4suns	2.5	95.1
200°C+5suns -vis	2.7	95.5
200°C+5suns	4.6	96.5
225°C	5.8	95.2
225°C+3suns-vis	7.0	97.1
225°C+3suns	8.9	95.6
225°C+4suns-vis	7.3	95.5
225°C+4suns	8.5	96.0
225°C+5suns -vis	7.9	97.8
225°C+5suns	13.0	98.0
250°C	16.0	96.5
250°C+3suns-vis	19.0	97.9
250°C+3suns	22.3	98.0
250°C+4suns-vis	19.5	97.2
250°C+4suns	23.1	97.4
250°C+5suns -vis	22.7	98.5
250°C+5suns	29.4	98.6

**Table A.1.3.** Relative intensities of the illumination ranges used in this work

Illumination range	Wavelength range, nm	Relative intensity, %
Full spectrum	250-2200	100
UV	250-400	10.5%
Visible	400-800	27.2%
IR	850-2200	22.3%
Visible+IR	400-2200	80.1%

## Appendix A.2. Transmission spectra of the optical long-pass filters

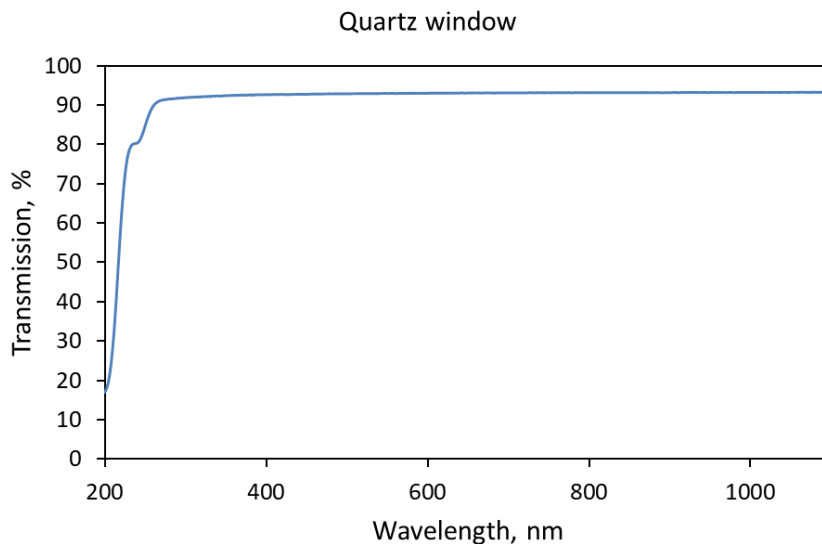


**Figure A.2.1** Transmission spectrum of the reactor quartz window

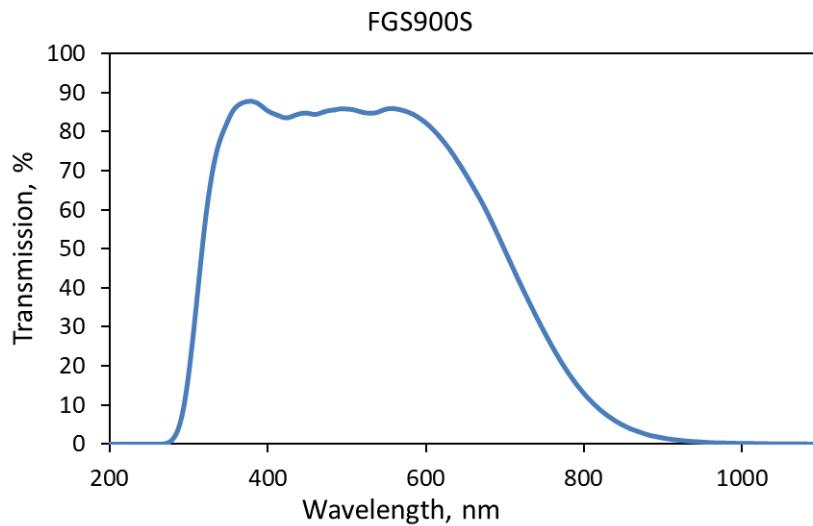


**Figure A.2.2.** Transmission spectrum of the FGS900S filter

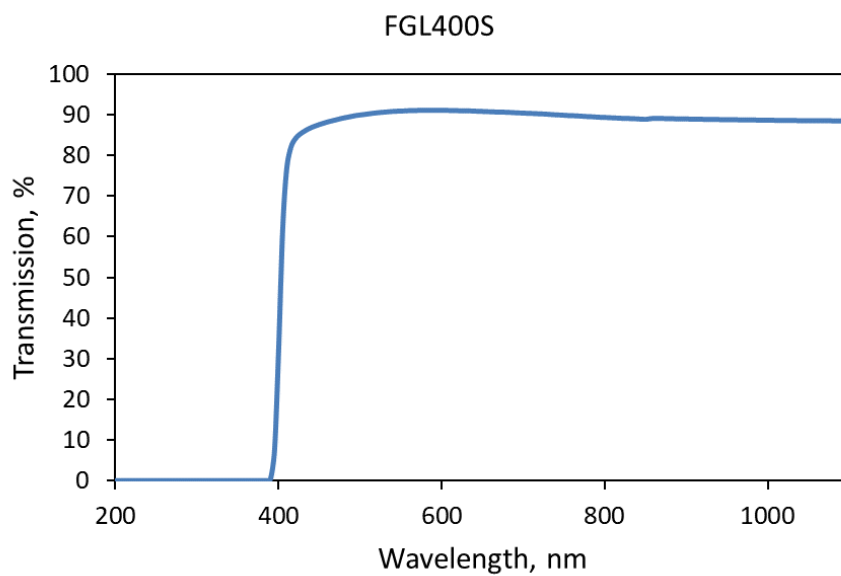


**Figure A.2.3.** Transmission spectrum of the FGL400S filter

## Appendix A.3. Supplementary in-situ HRTEM/EELS characterization

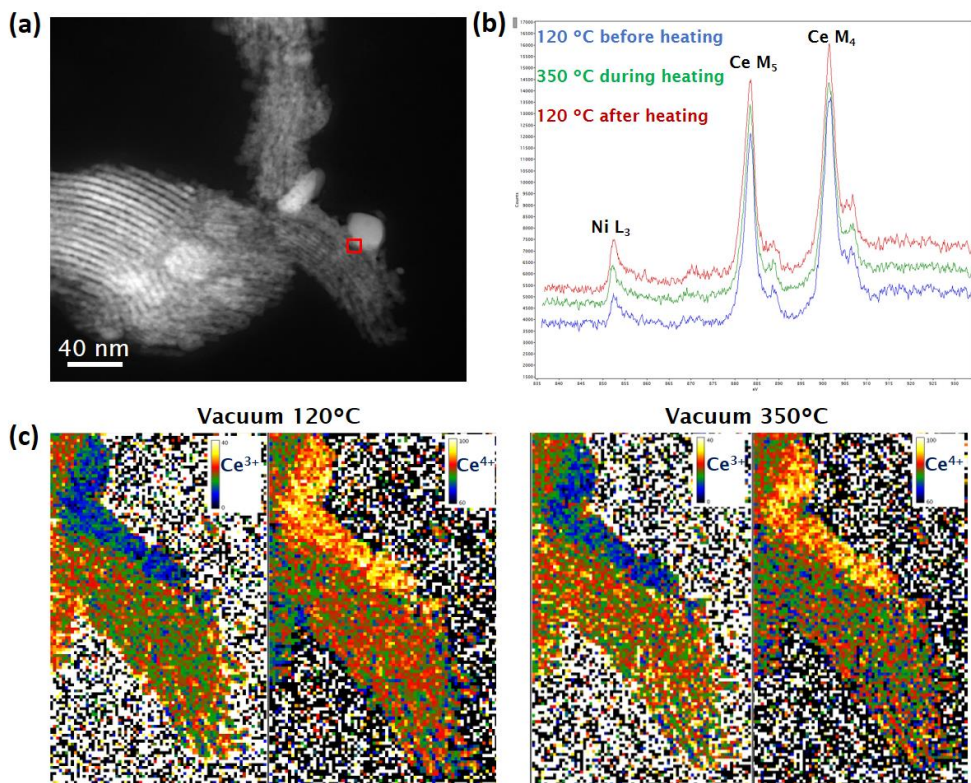


**Figure A.3.1.** (a) HAADF-STEM image of Ni/CeO<sub>2</sub> catalyst; (b) EELS spectra of the zone shown by a red box in (a) under corresponding conditions; (c) EELS Ce oxidation state mapping in vacuum at 120 °C and 350 °C.

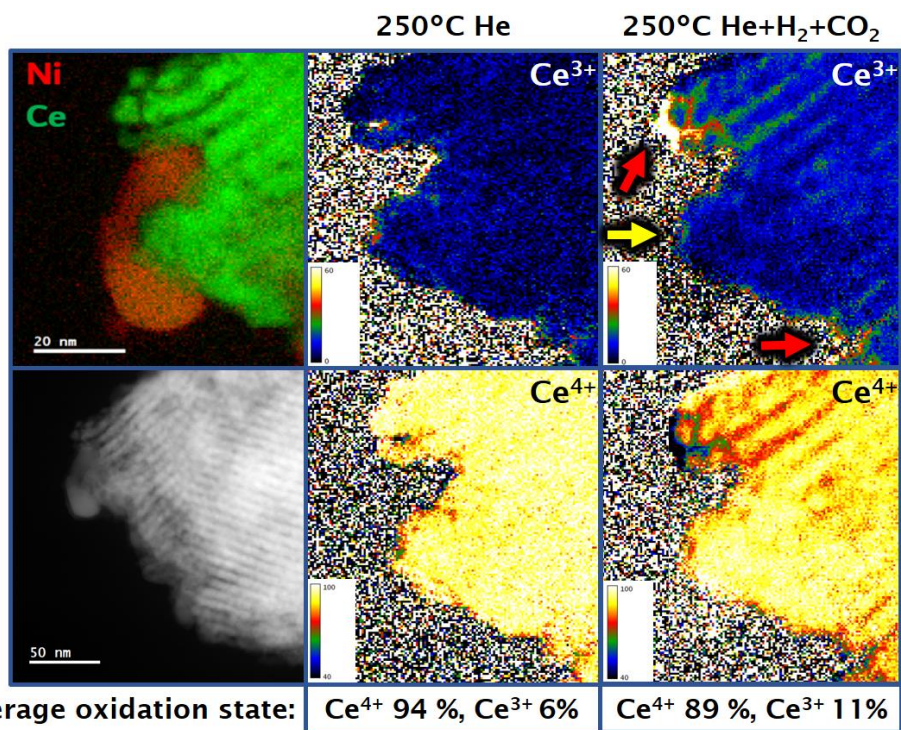
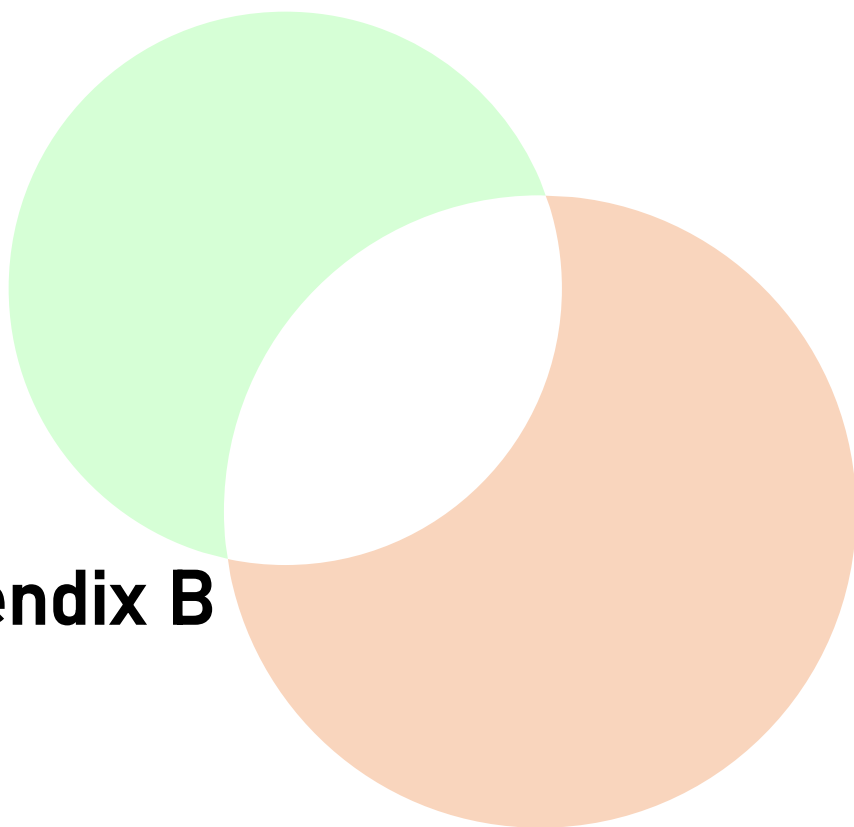


**Figure A.3.2.** STEM EELS composition map (top) and HAADF STEM image of Ni/CeO<sub>2</sub> catalyst (bottom). EELS oxidation state maps for Ce under He and He:CO<sub>2</sub>:H<sub>2</sub> gas mixture at 250°C are shown on the middle and right panels. Red arrows show the zones of high Ce<sup>3+</sup> concentration, and the yellow arrow points to the zone where Ni NP resides.



# Appendix B



## Appendix B.1. Supplement catalyst characterization

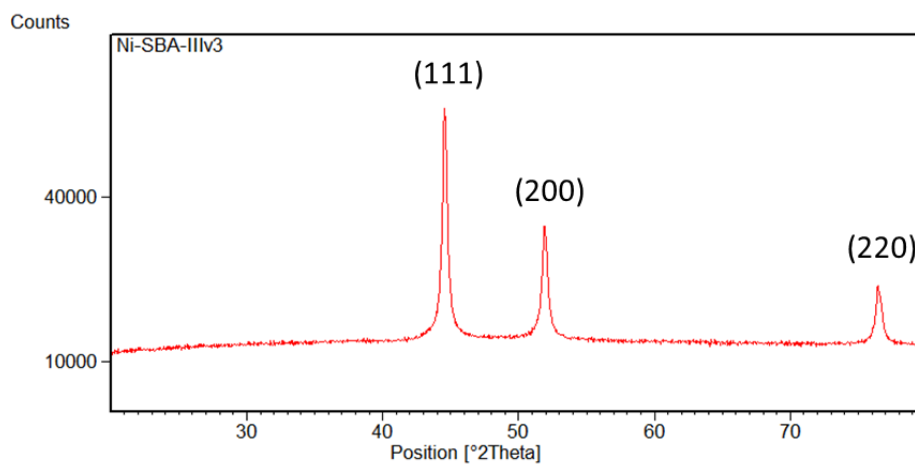


Figure B.1.1. XRD diffractogram of the synthesized Ni catalyst.

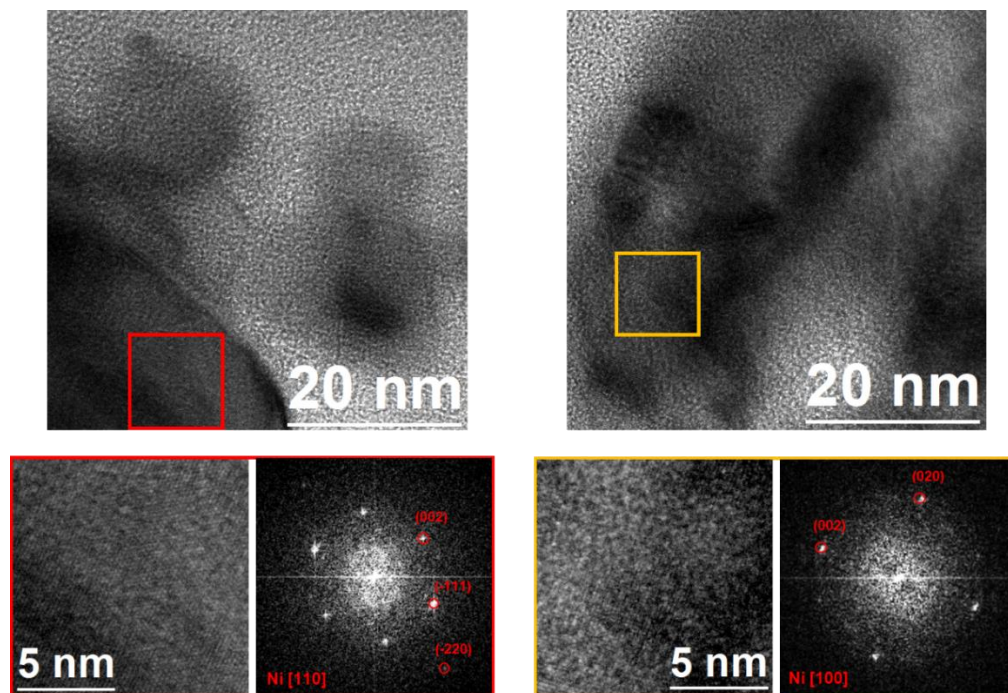
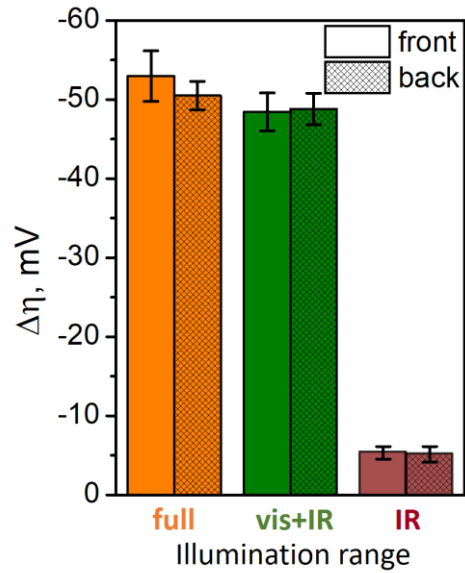
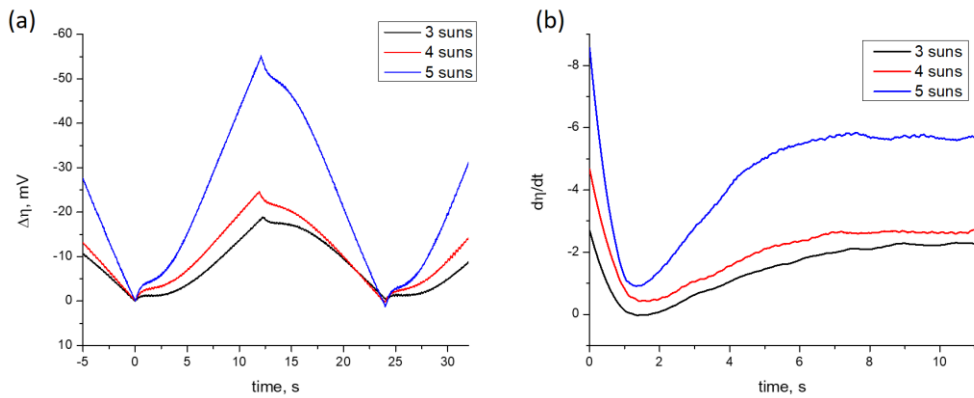


Figure B.1.2. HRTEM structural characterization of Ni nanoparticles. Ni nanorods are crystalline and present a cubic FCC structure (space group Fm-3m, 225). As shown in the images, the FFT proves the [110] and [100] axis of this crystalline phase.



**Figure B.1.3.** Peak overpotential variation value under the 12 s light pulses depending on the illumination range using front and back illumination of the electrode. The values were corrected on the transmittance of the filters used to cut the light range.



**Figure B.1.4.** (a) Change of the overpotential depending on the irradiation power density ( $j = -0.15 \text{ mA cm}^{-2}$ , light duration = 12s); (b) change of the overpotential derivative with time for different irradiation power densities.

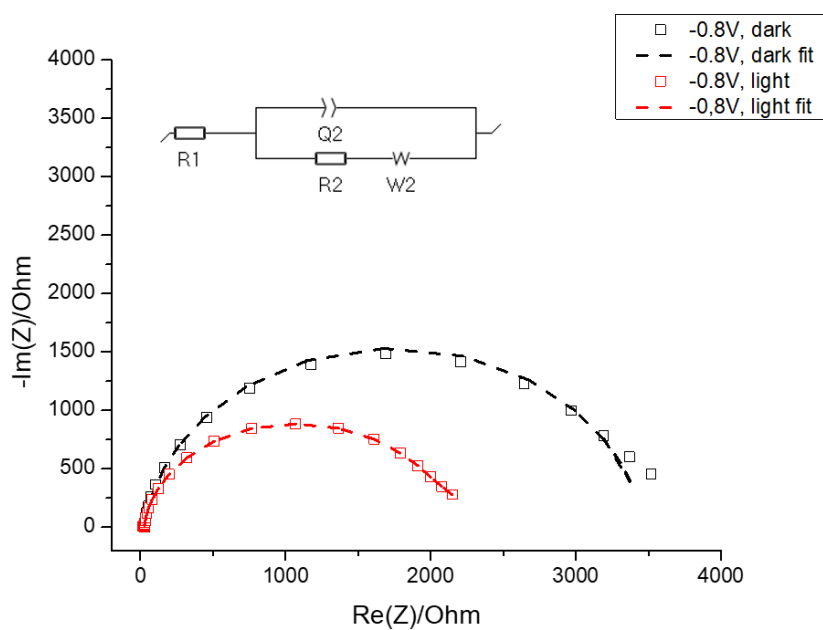


**Figure B.1.5.** Impedance spectra of the Ni electrode under constant working potential  $E_{we} = -0.8$  V under dark and illuminated conditions and the corresponding equivalent circuit.

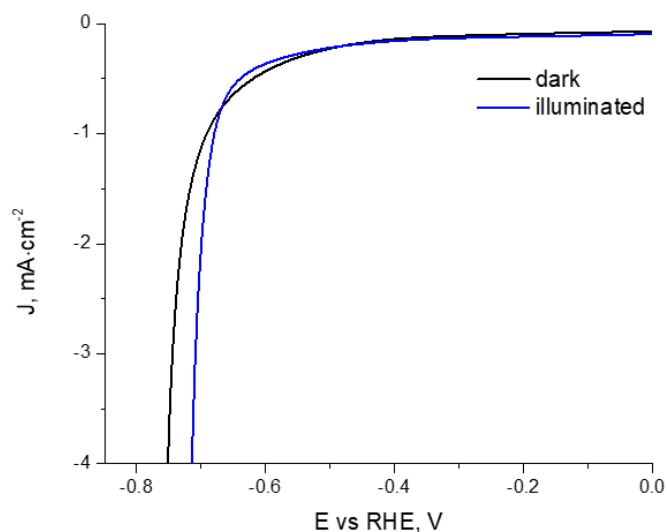
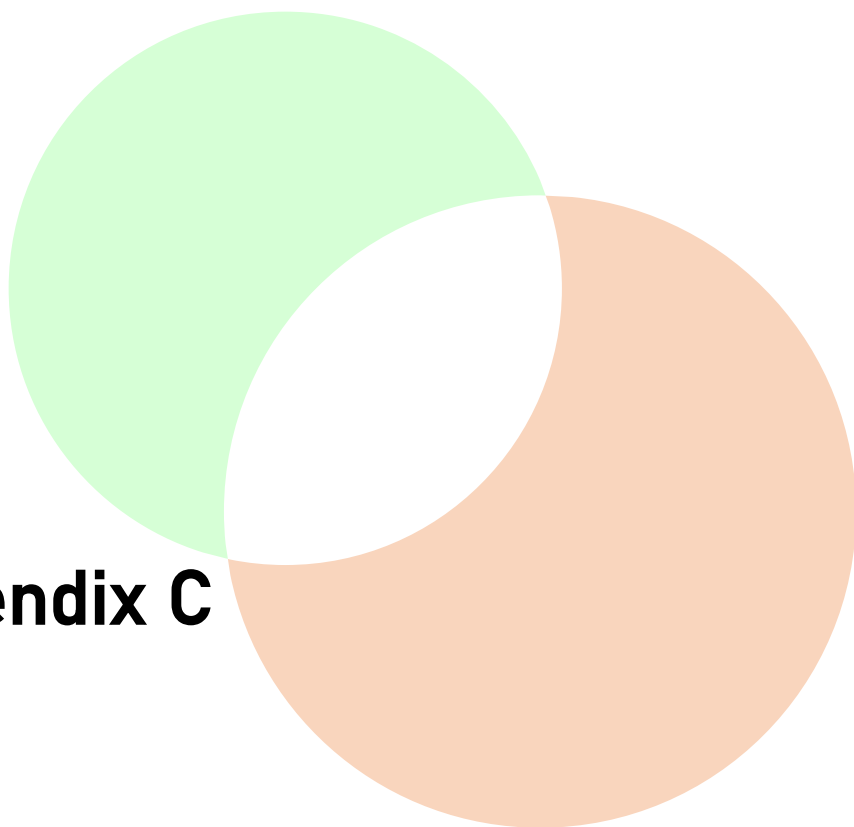


**Figure B.1.6.** Linear sweep voltammetry of the Ni electrode under dark conditions and under solar illumination ( $0.5 \text{ W cm}^{-2}$ ).

# Appendix C



### Appendix C.1. Theoretical calculations of the plasmon resonance wavelength angular dependence in the hexagonal metallic NHA.

If the incident light excites the plasmon along the  $\vec{x}$ -direction ( $\cos \varphi = 1$ ), the angular dispersion relation can be derived in the following way:

$$\vec{G}_x = \frac{4\pi}{\sqrt{3}L} \vec{x}, \quad \vec{G}_y = \frac{2\pi}{\sqrt{3}L} \vec{x} + \frac{2\pi}{L} \vec{y}$$

$$\vec{k}_{SPP} = |\vec{k}_0| \sin \theta \vec{x} + i \frac{4\pi}{\sqrt{3}L} \vec{x} + j \frac{2\pi}{\sqrt{3}L} \vec{x} + j \frac{2\pi}{L} \vec{y}$$

$$\begin{aligned} |\vec{k}_{SPP}|^2 &= \left( \frac{2\pi}{\lambda} \sin \theta + i \frac{4\pi}{\sqrt{3}L} + j \frac{2\pi}{\sqrt{3}L} \right)^2 + \left( j \frac{2\pi}{L} \right)^2 \\ &= \left( \frac{2\pi}{\lambda} \sin \theta + i \frac{4\pi}{\sqrt{3}L} \right)^2 + \left( \frac{2\pi}{\lambda} \sin \theta + i \frac{4\pi}{\sqrt{3}L} \right) \left( j \frac{4\pi}{\sqrt{3}L} \right) + \left( j \frac{4\pi}{\sqrt{3}L} \right)^2 \end{aligned}$$

If we divide both parts of the expression on  $|\vec{k}_0|^2$ , we will obtain:

$$\frac{|\vec{k}_{SPP}|^2}{|\vec{k}_0|^2} = \sin^2 \theta + \frac{2\lambda}{\sqrt{3}L} \sin \theta (i + 2j) + \frac{4\lambda^2}{3L^2} (i^2 + j^2 + ij)$$

Using the Bragg's condition, we can derive the following angular dependent dispersion relation:

$$\sin^2 \theta + \frac{2\lambda}{\sqrt{3}L} \sin \theta (i + 2j) + \frac{4\lambda^2}{3L^2} (i^2 + j^2 + ij) = \text{Re} \left[ \frac{\varepsilon_d \varepsilon_m(\lambda)}{\varepsilon_d + \varepsilon_m(\lambda)} \right]$$

In case of the incident light exciting the plasmon in the  $\vec{x} + \vec{y}$  direction ( $\cos \varphi = \frac{\sqrt{3}}{2}$ ), the angular dispersion relation can be derived as follows:

$$\vec{k}_{SPP} = |\vec{k}_0| \sin \theta \frac{\sqrt{3}}{2} \vec{x} + |\vec{k}_0| \sin \theta \frac{1}{2} \vec{y} + i \frac{4\pi}{\sqrt{3}L} \vec{x} + j \frac{2\pi}{\sqrt{3}L} \vec{x} + j \frac{2\pi}{L} \vec{y}$$

$$\begin{aligned} |\vec{k}_{SPP}|^2 &= \left( \frac{2\pi}{\lambda} \sin \theta \frac{\sqrt{3}}{2} + i \frac{4\pi}{\sqrt{3}L} + j \frac{2\pi}{\sqrt{3}L} \right)^2 + \left( \frac{2\pi}{\lambda} \sin \theta \frac{1}{2} + j \frac{2\pi}{L} \right)^2 \\ &= \left( \frac{\sqrt{3}\pi}{\lambda} \sin \theta + i \frac{4\pi}{\sqrt{3}L} \right)^2 + 2 \left( \frac{\sqrt{3}\pi}{\lambda} \sin \theta + i \frac{4\pi}{\sqrt{3}L} \right) \left( j \frac{2\pi}{\sqrt{3}L} \right) \\ &\quad + \left( j \frac{2\pi}{\sqrt{3}L} \right)^2 + \left( \frac{\pi}{\lambda} \sin \theta \right)^2 + 2 \frac{\pi}{\lambda} \sin \theta \cdot j \frac{2\pi}{L} + \left( j \frac{2\pi}{L} \right)^2 \end{aligned}$$

After dividing both parts of the expression on  $|\vec{k}_0|^2 = \left(\frac{2\pi}{\lambda}\right)^2$ , we will obtain:

$$\frac{|\vec{k}_{SPP}|^2}{|\vec{k}_0|^2} = \sin^2 \theta + \frac{2\lambda}{L} \sin \theta (i + j) + \frac{4\lambda^2}{3L^2} (i^2 + j^2 + ij)$$

The final angular dependent dispersion relation for the light exciting the plasmon in the  $\vec{x} + \vec{y}$  direction is:

$$\sin^2 \theta + \frac{2\lambda}{L} \sin \theta (i + j) + \frac{4\lambda^2}{3L^2} (i^2 + j^2 + ij) = \text{Re} \left[ \frac{\varepsilon_d \varepsilon_m(\lambda)}{\varepsilon_d + \varepsilon_m(\lambda)} \right]$$

## Appendix C.2. Supplementary characterization results

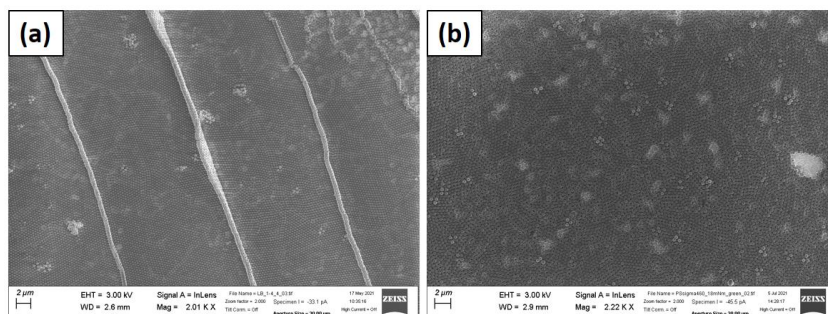


**Figure C.2.1.** Defects on the LB films deposited at the pressure (a)  $20 \text{ mN m}^{-1}$  and (b)  $10 \text{ mN m}^{-1}$ .

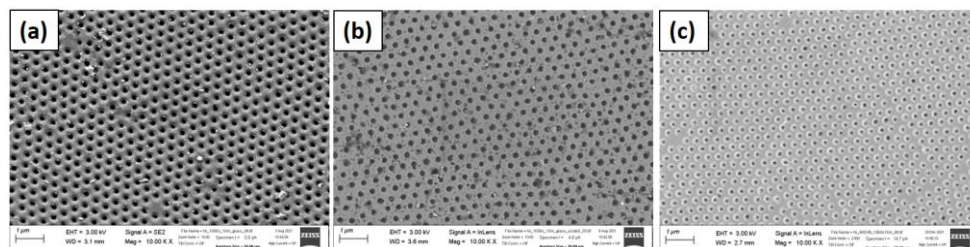


**Figure C.2.2.** Low-magnification (10,000X) SEM images of Ni NHAs with (a) 5 min, (b) 10 min and (c) 15 min of plasma treatment.

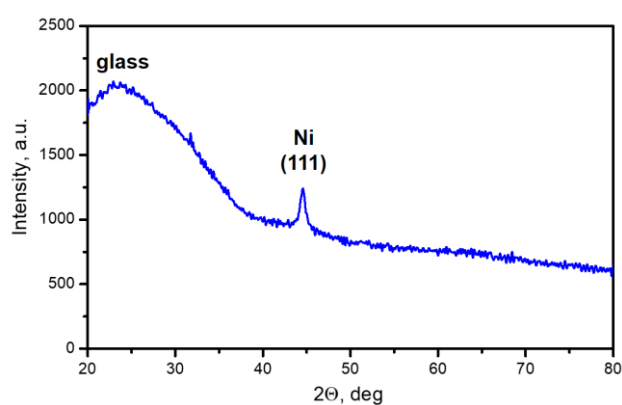


**Figure C.2.3.** XRD diffractogram of the Ni NHA ( $p = 420 \text{ nm}$ ,  $d = 100 \text{ nm}$ ,  $\phi = 160 \text{ nm}$ ) on the glass substrate.



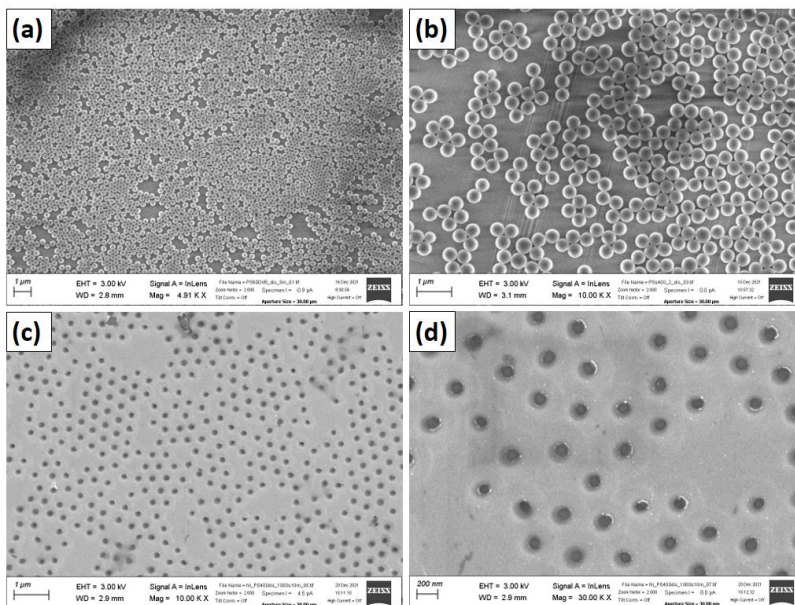


**Figure C.2.4.** (a-b) PS spheres monolayers that were obtained by “fishing”; (c-d) non-periodic Ni NHAs.

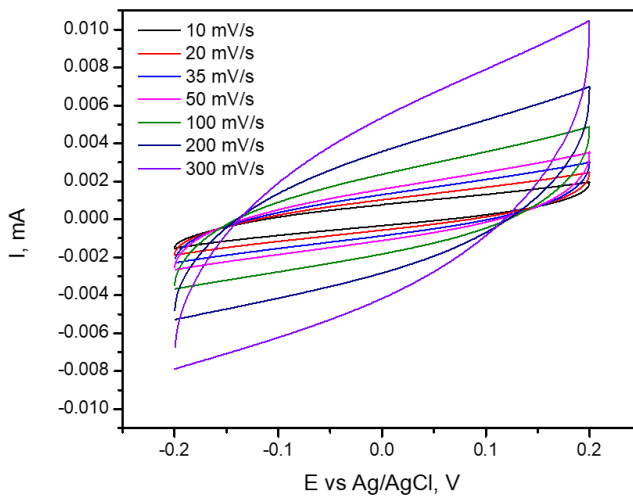


**Figure C.2.5.** Typical CVs of Ni NHA electrodes measured for ECSA comparison

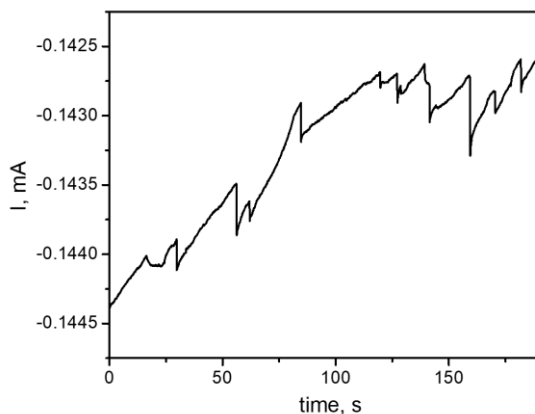


**Figure C.2.6.** Baseline of the current density value over the 5mm<sup>2</sup> of the Ni NHA for HER.

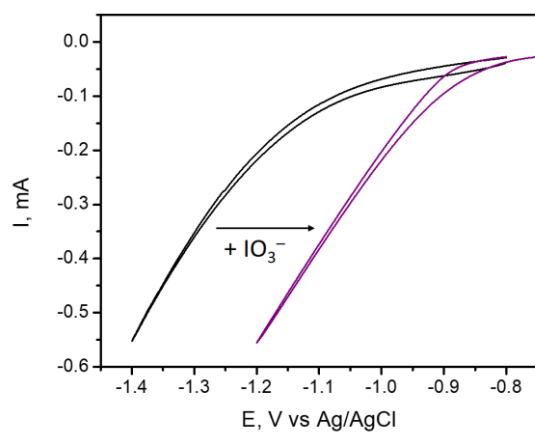


**Figure C.2.7.** Change of the CV of Ni NHA with addition of the  $\text{IO}_3^-$  electron scavenger

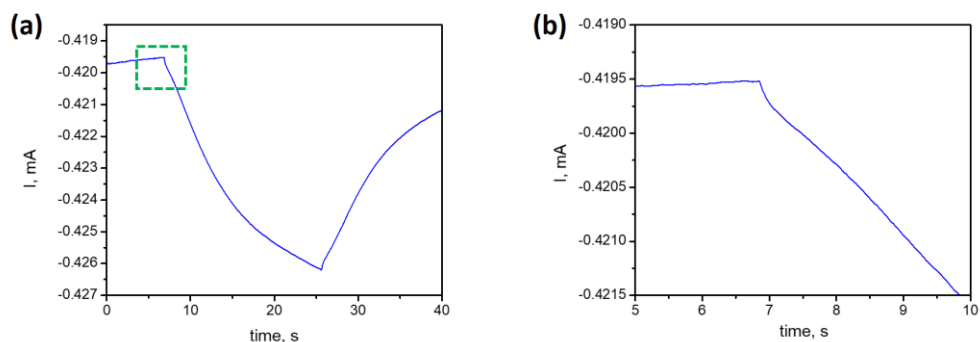


**Figure C.2.8.** (a) Current density variation under the light pulse (532 nm) with duration  $t = 20$  s at the working potential  $E_{we} = -1.3$  V vs. Ag/AgCl; (b) magnified part of the curve highlighted by a green square.

## Appendix C.3. Numerical modeling of metallic NHA optical properties.

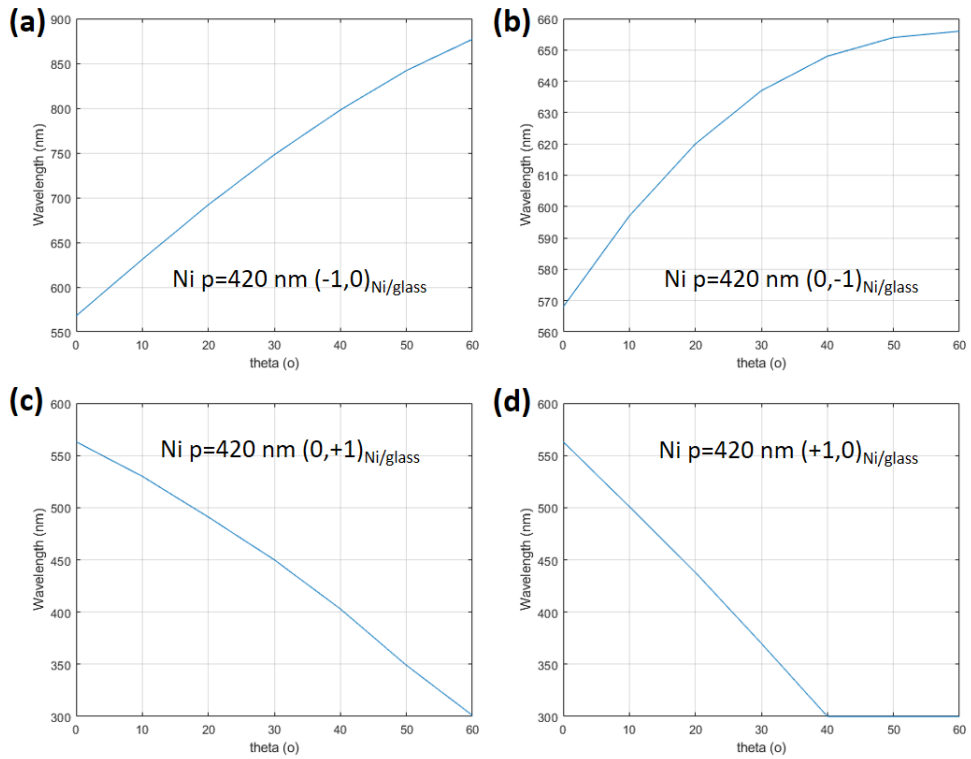


**Figure C.3.1.** Angular dependence of (a)  $(-1,0)_{\text{Ni/glass}}$ , (b)  $(0,-1)_{\text{Ni/glass}}$ , (c)  $(0,+1)_{\text{Ni/glass}}$  and (d)  $(+1,0)_{\text{Ni/glass}}$  SPP modes for the Ni NHA with periodicity  $p = 420$  nm.

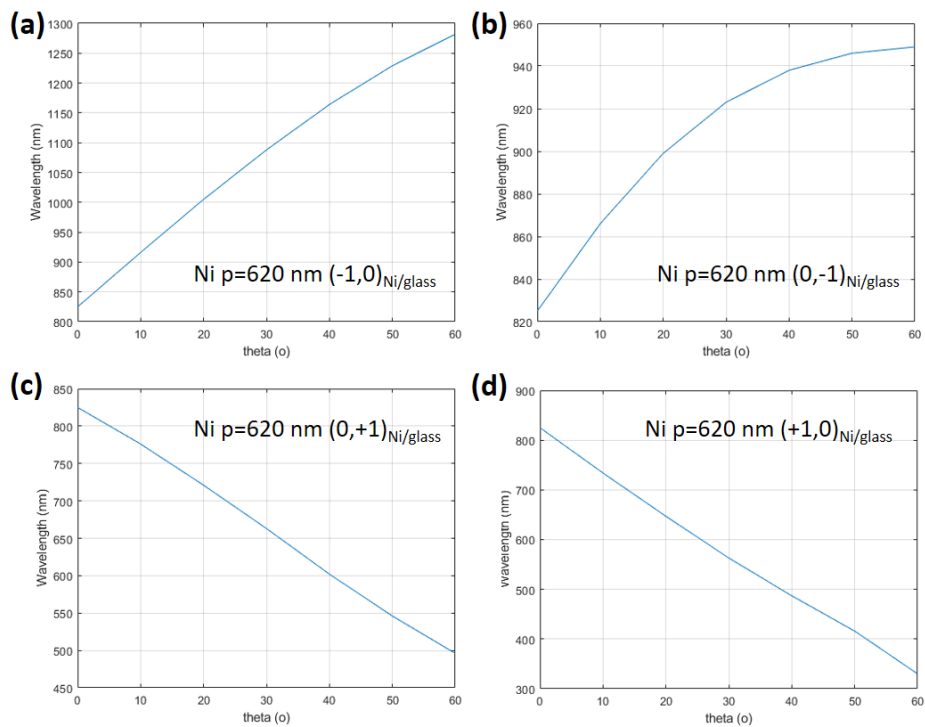


**Figure C.3.2.** Angular dependence of (a)  $(-1,0)_{\text{Ni/glass}}$ , (b)  $(0,-1)_{\text{Ni/glass}}$ , (c)  $(0,+1)_{\text{Ni/glass}}$  and (d)  $(+1,0)_{\text{Ni/glass}}$  SPP modes for the Ni NHA with periodicity  $p = 620$  nm.

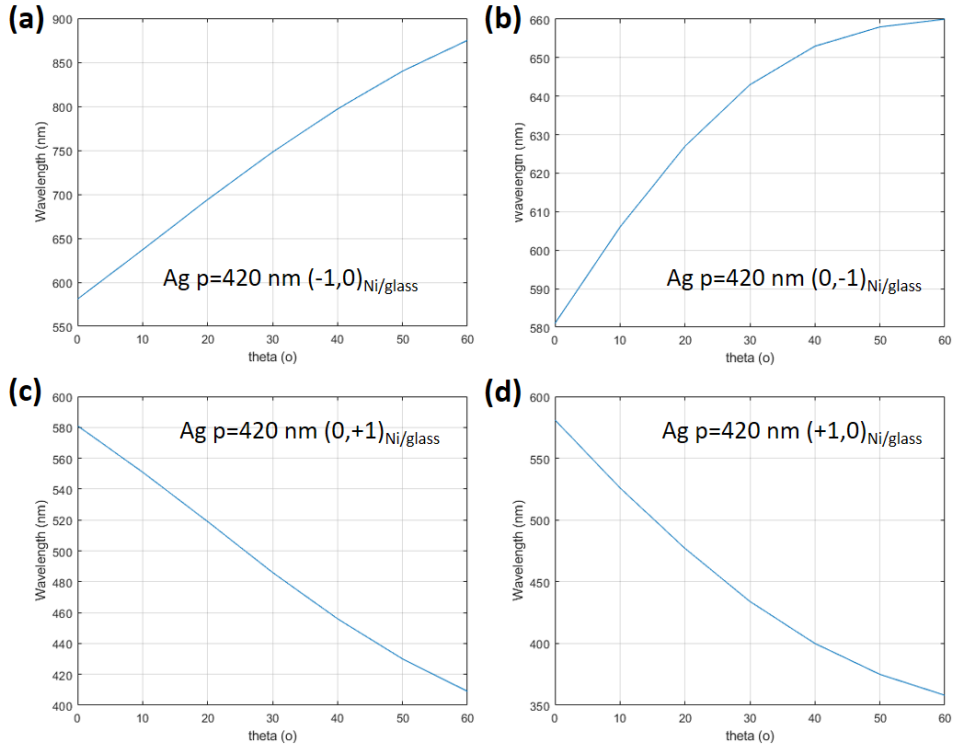


**Figure C.3.3.** Angular dependence of (a)  $(-1,0)_{\text{Ag/glass}}$ , (b)  $(0,-1)_{\text{Ag/glass}}$ , (c)  $(0,+1)_{\text{Ag/glass}}$  and (d)  $(+1,0)_{\text{Ag/glass}}$  SPP modes for the Ag NHA with periodicity  $p = 420$  nm.

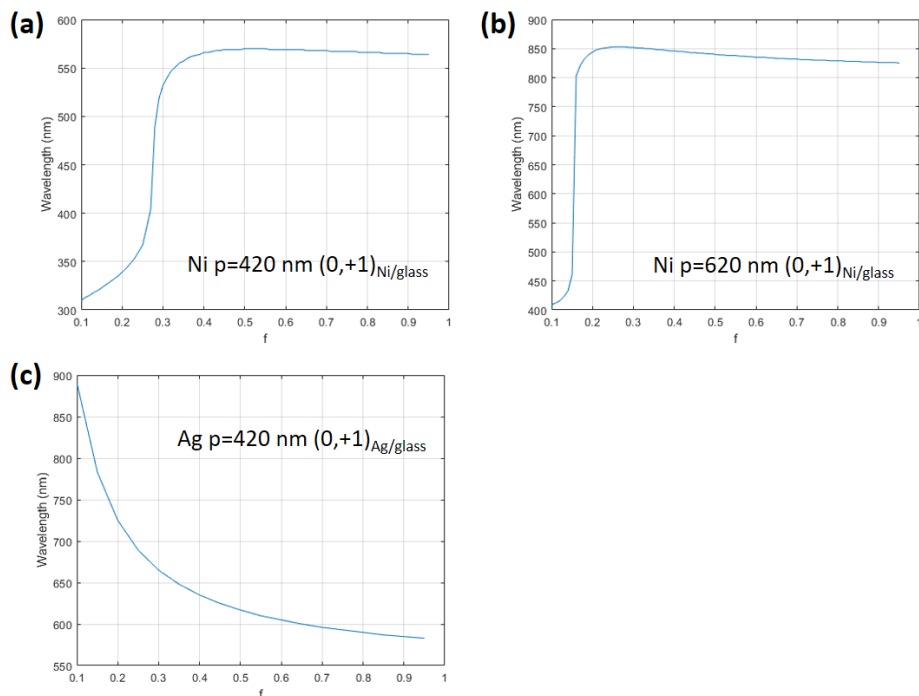
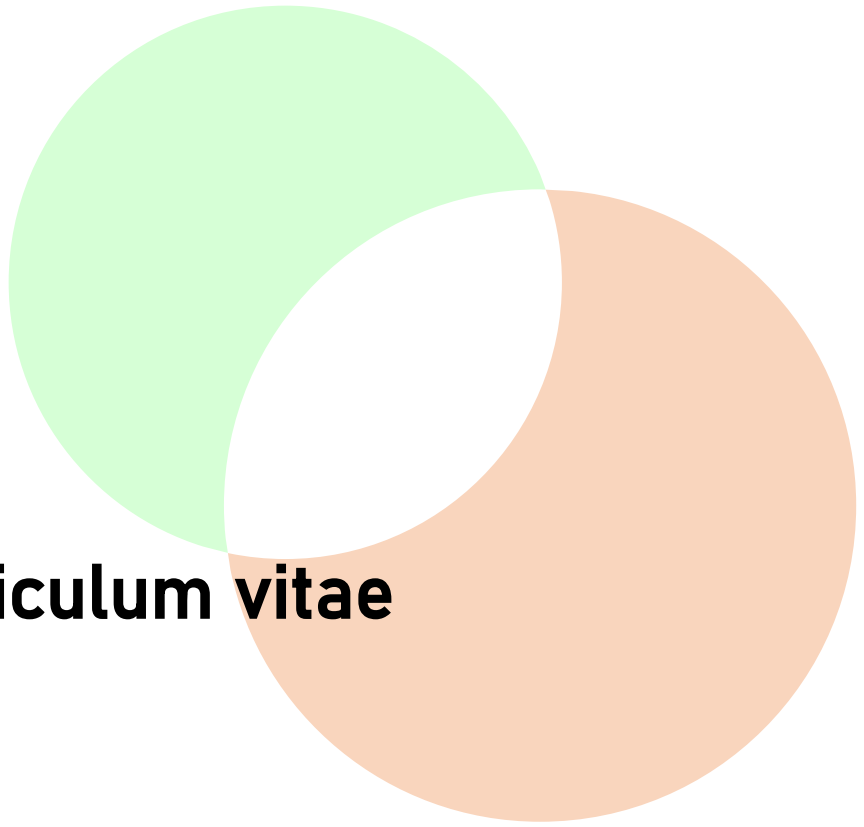


**Figure C.3.4.** Change of the (0,+1) SPP metal/glass mode with the filling factor (Equation 4.6) for (a) Ni  $p = 420$  nm NHA; (b) Ni  $p = 620$  nm NHA; (c) Ag  $p = 420$  nm NHA.



# **Curriculum vitae**

## Viktorija Golovanova

### Personal information

---

**Date of birth:** 18.06.1995

**Nationality:** Ukrainian

**Email:** viktorija.v.golovanova@gmail.com

**ORCID:** 0000-0002-4008-0733

**ResearcherID:** A-2539-2019

**Scopus Author ID:** 55893634400

### Education

---

2018 – present

#### **PhD in Material Science**

Thesis: *Plasmon-enhanced catalytic reactions for renewable fuels*

Autonomous University of Barcelona (UAB)

Barcelona, Spain

2015 – 2016

#### **Master of Science in Theoretical Physics**

Odessa National University (ONU)

Odessa, Ukraine

2011 – 2015

#### **Bachelor of Science in Theoretical Physics**

Odessa National University (ONU)

Odessa, Ukraine

### Professional experience

---

2021 – present

#### **Laboratory Assistant**

Catalonia Institute for Energy Research (IREC)

Barcelona, Spain

2018 – 2021

#### **Marie Curie Early Stage Researcher**

Catalonia Institute for Energy Research (IREC)

Barcelona, Spain



2016 – 2017

**Visiting Researcher**

Tampere University (TUNI)  
Tampere, Finland

2016 – 2018

**Researcher**

South-Ukrainian University (SUU)  
Odessa, Ukraine

Internships

---

2021

**ICFO (Institut de Ciències Fotòniques)**

Castelldefels, Spain

2018

**TUNI (Tampere University)**

Tampere, Finland

2012 – 2013

**TUT (Tampere University of Technology)**

Tampere, Finland

Awards

---

2016

First place in the All-Ukrainian student  
competition of scientific works

2016

Fifth place among the top 12 teams out of 700 in  
the world final round of the student training  
program Calculus, Taiwan

Publications

---

**V. Golovanova**, M.C. Spadaro, J. Arbiol, V. Golovanov, T.T. Rantala, T. Andreu, J.R. Morante, Effects of solar irradiation on thermally driven CO<sub>2</sub> methanation using Ni/CeO<sub>2</sub>-based catalyst, Appl. Catal. B 291 (2021) 120038.

C. Baratto, **V. Golovanova**, G. Faglia, H. Hakola, T. Niemi, N. Tkachenko, B. Nazarchuk, V. Golovanov, On the alignment of ZnO nanowires by Langmuir-Blodgett technique for sensing application, Appl. Surf. Sci 528 (2020) 146959.

**V. Golovanova**, B. Nazarchuk, O. Postnyi, T. Rantala, N. Tkachenko, V. Golovanov, Photoreactions of macrocyclic dyes on (1010) wurzite surface – Interplay between conformation and electronic effects, *Ukr. Phys. Journal* 64 (2019) 62-70.

K. Virkki, H. Hakola, M. Urbani, L. Tejerina, M. Ince, M. Diaz, T. Torres, **V. Golovanova**, V. Golovanov, and N. Tkachenko, Photoinduced electron injection from zinc phthalocyanines into zinc oxide nanorods – Aggregation effects, *Journal of Physical Chemistry C*, 121(17) (2017) 9594-9605.

V. Golovanov, **V. Golovanova**, N. Tkachenko, T. T. Rantala, Effects of orientation at the phthalocyanine – CdSe interface on the electron transfer characteristics, *Phys. Chem. Chem. Phys.*, 19 (2017) 10511-10517.

V. Golovanov, **V. Golovanova**, T. Rantala, Thermal desorption of molecular oxygen from SnO<sub>2</sub> (110) surface: Insights from first-principles calculations, *Journal of Physics and Chemistry of Solids*, 89 (2016) 15-22.

V. Golovanov, **V. Golovanova**, M. Kuisma and T. T. Rantala, Electron spin resonance parameters of cation vacancies in tin dioxide doped with fluorine and hydrogen, *Journal of Applied Physics*, 114 (2013) 143907.

## Conferences

---

**V. Golovanova**; T. Andreu; J.R. Morante, Photothermal approach to enhancing of the hydrogen production via water splitting, EMRS Fall Meeting 2021, 20-23 September, 2021 (online).

M. C. Spadaro; **V. Golovanova**; T. Andreu; J. R. Morante; J. Arbiol, Ceria-supported nickel catalyst for Sabatier reaction: a detailed nanoscopy investigation, Virtual Early Career European Microscopy Congress 2020 (EMC 2020), 24-26 November, 2020 (online)

C. Baratto; **V. Golovanova**; G. Faglia; Thi Thanh Le Dang; H. Hakola; T. Niemi; N. Tkachenko; B. Nazarchuk; V. Golovanov, Effect of light activation on chemical gas sensors based on aligned nanowires, The proc. of IEEE SENSORS, Rotterdam, the Netherlands 25-28 October, 2020 (online).

**V. Golovanova**; T. Andreu; J. R. Morante, 5th Scientific Meeting of BNC-b Students JPhD2020, Barcelona, Spain, 17-18 September, 2020 (online).

**V. Golovanova**; T. Andreu; J. R. Morante, Combined photo- and thermocatalytical approach for efficient CO<sub>2</sub> hydrogenation, EMRS Fall Meeting 2019, Warsaw, Poland, 16-19 September, 2019.

**V. Golovanova**; T. Andreu; J. R. Morante, Combined photo- and thermocatalytical approach for efficient CO<sub>2</sub> hydrogenation, DIPC School on Photo and ElectroCatalysis at the Atomic Scale PECAS 2019, Donostia-San Sebastián, Basque Country, Spain August 27-30, 2019.

V. Golovanov; **V. Golovanova**; N. Tkachenko, Organic dyes on wurtzite surface – orientation effects on the photoinduced charge transfer, The proc. of the 21st International Conference on Solid State Ionics, Padua, Italy, 18-23 June, 2017.